

# Tailored Bio-Hybrid Matrices for 3D Printed Tissue Models

**Radeke, Carmen**

*Publication date:*
2023

*Document Version*
Publisher's PDF, also known as Version of record

DTU Health Technology
Biomimetics – Tailored Materials and Tissues

# Tailored Bio-Hybrid Matrices for 3D Printed Tissue Models

Doctoral Dissertation
February 2023

Carmen Radeke

Supervisors:
Johan Ulrik Lind (Associate Professor, Technical University of Denmark)
Andrew James Urquhart (Associate Professor, Technical University of Denmark)

# Preface

This thesis fulfills the requirements for the Ph.D. degree set by the Technical University of Denmark (DTU). Most of the work described was performed at the group for Tailored Materials and Tissues (TMAT) led by Associate Professor Johan Ulrik Lind in the section for Biomimetics at the Department of Health Technology at DTU. Some experimental work was performed at other locations (stated in the respective sections). Parts of the experimental work presented in Chapter 3 was performed at the Università degli Studi di Pavia in the group of Synthetic Physiology led by Associate Professor Francesco Pasqualini. Parts of the experimental work presented in Chapter 4 were performed by a collaborating Ph. D. student Shaolong He at Københavns Universitet.

The presented projects were carried out from November 2019 until February 2023 under the supervision of Associate Professor Johan Ulrik Lind (main supervisor) and Associate Professor Andrew James Urquhart (co-supervisor).

Copenhagen, 1st of February 2023

Carmen Radeke

# Acknowledgements

First of all, meget stor tak to Johan for following his gut feeling and giving me the opportunity of doing my Ph. D. in his newborn group. It was truly an exciting and eventful journey. I am proud to be one of the first tomatoes growing on the now plentiful vine, that you are cultivating with security. Thank you for creating a safe space, in which we could discuss (scientific) ideas at eye level and always speak our minds.

Thanks to my co-supervisor Andrew, who co-led my interview when I first applied for the position and eased off this interview. I also appreciate your availability when we needed to perform last-minute experiments.

Grazie mille a Francesco & his team for taking me in his lab, guiding me not only through the fascinating world of microscopy but also through new perspectives.

Eternal thanks to Lotte, Lene, Helene, and Ole. We all know we'd be lost without them. Og tak Lene, for at være tålmodig og snakke Dansk med mig :).

It was great to experience our Biomimetics section come alive and actually have some socio-scientific events. Tak for vores sektionsleder Niels & everyone in this section for making this experience always pleasurable. Special thanks to Christina, the always inclusive and beerable 3B's Clara, Michelle, Shahana, Asli, Janko and of course our beloved lunch-crew: The Wellers Arji and Sven, Li – the one who caught a bee with chopsticks, Gaelin, Alexito and Ann-Kristin. That was much fun!

Thanks as well to every single Tomato: The founding tomatoes Selgin and Christian, Irene, Shayla, Marko, and Sarkhan, and my fantastic students Raphaël, Freja, Sara, Tasnim, and Jason. It is great to see our group grow and organize after-work dinners and boulder sessions :)

Lastly, I would like to thank my good friends, who accompanied me throughout the years and have always been an emotional support, specially Catrin and Lena for proofreading and (hopefully?) travelling to my defense! Meine Familie, Alina & Corina & Dorin & Maricarmen für bedingungslose Unterstützung, Verständnis in allen Lebenslagen, und Vertrauen in meine Entscheidungen. Muchisimas gracias a nuestra familia elegida en España, con la que nunca pasaremos un verano lluvioso. Ao final, serei eternamente grata pelo meu companheiro Marco, que me acompanhou durante boa parte deste tempo com paciência e compreensão e sempre conseguiu fazer as nuvenes escuras desaparecerem com um abraço mágico.

# List of Contributions

**Publications included in this thesis:**

**I)** **Radeke, C.,** Pons, R., Mihajlovic, M., Budayev, S., Roland, J. B., Kempen, P., Segeritz, C. P., Andresen, T. L., Pehmøller, C. K., Jensen, T. E., Lind, J. U. (2023). Transparent and Cell-Guiding Cellulose Nanofiber 3D Printing Bioinks. *ACS Applied Materials and Interfaces* 15, 2, 2564-2577. DOI:10.1021/acsami.2c16126

**II)** He, S., **Radeke, C.,** Jacobsen, J., Lind, J. U., Mu, H. (2021). Multi-material 3D printing of programmable and stretchable oromucosal patches for delivery of saquinavir. *International Journal of Pharmaceutics* 610. DOI:10.1016/j.ijpharm.2021.121236

**Publications not included in this thesis:**

**I)** Kajtez, J., **Radeke, C.,** Lind, J. U., Emnéus, J. (2023). Microgel-extracellular matrix composite support for embedded 3D printing of human neural constructs. *Journal of Visualized Experiments*. Submitted.

**II)** Cakal, S. D., **Radeke, C.,** Alcalá, J. F., Ellman, D. G., Butdayev, S., Andersen, D. C., Calloe, K., Lind, J. U. (2022). A simple and scalable 3D printing methodology for generating aligned extended human and murine skeletal muscle tissues. *Biomedical Materials* 17 045013. DOI:10.1088/1748-605X/ac6b71

**III)** Pless, C. J., **Radeke, C.,** Cakal, S. D., Kajtez, J., Pasqualini, F. S., Lind, J. U. (2022) Emerging strategies in 3D printed tissue models for in vitro biomedical research. *Bioprinting – Chapter 7* 207-246. DOI:10.1016/B978-0-323-85430-6.00007-8

**IV)** Jensen, J. H., Cakal, S. D., Li, J., Pless, C. J., **Radeke, C.,** Jepsen, M. L., Jensen, T. E., Dufva, M., Lind, J. U. (2020). Large-scale spontaneous self-organization and maturation of skeletal muscle tissues on ultra-compliant gelatin hydrogel substrates. *Scientific reports* 10, 13305. DOI:10.1038/s41598-020-69936-6

**Conference attendance:**

I) **Radeke, C.,** Pons, R., Butdayev, S., Kempen, P., Andresen, T. L., Lind, J. U. Transparent nano-fibrillar ECM-mimicking 3D bio-printing inks. Poster presentation at annual meeting of the European Organs-on-Chips Society in Grenoble (EUROoCs 2022).

**Patents:**

**I)** Lind, J. U., **Radeke, C.** Optically transparent carboxymethylated fibrillar cellulose with cell-instructive sizes and composites thereof for 3D printing (2022). Application filed.

# Abstract

Multi-material micro-extrusion three dimensional (3D) printing, also known as Direct-ink-writing (DIW), has opened new unique opportunities for the design and fabrication of complex bio-devices for in vitro and in vivo applications. Regardless of the application, the formulation of inks that are simultaneously printable and functional is perhaps the most critical challenge. Cellulose is appealing in this regard, as it is a versatile and affordable biomaterial that can be tailored extensively in terms of size, shape, and chemistry towards a specific intended application. In this thesis, I have studied the formulation of novel cellulose-based inks and print procedures towards two diverse applications: i) *in vitro* models of living mammalian tissue, and ii) oral drug-delivery patches.

Development of enhanced in vitro tissue models is of great interest to improve pre-clinical testing of novel drugs and development of patient-specific disease models. Within this thesis, the major focus was the development of new bio-inks for in vitro tissue models of mammalian tissues, based on logical modifications of microfibrillated cellulose (MFC). MFC has excellent printing properties while its fibrillar structure resembles the fibrillar network of the extracellular matrix (ECM). However, it is not translucent, which complicates microscopy, has no specific cell-adhesive motifs, and it is not miscible with protein biomaterials.

To overcome these shortcomings, we have here developed a procedure for partial carboxymethylation of MFC, to yield transparent, carboxymethylated nanofibrillated cellulose (cNFC) hydrogels, that can be combined with ECM-derived proteins. The procedure relies on careful adjustment of reaction degree by adjusting the polarity of the reaction solvents. The cNFC-derived inks show interesting properties for 3D printing functional tissue models. In addition to serving as rheological modifiers, they display unique cell-guiding abilities. Specifically, we demonstrate their ability to organize human and murine myotubes into anisotropic linear and complex patterns.

We also investigated cNFC as support matrices for embedded printing of cell-laden inks. We speculate, that the fibrillar structure of cNFC hydrogels might enhance cellular migration of cells within cNFC hydrogels compared to commonly used supports based on granular gel microparticles. However, studies are yet inconclusive. Still, we did observe that the spatial resolution of traces printed into cNFC supports was inferior to conventional granular hydrogel supports, likely due to viscous properties dominating.

A secondary project was the development of complex cellulose-based drug-delivery patches for the oral mucosa via DIW. Here, we tailored the design of the patches to increase their flexibility while decreasing the stiffness. Using multi-material printing further allowed us to precisely determine the drug-load per patch. Further, we added effervescent agents for improving delivery of saquinavir in the mouth.

Our studies showcase the versatility of cellulose-derived biomaterials for 3D printed biodevices, and demonstrates how rational modifications in material chemistry and formulation can serve to achieve complex functionalities. It is my hope that my work thus contributes to the ongoing

transformation of DIW 3D printing from mainly being research topic to becoming a tool for solving real-world problems and questions.

# Resumé

Multimateriale mikro-ekstruderings 3D-print har åbnet nye unikke muligheder for design og fremstilling af komplekse bio-systemer til in vitro og in vivo applikationer. Uanset applikationen, så er udviklingen af printbare og funktionelle printmaterialer den centrale udfordring. Cellulose er interessant i den henseende, da det er et alsidigt og billigt biomateriale, der i vid udstrækning kan skræddersyes til en given tilsigtet anvendelse, med hensyn til størrelse, form, og kemi. I denne afhandling har jeg studeret formuleringen af nye cellulosebaserede print-materialer og -procedurer til to forskellige anvendelser: i) in vitro-modeller af levende pattedyrsvæv og ii) orale lægemiddelindføringsplastre.

Udvikling af bedre in vitro vævsmodeller er af stor interesse for at forbedre præklinisk afprøvning af nye lægemidler og udvikling af patientspecifikke sygdomsmodeller. Inden for denne afhandling var hovedfokus udviklingen af nye bio-materialer til in vitro vævsmodeller af pattedyrvæv, baseret på logiske modifikationer af mikrofibrilleret cellulose (MFC). Mikrofibrilleret cellulose (MFC) har fremragende printegenskaber, mens dens fibrillære struktur minder om det fibrillære netværk i den ekstracellulære matrix (ECM). MFC er dog ikke transparent, hvilket komplicerer mikroskopi, har ingen specifikke celleadhæsive motiver, og er ikke blandbar med protein-baserede biomaterialer.

For at overvinde disse mangler har vi her udviklet en procedure til delvis carboxymethylering af MFC, for at give transparente, carboxymethylerede nanofibrillerede cellulose (cNFC) hydrogeler, der kan kombineres med ECM-afledte proteiner. Fremgangsmåden er afhængig af omhyggelig justering af reaktionsgraden ved at justere polariteten af reaktionsopløsningsmidlerne. De cNFC-afledte materialer har interessante egenskaber til 3D-print af funktionelle vævsmodeller. Ud over at fungere som rheologiske modifikatorer, udviser de unikke cellestyrende evner, når de printes på geloverflader. Specifikt demonstrerer vi deres evne til at organisere menneske- og musse-myotuber i anisotrope lineære og komplekse mønstre.

Vi undersøgte også cNFC som støttematricer til indlejret udskrivning af celle-bærende printmaterialer. Vores hypotese var, at den fibrillære struktur af cNFC-hydrogeler kan forbedre migration af celler i cNFC-hydrogeler sammenlignet med almindeligt anvendte understøtninger baseret på granulære gel-mikropartikler. Undersøgelserne er dog endnu usikre. Imens observerede vi at den rumlige opløsning af print-spor udskrevet i cNFC-understøtninger var ringere end konventionelle granulære hydrogel-understøtninger, sandsynligvis på grund af tyktflydende egenskaber, der dominerer.

Et sekundært projekt var udviklingen af komplekse cellulosebaserede lægemiddelindføringsplastre til mundslimhinden. Her skræddersyede vi designet af plastrene for at øge deres fleksibilitet og samtidig mindske stivheden. Brug af multi-materiale udskrivning gav os yderligere mulighed for præcist at bestemme lægemiddelbelastningen pr. plaster. Yderligere tilføjede vi brusemidler for at forbedre leveringen af saquinavir i munden.

Vores undersøgelser viser alsidigheden af cellulose-afledte biomaterialer til 3D-printede bio-systemer og hvordan rationelle ændringer i materialekemi og formulering kan tjene til at opnå

komplekse funktionaliteter. Det er mit håb, at mit arbejde dermed bidrager til den igangværende transformation af mikro-ekstruderings 3D-print fra hovedsageligt at være forskningsemne til at blive et værktøj der kan løse virkelige problemer og spørgsmål.

# Abbreviations

| | |
|---|---|
| Two dimensional | 2D |
| Three dimensional | 3D |
| Anhydroglucose unit | AGU |
| Alginate | ALG |
| Immortalized murine C3H mouse myoblast | C2C12 |
| Computer aided design | CAD |
| Cellulose crystal structure Type I-III | CELL I – III |
| Cellulose nanocrystals | CNC |
| Carboxymethylated nanofibrillated cellulose | cNFC |
| cNFC substituted with 20% or 40% more reactants | cNFC20/cNFC40 |
| Collagen | COL |
| Carboxyl | COOH |
| Decellularized extracellular matrix | dECM |
| Direct-ink-writing | DIW |
| Dulbecco's modified eagle medium | DMEM |
| Relative degree of substitution | $DS_{rel}$ |
| Young's Modulus | E |
| Ethyl cellulose | EC |
| Extracellular matrix | ECM |
| N-ethyl-N'-(3-(dimethylamino)propyl)carbodiimide/N-hydroxysuccinimide | EDC/NHS |
| Ethanol | EtOH |
| Fibronectin | FN |
| Fourier-transformed infrared spectroscopy | FT-IR |
| Storage modulus | G' |
| Loss modulus | G'' |
| Primary normal human epidermal keratinocytes | HaCaT |
| Hot melt extrusion | HME |
| Hydroxypropyl cellulose | HPC |
| High-performance liquid chromatography | HPLC |
| Hydroxypropyl methyl cellulose | HPMC |
| Human skeletal muscle cells | HSkM |
| Human fibrosarcoma cell line | HT1080 |
| Inner diameter | ID |
| Isopropanol | IPA |
| Low Bloom gelatin | LBG |
| Laminin | LN |
| Methyl cellulose | MC |
| Monochloroacetic acid | MCA |
| Methanol | MeOH |
| Melt electrospinning writing | MEW |

| | |
|---|---|
| Microfibrillated cellulose | MFC |
| Microphysiological platforms | MPS |
| Microbial transglutaminase | mTG |
| Sodium hydroxide | NaOH |
| Nanofibrillated cellulose | NFC |
| Polydimethylsiloxane | PDMS |
| Poly (methyl methacrylate) | PMMA |
| Microenvironmental pH | $pH_M$ |
| Arginine-glycine-aspartic acid | RGD |
| Solvent casting | SC |
| Scanning electron microscope | SEM |
| Standard error of the mean | SEM |
| Self-healing annealable particle-extracellular matrix | SHAPE |
| Stereolithography | SLA |
| Transmission electron microscopy | TEM |
| (2,2,6,6 – tetramethylpiperidin-1-yl)oxyl | TEMPO |
| Trypsinized gelatin | TG |
| Ultraviolet | UV |
| Xanthan gum | XG |
| X-ray photoelectron spectroscopy | XPS |

# List of Figures

# List of Tables

# List of Equations

# Table of Contents

# Chapter 1
# Introduction

## 1.1 Motivation

The development of novel drugs is a long, expensive process, in which approximately 90% of drug candidates fail to succeed in clinical trials.[1] Two of the main causes for clinical failure have found to be either lack of efficacy or safety,[2] despite the diverse array of currently available complex *in vivo* and *in vitro* tests. One major challenge is the inability to predict human reaction from typically relied upon animal models.[3,4] It is therefore of great interest to find new *in vitro* models based on human-derived cells that are more predictive of human reaction. Microphysiological platforms (MPS) with engineered human-derived tissues attempt to mimic physiological tissue and may help to model some aspects of human safety more accurately before clinical trials, reducing the rate of drug failure.[5–9] For this purpose, the 3D environment of engineered tissue requires high resemblance with the cellular composition, physical microenvironment, and chemistry of native tissue. 3D bioprinting was shown to be a promising tool for the potential construction of functional tissue models. Particularly DIW techniques allow multi-material printing of a broad range of soft and stiff (bio)inks. A core challenge remains in maintaining high printability and shape fidelity, while ensuring the formation of functional tissue. The most used bioinks to reconstruct the ECM of native tissue, are either ECM derived proteins and decellularized ECM (dECM) or fibrillar biopolymers, such as cellulose. MFC has been widely used as cell-laden ink due to its biocompatibility and excellent printing properties. Still, fibrillar ink-formulations are not transparent and impede the use of optical microscopy during tissue engineering.

The aim of this dissertation was to explore the fabrication and formulation of cellulose-based inks in 3D printing. Within this scope, I focused on the fabrication of i) *in vitro* models of living mammalian tissues based on transparent, fibrillar cellulose-based inks, and ii) oral drug-delivery patches with commercially available, transparent, crystalline cellulose-based inks. The new insights provided in this work will contribute to the development of 3D printed MPS by enabling the development of more accurate tissue models.

## 1.2 General introduction

### 1.2.1 Engineered tissues and *in vitro* tissue models

*The importance of developing more predictive preclinical assays*

The development of new drugs is a long, expensive process, in which half of possible drug candidates pass preclinical testing while only one out of nine succeeds in clinical trials.[10] A major challenge lies in identifying drugs that will fail in clinical trials earlier in the process of development. A reason for this is poor translation of toxicity studies from animal models to humans. Great interest in bridging this gap with engineered tissues and microphysiological systems has risen. Human-derived cells are incorporated in platforms that are supposed to mimic native organs. Different model systems for the brain,[11–14] heart,[5,9,15] lung,[16,17] and intestine[18–21] already show promising physiological responses to drugs.

*Engineered tissues mimic the native architecture and biochemistry of tissues*

In tissue engineering, a 3D scaffold is created to mimic the ECM and guide cellular growth and differentiation into functional tissue. For this, biochemical and -physical cues need to be incorporated in the scaffold to recapitulate native mechanics, architecture, and signaling. These scaffolds can be composed of synthetic and natural materials. The advantages of using synthetic polymers include high adjustability, control of molecular weight, and conjugation to cell-adhesive and cross-linkable motifs. Natural materials are usually biopolymers composed of amino acid sequences, such as proteins, or carbohydrates. While these biopolymers are not as easily modified as synthetic biocompatible polymers, protein-based biopolymers fully resemble the biochemistry of native tissue. Some are ionically or enzymatically cross-linkable and allow the production of stable gels in cell-culture. The choice of material is highly dependent on the final application and will vary depending on the requirements to mimic the tissue of interest.

Different tissues demand different properties of the materials they are cultured in. Apart from the stiffness of individual tissues, also the native working mechanisms vary. While heart and skeletal muscle tissue is composed of anisotropic layers of multinucleated myofibrils that are electrically connected and compact upon electrical stimulation,[5,22] lung tissue is composed of alveoli that rhythmically expand and contract with an ultrathin cell barrier at the air-blood interface.[16,23] Similarly, the intestine is composed of several crypt-villi subunits with a large surface area.[21] Lastly, the softest tissue in our body is the brain, natively almost completely isolated from its mechanical environment (Fig. 1).[24] Most examples of engineered tissues choose one major characteristic of a given tissue as design criteria for developing a scaffold.

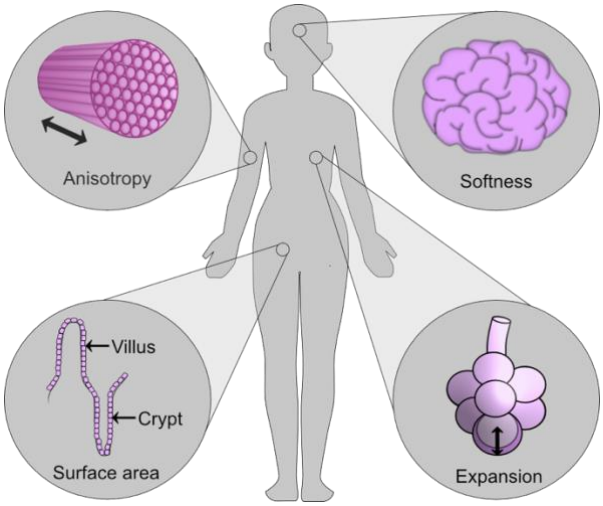


**Figure 1.** Illustration of the varying mechanical properties of different body parts.
Muscle tissue exhibits anisotropy. Brain tissue is the softest tissue in the body. The surface area of the intestine is comparatively huge due to protrusions, referred to as villi and valleys, referred to as crypts. The lung alveoli expand during breathing. Illustrations were made with Affinity Designer.

To specifically create a scaffold for cardiac and skeletal tissue models, the native anisotropy of these tissues needs to be replicated. It is well known that surface anisotropy and material stiffness not only guide cellular alignment but also differentiation.[25,26] Commonly used scaffolds rely on either micropatterned or nanofiber-based substrates. The fabrication of micropatterned substrates is often based on photolithographic techniques.[22,25,27–29] Ultraviolet (UV) light is used to transfer a pattern from an optical mask onto an either positive- or negative-photoresist-coated substrate. This pattern is then used to create a polydimethylsiloxane (PDMS) stamp to transfer the pattern onto different substrates via soft lithography, as illustrated in figure 2a. Resolutions of up to 70 nm and below can be achieved using specialized equipment.[30] The whole fabrication procedure is usually conducted in a clean room and varying the design of the optical mask is laborious. Apart from structural micropatterns, hydrogel-embedded and aligned fibers composed of polycaprolactone with gelatin/carbon nanotubes,[31–33] and modified myaluronic acid[34] have shown to guide cellular alignment. In this case, the fibers are synthesized via electrospinning. An electric field forces charged polymer fiber threads onto a solution or substrate. Similarly, in melt electrospinning writing (MEW) a polymer is melted and due to its high viscosity deposited accurately on a moving collector.[35] Nonetheless, harsh solvents are often used to fabricate fibers via electrospinning which might compromise cell viability in final applications. As an alternative, 3D printing has become an appealing technique as a wide range of water- and solvent-based materials can be used and designs can be easily tailored.

### 1.2.2 3D printing of engineered tissues: Technical and rheological requirements

*3D printing techniques for the fabrication of tissue models*

Additive manufacturing or 3D printing techniques have been rising to produce microphysiological platforms and engineered tissues due to the automated fabrication and flexibility in design and

fabrication methods. The term 3D printing encapsulates different working techniques, namely laser-based systems, inkjet-based systems, and nozzle-based extrusion systems. In 1986, the first laser-based printing technique was commercialized by Chuck Hull and is based on stereolithography (SLA). Herein, a photocurable resin is contained within a tank. A laser source induces polymerization and concomitant cross-linking of the liquid resin. The laser beam projects a pattern in the x- and y-plane, while a stage, onto which the resin polymerizes, moves in z-plane (Fig. 2b). By doing so, a 3D object is created layer-by-layer. Non-reacted resin is washed off in a post-treatment. With this technique a resolution of up to 30 µm can be achieved.[36] In Inkjet printing ink droplets are ejected from an either drop-on-demand or continuous inkjet system. In on-drop-demand systems an actuator leads the discharge of individual droplets with a predefined volume by creating a pulse. Continuous inkjet systems are based on a continuous inkjet stream, as the name suggests. Here, the jet is broken into individual droplets by an electrical signal that defines the movement of the droplet. The resolution of inkjet printing is similar to SLA ranging from 50 – 500 µm, with the smallest structure being printed in the range of 5 µm.[37] Lastly, extrusion-based systems, such as the previously described MEW or fused deposition modelling, are based on the layer-by-layer deposition of either melted or viscous and viscoelastic polymers, dispersions, and pastes.

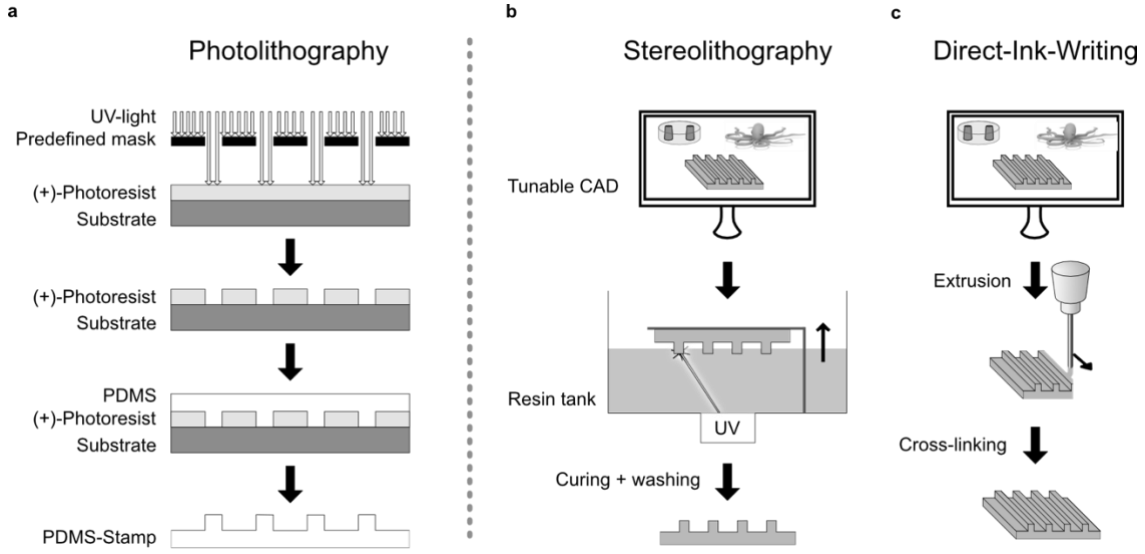


**Figure 2.** Illustrations describing production of anisotropic surfaces.
(a) Classical way of producing anisotropic surfaces via photolithography with a positive photoresist. (b) and (c) represent 3D printed substrates based on (b) stereolithography and (c) direct-ink-writing. Illustrations were made with Affinity Designer.

The working principle in extrusion-based systems, or DIW systems, is based on the extrusion of a material through a nozzle via pneumatic or mechanical pressure (Fig. 2c). The design of the printed structure is easily tailored via computer aided design (CAD). Material selection for DIW is straight forward compared to other techniques, such as SLA or MEW: Liquid inks for DIW solidify via solvent evaporation while viscous and viscoelastic inks exhibit shear-thinning properties and rapid thixotropic recovery. Cross-linking of the printed constructs occurs either through temperature-dependent gelation or (physico-)chemically. The overall resolution of the prints depends on the working mechanism of the printer (x-y-z movement), the nozzle diameters, and the speed of

deposition of the materials. Thin nozzles with a diameter of 30 µm have been used to print scaffolds with a spatial resolution of 60 µm.[5] While the resolution of SLA is higher, a wider range of materials can be used for DIW.

*Rheological requirements for DIW printing*

The working principle of DIW relies on a material being extruded through nozzle and deposited upon a substrate. Liquid, viscous, and viscoelastic materials can be used as inks. Depending on the material's mechanical properties, the mechanism of keeping the shape-fidelity of the printed structure varies. Thin films can be printed by using liquid or low-viscosity inks at low pressures. Film formation occurs after solvent evaporation. To print 3D structures, shape-fidelity is achieved by using viscoelastic materials (Fig. 3a). The mechanical properties of viscoelastic materials are based on interactions between particles and polymers, which will behave solid-like or elastic under no stress, while rearrangement occur when stress is exerted on them.

The shear stress $\tau$ exerted upon a material depends on the area A ($m^2$) and force F (N) (1), and causes the material to strain $\gamma$ (2) depending on its height h (m) and total deflection s (m) (Fig. 3c). The mechanical properties of the material will be reflected when applying shear stress at varying shear rates $\dot{\gamma}$ (1 $s^{-1}$) (3). The viscosity $\eta$ (Pa s) is dependent on the shear stress and shear rate (4):

$$\tau = \frac{F}{A} \tag{1}$$

$$\gamma = \frac{\mathrm{s}}{\mathrm{h}} \tag{2}$$

$$\dot{\gamma} = \frac{\mathrm{v}}{\mathrm{h}} \tag{3}$$

$$\eta = \frac{\tau}{\dot{\gamma}} \tag{4}$$

For Newtonian liquids, such as water, shear stress exerted on the material is linearly correlated to the strain rate. Non-Newtonian fluids exhibit a non-linear correlation between shear stress over strain. The flow behavior of non-Newtonian fluids can be divided into time dependent and time independent, which can be further broken down into shear dependent and independent. Here, we will only focus on shear dependent shear-thinning pseudoplastics. Micro-structural rearrangements of particles or fibers within shear-thinning fluids need to be broken down to induce flow. The flow is induced by surpassing a minimum stress threshold referred to as "yield stress" (Fig. 3b,e), which is the stress needed to break down or rearrange microstructural formations of particles or polymers within the materials. At low shear rates, the viscosity will not change. This region is referred to as zero-shear viscosity ($\eta_0$, Fig. 3b), which results from interactions between particles or polymers such as particle jamming, or polymer entanglement (Fig. 3f). Shear-thinning materials regain their viscoelastic

properties immediately after a shearing force is removed. In contrast, thixotropic shear-thinning materials exhibit time-dependent recovery.

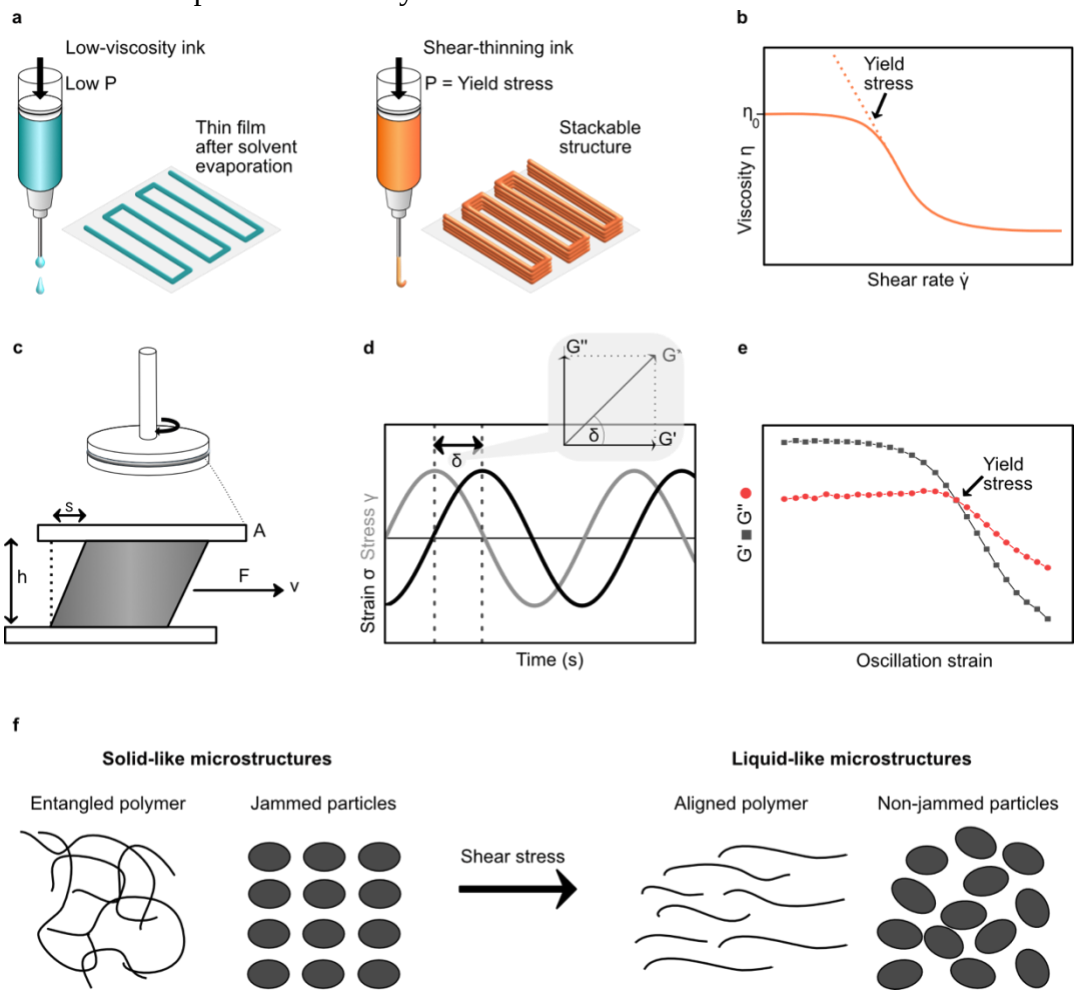


**Figure 3.** Rheology of Direct-ink-writing.
(a) Extrusion of a low-viscosity (blue) and shear-thinning (orange) ink. Low shape-fidelity of low-viscosity inks allows for fabrication of thin films after i.e. solvent evaporation. Shear-thinning inks recover shape-fidelity after extrusion and can be stacked. (b) Illustration of shear rate dependent viscosity of shear-thinning ink. Zero-shear viscosity ($\eta_0$) at low shear rate and apparent yield stress indicated with dotted line. (c) Illustration of two-plate model used to calculate shear stress, shear strain, shear rate, and viscosity of materials. (d) Strain curve and stress response of a material during an oscillatory experiment. Phase shift δ indicates viscoelastic properties of material and is used to calculate storage G', loss G'', and complex G* modulus of the material. Insert: vector representation of the individual moduli. (e) Storage G' (grey square) and loss G'' (red dot) modulus of shear-thinning material yielding at increasing oscillatory strain. (f) Illustration of microstructural arrangements of polymers and particles at rest (left) and under shear stress (right). Illustrations and graphs were made with Affinity Designer.

The viscoelastic properties of a material can be examined during oscillatory shear experiments. Here, the material is placed at a predefined height and geometry between a stationary and a rotating plate (Fig. 3c). The rotating plate applies a sinusoidal stress γ (5) upon the material, while the strain response σ (6) is detected. The phase shift δ between the stress curve and strain response indicates, whether a material behaves purely elastic ($\delta = 0°$), purely viscous ($\delta = 90°$), or viscoelastic ($0° > \delta > 45°$). From this, the storage G' and loss G'' modulus can be calculated, which further describe the

viscoelastic properties of the material, as well as the overall stiffness, defined as Young's modulus E with ν = Poisson's ratio (7):

$$\gamma = \gamma_0 \sin(\omega t) \quad (5)$$

$$\sigma = \gamma_0 (G'(\omega)\sin(\omega t) + G''(\omega)\cos(\omega t)) \quad (6)$$

$$E = 2G'(1 + \nu) \quad (7)$$

The Young's modulus is a great indicator to predict, whether a material is suitable for tissue engineering by comparing it with known Young's moduli of different tissues.[38]

*Considerations for 3D bioprinting*

In DIW the shear-thinning and thixotropic behavior of the inks dictates the printability. The initial viscosity of the material will influence the stress that has to be applied for the material to flow. Stress acting upon the material before it flows will strain the material. When performing bioprinting with living cells, this must be considered. Cells experience fluid shear within a needle with cylindrical cross section, compressive and extensional stress when being extruded within a viscous material in a nozzle. Mechanical stress upon the cells has shown to reduce cell viability during bioprinting.[39–41] Depending on the pressure or velocity, at which the bioink is extruded, the cells will feel velocity gradients, with the maximum shear stress being near the inner walls of the nozzle, causing extensional stress. This maximum shear stress will increase with increasing pressure and inner diameter of the needle.[42] This fluid shear stress is solely dependent on pressure and needle geometry, while the viscosity of the ink may be neglected. Still, the higher the viscosity of the ink, the higher the pressured needed to extrude it. Conversely, the use of nozzles with inner diameters of > 200 µm and lower viscosity and shear-thinning bioinks require lower pressure and therefore lower fluid shear stress.[43] The most prominently used materials for bioprinting are protein-based materials, such as gelatin[44] or collagen,[45] and biopolymers like alginate and cellulose.[46,47] The mechanical properties are concentration-dependent and can be tailored depending on the application. Furthermore, gelatin and collagen undergo thermal gelation and can be used prior to gelation as cell-laden inks without compromising cell-viability due to their low viscosity. During deposition of the bioink gelation is induced, allowing to maintain shape-fidelity. Biopolymers like alginate and cellulose exhibit low viscosity and shear-thinning behavior and will maintain their shape after printing. Still, low concentrations must be used to avoid over shearing the cells at high pressures.

*Embedded printing of soft tissues*

The fabrication of dense 3D tissues is limited by two major factors. Firstly, choosing low-viscosity cell-laden inks maintains cell viability but compromises shape stability of complex bioprints. Secondly, 3D tissue is limited in size to avoid necrosis. To circumvent the use of low-viscosity cell-laden inks, 3D tissue models have been relying on suspending the tissue within two anchoring points, such as pillars or ribbons.[9,48] Here, the cells are seeded onto the platform and compact the matrix into a dense, free-standing tissue. Other approaches include 3D printing into a support matrix that

counteracts the flow of the printed, low-viscosity cell-laden ink. This technique called embedded printing has shown promising results in the fabrication of soft tissues with the additional option of vascularization to perfuse oxygen and nutrients. The support matrix is composed of non-thixotropic, shear-thinning, jammed microparticles of cross-linked hydrogels, such as alginate or gelatin.[49–52] The cross-linked hydrogel-based microparticles are tightly packed within a confined space. When a low shear is applied, the particles undergo rearrangements that cause a localized collective flow. The transition from the disordered, chaotic state, to the rearranged, non-chaotic state, is referred to as jamming transition.[53] At a larger scale, the jammed particles behave as solid, and a moving needle causes yield stress allowing for deposition of a material within the solid due to immediate re-solidification or rearrangement of the particles. By doing so, low-viscosity inks can keep their shape within the printed structure. The low stiffness of the support matrices further mimics the ECM and presents a deformable matrix for cells to expand. The addition of ECM-derived proteins such as collagen further showed enhancement in rheological properties of the support matrix, resulting in higher resolution during printing due to a decreased fluidized area.[54]

### 1.2.3 Biomaterials as ink candidates for Direct-ink-writing of tissue models

*Common ink biomaterials: Biochemistry vs. shape fidelity*

The classical approach to mimic native ECM is using ECM-derived proteins and polymers, such as collagen, gelatin, fibrin, hyaluronic acid, and Matrigel®, or dECM. The biochemical and mechanical properties of these materials make them promising choices since they replicate the ECM to the fullest. dECM, collagen and Matrigel® undergo irreversible polymerization affiliated with their collagen content. Its peptide sequences polymerize into tertiary triple helical structures triggered by increasing temperature to 37 °C. At temperatures below 5 °C, they exhibit low viscosity and flow under low pressure. Extrusion of these inks onto heated plates initiates the polymerization into soft gels. Furthermore, the triple helical structure serves not only as anchoring point but as guidance for cellular alignment.[45] Gelatin, which is derived from collagen, polymerizes reversibly at low temperatures, while it is liquid under physiological conditions. Enzymatic cross-linking is necessary to maintain shape-fidelity under cell-culture conditions. The length of the triple helical structures defines the Bloom of the gelatin and the concomitant gel strength after polymerization. The length of the polymerized helical structures is not comparable to collagen and does not guide cell alignment. Nonetheless, the stiffness of substrates has been known to induce spontaneous organization of skeletal muscle cells on ultra-soft gelatin substrates.[55] This has led to the development of a printed gelatin substrate with spatially alternating concentrations of gelatin and Bloom that induced cellular alignment.[56] Similarly, fibrinogen is cross-linked enzymatically by thrombin to yield fibrillar fibrin. These examples demonstrate the high variability of choice of low-viscosity inks and concomitant approaches to maintain the printed structure complexity and the development of functional tissues. Some examples of functionalizing ECM-derived materials exist, with the most prominent being methacrylated gelatin that allows for cross-linking after printing via UV-light.[57,58]

Yet, dECM and ECM-derived proteins from native tissue are accompanied by large batch-to-batch variations. In addition, further functionalization of these materials is limited. (Bio)polymers are easily tailored and functionalized to better mimic the biochemical properties of the ECM. Examples

of biopolymers often used in tissue engineering are carbohydrates such as alginate and xanthan gum (XG),[59,60] and cellulose,[47] and other synthetic polymers such as polyethylene glycol[61] and poloxamers.[62] Particularly fibrillar biomaterials have gained great interest due to their excellent printing properties and replication of the fibrillar network of the ECM. Cellulose fibers have been widely used and printed into human tissue-resembling structures, such as e.g. an ear.[47,63] The free hydroxyl groups of the cellulose polymer are easily chemically modified, and a variety of functional groups can be added. Additionally, the fibers can be degraded into smaller parts yielding new mechanical and optical properties. It has been shown that by oxidizing the hydroxyl groups the cellulose fibers are broken down to the nm scale and act as transparent, shear-thinning hydrogel. The use of this material as a support matrix for embedded printing showed high shape-fidelity of prints and can be compared to its particle-based counterparts.[64] The versatility of modifications and promising printing properties make it an interesting material for 3D printing.

*Cellulose: Chemistry and extraction of primary pulp*

Cellulose is the most bountiful biopolymer on earth as the main structural component of all trees and plants. The smallest structure of cellulose belongs to the group of carbohydrates, being composed of β-d-glucopyranose units that are interconnected through β-1-4-glycosidic bonds. The monomeric unit of this biopolymer is the combination of two β-d-glucosepyranose units also referred to as anhydroglucose units (AGU), of which one is turned by 180 °. The β-d-glucosepyranose units take a $^4C_1$ conformation. The hydroxyl groups are therefore laying horizontally, while all hydrogen atoms are positioned vertically. Intramolecular hydrogen bonds stabilize this structure and further determine the crystalline structure of some parts of the cellulose fibers. The individual polymer molecules are packed together forming long, water insoluble fibrils that take alternating amorphous and crystalline conformations (Fig. 4). These crystalline regions form due to strong intra- and intermolecular hydrogen bonds between the hydroxyl groups. The crystallinity of naturally extracted cellulose is referred to as Type I cellulose (CELL I) and comprises parallel packing of the hydrogen-bonded cellulose network. CELL II exhibits antiparallel packing of the hydrogen-bonded network. CELL II allomorphs arise from swelling native cellulose in NaOH, a process referred to as mercerization, named after its inventor John Mercer,[65–67] or by regeneration of native cellulose, which means preparing a dissolution of native cellulose in a solvent, followed by precipitation in water.[68] Modifications with ammonia leads to CELL III, while additional heating of CELL III leads to CELL IV. The different types of crystallinities influence the physical properties of the cellulose and therefore, its stiffness. The Young's modulus of CELL I structures is higher compared to CELL II or CEL III.[69] Breaking down cellulose fibrils into its crystalline units leads to nanocellulose or cellulose nanocrystals (CNC), which are often also referred to as whiskers, nanorods, microcrystals, nanofibers, or nanoparticles due to their small size and spike-like appearance. Their length spans from 100 – 600 nm and diameters between 2 – 20 nm. Maintaining the fibrillar structure of native cellulose and keeping lengths of over 1 µm with diameters between nm and µm leads to microfibrillated cellulose (MFC). Naturally, approximately 36 cellulose polymers form an individual fibril, of which several assemble to form microfibrils, while several microfibrils assemble into cellulose fibers (Fig. 4). Breaking down of cellulose fibers into its subunits and pulp and subsequent functionalization is

highly influenced by the source, with wood being the most prominent one, followed by sugar beet pulp,[70] wheat straw,[71] palmtrees,[72] and even carrots.[73]

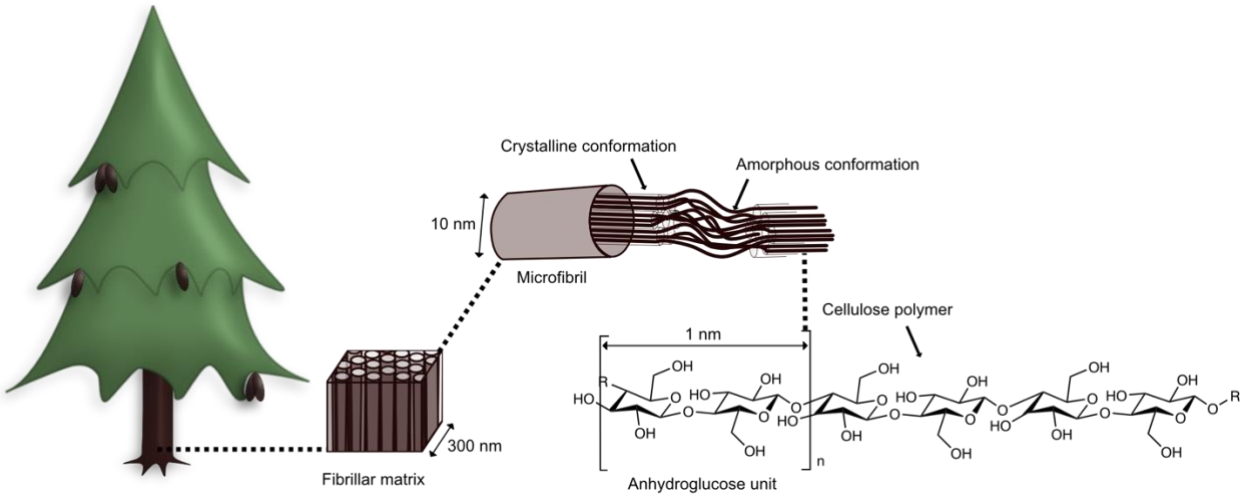


**Figure 4.** Illustration of cellulose polymer-based fibrils.
Illustration adapted from Moon *et al.*[74] Wood is composed of a fibrillar matrix made up of individual microfibrils. Each microfibrils comprises approximately 36 cellulose fibers. Each cellulose fiber has crystalline and amorphous parts. The molecular structure of each fiber is the cellulose polymer. The cellulose polymer can be further broken down into its anhydroglucose units. Illustration was made with Affinity Designer and ChemSketch.

The main route of obtaining CNC is by hydrolysis of the cellulose fibers into its crystal subparts by acids. The hydrogen ions will attack the glycosidic bonds between monosaccharide units of the amorphous regions, hydrolyzing these bonds and breaking down the fibrils into small, intact crystalline parts. The final physicochemical properties of CNC depend on where the cellulose was extracted from and how the hydrolysis was performed. Commonly, hydrochloric and sulfuric acid are used. While hydrolyzing the fibers with hydrochloric acid yields CNC with low water solubility,[75] sulfuric acid enhances dispersion in water. A negative charge is introduced to the CNC by addition of sulfate esters onto the hydroxyl groups.[76] This surface modification further influences the rheological behavior of CNC. Sulfate-modified CNC is purely shear-thinning, while hydrochloric acid-treated CNC is thixotropic.[75]

In contrast to CNC, MFC is composed of amorphous and crystalline parts and comprises the whole length of a microfibril. It is easily obtained by mechanical disintegration of cellulose, the procedure for which was first patented in 1983.[77] A so-called Gaulin homogenizer is used, in which cellulose fibers are highly sheared under low pressure due to the rapid sequences of opening and closing of a spring-loaded valve. Alternatively, the pulp is squeezed through thin z-shaped chambers in a microfluidizer under pressures around 2070 bar.[73] Other techniques include grinding in a rotating and a static grindstone grind the fibers at 1500 rpm,[78] cryocrushing of frozen pulp,[79] and electrospinning.[80] Mechanical disintegration of cellulose fibers is laborious and linked to a high energy consumption. Pre-treatments of the pulp can enhance the procedure and reduce its energy cost. Enzymatic degradation with endoglucanases facilitates mechanical disintegration but decreases the final size of the microfibrillated cellulose fibers.[81,82] Apart from breaking down the fibrillar structure,

adding surface charge will improve electrostatic repulsion and breaking of fibrillar aggregates within MFC fibrils.

*Functionalization of cellulose nanocrystals and microfibrillated cellulose*

Functionalization of CNC and MFC not only enhances their dispersibility in aqueous medium, but also presents the possibility of changing the chemical properties. An easy way of adding charge to CNC and MFC is by oxidizing the hydroxyl groups to aldehyde or carboxyl groups. For this, the frequently known catalyst for oxidation (2,2,6,6-tetramethylpiperidin-1-yl)oxyl (TEMPO) is used. When using native cellulose with predominantly crystal structures CELL I, the hydroxyl groups are not as accessible as needed for successful oxidation. Treating native cellulose to yield allomorphs with crystalstructure CELL III was shown to increase efficiency of oxidation.[83] Isogai and Kato were the first ones to compare oxidizing native cellulose and mercerized cellulose with TEMPO, sodium hypochlorite and sodium bromide. They observed that only oxidation of mercerized cellulose yielded a clear solution.[84] Since then, TEMPO-oxidized cellulose is widespread and used in different areas due to its biocompatibility, degradability, accessibility, optical properties, and the possibility of additional functionalization. Nevertheless, its transparency comes with the price of reducing the size of the fibers to the nanometer scale.

A different approach to provide charged fibers is by functionalizing the hydroxyl groups via carboxymethylation. Here, a carboxymethyl group is added to the hydroxyl group during a substitution reaction. It was shown that the polarity of the solvents further drove the efficiency of the reaction, with more apolar solvents yielding higher substituted carboxymethylated MFC fibers.[85–87] As mentioned in the previous paragraph, the mercerization of cellulose or its treatment with certain solvents might influence the type of packing in the crystalline sections. Interestingly, in these examples the fibrillar morphology of MFC was maintained, while the dispersion of MFC in aqueous solution was stable, yet not fully transparent. Carboxymethylation has also been used to produce transparent, carboxymethylated CNC and is widely used and commercially available.[64,88–90]

TEMPO-oxidation and carboxymethylation are both examples of providing surface charge to otherwise water-insoluble CNC and MFC, therefore increasing their stability in aqueous solutions. In contrast, etherification can be used to tune amphiphilic properties. Etherification occurs by alkylation of the hydroxyl group with alkyl halides in alkaline solution after Williamson, or after Michael by addition of reagents with activated double bonds. Ethyl cellulose (EC) is the most used derivate. EC is applied in food packaging and as additive in nail polish and plastics. Its solubility in different solvents is dependent on the degree of substitution.[91] Methyl, hydroxypropyl, and hydroxypropyl methyl cellulose (MC, HPC, HPMC) are further examples of amphiphilic, biocompatible cellulose derivates, with HPMC gaining special attention due to its increased thermal stability (Fig. 5).[92] Its use in food packaging and drug delivery has been extensively studied. Particularly HPMC is an appealing material for drug delivery due to its amphiphilicity, transparency, and rheological properties.[93,94] Its chemical structure provides hydrophobic interactions with drug candidates while simultaneously being soluble in water. Furthermore, it swells in aqueous solution and has been used as thickener in food as an alternative to gelatin. Additionally, its viscous properties have allowed its demonstration as a print-material for 3D printing applications.[95,96]

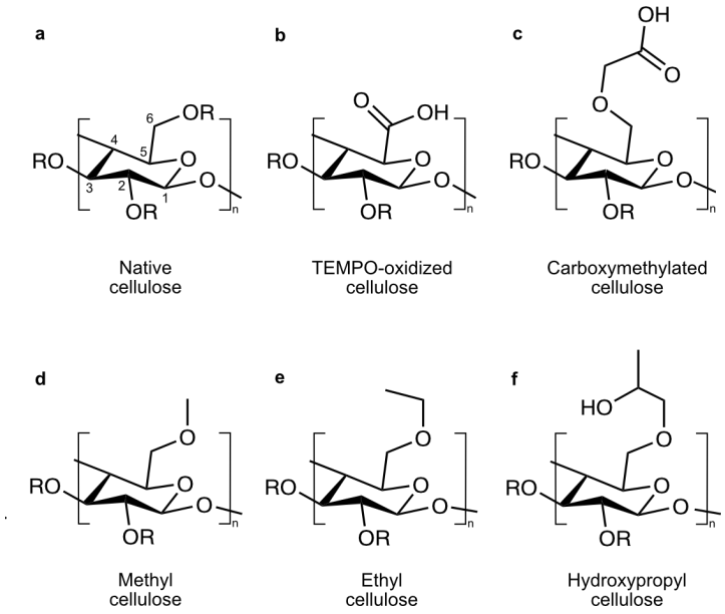


**Figure 5.** Modifications of cellulose.
(a) Native cellulose, (b) TEMPO-oxidized cellulose, (c) carboxymethylated cellulose, (d) methyl cellulose (MC), (e) ethyl cellulose (EC), (f) hydroxypropyl cellulose (HPC). Chemical structures were created with ChemSketch.

*Current limitations of cellulose-based tissue models*

Functionalization of cellulose fibers is only limited by the creativity of the scientists working with it. Other examples of surface functionalization include carbamation,[97] esterification,[98] silanization,[99] and amidation.[100] Considering its application in DIW of engineered tissues and microphysiological platforms, the functionalization of CNC and MFC with cell-active substances is of great interest. The functionalization of TEMPO-oxidized and carboxymethylated cellulose with arginine-glycine-aspartic acid (RGD) sequences and carbohydrate-binding, recombinant proteins was already shown to promote cell-adhesion.[101–103]

The versatility of cellulose enables opportunities to explore its use in direct-ink-writing applications. Commercially available CNC, MFC, TEMPO-oxidized, and carboxymethylated variants have been extensively explored in tissue engineering and DIW. Demonstrations of transparent cellulose in tissue engineering include carboxymethyl cellulose as a 3D printed porous scaffold for active wound dressing,[88] as well a support matrix for embedded printing,[64] and TEMPO-oxidized cellulose as osteoblast-bioink capable of inducing osteogenesis in 3D printed scaffolds.[104] Still, independent on whether these transparent cellulose derivates are functionalized with a carboxymethyl group or TEMPO-oxidized, their fibrillar structure is lost. MFC cellulose derivates, while exhibiting excellent printing properties,[47] are less frequently used in tissue engineering due to their impaired optical properties. Still, while both CNC and MFC exhibit shear-induced alignment during 3D printing,[105,106] only MFC matches the length of native collagen in the ECM and will induce cellular alignment. The fabrication of transparent yet fibrillar, functionalized MFC derivates for 3D printing applications is therefore highly appealing. Its excellent printing properties and ease of modification will enhance the fabrication of anisotropic surfaces and the development of mature, functional muscle tissue.

### 1.3 Outline

In this work, the fabrication and formulation of cellulose-based inks in 3D printing is explored within two major applications: i) *in vitro* models of living mammalian tissues, and ii) oral drug-delivery patches. This work is presented as the following chapters:

I. **Chapter 2: Cell-guiding nanofibrillar bioinks.** An alternative method to fabricate transparent but microfibrillar, cellulose-based inks is presented. For this, the solvents used for the carboxymethylation reaction will be tailored to preserve the fibrillar structure of the cellulose microfibrils while yielding a transparent gel. We will investigate further functionalization of the carboxymethylated fibers with proteins. In addition, the formulation of composite-inks will be discussed, and how they can be used to promote cell-alignment of human and murine skeletal muscle cells for functional, engineered muscle tissues.

II. **Chapter 3: Carboxymethylated nanofibrillated cellulose as support matrix for embedded printing.** As a continuation of chapter 2, the formulation of carboxymethylated fibers will be used as support matrix for embedded printing of tissues. Here, we explore increasing the degree of substitution and scaling up the overall reaction to increase the yield. This hydrogel formulation will be compared to commonly used, particle-based systems in terms of shape-fidelity of prints within the matrix. Lastly, the migration of cells within the material will be explored using a fluorescently labeled epithelial cell line.

III. **Chapter 4: Multi-material 3D Printing of Programmable and Stretchable Oral Patches for Buccal Delivery of Saquinavir.** Lastly, the use of cellulose-based inks for printing of oral drug-delivery patches will be explored. The formulation of stretchable oral patches will be based on commercially available, functionalized cellulose as drug-carrier material. The design of the patches will be varied to increase its stretchability while decreasing its stiffness for optimal patient comfort. In addition, we show multi-material printing of programmable drug content, as well as effervescent agents.

IV. **Chapter 5: Conclusion and outlook.** Here, a conclusion and outlook into additional work will be provided.

# Chapter 2
# Cell-guiding nanofibrillar bioinks

---

The following chapter is based on the accepted manuscript "Transparent and cell-guiding cellulose nanofiber 3D printing bioinks" and discusses cellulose-based, fibrillar inks for cell guidance. The following passages have been cited with minor changes: Section 2.3 except 2.3.2 and the first part of 2.3.3. Experimental and supplementary sections 2.5, 2.6.

## 2.1 Introduction

3D extrusion-based printing is becoming an essential tool in tissue engineering revolutionizing platform production for tissue culturing and the development of organs-on-chips.[5,52,107] In 3D bioprinting, CAD is used to develop patient specific, complex tissue scaffolds that are 3D printed by deposition of biomaterials and cell-laden inks with precise spatial control. The main obstacle here is to choose a biomaterial with excellent printing properties while mimicking the native ECM and promote cellular growth and differentiation into functional tissue.[108,109] Traditionally, the main types of materials used as bioinks are either based on proteins derived from the ECM (Collagen, Matrigel, dECM) or natural and synthetic fibrillar inks (alginate, hyaluronic acid, cellulose). Fibrillar bioinks are of great interest due to their shear-thinning properties and high shape-fidelity while also recapitulating the fibrillar architecture of the ECM.[47,104,110–112]

ECM-derived proteins have been widely studied as main ink material. Here, shape-fidelity of the printed structure is obtained by thermally induced polymerization of the fibrillar proteins within the gels upon deposition. Prevailing examples for this are collagen and Matrigel, where the increase of temperature after printing triggers polymerization of the proteins into fibrils.[113,114] Similarly, fibrinogen undergoes post-printing polymerization by addition of thrombin, which converts fibrinogen into fibrillar fibrin.[115] A different approach comprises the pre-production of micro- and nanofibrils based on collagen,[116] hyaluronic acid,[34] electrospun, fragmented polymers such as polycraprolactone,[33] and cellulose.[47,104,110–112]

Cellulose based micro- and nanofibers often appear in literature under a variety of names linked to different structural properties. The smallest structures are often referred to as CNC and have diameters of ~2 – 20 nm and lengths of 100 – 600 nm. The longest fibers are referred to as MFC with lengths above 1 µm and diameters stretching from the nano- to micro-scale. The intermediated term nanofibrillated cellulose (NFC) often refers to fibers with a similar length as MFC with diameters in the nano-range. All the mentioned types of cellulose are biocompatible, shear-thinning, easy to produce, and have been therefore studied for 3D printing applications.[47,64,105,106,117,118] A common example of a human-like, 3D printed structure is an ear printed with an ink based on MFC and alginate and cross-linked with calcium.[47] Herein the complex architecture of the ear is recapitulated in detail, but the construct lacks optical clarity to track cellular development within the print. Since MFC is

composed of large, wide fibrils, light is diffracted and causes opacity. Examples of shorter cellulose fibrils overcome this problem and exhibit transparency while maintaining shear-thinning properties.[104,111,112,119,120] Shorter fibrils are produced by oxidizing the fibers using TEMPO. The oxidized moieties can be further functionalized with peptides and proteins.[121,122] Still, the size of the fibers is decreased to the range of single microns and less[123,124] failing to recapitulate the size of collagen fibers (20-200 μm[125]) and therefore failing to guide spatial tissue organization.

We present an alternative protocol to functionalize cellulose fibers achieving optically transparent MFC inks with fiber lengths of above 10 μm and widths below the wavelength of light. Herein, we tune the carboxymethylation reaction[85–87,89] to partially functionalize MFC and yield transparent, fibrillar, shear-thinning hydrogels.

## 2.2 Aims

In this chapter, we defined the following aims:

I. **Partial functionalization of MFC via carboxymethylation:** We aimed at maintaining the fibrillar structure of MFC while partially functionalizing the surface to yield a transparent, shear-thinning cNFC hydrogel. The fibrillar structure of MFC will preserve lengths above 10 µm and widths below the wavelength of light.

II. **Coupling of small proteins onto functionalized cNFC**: The carboxymethyl-functionality of cNFC allows to couple molecules onto the fibers. Here, coupling of small, cell-adhesive proteins onto cNFC will be explored to yield a printable, transparent and cell-adhesive ink.

III. **Formulation of cross-linkable composite-inks:** Pure cNFC hydrogels are not cross-linkable and will disintegrate when submerged in aqueous solutions. We will formulate cross-linkable composite-inks based on carbohydrates, such as alginate, and ECM-derived proteins, such as gelatin.

IV. **Printing of cell-guiding substrates for skeletal muscle cell maturation:** Our hypothesis of shear-induced fiber alignment in our cNFC:gelatin inks will be examined using human and murine derived skeletal myoblasts. Myoblasts will fuse into polynucleated myofibers and show signs of maturation and striated muscle tissue on anisotropic cNFC:gelatin substrates.

## 2.3 Results and discussion

As our base material, we applied a commercially available aqueous MFC paste, which was generated from wood pulp cellulose by mechanical shearing. Without further modifications, the MFC was readily printable from concentrations ≥ 1% w/v with a characteristic white appearance, indicative of fibers and aggregates scattering visible light. To improve material transparency, we chose carboxymethylation, which has previously been applied to generate transparent MFC.[126,127] However, similarly to cellulose nanofibrils generated using TEMPO oxidation, reported transparent carboxymethylated fibers have diameters < 20 nm and lengths ~ 1 µm, limiting their structural similarity to ECM protein nanofibers.[126,128,129] To gain transparency while retaining structural properties, we here aimed to generate fibrils with diameters just below the wavelength of visible light.

### 2.3.1 Partial functionalization of MFC via carboxymethylation

*Influence of solvent polarity and reactants on carboxymethylation of fibers*

To control the degree of carboxymethylation, we investigated the effect of adjusting solvent composition in detail. In addition to amount of reactants, solvents have previously been shown to influence the overall degree of reaction[130] in bulk cellulose treatments. In general, the reaction comprised two steps: i) Dispersing a stock MFC aqueous paste (10% w/v) in polar organic solvent for mercerization with sodium hydroxide (NaOH), ii) etherification with monochloroacetic acid (MCA), see Figure 6a. For the majority of our studies the amount of reactants relative to cellulose AGUs were 2.5:1 NaOH:AGU and 1:1 MCA:AGU. In addition, 1.25:1 NaOH:AGU and 0.5:1 MCA:AGU were tested. To evaluate the degree of reaction we applied Fourier transformed-infrared spectroscopy (FT-IR) and quantified the relative degree of substitution ($DS_{rel}$) by relating the stretching vibration of the carboxylate peak at 1595 $cm^{-1}$ to the stretching vibration of the C-H group at 2894 $cm^{-1}$, similarly to Miyamoto *et al.:*[131]

$$\mathrm{DS_{rel}} = \frac{\mathrm{NA_{1595\ cm^{-1}}}}{\mathrm{NA_{2894\ cm^{-1}}}} - \mathrm{C} \tag{8}$$

We initially screened common polar alcohols including methanol (MeOH), ethanol (EtOH), and isopropanol (IPA). Only in the least polar alcohol, IPA, did we observe a notable carboxylate peak, indicative of a successful reaction (Fig. 6b). We therefore hypothesized that the degree of reaction may be tuned by adjusting the polarity of IPA:EtOH mixtures. Fourier-transformed infrared spectroscopy (FT-IR) indicated that this was indeed the case (Fig. 6c). We further observed that the optical transparency qualitatively increased with decreasing solvent polarity (Fig. 6d).

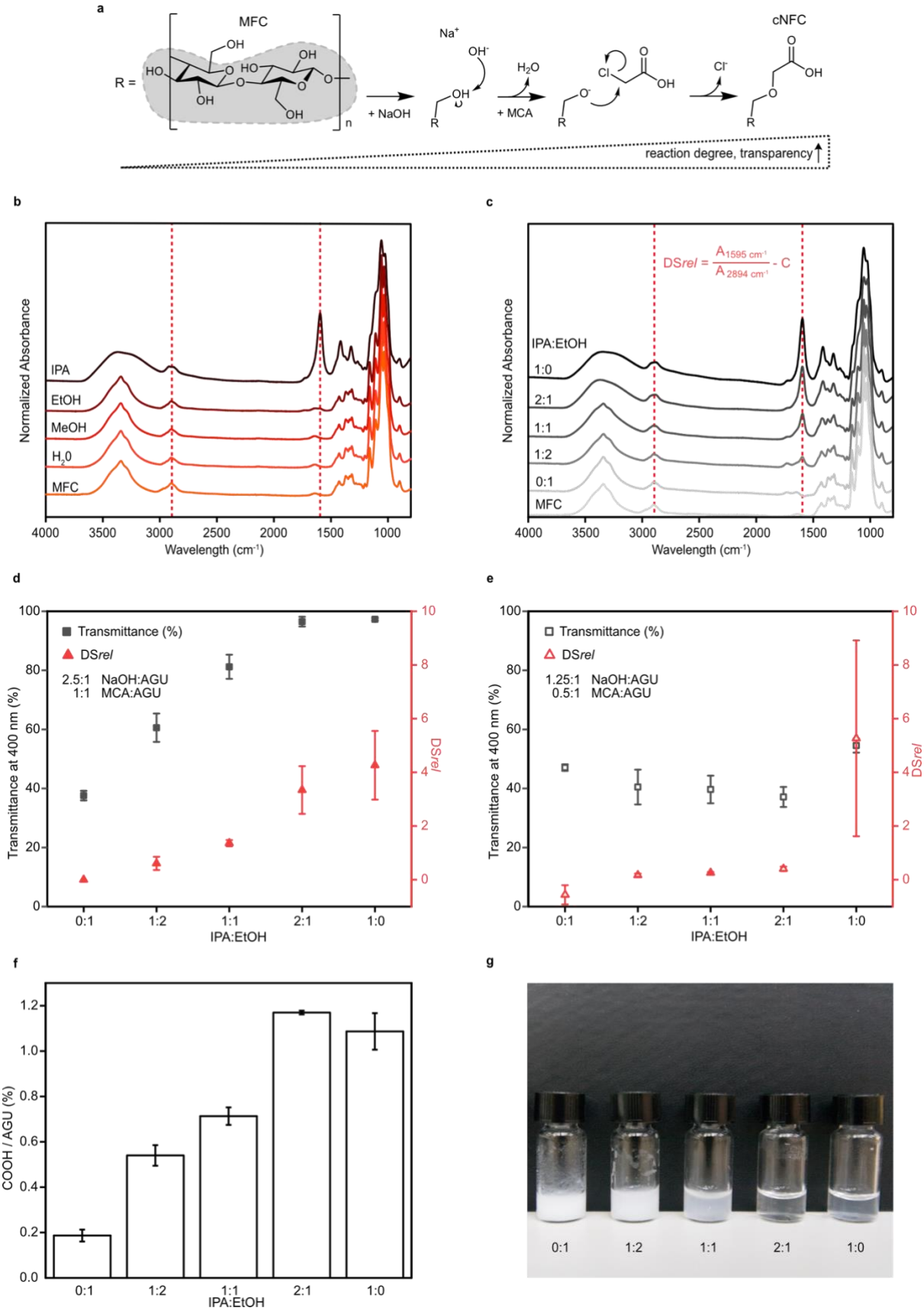


**Figure 6.** Carboxymethylation of MFC in different solvents and reactant ratios.

Comparison of $DS_{rel}$ and transmittance.(a) Reaction mechanism of carboxymethylation of MFC. Increasing the degree of reaction increases transparency of substituted fibers. (b) FT-IR of MFC reacted in IPA, EtOH, MeOH, $H_2O$ compared to the non-reacted batch and (c) reacted in 1:0, 2:1, 1:1, 1:2, 0:1 IPA:EtOH ratios. Normalized absorbance at 1050 $cm^{-1}$. Normalized absorbance used to calculate degree of substitution (rel). (d) Transmittance at 400 nm in % (■) and $DS_{rel}$ (▲) calculated based on IR data of 2.5:1 NaOH:AGU/1:1 MCA:AGU and (e) 1.25:1 NaOH:AGU/0.5:1 MCA:AGU. Standard error of the mean (SEM) for n = 3. (f) Degree of substitution calculated by titration of fibers and SEM for n = 3. (g) Photograph of fibers reacted in respective IPA:EtOH mixes at 2.5:1 NaOH:AGU/1:1 MCA:AGU.

This was confirmed quantitatively, as we found that both $DS_{rel}$ and transparency increased gradually with decreasing polarity of the solvent mix from 1:2 IPA:EtOH to pure IPA (Fig. 6d). Notably the absorption was decreased across the visible spectrum and into the UV range, with minimal absorption for all wavelengths ≥ 250 nm and compared to diluted MFC (Supp. Fig. 17). This trend was further confirmed when determining the degree of substitution via titration (Fig. 6f). Interestingly, when we repeated the solvent composition study with lower amounts of reactants of 1.25:1 NaOH:AGU and 0.5:1 MCA:AGU, the degree of control was somewhat diminished. For this set of reactants, the $DS_{rel}$ as well as the transmittance, was negligible for all solvent mixtures except pure IPA (Fig. 6e). Also, for this condition we observed a large variance in the degree of reaction. We speculate that this could be due to a larger sensitivity to external factors that were not controlled, such as the humidity, for reactions performed in pure IPA. We thus conclude that the degree of substitution can be fine-tuned by changing the polarity IPA:EtOH mixed solvents for reactant concentration of at least 2.5:1 NaOH:AGU and 1:1 MCA:AGU.

The gradual increase in transparency and degree of substitution with decreasing polarity of the solvent can be explained by the first step of the carboxymethylation reaction: The mercerization occurs in the respective solvent mixes and NaOH is pre-dissolved in the same solvent mix used for the reaction. MFC was not used in dried state but as aqueous paste, the surface of the fibers is in a semi-hydrate state due to residual water. When mixing the fibers with the NaOH solution in the solvent mix, the driving force of NaOH to accumulate on the surface of the fibers is highest in the most apolar solvent mix, since here, NaOH is poorly soluble compared to EtOH or water.[85] This is reflected in the degree of substitution of the different samples: The most substituted samples were functionalized in pure IPA. The degree of substitution further correlated with transparency, yielding highly transparent fibers for IPA:EtOH solvent mixtures containing at least 66% v/v IPA.

*Solvent mix-dependent morphology and rheology of cNFC*

The increasing transparency of the fibers indicates a decrease in fiber size as well as a better dispersion of the fibers. To evaluate fiber size as a function of IPA:EtOH solvent composition, we applied electron microscopy, see Figure 7. Interestingly, the scanning electron microscope (SEM) analysis showed that the average fiber diameter gradually decreased from roughly 350 nm to 250 nm when increasing the IPA content, while maintaining lengths of tens of microns or more across all conditions. These observations were in excellent correlation with transparency data. Moreover, the SEM data showed that we successfully achieved transparent fiber samples that maintained physiologically relevant sizes. Still, while micrometer-long fibers dominated, smaller structures could also be identified in transmission electron microscopy (TEM), especially for the reactions in pure IPA (Supp. Fig. 18). Thus, for the majority of our subsequent studies we focused on the transparent nanofiber samples obtained when performing the carboxymethylation in 2:1 IPA:EtOH. We will

therefore refer to cNFC functionalized in 2:1 IPA:EtOH as cNFC. If a different batch was used it will be stated separately.

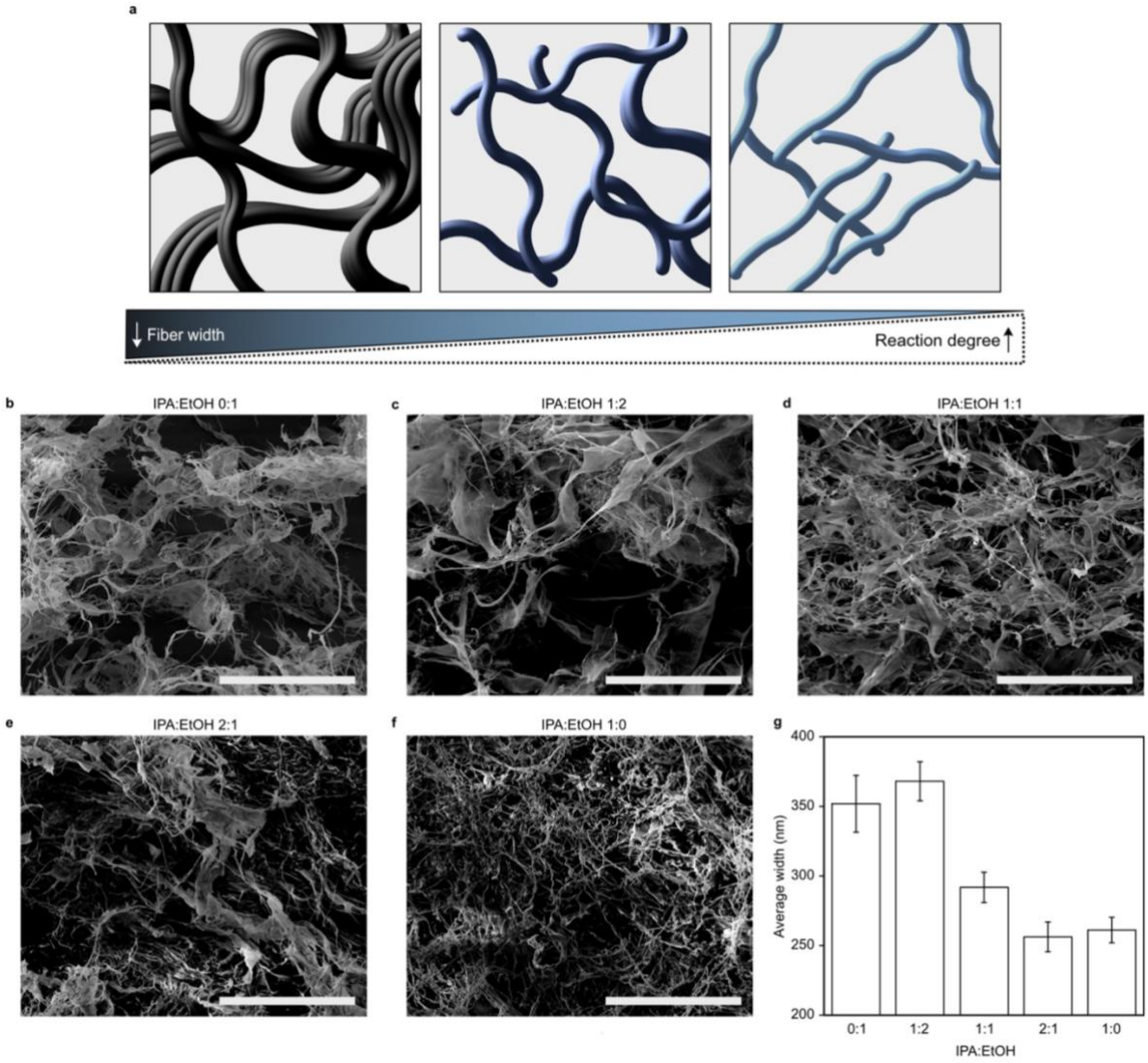


**Figure 7.** Size and appearance of carboxymethylated fibers analyzed via SEM.
(a) Illustration of breakdown of fibers with increasing degree of reaction. (b) SEM images of fibers reacted in 0:1, (c) 1:2, (d) 1:1, (e) 2:1, and (f) 1:0 IPA:EtOH. Scale Bar: 50 µm. (g) Average fiber width in nm and SEM for n = 100, calculation based on different fields of view of same sample. Illustration made with Affinity Designer.

While all the carboxymethylated cellulose fibers preserved lengths of at least tens of micrometers, the rheological properties were affected notably with increasing degree of substitution, see Figure 8a-f. For samples with a low degree of substitution, shear-thinning gels with a defined yield stress were maintained for 1% w/v samples. However, for transparent samples with a higher degree of reaction, these beneficial properties for 3D printing were largely lost (Fig. 8g).

Since the images obtained from electron microscopy do not indicate a decrease in fiber size, we hypothesize decrystallization of the cellulose as a reason for this decrease in mechanical properties. It is known that IPA drives decrystallization of the crystal structure of cellulose and changes its polymorphism from CELL I to CELL II.[85,132] This change in crystal structure is accompanied by a

decrease in elasticity, resulting in a dominant G'' over G'.[69,133] However, the rheological properties required for 3D printing can be recovered by adjusting fiber concentration. (Fig. 9a-c).

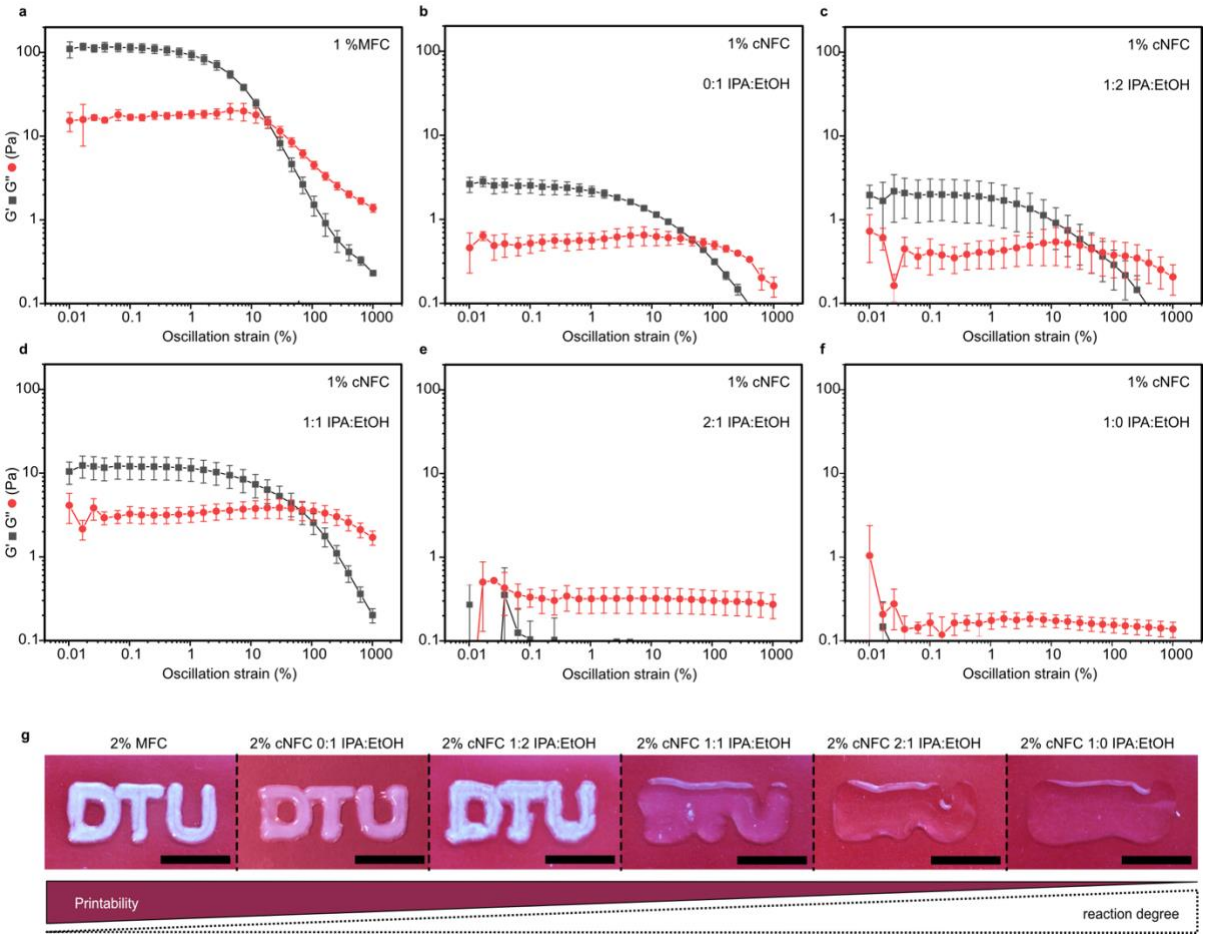


**Figure 8.** Rheology and printability of carboxymethylated fibers.
1% in milliQ water. Rheology of (a) MFC, fibers oxidized in (b) 0:1, (c) 1:2, (d) 1:1, (e) 2:1, and (f) 1:0 IPA:EtOH. The oscillation sweep was recorded at 25°C in milliQ water at 1 Hz. ■: Storage modulus G'. ●: Loss modulus G''. SEM for n = 3. (g) Optical appearance and print of DTU logo with steel needle (Inner diameter (ID) 400 µm) with 2% MFC, 2% cNFC 0:1, 2% cNFC 1:2, 2% cNFC 1:1, 2% cNFC 2:1, and 2% cNFC 1:0. Scale bars: 1 cm.

Specifically, by increasing the concentration up to 3% w/v the transparent fibers obtained by carboxymethylation in 2:1 IPA:EtOH, shear thinning gels were re-established. As expected, these rheological improvements are immediately reflected in excellent 3D printing properties (Fig. 9d-f). Moreover, the storage modulus of the shear-thinning gels could readily be tuned in the printable window from ~50 Pa to ~2.5 kPa, by increasing cNFC concentration, thus spanning a large part of the physiologically relevant range for soft tissue, (Fig. 9g). Importantly, while increasing the fiber concentration leads to some decrease in sample transparency, the transmittance does not fall below 95% in a 3% w/v fiber solution, (Fig. 9h). Therefore, it is possible to recover printability and shape fidelity of the fiber dispersion by increasing its concentration, without losing transparency.

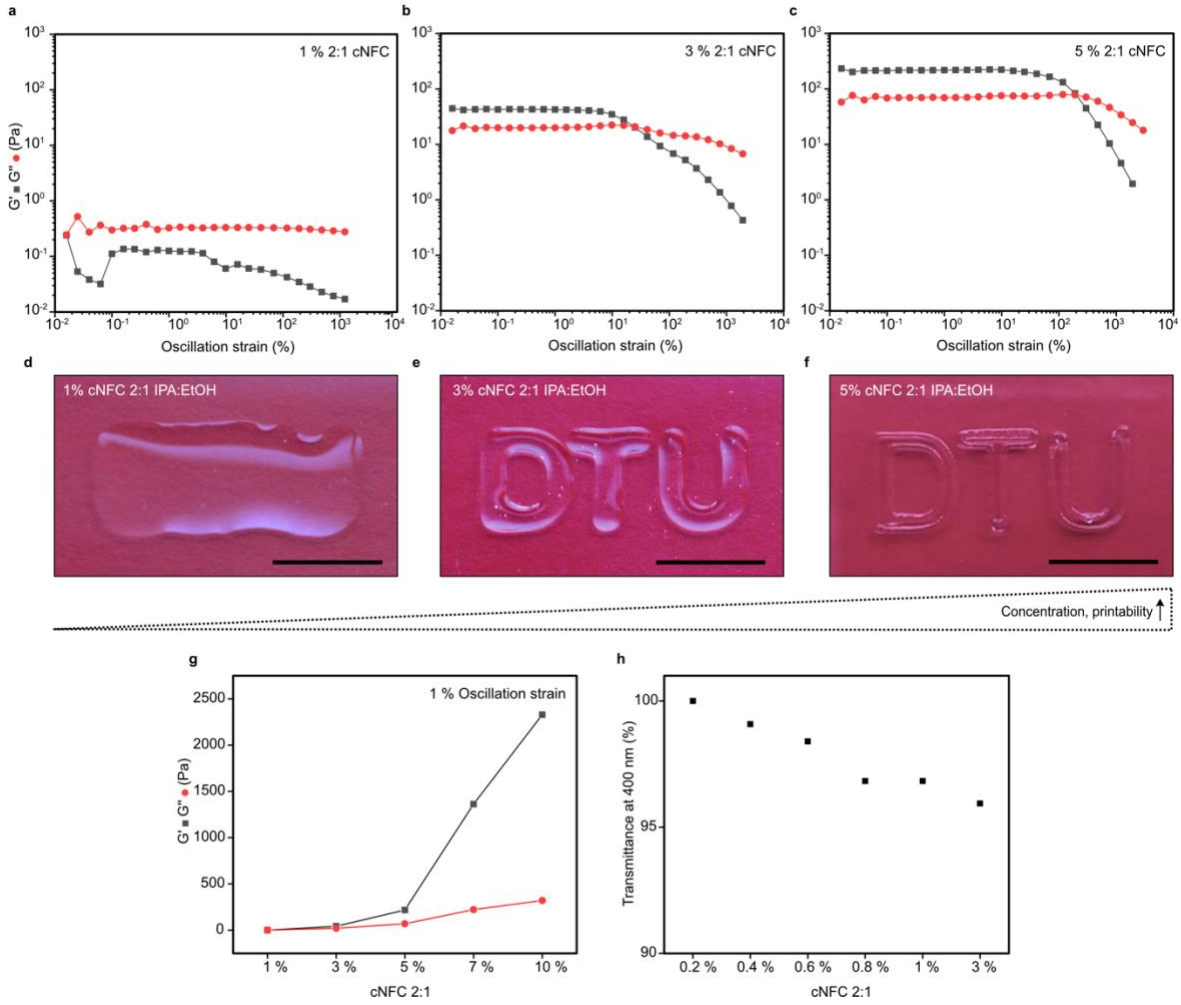


**Figure 9.** Rheology, transmittance and printability of cNFC 2:1 at higher concentrations.
The oscillation sweeps were recorded at 25°C in milliQ water at 1 Hz. ■: Storage modulus G'. ●: Loss modulus G'' for n = 1. (a) Rheology of (a) 1 % cNFC 2:1, (b) 3 % cNFC 2:1, and (c) 5% cNFC 2:1. (d) Printability of DTU logo at 1 %, (e) 3%, and (f) 5% cNFC 2:1 in milliQ water. Scale bar: 1 cm. (g) Storage G' and loss G'' modulus at 1 % oscillation strain as a function of increasing concentration of cNFC 2:1 in %. (h) Transmittance at 400 nm in (%) as a function of increasing concentration of cNFC 2:1 in milliQ water.

### 2.3.2 Coupling of small proteins onto functionalized cNFC

The printability and shape-fidelity of cNFC shows promising results for its application as bioink in DIW. Still, carboxymethylated cellulose does not bear any cell-adhesion sites and despite its biocompatibility cells will not adhere to it. To increase cell-adhesiveness, cell-adhesive molecules were coupled to the carboxymethyl-group of the cNFC. For this, we functionalized cNFC via carbodiimide chemistry with trypsinized gelatin (TG), collagen (COL), laminin (LN), and fibronectin (FN). The coupling-experiments were performed on cNFC reacted in 1:1 IPA:EtOH due to its higher initial elasticity compared to the fibers reacted in 2:1 and 1:0 IPA:EtOH. Later on, printing experiments were continued with a more transparent but higher concentrated sample reacted in 2:1 IPA:EtOH. The IR spectra of 1:1 cNFC coupled to TG, FN, COL, and LN all exhibit a distinctive peak at 1650 $cm^{-1}$ corresponding to the stretching vibration of an amide bond. Subsequently, the

carboxylate peak at 1595 $cm^{-1}$ decreased, indicating the successful coupling onto the different proteins (Fig. 10a-c). The negative charge on the fibers surface might induce polymerization of the different proteins onto its surface, probably exhibiting a similar IR spectrum. This possibility was excluded by mixing 1:1 cNFC with fibronectin and measuring the resulting IR before purification (Fig. 10b). To further have an approximation for the amount of coupled protein, the atomic percentage of nitrogen in TG-coupled fibers was quantified via x-ray photoelectron spectroscopy (XPS). A high resolution spectrum of nitrogen of non-coupled 1:1 cNFC compared to TG-coupled 1:1 cNFC reveals a nitrogen signal that adds up to approximately 4% total mass in the sample (Fig. 10d, e). Based on these results we concluded a successful coupling of different cell-adhesive peptides and printed alternating lines of FN-coupled and non-coupled 1:1 cNFC. Interestingly, murine myocytes adhered to the parts of the hydrogel, that were printed with 1:1 cNFC-FN while no cells adhered to 1:1 cNFC (Fig. 10f). Still, a repetition of this experiment, as well as with 1:1 cNFC-TG,-COL, and -LN did not demonstrate cell adhesion onto the hydrogels. It was further observed that 1:1 cNFC hydrogels degraded under cell-culture conditions if not formulated with a cross-linkable hydrogel as described before.

Binding of proteins onto surfaces and particles via N-ethyl-N'-(3-(dimethylamino)propyl)carbodiimide/N-hydroxysuccinimide (EDC/NHS) is a commonly used method.[134–136] The IR spectra indicate successful coupling, but a carboxylate signal is still visible. Based on this data, we cannot assume all carboxylate groups to be coupled to a protein. For cNFC functionalized in 1:1 IPA:EtOH, we calculated a degree of substitution of approximately 0.7 % COOH/AGU. Each AGU unit can be functionalized on 3 available hydroxyl groups. A DS of 30% COOH/AGU indicates 1 hydroxyl group per AGU being functionalized, 15% would indicate every second AGU unit being functionalized, and lastly 0.7% COOH/AGU suggests every 32$^{nd}$ AGU unit being functionalized, making it roughly 3% of all AGU units being functionalized with a carboxylate group. Assuming all carboxylate groups were coupled to a protein, 3% of all AGU units would bear a cell-adhesive motif. It is well known that a certain threshold of adhesion sites for cell-binding must be met for successful binding and proliferation, as well as clustering of adhesion sites.[137,138] Our results indicate too scarce distribution of cell-adhesion sites after the coupling reaction. Increasing the degree of substitution and choosing small peptide sequences instead of big proteins might enhance the adhesion of cells onto the fibers surface.

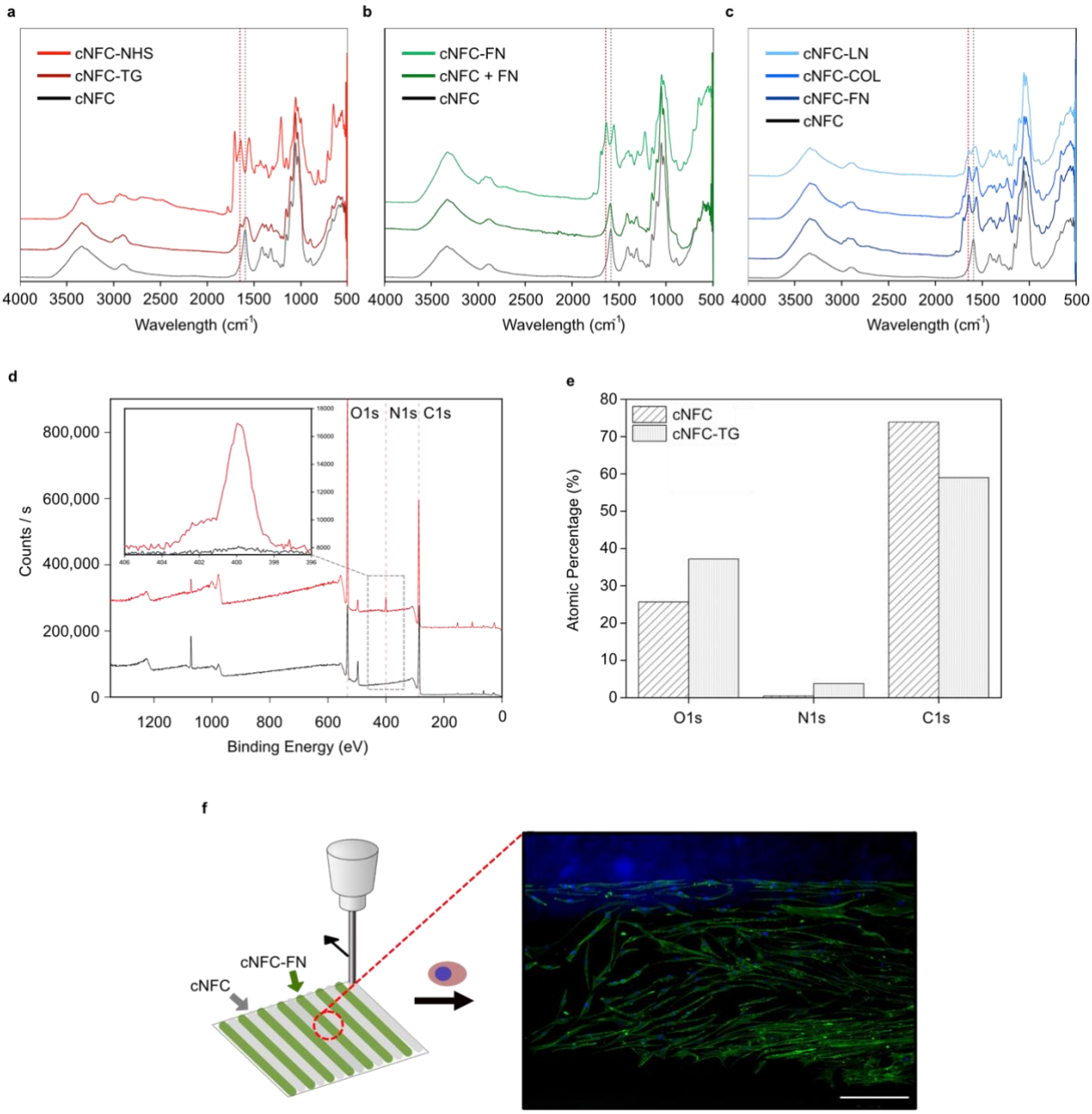


**Figure 10.** Characterization of protein-coupled cNFC reacted in 1:1 IPA:EtOH.
Normalized IR spectra at 1050 $cm^{-1}$ of (a) cNFC (black), cNFC-TG and cNFC-NHS (red), (b) cNFC-FN and cNFC + FN (green), (c) cNFC-LN/-COL/-FN (blue). Reference lines at 1595 $cm^{-1}$ and 1650 $cm^{-1}$ indicate carboxylate and amide peaks, respectively. (d) High-resolution XPS of cNFC-TG (red) compared to cNFC (black). (e) Atomic percentages calculated and measured via XPS of oxygen (O1s), nitrogen (N1s), and carbon (C1s) of cNFC (striped) and cNFC-TG (dotted). (f) Illustration of alternating prints with 4% cNFC-TG (grey) and 6% cNFC-FN (green) with subsequent seeding of C2C12 myoblasts. Fluorescent image of actin stain (green), and the cell nuclei (blue). Scale bar: 250 µm.

### 2.3.2 Formulation of cross-linkable composite-inks

Further functionalization of cNFC with cell-adhesive motifs did not yield the desired results of increased cell-adhesion on printed cNFC substrates. Therefore, we formulated cNFC-based composite gels. cNFC serves as rheological modifier, while its intact fibrillar structure recapitulates the native ECM network.

*Ionically cross-linkable cNFC:alginate ink*

The excellent shape fidelity at higher cNFC concentrations allowed us to develop cross-linkable, transparent inks for complex structures. To demonstrate this, we formulated composite inks composed of transparent carboxymethylated fibers and alginate (ALG). MFC:alginate composite inks have been studied extensively for bioprinting, yet for unreacted fibers these composites have very limited transparency.[139] The use of fibers during the printing procedure highly improves the rheological properties of alginate (Fig. 11a-c). To demonstrate shape-fidelity after printing, an octopus was designed using CAD and printed with a MFC:alginate composite ink and cNFC:alginate (Fig. 11d).

The shape fidelity of the printed octopus was maintained after printing, yielding a complex, transparent, cross-linked 3D structure. The rheology of the three ink compositions clearly shows the advantages of using fibrillar inks as rheological modifiers: Pure alginate shows viscous behavior. An octopus printed with a 3 % alginate ink will start flowing after printing, while the yield stress of MFC and cNFC needs to be surpassed to induce flow.

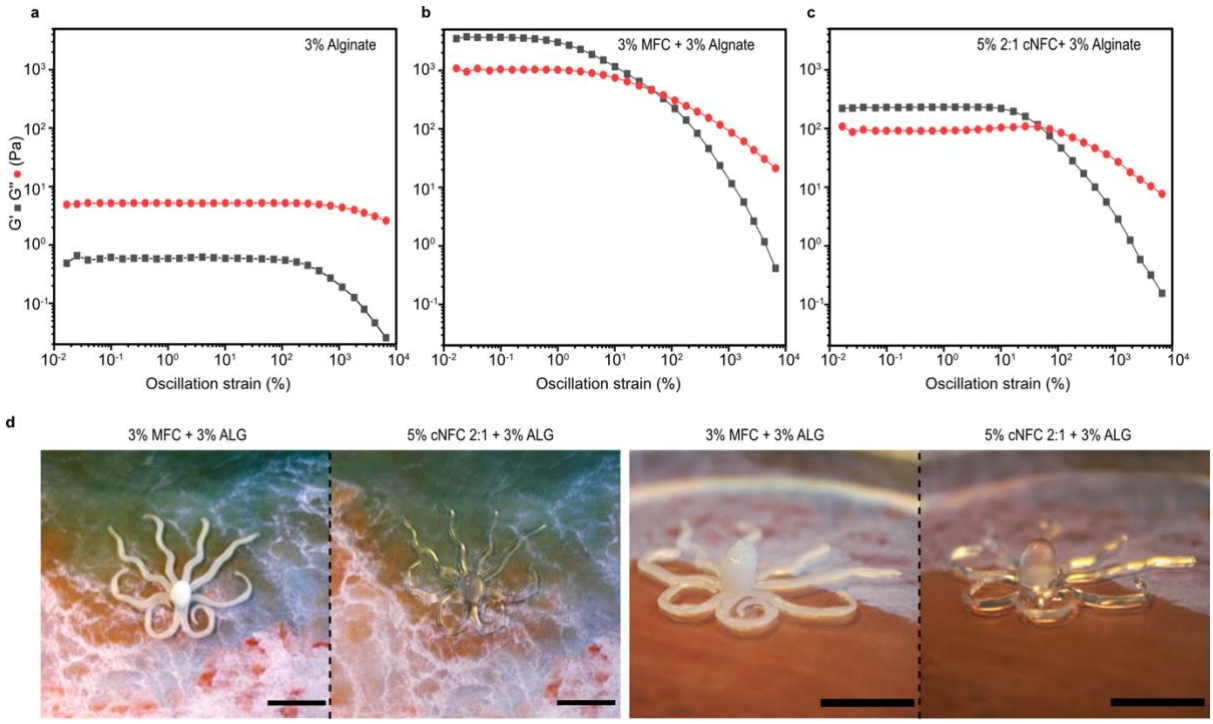


**Figure 11.** Rheology and 3D print of cross-linkable cNFC:alginate composite inks.
The oscillation sweeps were recorded at 25°C in milliQ water at 1 Hz. ■: Storage modulus G'. ●: Loss modulus G'' for n = 1. (a) Rheology of 3% alginate. (b) Rheology of 3% MFC + 3% alginate composite ink. (c) Rheology of 5% cNFC 2:1 + 3% alginate composite ink. (d) Octopus printed with 3% MFC + 3% alginate composite ink, side and top view (Scale bar: 1 cm). Octopus printed with 5% cNFC 2:1 + 3% alginate composite ink, side and (g) top view (Scale bar: 1 cm).

*Cell-adhesive cNFC:gelatin composite inks*

Although alginate is a widely applied biomaterial, cNFC:alginate as largely irrelevant as ECM-mimicking bioink as it lacks the native protein landscape and cell-adhesive motifs. As a simple solution, we found that cNFC was readily miscible with both gelatin and collagen-based gels at a

wide range of ratios and concentrations. Notably, this is not the case for unmodified MFC, where phase separation occurs. For formulating cNFC:gelatin inks, we aimed to decouple ink gelation and rheology during printing from stiffness of the final printed construct (Fig. 12., Supp. Fig. 20). This would be advantageous as compared to pure gelatin or gelatin-methacrylate inks, where these properties are highly correlated and thermal control during printing is essential. For our composite inks, we thus focused on Bloom gelatin at low concentrations that do not gel at RT (Fig. 12a). On the other hand, since cNFC behaves like physical gels with concentration-defined yield stress for concentrations ≥3% w/v, the rheology of cNFC:gelatin inks at RT can be completely dominated by the fiber content at RT (Fig. 12b-c, Supp. Fig. 20).

Yet, while cNFC content dominates printability, gelatin content largely defines the final stiffness of the final material after cross-linking enzymatic microbial transglutaminase (mTG) (Fig. 12d-e). It is thus straight-forward to formulate printable cNFC:gelatin composite inks with independent control of flow and final material mechanics (Supp. Fig. 20). We found that for ~5% w/v cNFC and ~5% w/v the cNFC:gelatin the Young's modulus matched well with that of native muscle tissue[140] (Fig. 12e).

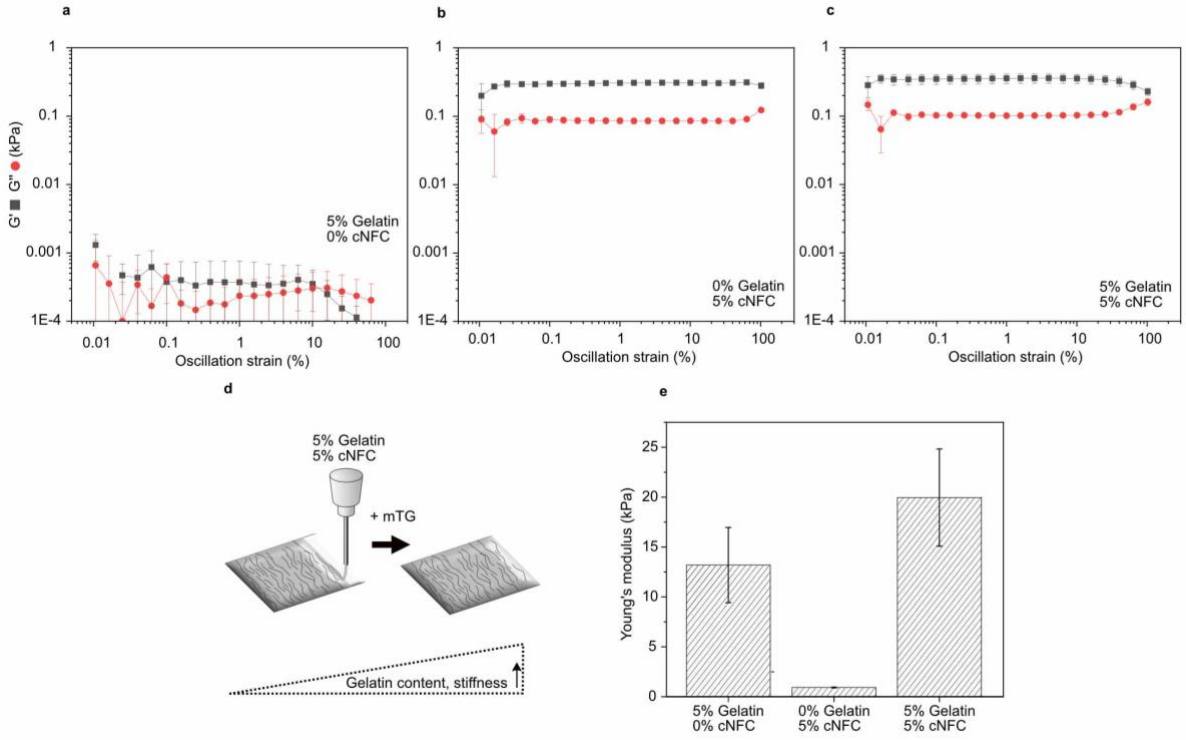


**Figure 12.** Rheology and stiffness of cNFC:gelatin composite inks.
The oscillation sweeps were recorded at 25°C in PBS at 1 Hz. ■: Storage modulus G'. ●: Loss modulus G'' SEM for n=3. Rheology of (a) 5% gelatin + 5% cNFC, (b) 0% gelatin + 5% cNFC and (c) 5% gelatin + 0% cNFC composite inks. (d) Illustration of printing of cell-instructive coatings: substrates are subsequently cross-linked with mTG at 4 °C over night. The gelatin content defines the final stiffness of the substrate. (e) Young's modulus E in kPa of cross-linked substrates printed with 5% gelatin + 5% cNFC, 5% gelatin + 0% cNFC, and 0% gelatin + 5% cNFC composite inks. E calculated from G' at 1 % oscillation strain and SEM for n=3.

*Shear-induced alignment of cellulose fibrils*

Given their length and structural similarity to native collagen, we hypothesized that the cNFC fibers may serve as cell-guiding structures within cNFC:gelatin composites. Further, inspired by previous studies that have used cellulose fibrils as basis for printable composites with programmable

swelling or diffraction[141,142] we aimed to explore if extrusion-driven orientation of cNFC would suffice to define the orientation of cells and tissues. We investigated shear-induced alignment of MFC and cNFC after extrusion by fluorescently staining the cellulose with calcofluoro white (Fig. 13a). The alignment of printed MFC is clearly visible as suggested in Figure 13a, left. The size of the fibers ranges in the micron scale, which makes it easy to determine individual fibers. cNFC printed under the same conditions suggests the alignment of thin, fibrillar aggregates (Fig. 13a, right). Since the width of the fibers lays below the wavelength of light, it is difficult to clearly identify the alignment with light microscopy. Still, the seeding of murine myoblasts onto printed cNFC:gelatin substrates clearly shows alignment of the cells in print direction (Fig. 13b), indicating alignment of the fibers within the hydrogel. Induced cell guidance through topological cues was excluded by recording the side-view of the printed substrates with seeded cells (Fig 13c). From this we conclude that cNFC undergoes shear-induced alignment during extrusion, allowing to produce cell-guiding substrates.

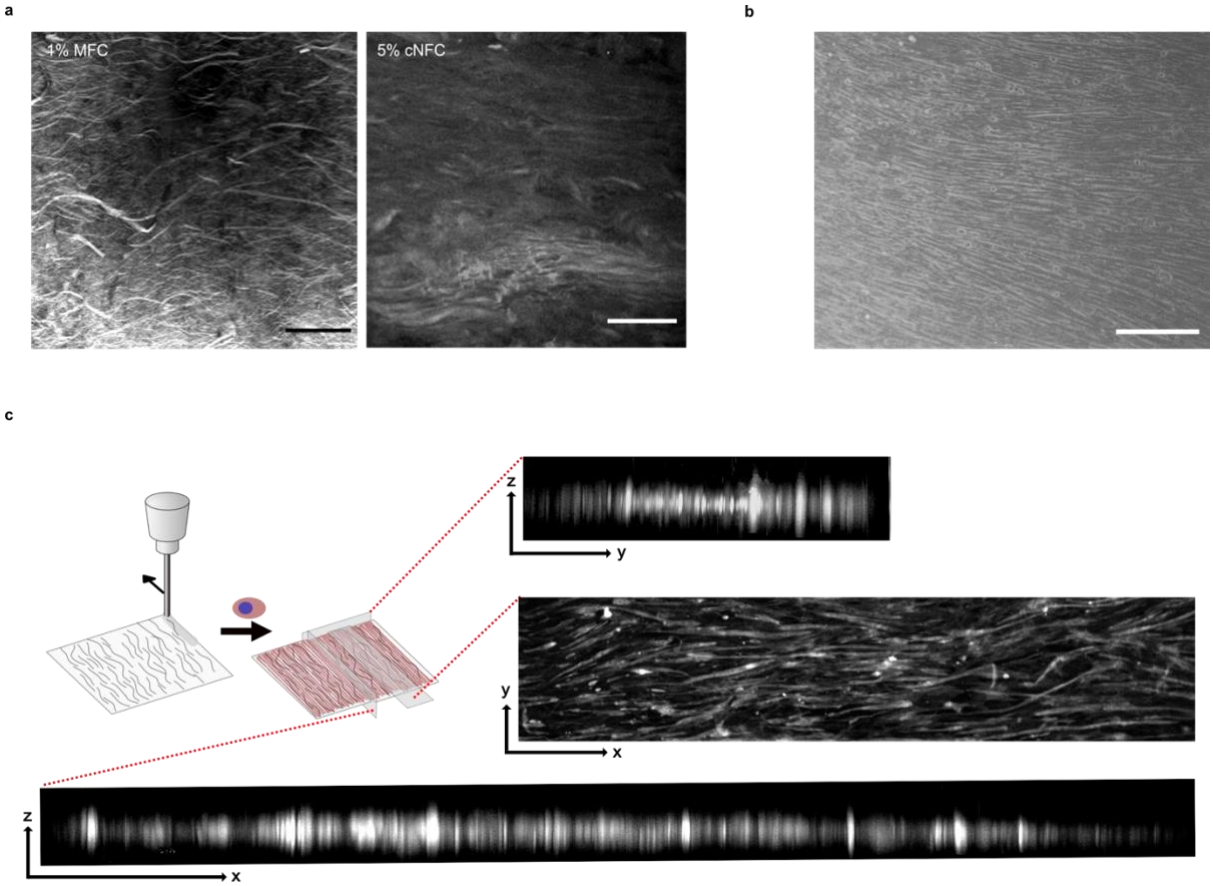


**Figure 13.** Shear-induced alignment of MFC/cNFC and cell-alignment on printed substrates.
(a) 1 % MFC and 5 % cNFC printed with a steel nozzle (ID 200 µm) and stained with calcofluoro white. Scale bar MFC: 50 µm. Scale bar cNFC: 25 µm. (b) Brightfield image of C2C12 myoblasts aligned on 5 % cNFC + 5% LBG composite gel printed with steel nozzle (ID 200 µm). Scale bar: 250 µm. (c) Illustration of printing a cNFC:gelatin composite gel and subsequent cell seeding. Fluorescent images of actin stain. x-plane, z-plane and y-plane. Scale bar x: 500 µm, y: 250 µm, z: 130 µm. White: actin stain.

### 2.3.3 Printing of cell-guiding substrates for skeletal muscle cell maturation

We printed a range of cNFC:gelatin tissue culture substrates, and studied whether murine and human skeletal myoblasts develop into local, parallel alignment following the print direction. While previous studies already revealed 5% cNFC to be a suitable concentration with excellent printing properties and muscle-like stiffness, we wanted to investigate the concentration threshold for cellular alignment at constant gelatin content. We saw a rapid decrease in cellular alignment with decreasing fiber concentration, with only concentrations above 3% inducing significant guidance for cell-alignment (Fig. 14). Therefore, we conducted most experiments with concentrations above 4% cNFC.

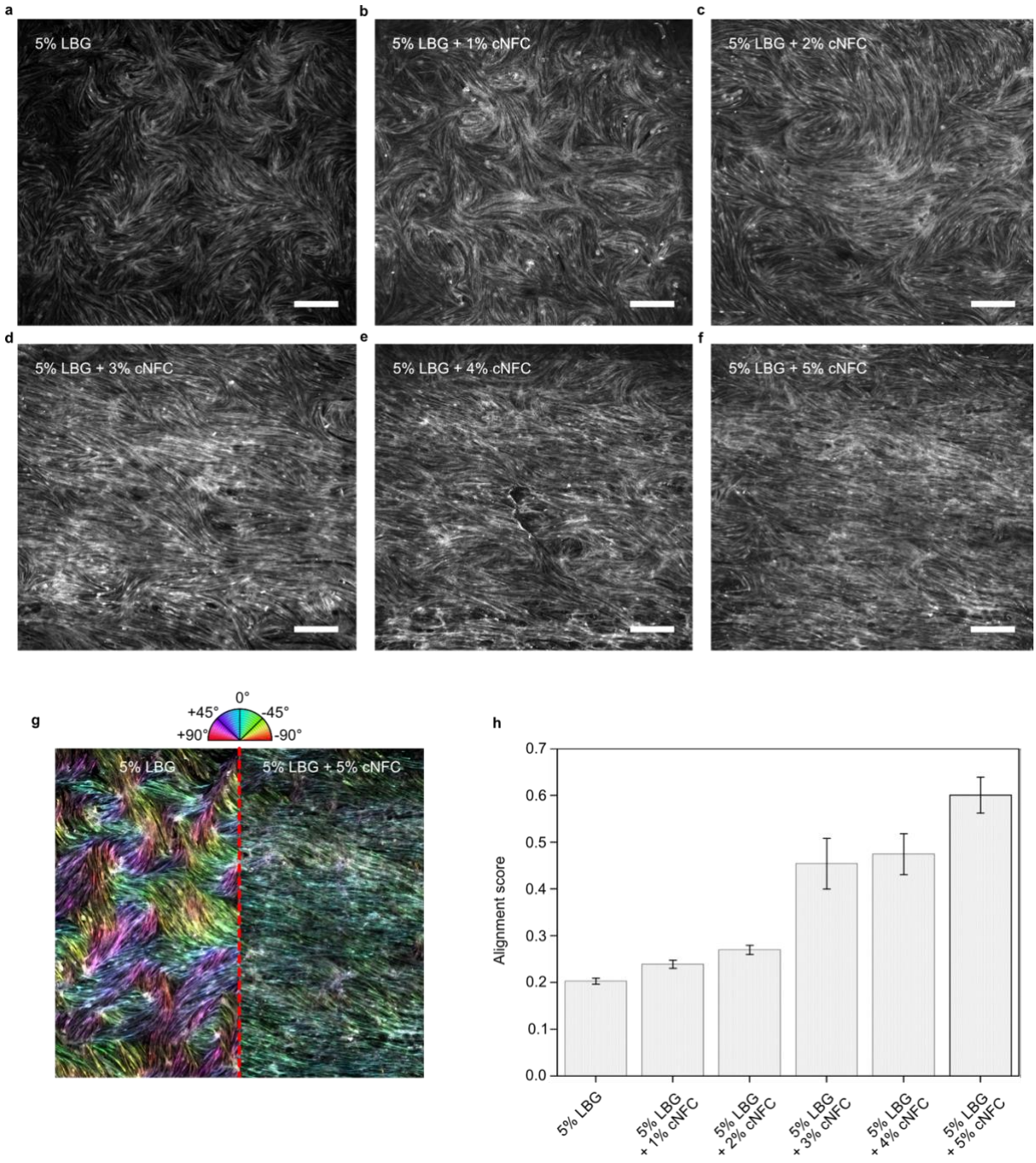


**Figure 14.** Cell-alignment on cNFC:gelatin composite gels.
C2C12 myoblasts seeded on 5% LBG (a), 5% LBG + 1% cNFC (b), 5% LBG + 2% cNFC (c), 5% LBG + 3% cNFC (d), 5% LBG + 4% cNFC (e), and 5% LBG + 5% cNFC (f). (g) False color mapping of myotube (actin) orientation of C2C12 on 5% LBG compared to 5% LBG + 5% cNFC. (h) Alignment score based on orientation distribution calculated by OrientationJ plug in and SEM for n = 3.

Furthermore, the complexity of the printed structures could be easily tailored by adjusting the design. We observed fusion of myocytes into myotubes on circular and checkerboard-like patterns, allowing us to have high control over the geometry of the printed pattern and subsequent cellular alignment (Fig. 15).

The shear-induced alignment of cellulose fibers has been demonstrated before showing anisotropic swelling behavior or programmable optical properties.[105,106] Still, the use of transparent

cellulose fibers for organizing engineered tissues was not shown before. Most examples of transparent cellulose rely on short fiber sizes in the nano range,[88,143] while our fiber formulation surpasses the length of a single myoblast, providing physical cues for myoblast orientation and myotube formation.

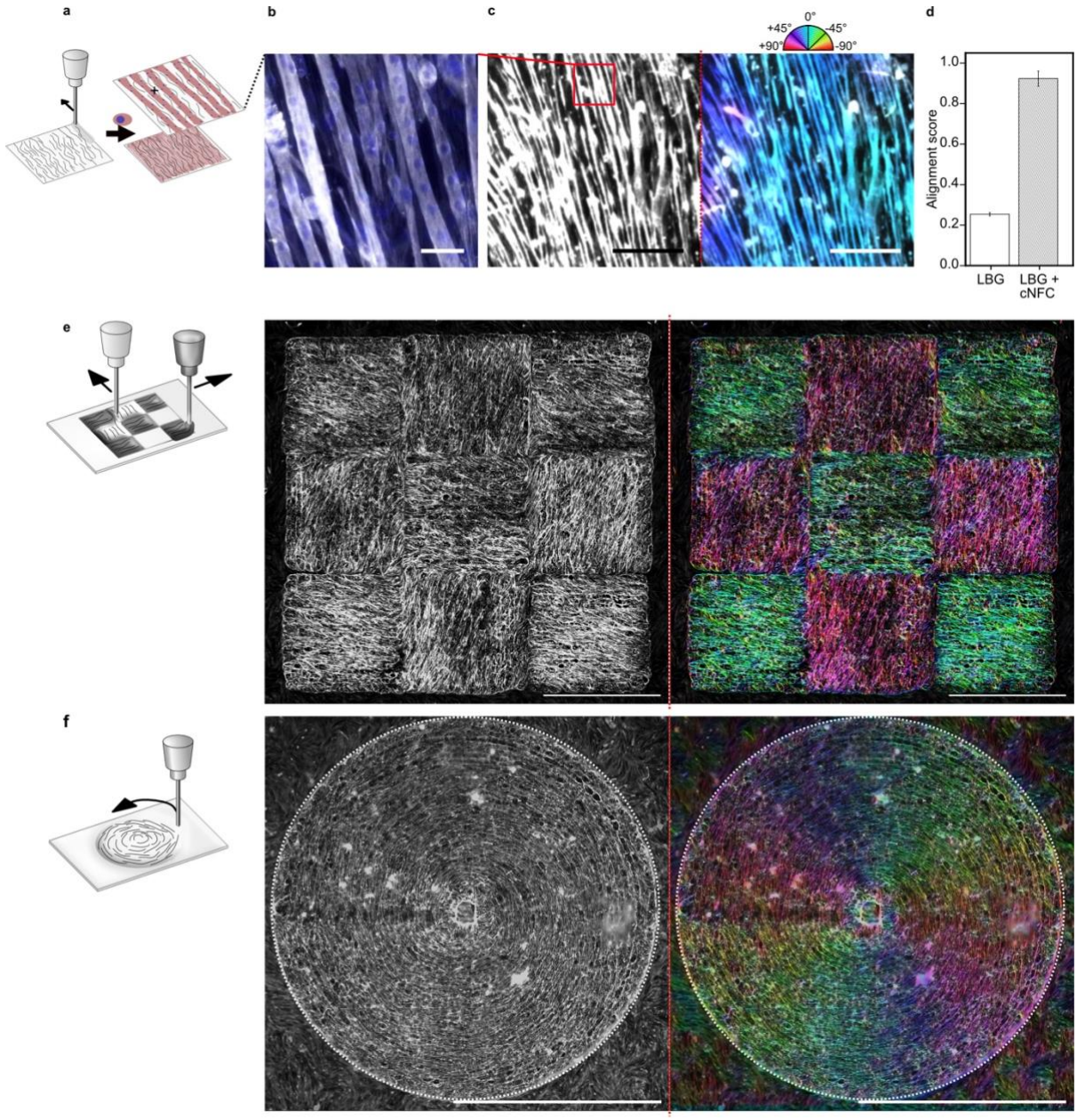


**Figure 15.** Self-alignment of $C_2C_{12}$ on cNFC:gelatin substrates.
(a) Illustration of seeding of $C_2C_{12}$ muscle cells onto cross-linked, printed substrates. (b) Polynucleated myotubes of seeded cells differentiated on printed substrate. White: Actin. Blue: Nucleus. Scale bar: 50 µm. (c) False-color mapping of myotube (actin) orientation with OrientationJ. Scale bar: 500 µm. (d) Alignment score (0-1) of $C_2C_{12}$ myotube alignment on 5% LBG compared to 5% LBG + 5% cNFC. SEM for n = 3. (e) Illustration of printing of alternating blocks of horizontal and vertical lines in a checkerboard-like fashion and false-coloured 15x15 mm checkerboard with alternating orientation of seeded cells. Scale bar: 5 mm. (f) Illustration of printing of concentric circles with r = 3.5 mm and false-colored print with circular oriented cells. Scale bar: 5 mm.

The substrates were additionally well-suited for maturation of human skeletal myotubes (HSkM). These increased in both alignment and width and showed no indication of delamination during 17 days of culture and physiological responses to insulin stimulation (Fig. 16).

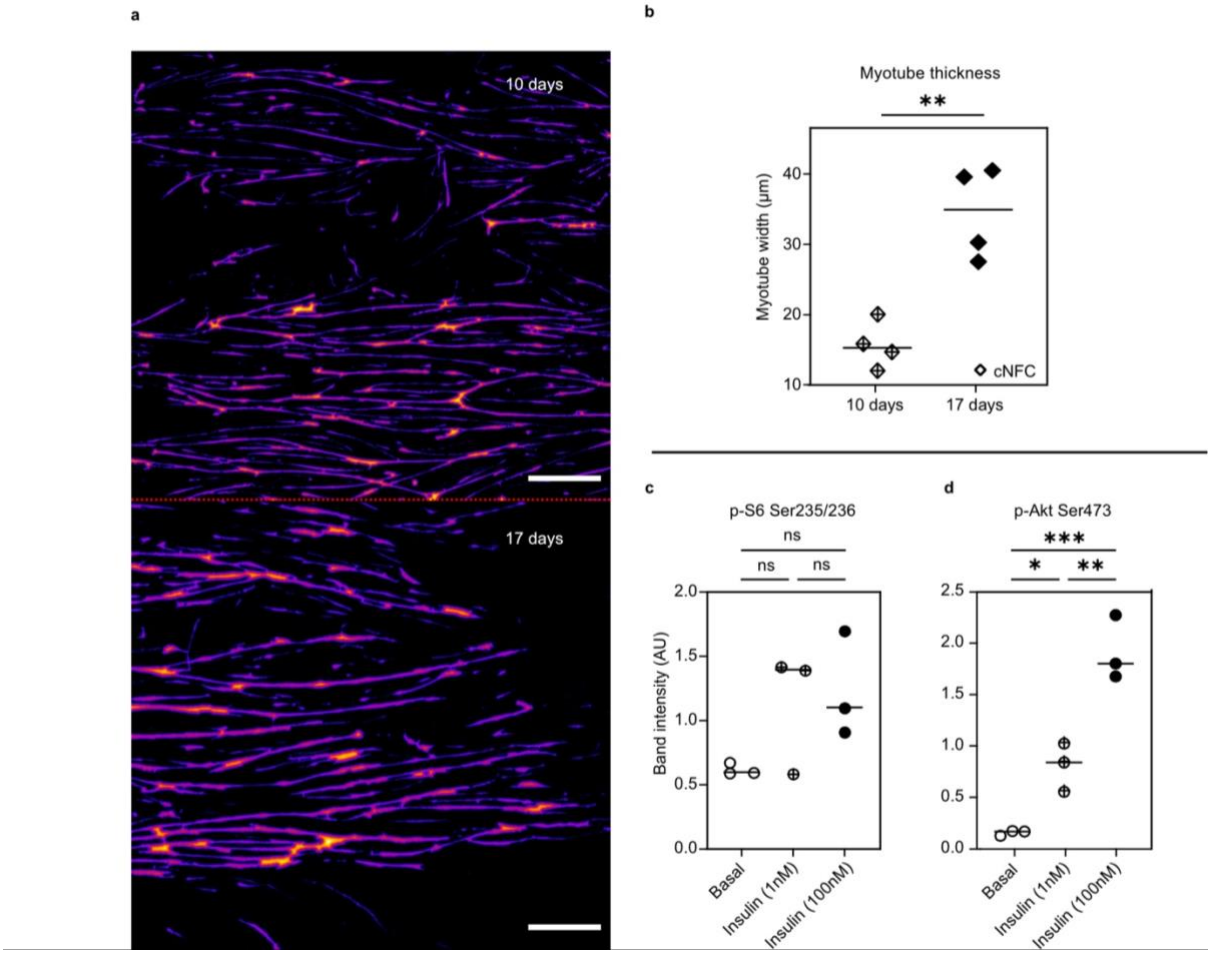


**Figure 16.** Alignment of HSkM on cNFC:gelatin substrates.
(a) Heat map based on local thickness of actin stain of HSkM kept in culture for 10 (up) and 17 days (down) on parallel printed substrates of 4% gelatin + 4% cNFC. Scale bar: 500 µm. (b) Myotube width index of HSkM cultured on cell-instructive cNFC substrates after 10 and 17 days. For myotube width analysis, the geometry to distance map in the local thickness feature in ImageJ was used to generate a histogram where all pixels were indexed into columns based on the thickness of the myotube the pixel originated from. From each column in the histogram a score was generated by multiplying the number of pixels within the column with the ranking of the column based on thickness. Myotube thickness was then calculated by taking the average of the column scores. ** equals $p < 0.01$, *** equals $p < 0.001$. (c,d) Immunoblotting of S6 Ser235/236 (c) and Akt Ser473 (d) phosphorylation in basal and insulin-stimulated myotubes. Myotubes were starved from serum and glucose for 3 hours and then kept basal or stimulated with 1 or 100 nm insulin for 15 min prior to harvest.

Maturing engineered muscle tissues has been previously performed on structured hydrogel substrates or synthetic nanofibrillar anisotropic scaffolds.[29,55,56,144] Our approach combines the synthesis of nanofibers with the formulation of anisotropic hydrogels. Most importantly, we here present an easily tailorable, automated procedure at RT for generating anisotropic surfaces without relying on high-resolution nozzles.

## 2.4 Conclusion

Tissue engineering based on DIW of transparent CNC and non-transparent MFC has shown promising results due to their biocompatibility, excellent printing properties, and high tunability. Still, the short crystal structure of CNC does not replicate the fibrillar structure of the native ECM, while non-transparent MFC impairs optical microscopy during the development of functional tissue. In this chapter, we present a protocol for controlling the production of fibrillar cellulose nanofibers and the formulation of transparent, cell-guiding inks. The main goal was to preserve fiber lengths of > 10 µm while increasing the transparency. The transparency of the fibers is achieved by carboxymethylation, which can be easily controlled by controlling the polarity of the isopropanol:ethanol mix used. Reducing the amount of reactants did reduce the overall control over the carboxymethylation reaction and yielded less transparent fibers. We observed that higher transparency and degree of substitution is achieved at higher isopropanol content, yielding cNFC, a transparent, shear-thinning gel with excellent printing properties and ECM-like fiber sizes.

Functionalizing the fibers with carboxylate groups reveals the opportunity of coupling cell-adhesive proteins and peptides onto the fibers. First results on less substituted cNFC indicate successful coupling of trypsinized gelatin, collagen, fibronectin, and laminin to the fibers. Still, cell adhesion onto protein-coupled fibers was not clearly demonstrated. Additionally, the printed constructs degraded under cell-culture conditions due to lack of chemical cross-links.

Cell-adhesiveness and cross-linkable constructs were thus formulated using cNFC:gelatin composite gels. We observed shear-induced alignment of cNFC:gelatin inks. Their cell-guiding properties and allowed us to highly control the spatial orientation of murine and human skeletal myoblasts and their fusion into polynucleated myotubes. The myotubes were cultured for several weeks and showed higher maturity compared to non-aligned myotubes. This approach allows us to tailor material properties and easily scale the production of maturation platforms for relevant tissue models.

In summary, we here presented an alternative route to produce a transparent, shear-thinning, fibrillar cNFC hydrogel with cell-instructive properties. We formulated composite-inks and printed anisotropic surfaces to mature skeletal muscle tissue. To improve the coupling of cell-adhesive peptide motifs onto the fibers surface, the total degree of substitution needs to be tailored first. This will expand the possibilities of using specific cNFC-based bioinks for specific cell types.

## 2.5 Experimental section

### 2.5.1 Partial functionalization of MFC

*Carboxymethylation*

MFC was obtained from norwegian spruce by Borregaard in Sarpsborg (NO) and delivered as 10% aqueous paste. Isopropanol (IPA), methanol and ethanol absolut ≥ 99.9% were purchased from VWR and always freshly opened before each experiment as the usage of old IPA and EtOH will reduce the reactivity of the reactants. NaOH (S5881) and monochloroacetic acid (MCA, 402923) were purchased at Sigma Aldrich as solids. First, MFC was disintegrated using an Ultra-Turrax homogenizer with a S25N - 18G - ST dispersing element. The dispersion was conducted in pure solvent and the following solvent combinations IPA:EtOH: 0:1, 1:2, 1:1, 2:1, 1:0. . The day before the experiment, a 5% w/v NaOH (2% w/v in pure IPA) solution was prepared in the respective solvent. The day after, 10 g of MFC pulp (1 g dry content) were homogenized for 10 min. at 10,000 rpm. The homogenized MFC was heated up to 35 °C while stirring. 12 mL of a 5% w/v NaOH solution (600 mg) were added to the dispersed fibers and left stirring at 35 °C for 30 min. After, the temperature was increased to 45 °C. Once the temperature was reached, 4 mL of a 142.2 mg/mL (570 mg total) MCA solution in the respective solvent was added and left stirring at 45 °C for 3 h. The substitution reaction was repeated in the same solvents with half amount of reactants (300 mg NaOH and 285 mg MCA).

Around 10 mL of a 10% v/v acetic acid solution was added to the fibers for neutralization and the fibers were filtered. The filtered fibers were washed 3x with methanol, followed by dialysis against deionized water for three days in a 12-14 kDa cut-off dialysis tube with 2 daily water changes. The dialyzed fibers were freeze-dried and stored at room temperature until further use.

### 2.5.2 EDC/NHS coupling of proteins onto cNFC functionalized in 1:1 IPA:EtOH

*Coupling via EDC/NHS*

A 10 mM NaOAc buffer was prepared, and the pH adjusted to 5. A total of 905 mg fibers functionalized in 1:1 IPA:EtOH were dispersed by homogenizing for 10 min at 10,000 rpm with an Ultra-Turrax homogenizer in 270 mL of the 10 mM NaOAc buffer (0.3 % w/v cNFC in buffer). A 2 M EDC solution and 4.25 M NHS solution were prepared in NaOAc. The EDC solution was prepared under exclusion of light. A total of 6.4 mmol EDC and 16.5 mmol NHS were mixed with 270 mL 0.3% w/v cNFC and stirred vigorously under exclusion of light for 20 min at RT. Afterwards, the pH was adjusted to 7 and 0.1 mg of either trypsinized gelatin, fibronectin, laminin, or collagen were added to the solution and stirred vigorously over night at 4 °C or on ice. The next day, the solution was dialyzed against milliQ water for 3 days with 1 water exchange per day. The fibers were freeze-dried and kept at -20 °C until further use.

### 2.5.3 Characterization of cNFC and cNFC-protein

*IR*

IR spectra were recorded on a PerkinElmer Spectrum 100 FT-IR spectrometer. The spectra were recorded with a resolution of 1 $cm^{-1}$ from 4000 – 800 $cm^{-1}$. All spectra were recorded in absorbance units and normalized at 1050 $cm^{-1}$. The relative degree of substitution ($DS_{rel}$) was calculated by relating the intensity of the normalized absorbance (NA) of the stretching vibration of the carboxyl group (C=O) at 1595 $cm^{-1}$ to the stretching vibration of the glucose backbone (C-H) at 2894 $cm^{-1}$ as presented in (8).

*Titration*

Between 20 and 50 mg of cNFC were weight in and transferred to a clean 100 mL Erlenmeyer flask. Calcium acetate (10229177, Thermo Fisher) solution 2 % w/v was added to the fibers (10 ml) and let the solid material imbibe for 30 minutes. 2 drops of phenolphthalein indicator (A0424229, Thermo Fisher) were added to the flask (prepared as 1.0 % w/v in ethanol). A burette was filled with standardized NaOH solution (0.0121 M or 0.00121 M). The cNFC solution was titrated until the faint, pink endpoint is reached (persisting for at least 30 seconds). Three separate weighed samples of each cNFC sample were analyzed. The percentage of carboxyl content was calculated using the following equation:

$$\text{Carboxyl groups } [\%] = \frac{\mathrm{N} \cdot \mathrm{V} \cdot \mathrm{MW_{COOH}}}{\mathrm{m[mg]} \cdot 100} \quad (9)$$

Where N is normality of NaOH solution, V is the volume of NaOH consumed to reach the endpoint (corrected for the blank). MWCOOH is 59, corresponding to the introduced group - CH2COOH.

*Transmittance*

The absorbance of MFC and cNFC was measured using a Thermo Scientific NanoDrop 2000, at a path length of 1 mm. In general, the samples were homogenized at 1 % w/v for 10 min. using an Ultra-Turrax homogenizer at 10,000 rpm for 10 min. The absorbance was measured right after. Transmittance at 400 nm was compared and calculated as follows:

$$\%T = 10^{2-A} \quad (10)$$

*Rheology*

The rheology of each ink was analyzed using a Discovery Hybrid Rheometer (TA instruments, DE, USA) equipped with a Peltier plate thermal controller and a plate geometry with a diameter of 40 mm and a fixed gap of 1 mm. All samples were freshly prepared right before measurement. Fiber dispersion where prepared right before measurement and homogenized as described before. As a

standard, amplitude sweeps were recorded at 25°C in milliQ water at 1 Hz at an oscillation strain of 0.01 – 10,000 %. For calculation of Young's modulus, hydrogel precursor solutions with desired conditions (gelatin and cNFC content) were casted in between two poly(methyl methacrylate) (PMMA) slides with 1 mm spacer. Prior to gelation, the slides were coated with polyvinylalcohol to avoid the hydrogel from sticking to the PMMA surfaces. The hydrogels are incubated at 4 °C for 30 min. to achieve pre-polymerization of gelatin. Then, the PMMA slides were removed and the gels are replaced in the micro plate with 10 U/ml mTG solution for 1 day at 4 °C to achieve the enzymatic cross-linking. The storage modulus of the gels was determined by performing oscillatory shear experiments with parallel plate geometry as described above. The Young's modulus E is calculated as follows $E=2G'(1+\nu)$, assuming $\nu = 0.5$.

*SEM*

Freeze-dried fibers were deposited on a carbon sticker. The samples were sputtered with a 2.4 nm gold layer. Images were recorded using a Quanta 200 FEG Cryo ESEM at an acceleration voltage of 5 kV, an aperture of 40 µm, spot size of 3.5 µm and working distance of 6 mm. Different fields of view of the same sample were analyzed at different magnifications and used for fiber counting.

*TEM*

5 µl of fiber solution was drop cast onto freshly glow discharged carbon stabilized formvar coated 200 mesh nickel TEM grids (EMS Diasum). The fibers were allowed to adsorb for 5 min. before the excess solution was wicked away using filter paper. The fibers were imaged using a Tecnai T20 G2 TEM at 200 kV and images were acquired using a TVIPS XF416 CCD camera.

*XPS*

XP spectra were recorded on an XPS Nexsa (Thermo Scientific). The measurements were performed using monochromated Al kα x-ray irradiation at 1486.6 eV and an ion flood source at 10 eV. Samples were dried overnight under vacuum on a Silicon-wafer and mounted on a sample holder. The scans were performed with ultra-high vacuum at pressure below $10^{-7}$ mbar during the analysis. Each sample was scanned at 3 different points within the sample and scanned 5 times with a Ø: 200 µm point.

*Fiber alignment staining*

The alignment of fibers of a printed construct was performed by preparing 5 mL of a 0.01 % v/v calcofluoro white (18909, Sigma-Aldrich) solution with 5 drops of 10 % KOH. The prints were incubated with a few drops of the staining solution for 1 h and then mounted with a glass slide and mounting solution (P10144, Molecular Probes). Images were recorded with a Nikon Eclipse Ti2 microscope and NIS-Elements software.

### 2.5.4 Direct-ink-writing of cNFC:composite (bio)inks and cell culture

*Printing of 3D structure*

A 3D CAD of an octopus was created using Fusion360 and printed on a RegenHU 3D Discovery bioprinter. A cross-linkable composite-ink based on non-reacted MFC was prepared using 3% w/w MFC and 3% w/v alginate (Dynamic viscosity: 80-120 cP, 194-13325, FUJIFILM Wako) in milliQ water. The MFC:alginate composite-ink was printed with a pneumatic syringe and a steel nozzle (ID 250 µm, Cellink Swe) at a pressure of ~ 230 kPa. A transparent, cross-linkable composite-ink was prepared using 5% w/v cNFC and 3% w/v alginate in milliQ water and printed with a pneumatic syringe and steel nozzle (ID 250 µm, Cellink Swe) at ~ 560 kPa.

*Culturing of $C_2C_{12}$ murine myoblasts*

$C_2C_{12}$ cell-culture was performed under sterile conditions and incubated at 37 °C, 100% humidity, 5% $CO_2$. $C_2C_{12}$ murine myoblasts were cultured in growth medium containing DMEM (D5796, Sigma-Aldrich), 10% fetal bovine serum (S1810, Sigma-Aldrich) and 1% P/S (P0718, Sigma-Aldrich). Cells were passaged and harvested at 80% confluency. Differentiation was initiated by changing growth medium to differentiation medium containing DMEM, 2% horse serum (H1270, Sigma-Aldrich).

*Culturing of human primary skeletal muscle cells*

Human single-donor skeletal muscle cells (SK111, Cook Myocite) were maintained and passaged in myotonic basal media (MB-2222, Cook Myocite) supplemented with 10% myotonic growth supplement (MS-3333, Cook Myocite) and 1% P/S antibiotic in a humidified atmosphere containing 5% $CO_2$ and 95% air at 37°C.

*Printing of cell-instructive surface and cell seeding*

The following procedure was performed under sterile conditions: sterile solvents with 1% penicillin/streptomycin (P/S, P0718, Sigma-Aldrich) were used and cross-linking solutions were sterile filtered with a 0.45 µm pore sized filter. All syringes and needles were additionally sterilized with UV light. A composite ink consisting of 5% w/v low bloom gelatin (164 G bloom, 48723, Sigma Aldrich) and 5% w/v cNFC was prepared as follows: dried fibers were suspended in DMEM at 10,000 rpm for 10 minutes. Low bloom gelatin was added to the fiber suspension and heated to 45 °C for approx. 45 minutes. The solution was stirred from time to time with a spatula and shortly centrifuged to exclude air bubbles. The composite ink was printed with a steel nozzle (ID 200 µm, Cellink Swe) at a pressure of 580 kPa and feed rate of 12 mm/s. Subsequently, the print was cross-linked with a 5 U/mL microbial transglutaminase (mTG, ACTIVA® TI Transglutaminase, 100 U $g^{-1}$, 1002, Modernist Pantry) solution over night at 4 ˚C. Before cell-seeding, the prints were washed 3x for 10 min. with PBS (D8537, Sigma-Aldrich). Alignment experiment in Figures 14 and 15 were performed with murine $C_2C_{12}$ myocytes within 10 passages at a density of 20,000 cells per well of a 12-well or 50,000 cells of a 24-well plate. Differentiation was initiated after day 3 by changing the medium from growth medium to differentiation medium. The experiment was ended at differentiation day 7 by fixing the cells. Alignment experiment in Figure 16 was performed with human skeletal muscle cells

at passage 5 and at a density of 200,000 cells per well in 12-well plates directly on the printed substrates and kept in MEM (41090-028, Gibco) with 10% myotonic growth supplement for 2 days before differentiation were initiated by switching to 2% horse serum as growth supplement (26050088, Gibco). These samples were fixed after 10 and 17 days of differentiation.

*Printing of protein-coupled cNFC substrate and cell seeding*

Sterile handling of all materials was performed as previously described. A 6-well tissue culture plate was pre-coated with 5 % w/v low Bloom gelatin in PBS and left drying. A 6 % w/v cNFC-FN and 4 % w/v cNFC-TG dispersion in milliQ was prepared and printed onto the coated plate alternatingly on a 6-well tissue culture plate with a line distance of 1.5 mm and a conical nozzle (ID 400 µm) at a pressure of 10 kPa and feed rate of 15 mm/s. The prints were subsequently cross-linked with 5 u/mL mTG in 137 mM NaCl for 50 min at 37 °C. Afterwards, the prints were irradiated with UV light for 20 min and washed 3x with PBS. The prints were seeded with 210,000 $C_2C_{12}$ within 10 days of passage and kept in culture for 10 days. Differentiation was initiated at day 3 of culture.

*Cell staining & imaging*

Printed constructs were washed 3x with PBS. After, cells were permeabilized and fixed with 0.1% v/v Triton X and 4% v/v paraformaldehyde and incubated for 20 min. at RT. The prints were washed 3x with PBS while shaking. A 1:1000 dilution of 4′,6-diamidino-2-phenylindole, dihydrochloride (DAPI, 62247, Thermo Scientific), 1:200 dilution of Alexa Fluor™ Plus 555 Phalloidin (A30106, Thermo Fisher) for F-actin staining in PBS was added and incubated overnight at 4 °C. The prints were washed 3x with PBS and kept in PBS at 4 °C until further use. Images of fluorescent stains were recorded with a Nikon Eclipse Ti2 microscope and NIS-Elements software and a Zeiss Observer Z1 microscope with a mounted Zeiss AxioCam.

*Myotube orientation quantification*

The ImageJ plugin OrientationJ[145] was used to determine the orientation of the myotubes on printed substrates. For this, F-actin stain was recorded after 7 days of differentiation. The hue and saturation of the false colored images correspond to the orientation angle and coherency, respectively. The distribution of orientation was plotted against the principal orientation angle. The alignment score corresponds to the total fraction of distribution within ± 15 ° of the principal orientation angle to the total count of oriented pixels. The alignment score for Figure 14 was calculated for n = 3 fields of view of 1.75 mm x 1.65 mm of 3 different samples. The alignment score for Figure 15 was calculated for n = 3 except for 5% LBG + 5% cNFC where n = 2 for fields of view of 7 mm x 7 mm.

## 2.6 Supplementary information

### 2.6.1 Supplementary figures

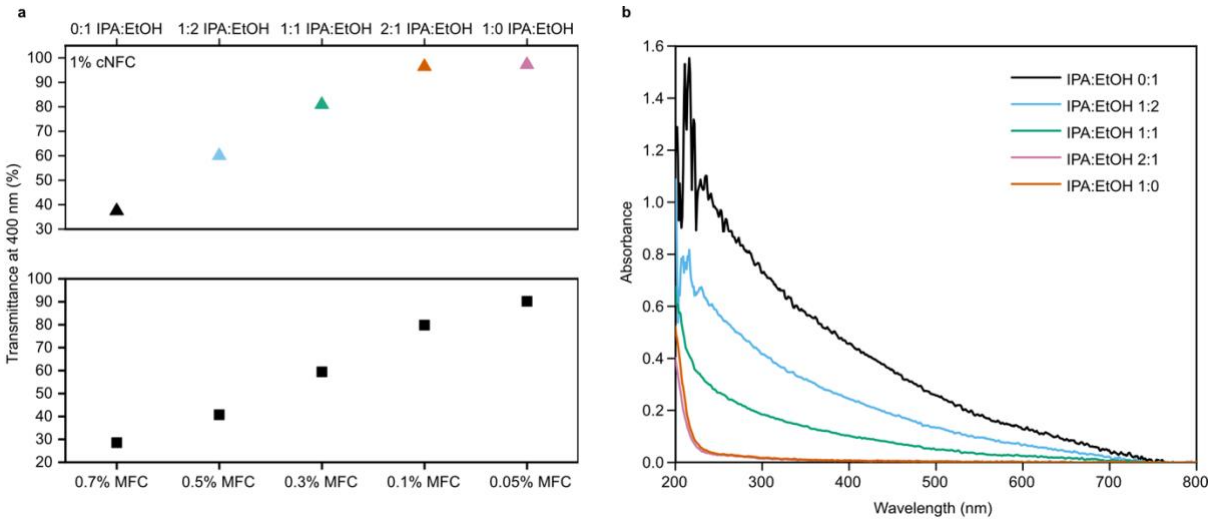


**Figure 17.** Optical properties of MFC compared to cNFC.
(a) Transmittance at 400 nm in % of cNFC reacted in IPA:EtOH 0:1 – 1:0 (upper graph, ▲) compared to dilution series of unreacted MFC from 0.05% - 0.7% (lower graph, ■). (b) Full absorbance spectra of 1% cNFC reacted in IPA:EtOH 0:1 - 1:0.

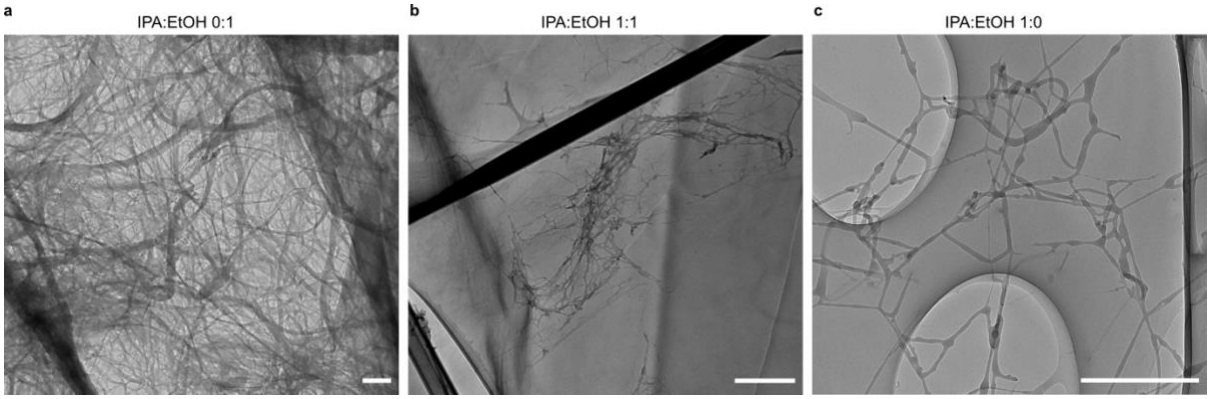


**Figure 18.** TEM images of cNFC 0:1, 1:1, and 1:0.
TEM images of cNFC oxidized in (a) 0:1, (b) 1:1, and (c) 1:0 IPA:EtOH. Scale bar: 500 nm.

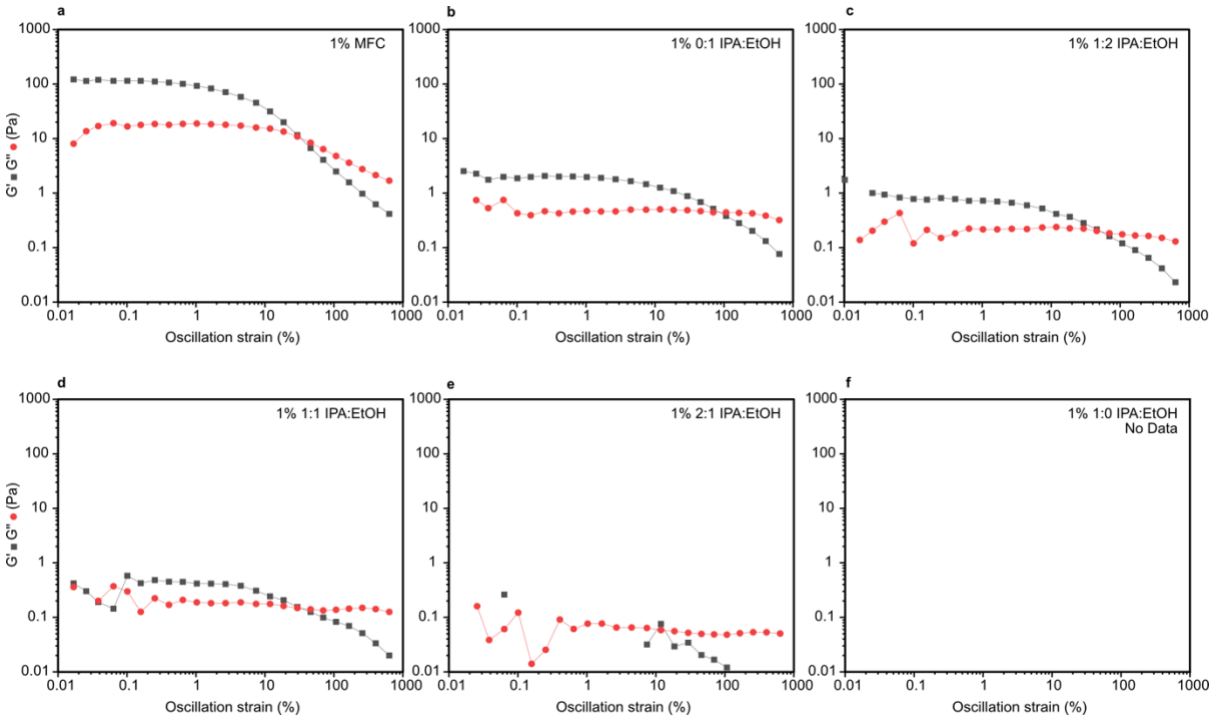


**Figure 19.** Rheology of MFC and cNFC oxidized at 1.25:1 NaOH:AGU, 0.5:1 MCA:AGU.
The oscillation sweep was recorded at 25°C in milliQ water at 1 Hz for n = 1. ■: Storage modulus G'. ●: Loss modulus G''. Rheology of (a) 1% MFC, (b) 1% cNFC 0:1, (c) 1% cNFC 1:2, (d) 1% cNFC 1:1, (e) 1% cNFC 2:1, and (f) 1% cNFC 1:0. The data for cNFC 1:0 was not collected due to sensitivity limits of the rheometer.

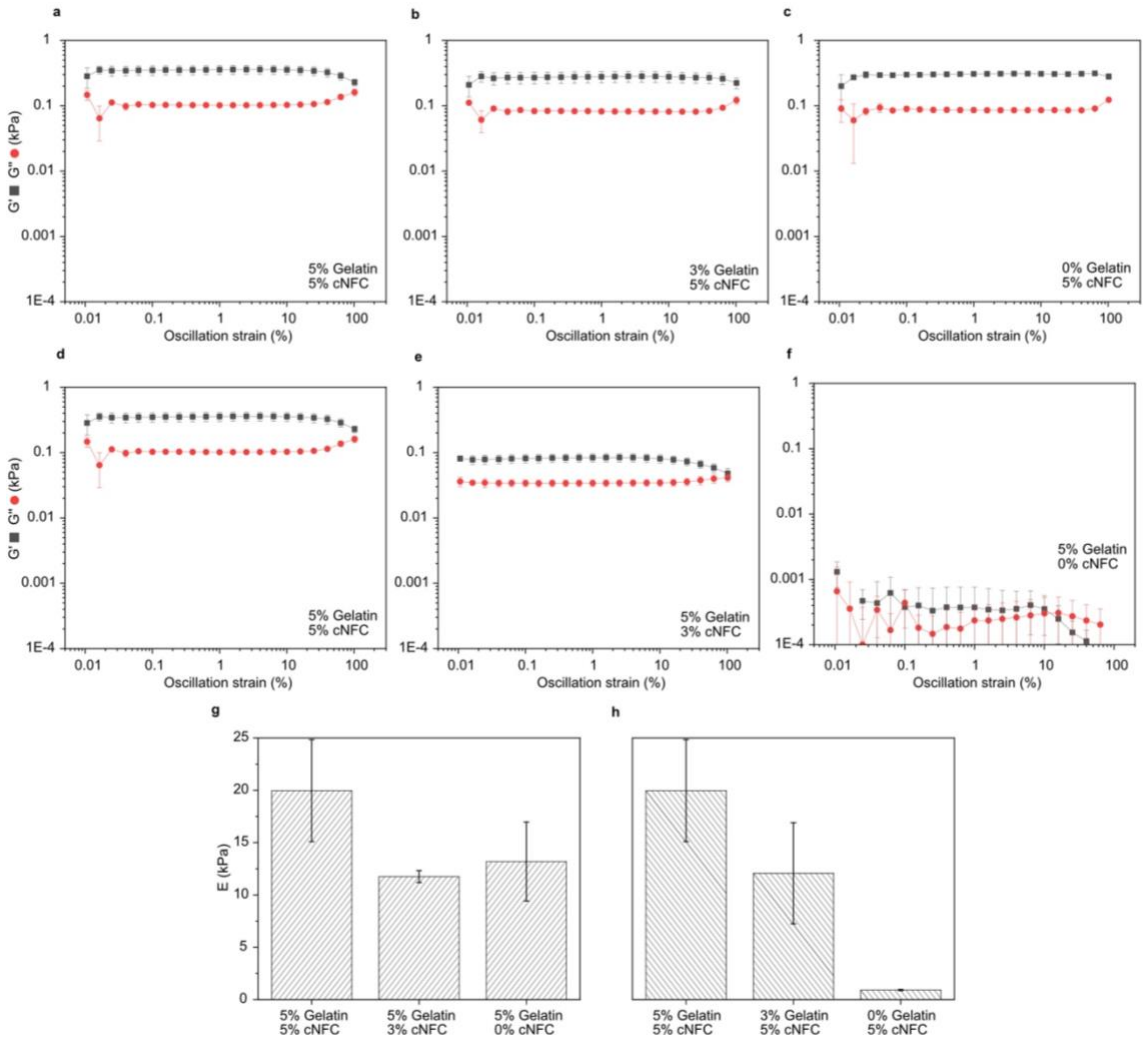


**Figure 20.** Rheology of cNFC:gelatin composites before and after cross-linking with mTG.
The oscillation sweeps were recorded at 25°C in PBS at 1 Hz. ■: Storage modulus G'. ●: Loss modulus G'' SEM for n=3. Rheology of composite inks with 5% cNFC and (a) 5% gelatin, (b) 3% gelatin, and (c) 0% gelatin. Rheology of composite inks with 5% gelatin and (d) 5% cNFC, (e) 3% cNFC, and (f) 0% cNFC. (g) Young's modulus E in kPa of cross-linked substrates printed with 5% gelatin and 5% cNFC, 3% cNFC, and 0% cNFC compared to 5% cNFC and 5% gelatin, 3% gelatin, and 0% gelatin. E calculated from G' at 1 % oscillation strain and SEM for n=3.

# Chapter 3

# Carboxymethylated nanofibrillated cellulose as support matrix for embedded printing

---

Experiments linked to the upscaling of the carboxymethylation reaction were conducted under the co-supervision of Prof. Dr. Lind by Jason Chan in the scope of a student course. Experiments linked to the enhancement of transparency of cNFC were performed in collaboration with Dr. Marko Mihajlovic. Experiments linked to fluorescently labeled cell-lines were conducted at the University of Pavia in the lab of Synthetic Physiology led by Prof. Dr. Francesco Pasqualini in collaboration with Eloisa Torchia and Dr. Moises di Sante in the scope of an external stay.

## 3.1 Introduction

Multi-material 3D printing, or DIW, as an emerging tool for the automated production of material scaffolds opens new possibilities in the field of tissue engineering. So far, direct-ink-writing of tissue models are somewhat restricted to two dimensions (2D) and small 3D structures within a few hundred micrometers and non-physiological cell densities.[5,9,48,146,147] This can be explained as follows: First, soft bioinks that exhibit shear-thinning rheology and high shape fidelity while simultaneously not jeopardizing cell viability due to shear-induced stress, are scarce. Most bioinks rely on soft hydrogels with liquid-like properties. 3D printed constructs with high aspect ratio will round up due to surface tension and tall structures will simply collapse due to gravitational forces. Secondly, thick voluminous tissues need to be vascularized to prevent cell death in the core of the tissue. To circumvent these effects and add the possibility of vascularization, the use of support matrices for embedded bioprinting is rising.

Support matrices for embedded bioprinting are composed of jammed microparticles that behave as elastic solids until a threshold yield shear stress $\tau_\gamma$ is applied. The movement of a needle within the elastic support matrix above $\tau_\gamma$ fluidizes spatially defined regions within the vicinity of the needle. An ink can be deposited and will be held in place by the re-solidifying support matrix. This procedure is also referred to as jamming transition of particles and is thought of a transition from a non-chaotic, solid state of the particles to a chaotic, liquid state under the influence of shear.[53] Ideally, the support matrix is non-thixotropic, as time-dependent re-solidification of the matrix, known as thixotropy, would led to crevasses within the matrix. The elastic modulus of the ink further plays a role in maintaining the printed shape. Previous simulations and studies have suggested a higher modulus ink compared to the support bath when printing non-Newtonian fluids to ensure a cylindrical shape of the printed filament. Using low-viscosity inks in high viscosity support baths yields fin shaped

filaments with sharp edges.[148,149] In conclusion, the following conditions must be fulfilled by ink materials, as summarized by Kajtez *et al.*: [109]

- Shear thinning ink material
- Shear thinning matrix material with low enough $\tau_\gamma$ to allow needle progression
- $G'_{ink} \approx 10\ G'_{matrix}$

The most prominently used materials for support matrices are based on microparticles. Bhattacharjee *et al.* provided a beautiful example of soft hydrogel prints within jammed Carbopol microparticles based on its non-thixotropic effect and concomitant rapid re-solidification after applied shear stress.[150] Hinton *et al.* presented ECM-protein based freeform reversible embedding of suspended hydrogels, short FRESH, within gelatin microparticle matrices.[51] Additional examples comprise degradable matrices based on alginate microparticles, and complex structures such as a cellularized, small-scaled, human heart have been successfully printed.[49,50,151] Most support matrices are composed of either alginate,[49,50,151,152] or gelatin microparticles,[51,52] commercially available microgel systems,[150,153] and carbohydrate-based hydrogels.[64,154–156]

In addition to microparticle systems, fibrillar systems have been used for embedded printing.[64,118] Herein, the viscoelastic gel will be sheared and yielded by the moving needle, allowing for extrusion of a bioink into the support bath. The use of a fibrillar matrix might enhance cellular outgrowth compared to tightly packed particle matrices (Fig. 21). Kajtez *et al.* proposed the use of a so-called continuous phase to increase inter-particle space within the Self-healing Annealable Particle-Extracellular Matrix (SHAPE) support bath. By adding collagen as continuous phase to the particle matrix, less particles were necessary to ensure shape-fidelity of the embedded prints and more space was provided for axon outgrowth of neural cells.[54] We observed low yield stress $\tau_\gamma$ of our cNFC hydrogels in Chapter 2 and will therefore explore the use of cNFC hydrogels as matrices for embedded printing in this chapter.

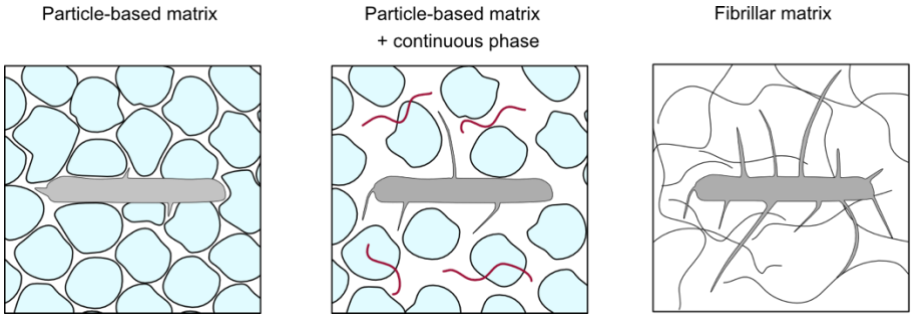


**Figure 21.** Illustration suggesting cellular outgrowth within support matrix.
Outgrowth of densely packed, printed tissue (grey) within jammed particle-based matrices (blue, left), particle-based matrices with a continuous phase (blue and red, middle), and purely fibrillar matrices (right). Illustration made with Affinity Designer.

### 3.2 Aims

This chapter presents a continuation of applications for the carboxymethylated nanofibrillar fibers presented in Chapter 02. Their transparency and viscoelastic properties opened up the possibility of using these fiber-based hydrogels as support matrices for embedded printing, aiming for the following:

I. **Adjusting carboxymethylation reaction for the use of cNFC as support matrix:** Preliminary results indicated compromised transparency when using large volumes of cNFC. Additionally, the quantity of cNFC needed as support matrix exceeds the quantities used as ink material. Therefore, the carboxymethylation reaction described in Chapter 02 will be adjusted and scaled up to yield large volumes of cNFC. Further, the degree of substitution will be increased to yield more transparent cNFC hydrogels.

II. **Print resolution and rheology of higher substituted cNFC support matrices:** An optimal ink-matrix combination needs to be found to ensure high shape fidelity of the prints while providing low yield shear stress of the matrix. For this, a range of inks will be tested in pure cNFC matrices and cNFC matrix composites.

III. **Cell adhesion and migration within cNFC-based support matrices:** Higher substitution of cNFC might decrease the adhesion of cells within the matrix. Therefore, the adhesion of a keratinocyte and epithelial cell line will be tested on a range of cNFC:collagen matrix compositions. Lastly, the migration of fluorescently labeled epithelial HT1080 cells embedded in cNFC:collagen matrices will be analyzed to ensure its use as support matrix.

## 3.3 Results and Discussion

### 3.3.1 Adjusting carboxymethylation reaction for the use of cNFC as support matrix

*Upscaling of carboxymethylation reaction*

The production of large quantities of cNFC was increased and the quantity of reactants scaled up. By simply increasing the volume and geometries, in which the reaction takes place, the outcoming product might be influenced. Therefore, we recorded IR spectra and analyzed the rheology to evaluate changes in mechanical properties of the fibers. The standard reaction was referred to as 1x and the reactants and volumes scaled up by 2x, 4x, 6x, and 8x. The IR spectrum of each reaction step reveals differences in degree of substitution: We can observe a slight decrease in degree of substitution with increasing batch size (Fig. 22a) when increased up to 4x. Interestingly, doubling the reaction does not seem to have an influence on the substitution. In contrast, the flowing properties of the 2x batch vary compared to the 1x batch and previous determination of the storage modulus. In Chapter 02, a storage modulus of around 50 Pa was determined for the 1x batch, similar to the results shown in Figure 22b. The moduli for the scaled up batches range between around 20 and 250 Pa. This could be attributed to batch-to-batch variations and is not a clear representation on the flowing properties dependent on the batch size.

The characterization of the fibers clearly indicates a decrease in substitution with increasing batch size, while the rheology shows mixed results. The original carboxymethylation reaction was conducted in a round bottom flask submersed in an oil bath, in which optimal stirring and heat distribution were ensured. The larger batches, as in 4x, 6x, and 8x, were performed in Schott-flasks without oil bath. The solutions were directly heated on a magnetic stirring plate. Here, we only heat a small surface area and might not ensure homogenous mixing compared to the overall volume. The influence of the experimental set up on the efficiency of reaction are reflected in our results. Nevertheless, our findings suggest a possibility of scaling up the reaction if the experimental set up is adjusted accordingly.

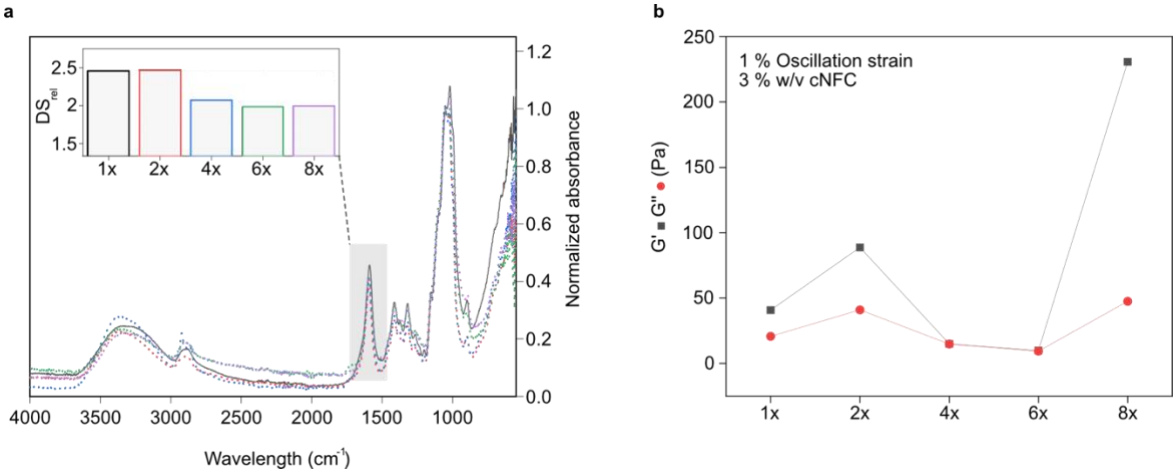


**Figure 22.** IR spectra & rheology of scaled-up carboxymethylation reaction.
(a) Normalized absorbance at 1050 $cm^{-1}$ for cNFC functionalized in scaled-up set up by 2x, 4x, 6x, and 8x compared to the original 1x reaction. Inset demonstrates calculated degree of substitution ($DS_{rel}$) by relating intensity peaks of carboxyl group (C=O) at 1595 $cm^{-1}$ to the stretching vibration of the glucose backbone (C-H) at 2894 $cm^{-1}$ as described in equation (8). (b) Storage G' and loss G'' modulus at 1 % oscillation strain of a 3 % w/v cNFC hydrogel in milliQ water for scaled-up cNFC functionalization.

*Preliminary embedded print into cNFC support bath*

Rheological studies on cNFC hydrogels indicated viscoelastic properties and low yield stress, making it a promising material for embedded printing. Furthermore, we speculate that the fibrillar network might enhance cellular outgrowth compared to jammed granular microparticle systems. We first printed a simple spiral within a pure cNFC hydrogel with a dyed alginate ink (Fig. 23). Notably, the transparency of the gel in this scale is decreased compared to smaller prints. Further, the resolution of the printed structure shows light compression.

In jammed microparticle systems, the resolution of the print is maintained due to quick re-solidification of a non-thixotropic material. Here, we see compression of our material, as well as the ink dragging within the matrix. The modulus of the ink was not adjusted to the modulus of the support material. A too low modulus-ink might be compressed by fast recovery of the surrounding matrix. Nevertheless, this preliminary result shows cNFC hydrogels as promising alternative for embedded printing.

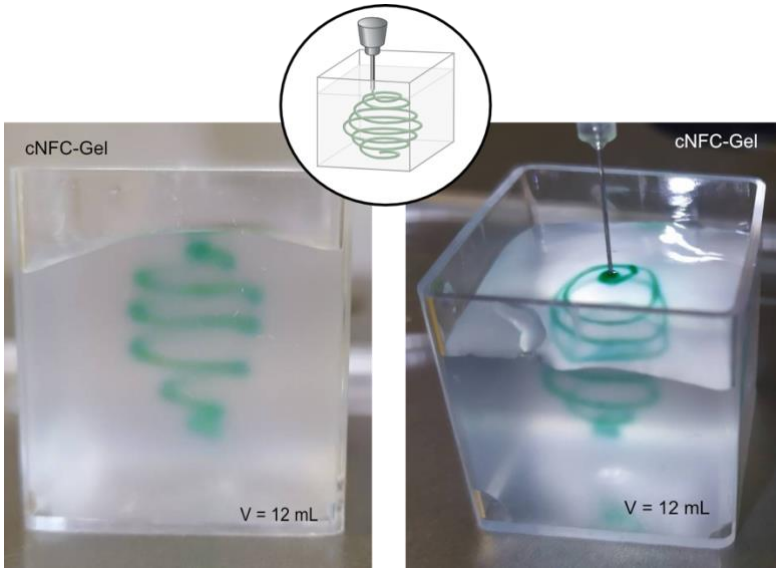


**Figure 23.** Embedded direct ink writing into cNFC hydrogel support matrix.
Illustration of print procedure and printing of a dyed 4 % alginate ink into 12 mL of a 2.5 % w/v cNFC hydrogel. Illustration made with Affinity Designer.

*Preliminary embedded bioprint of C2C12 myoblasts into cNFC-based support baths*

We hypothesized that the fibrillar network of cNFC-based support baths will enhance cellular outgrowth compared to commonly used microparticle systems. We performed a simple bioprint using a high density of C2C12 myoblasts and printed a line into cNFC support baths with 1 and 2 mg/mL collagen. After 1 day, we observed compaction of the printed tissue all cases (Fig. 24a,b,c). After 4 days, we observed maximum compaction in all cases and cellular outgrowth in cNFC support baths supplemented with 2 mg/mL collagen (Fig. 24d, e). Different concentrations of cNFC do not seem to influence outgrowth of cells. Still, at 2% cNFC the transparency of the hydrogel is significantly impaired compared to 1 % cNFC. Cells growing in 2 % cNFC and 1 mg/mL collagen compacted by 86 %, followed by a 73 % compaction in 1.5 % cNFC with 1 mg/mL collagen and finally, 61 % in

1 % cNFC and 2 mg/mL collagen. Additionally, fluorescent microscopy reveals how cells migrated into the matrix in the gel supplemented with 2 mg/mL compared to 1 mg/mL (Fig. 24d,e).

Cells adhere to collagen fibers via integrin receptors that recognize specific amino acid sequences. A higher concentration of collagen provides more adhesion sites for the cells, while a higher concentration of cNFC might impair cellular adhesion due to the negatively charged surface of the fibers. These first results indicate how the cell-matrix interactions can be tailored by varying the concentration of matrix-components and might be enhanced by increasing the amount of cell-adhesion sites within the matrix.

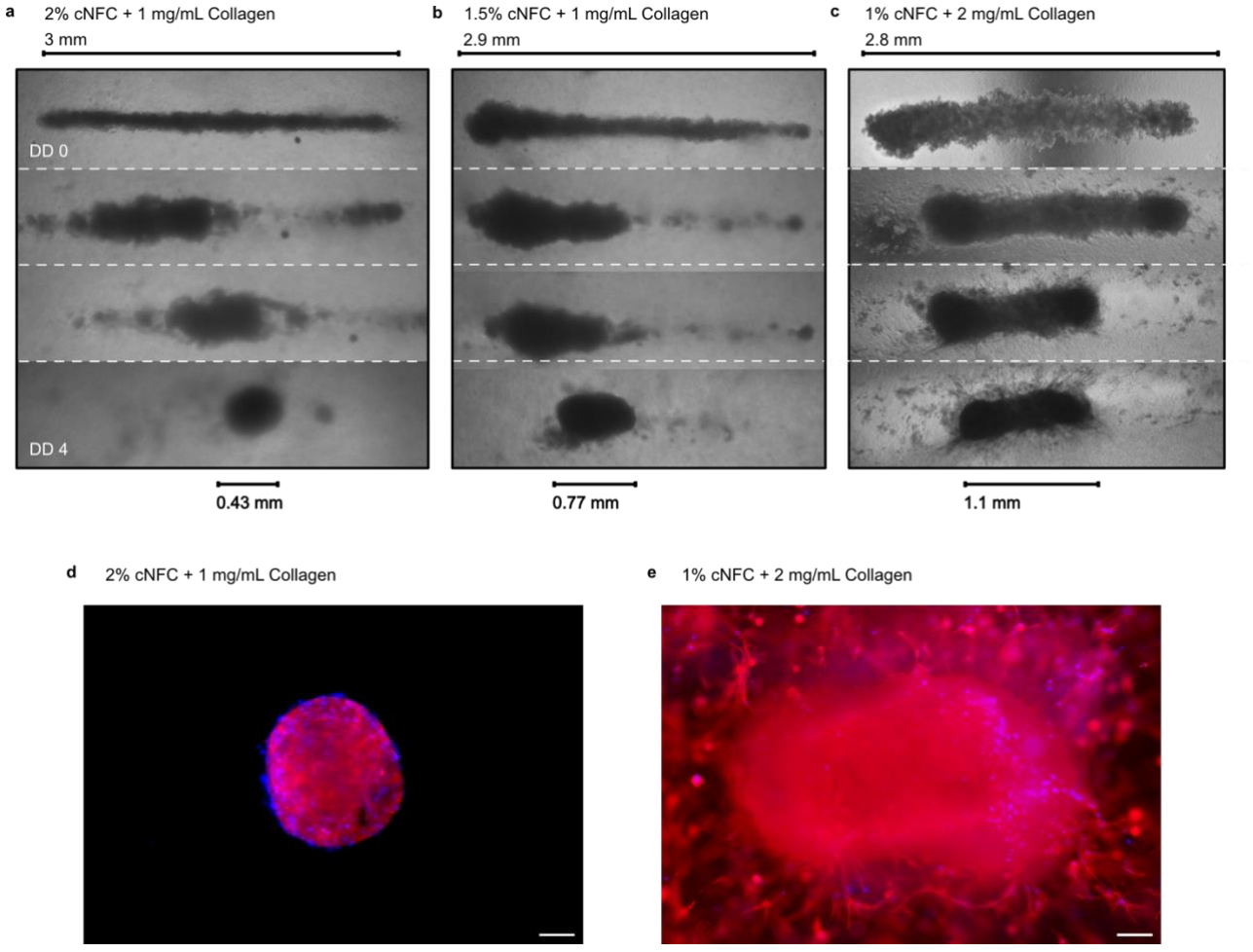


**Figure 24.** Compaction of C2C12 myocytes within cNFC:collagen composite gels.
(a) 2 % cNFC with 1 mg/mL collagen, (b) 1.5 % cNFC with 1 mg/mL collagen, (c) 1 % cNFC with 2 mg/mL collagen. Printed myocytes compact within 4 days of differentiation into condensed tissues. (d) Fluorescent stain of C2C12 myocytes in 2 % cNFC with 1 mg/mL collagen, and (e) 1 % cNFC with 2 mg/mL collagen. Red: Actin stain. Blue: Nucleus stain. Scale bar: 100 µm.

*Enhancing transparency of large cNFC volumes*

Preliminary experiments of embedded printing within these hydrogels showed compromised transparency at large volumes. For this reason, the carboxymethylation reaction was slightly modified to achieve higher transparency without losing the mechanical properties. The amount of reactants for activation of the fibers was increased by 20 % and 40 %, respectively. The IR spectra indicate a higher

degree of substitution the higher the concentration of reactants (Fig. 25b). This result was further confirmed by calculating the degree of substitution via titration (Fig. 25a). Higher substituted fibers disperse better in solution, which might influence the mechanical properties of the hydrogel. This is reflected in the rheology of the respective hydrogels (Fig. 2c-e). The highest substituted sample with + 40% more reactants (cNFC40) loses its viscoelastic properties and is dominantly viscous (Fig. 25e), while the batch functionalized with + 20 % reactants (cNFC20) does not indicate major changes (Fig. 25d).

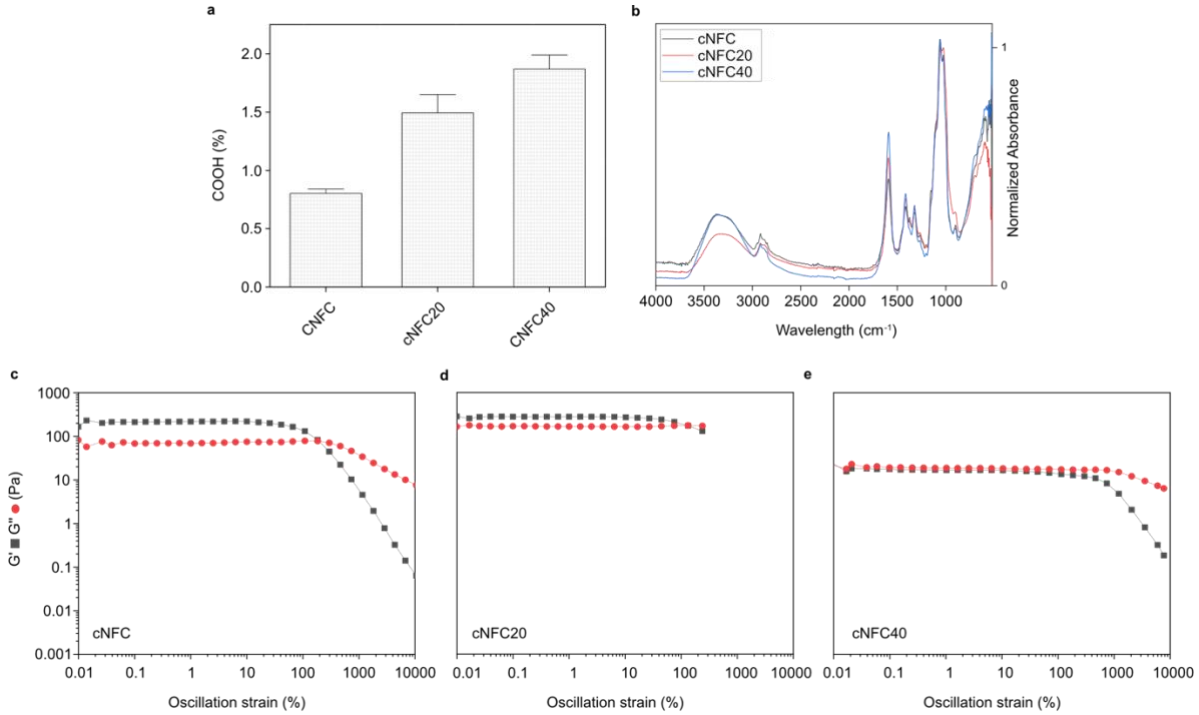


**Figure 25.** Degree of substitution and rheology of cNFC20 and cNFC40.
The amount of COOH groups for n = 3 (a), and normalized absorbance at 1050 $cm^{-1}$ (b) of cNFC functionalized in the standard protocol and with 20 % and 40 % more reactants were compared. (c-d) Storage G' and loss G'' modulus of cNFC at 1 Hz of the standard cNFC functionalization (c) compared to 20 % more reactants (d) and 40 % more reactants (e) at a concentration of 5 %.

The carboxymethylation reaction was performed with higher content of both, NaOH and MCA, which yielded higher substituted cNFC-derivates. With increasing degree of substitution, a reduction of viscoelasticity was observed. This could be attributed to the higher substituted fibers dispersing better in solution, with cNFC40 even losing its viscoelastic properties and being dominantly viscous. Still, cNFC substituted with + 20 % reactants was significantly more transparent compared to the standard batch. Therefore, we produced cNFC20 in a higher scale (8x) and explored its performance as support matrix for embedded printing.

### 3.3.2 Print resolution and rheology of higher substituted cNFC matrices

*Finding a suitable matrix-ink combination: Screening of print parameters and concentrations*

Preliminary results indicated the possibility of using cNFC hydrogels as support matrices. Yet, the mechanical properties of the ink did not match the requirements for embedded printing. We will therefore focus on cNFC20 as support matrices and investigate a suitable ink. For this, we first tested

different concentrations of cNFC20 support matrices with a low-viscosity ink based on XG. We observed increasing compression of a printed meander with increasing cNFC20 concentration, while at lower concentrations the structure was not held in place (Fig. 26a). Since the aim is to use cell-laden inks, the stiffness of the bioink is crucial for cell viability. Therefore, the concentration of the support matrix was kept below 4 %.

It has been reported that the viscosity of the ink should be higher than the viscosity of the support matrix to ensure a round cross-section of the printed filaments.[148,149] Therefore, we further screened different concentrations of cNFC20 as ink material within similar concentrations of cNFC20 as support bath. In accordance to the requirements for ink modulus, we found the best resolved structure with a 4 % cNFC20 ink in a 2.5 % cNFC20 support bath (Fig. 26b,c). We furthermore screened print parameters, such as feed rate (mm/s) and extrusion rate (µL/s) to achieve highest resolution (Fig. 26d). A low extrusion rate of 0.1 µL/s led to compression of the material, which indicates that stress exerted by the flow of the material out of the nozzle might not induce yielding. A high extrusion rate of 0.4 µL/s, in contrast, leads to over extrusion of the material. The results (Fig. 26d) suggest an extrusion rate of 0.2 µL/s and feed rate of 0.5 mm/s.

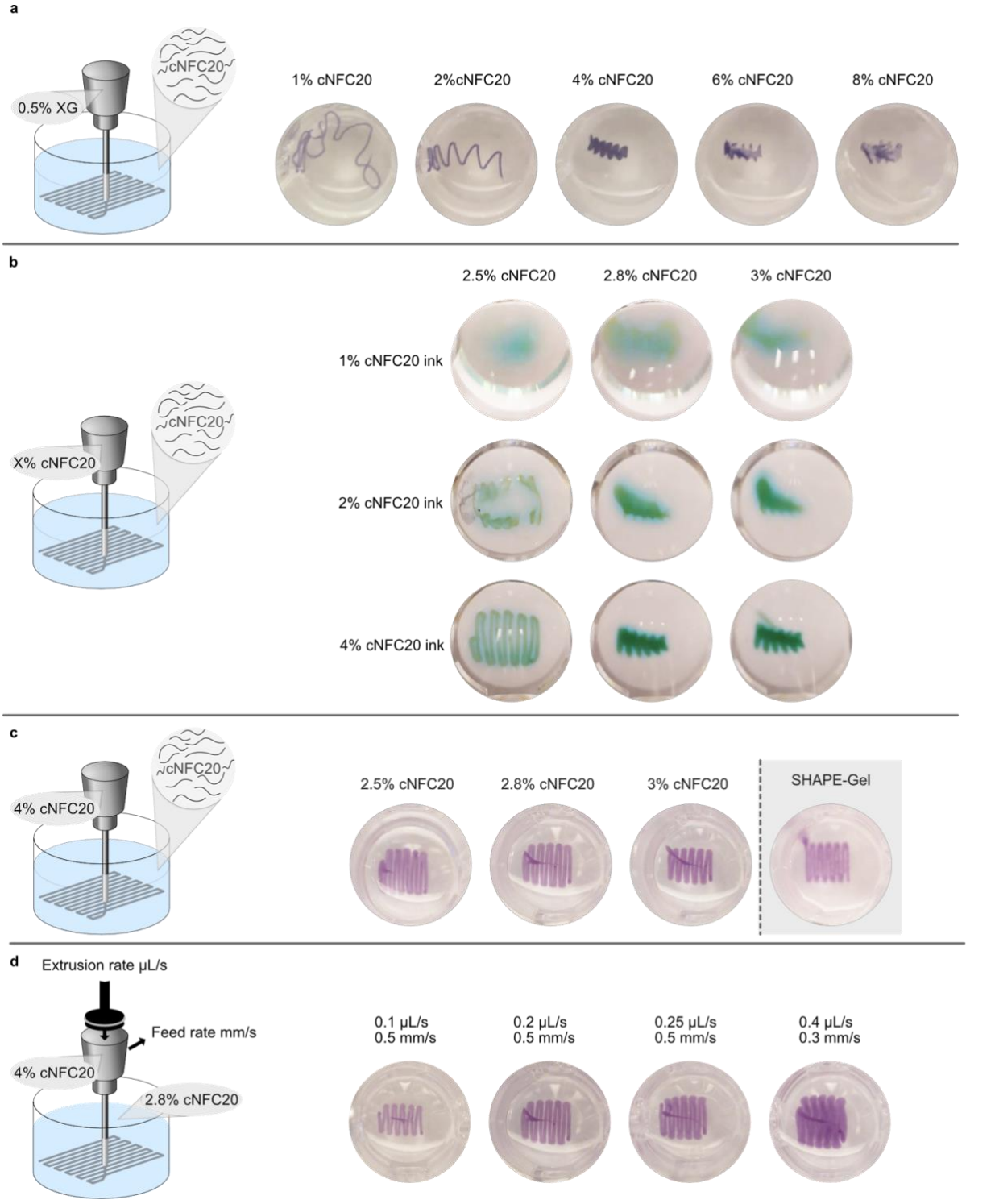


**Figure 26.** Embedded printing within different concentrations of cNFC hydrogels.
(a) A meander was printed with a 0.5 % dyed XG ink into 1 %, 2 %, 4 %, 6 %, and 8 % cNFC20, respectively, at a feed rate of 0.5 mm/s and an extrusion rate of 0.1 µL/s. (b) Dyed inks composed of 1 %, 2 %, and 4 % cNFC20 (vertical) were printed into 2.5 %, 2.8 %, and 3 % cNFC20 (horizontal), at an extrusion rate of 0.1 µL/s and a feed rate of 0.3 mm/s. (c) A dyed 4 % cNFC20 ink was printed into 2.5 %, 2.8 %, 3 % cNFC20 and the SHAPE gel, at an extrusion rate of 0.2 µL/s and feed rate of 0.05 mm/s. (d) Extrusion rate in µL/s and feed rate in mm/s were screened and printed with a 4 % cNFC20 ink within a 2.8 % cNFC20 support bath. Illustrations were made with Affinity Designer.

Since we achieved good print resolution by adjusting the concentration of the ink in relation to the support bath, we now added ECM-derived supplements to the support bath. We printed a 4 % cNFC20 ink into a 2.8 % cNFC support bath supplemented with 1.5 % LBG and 2 mg/mL COL. Interestingly, the support matrix supplemented with collagen slightly induces compression of the printed structure (Fig. 27). Since the print was performed at room temperature, the polymerization of collagen might be initiated, which might influence the viscoelastic properties of the support bath.

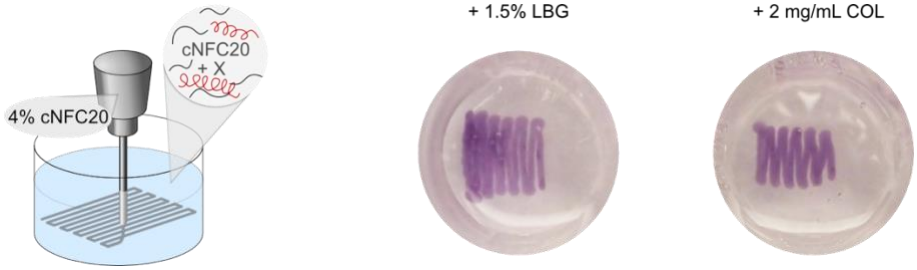


**Figure 27.** Support matrices with cell-adhesive additives.
A 4 % cNFC20 ink was printed into a 4 % cNFC20 support bath with 1.5 % LBG, and 2 mg/mL COL, respectively. The print was performed at an extrusion rate of 0.25 µL/s and a feed rate of 0.5 mm/s.

*Rheological properties of composite hydrogel support matrices*

Embedded printing into cNFC20 hydrogels and hydrogel composites revealed the importance of viscoelasticity of the support matrix, as well as the ink. A closer look was taken into the viscoelastic properties of the composite materials by means of rheology. For this, we formulated cNFC20 hydrogels with 2 mg/mL and 4 mg/mL collagen. The printing procedure occurs at room temperature, where collagen is still in liquid state and slowly polymerizing. Therefore, we conducted amplitude sweeps at 25 °C and compared them to the cross-linked state during cell culture at 37 °C. Pure 2.8 % cNFC20 exhibits viscous properties with a dominating loss modulus at 25 °C and 37 °C (Fig. 28a). Collagen hydrogels at 2 mg/mL and 4 mg/mL are dominantly elastic with similar storage moduli at both, 25 °C and 37 °C (Fig. 28b,c). Lastly, cNFC20 hydrogels supplemented with 2 mg/mL and 4 mg/mL collagen behave similar to pure cNFC20 (Fig. 28d,e).

These results indicate dominating mechanical behavior of cNFC20 over collagen, even though pure collagen samples are dominantly elastic at both, 25 °C and 37 °C. The polymerization of collagen might be impaired by the slightly acidic properties of cNFC20. Most interestingly, at 2.8 % cNFC20 no yield stress can be determined due to dominating viscous behavior. Higher concentrations of the support bath of at least 5 % might increase the print resolution. Still, the concentration of the ink needs to be adjusted accordingly and might impair cell viability. Finally, the motivation of this work was to enable cellular migration and growth within a cNFC-based support matrix due to its dynamic, fibrillar network, compared to a jammed microparticle system. A low modulus and viscous properties might still favor cellular expansion, while compromising the complexity of printing. The final composition of the support matrix needs to be considered for the desired application.

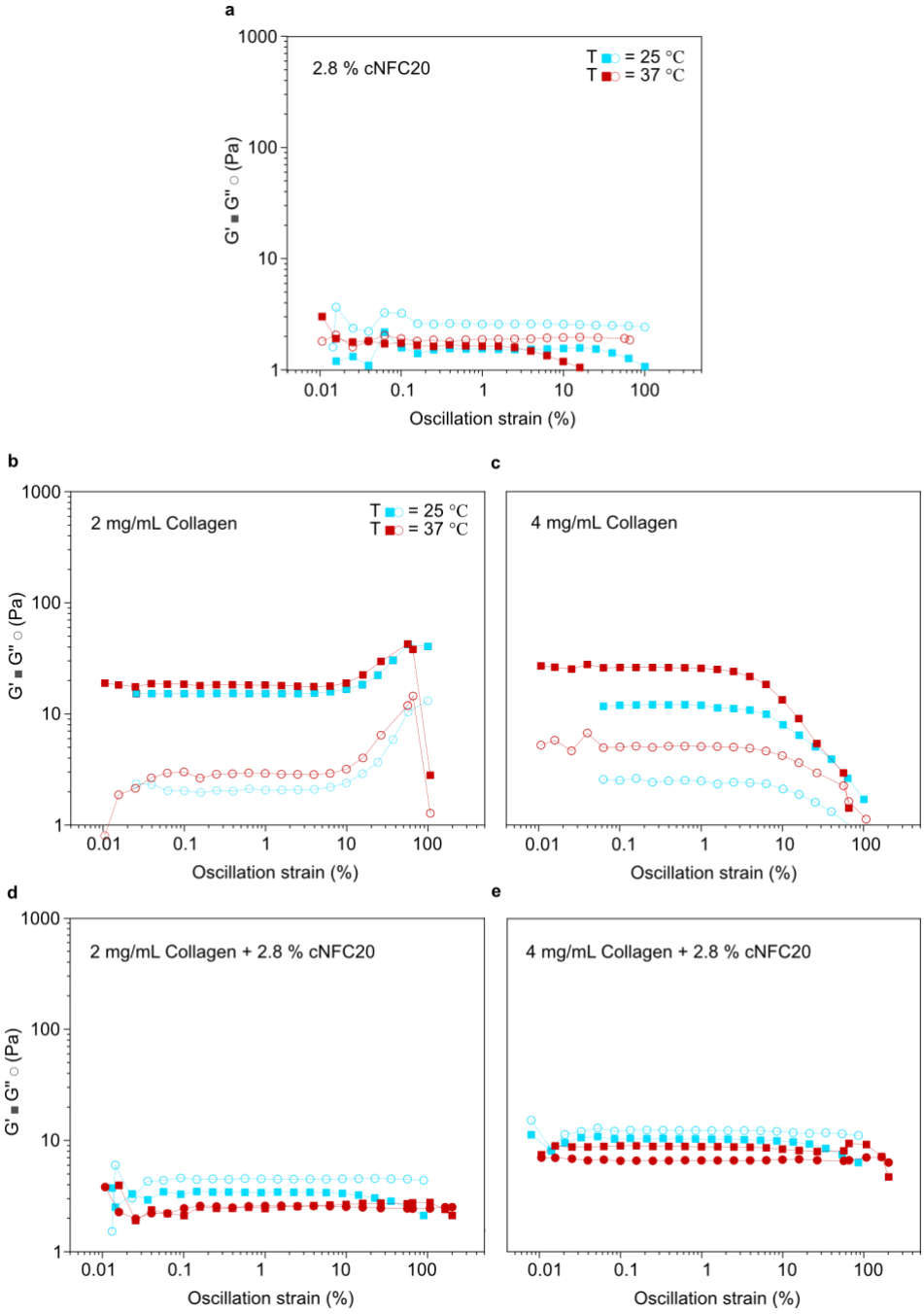


**Figure 28.** Rheology of cNFC20, collagen, cNFC20:collagen.
Storage G' (full icon) and loss G'' (hollow icon) modulus recorded at 25 °C (blue) and 37 °C (red), respectively. (a) 2.8 % cNFC20 hydrogel, (b) Rheology of 2 mg/mL collagen, (c) 4 mg/mL collagen, (d) 2 mg/mL collagen + 2.8 % cNFC20 composite gel, (e) 4 mg/mL collagen + 2.8 % cNFC20 composite gel. All spectra were recorded at 1 Hz. The gels were freshly prepared on ice and the rheology recorded after equilibrating temperature for 30 s.

### 3.3.3 Cell adhesion and migration within cNFC-based support matrices

*Cellular adhesion on cNFC20 hydrogels*

Higher substituted cNFC20 means more negative charge. While this enhances the transparency of the formulations, it might influence adhesion of cells onto the negatively charged fibers. We therefore explored cellular adhesion of cell-adhesive cNFC20 hydrogel formulations. For this, fluorescently labeled HT1080 epithelial cells and HaCaT keratinocytes were used and their migration observed via fluorescence microscopy. We observed HaCaT keratinocytes detaching the higher the cNFC20 content. At 2% cNFC20 and in the SHAPE gel, the HaCaT cells form islands, while at 4% cNFC20 they start detaching from the gels (Fig. 29a). HaCaT are a keratinocyte cell line that migrates in groups of multiple cells. The higher carboxylate content of the hydrogel might impair cell adhesion onto the collagen network within the gel and thus, lead to the formation of small islands, and lastly, detachment. Notably, HT1080 epithelial cells are known to migrate as single cells and seem to expand better at higher cNFC20 concentrations. At concentrations below 4% cNFC20, the cells seem to form bulges (Fig. 29b). Based on these results, we decided to observe single cell migration of HT1080 in 4% cNFC20 gels with slightly higher collagen content (2 mg/mL) to mainly enhance cell adhesion but also stability of the gel in culture.

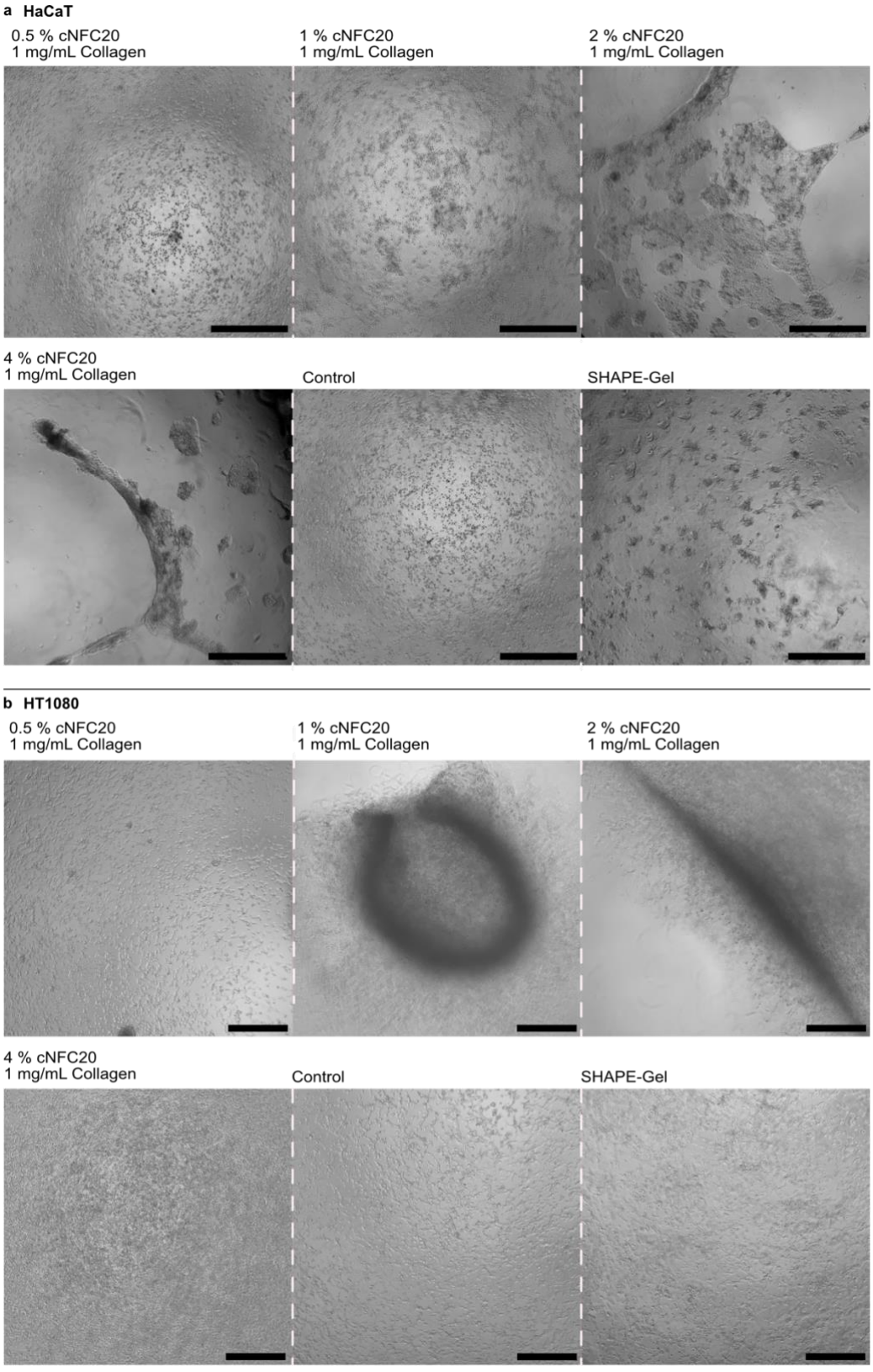


**Figure 29.** HaCaT and HT1080 cells seeded on different cNFC20:collagen and SHAPE gels.
(a) HaCaT and (b) HT1080 seeded at a density of 30,000 cells/cm$^2$ and observed over 5 days. The concentration of collagen was kept at 1 mg/mL and cNFC concentrations range from 0.5 % - 4 %. The control represents cells on the plain tissue culture plate. Scale bar: 1 mm.

*Migration of HT1080 epithelial cells within cNFC20 matrices*

During embedded printing, cells are extruded into the matrix and fully encapsulated by the surrounding matrix. To study the migration of HT1080 fibrosarcoma, we covered plated cells with a 4 % cNFC20 hydrogel supplemented with 2 mg/mL collagen and recorded their movement over time. At t = 0 h, the cells were sitting on the tissue culture plate referred to as z = 0 µm. Here, we can already see rounding of the cells, which often indicates incoming cell death (Fig. 30). After 10 h, the cells were not present in the initial z-plane, but had migrated 20 µm upwards (Fig. 30).

These results indicate active migration within the matrix. In 3D, different modes of migration can be differentiated and depend on the environment of the cell. Mesenchymal cell migration is dependent on actin polymerization and cell adhesion to the matrix, and comparable to motion in 2D. Amoeboid migration is independent of adhesive interactions with the matrix and mainly driven by actin protrusion or hydrostatic membrane blebs. The absence of any protrusion of the cells, referred to as lobopodia, indicates amoeboid migration. This type of motion does not rely on degrading the ECM with proteases, but on choosing the path of the least resistance. The cells squeeze through pores present in the ECM without adhering to the matrix nor degrading it.[157] Our results suggest the uninhibited migration through large pores within the matrix. Unfortunately, the reproduction of these experiments, as well as in SHAPE gels and pure collagen gels, only showed rounding or blebbing of the cells after addition of the hydrogel, but no motion. A driving force in the form of a nutrient gradient might enhance their motion through the gel.

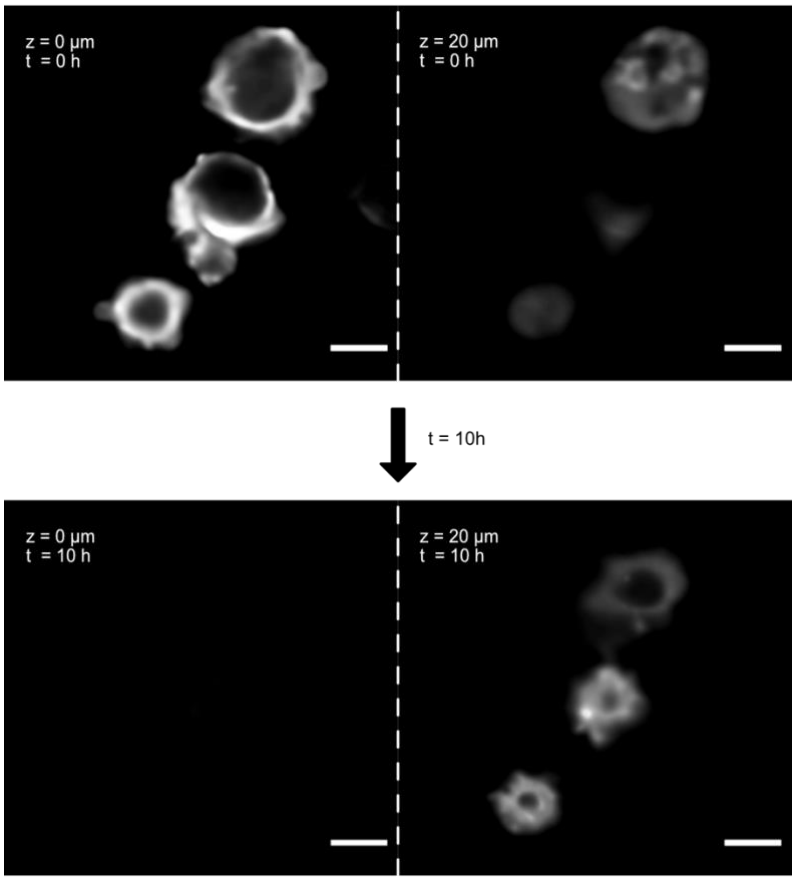


**Figure 30.** Migration of HT1080 in 4 % cNFC20 + 2 mg/mL collagen in z plane.
Images were recorded within a range of 20 µm in 3 µm steps for 10 h. At t = 0h, three cells are located at z = 0 µm. At z = 20 µm, the cells are barely visible. After 10 h, the cells do not appear in z = 0 µm but appear in z = 20 µm. Scale bar: 10 µm. White: Actin stain.

To further imitate print-like conditions, we designed an experiment where we extruded the HT1080 cells within a support matrix and observed their migration within the gel. Here, the migration occurred within 1 h and we observed cellular migration downwards towards the bottom of the tissue culture plate (Fig. 31). Due to the comparatively high viscosity of the gels, sedimentation can be excluded. A comparison to SHAPE gel indicated similar migration downwards (data not shown). From this we can conclude, that our cNFC20:collagen support matrices are well suited to allow cellular migration within the gel and show similar migration of cells compared to SHAPE-gels.

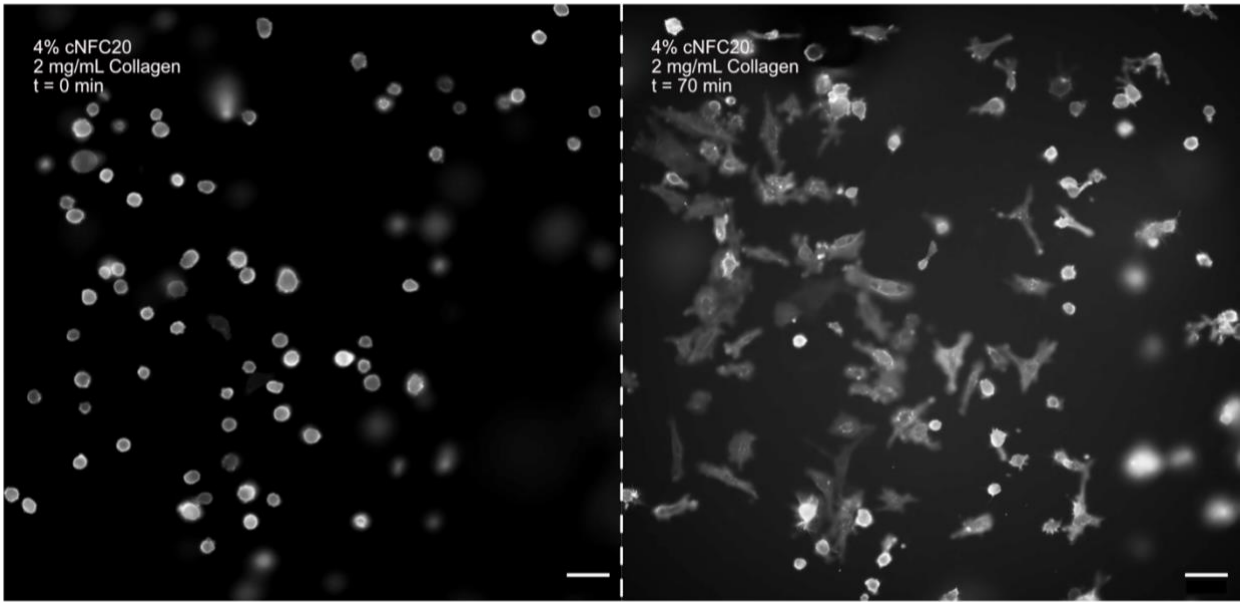


**Figure 31.** Print-like migration within matrix.
Migration of HT1080 pipetted into gels within 70 min in 4 % cNFC20 with 2 mg/mL collagen, at t = 0 min (left) and t = 70 min (right). Scale bar: 50 µm. White: Actin stain.

### 3.4 Conclusion

Embedded printing is a promising method to surpass the limits of printing complexity, mechanical stability, and enhance the formation of functional tissues. Common examples rely on packed gelatin or alginate microparticles. Herein, printed cells are surrounded by comparatively big particles, that might hinder the expansion of cellular protrusions. Our carboxymethylated nanofibrillated cellulose exhibits comparable rheological properties and similar formulations have already been explored in the field of embedded printing.[64,118,154]

Firstly, we aimed at adjusting the carboxyxmethylation reaction to yield large volumes of cNFC for embedded printing. First prints within cNFC matrices show average print resolution of complex structures. Still, we successfully performed an embedded print at a high density of C2C12 myoblasts within cNFC hydrogels supplemented with collagen. Here, we observed collagen-dependent outgrowth of myoblasts into the matrix. We further observed impaired transparency in larger volumes of cNFC. By increasing the amount of reactants by 20 %, we achieved higher substituted cNFC fibers (cNFC20) with enhanced transparency.

Secondly, we adapted the print resolution of cNFC20 inks into cNFC20 support matrices. Our results suggest higher concentrations of cNFC20 inks compared to the support matrix. We printed 4 % cNFC20 ink into a 2.8 % cNFC20 support matrix with a resolution comparable to granular microgels. In addition, we explored the rheology of cNFC20 support matrices supplemented with collagen. We found that 2.8 % cNFC20 does not yield and behaves viscous. The mechanical properties of the support matrices with collagen are dominated by the cNFC20 fibers even after cross-linking of the collagen at 37 °C.

Lastly, we aimed at observing cellular migration within cNFC20 support matrices. We found that HT1080 epithelial cells and HaCaT keratinocytes adhered between 2 – 4 % cNFC20 with 2 mg/mL and observed migration of HT1080 epithelial cells within our matrices. We compared our results with a granular microgel system and did not see differences in migration of HT1080 epithelial cells between fibrillar or granular microgel matrices.

Overall, cNFC-based support matrices show promising mechanical behavior for their use in embedded printing. Still, the concentration cNFC within support matrices might need to be increased to ensure yielding during printing of more complex structures. This, in turn, might compromise cell viability due to the necessity of higher ink concentrations. Further modifications of the fibers with cell-adhesive peptide motifs might enhance cellular outgrowth within the hydrogel. Nevertheless, the ease of production of cNFC hydrogels makes them an appealing alternative material for embedded printing of simple structures.

## 3.5 Experimental section

### 3.5.1 Chemical functionalization and slurry production

*Upscaling of carboxymethylation reaction*

The carboxymethylation reaction on MFC was performed as described in Chapter 02 with the following modifications: For the 1x reaction, 10 g of MFC (Borregaard in Sarpsborg (NO)) was homogenized for 10 min using an Ultra-Turrax homogenizer with a S25N-18G-ST dispersing element at 10,000 rpm in 100 mL of a freshly prepared 2:1 Isopropanol:Ethanol (IPA:EtOH) mixture (Isopropanol, methanol and ethanol absolut ≥ 99.9% were purchased from VWR). Reactions performed at 1x and 2x were performed in a round bottom flask with an oil bath. The heat was controlled over the heat bath and measured directly in the solution. The reactions scaled up by 4x, 6x, and 8x were performed in a 1.5 L Schott-Flask. The solutions were stirred vigorously and heated to 35 °C. Once the temperature was reached, 12 mL of a 5 % w/v NaOH (S5881) solution was added and left stirring at 35 °C for 30 min. Then, the temperature was risen to 45 °C and 570 mg of monochloroacetic acid (MCA, 402923) dissolved in 3-4 mL IPA:EtOH was added. For the 2x reaction, 20 g MCA was homogenized in 200 mL 2:1 IPA:EtOH. 24 mL of a 5% w/v NaOH solution was added and 1.14 g MCA in approx. 6-8 mL 2:1 IPA:EtOH. For the 4x reaction, double amount of reactants and volumes were used, and so on. The flasks were heated up directly on the heat plate and temperature controlled in the solution. The purification of the fibers was performed as described in Chapter 02, section 2.5.

*Increasing of transparency of fibers by increasing amount of reactants*

The following protocol was established by Dr. Marko Mihajlovic. The carboxymethylation reaction was performed scaled up by 8x in a round-bottom flask with a suitable oil bath as described before. The following changes were made to achieve higher transparency: First, the reactants were increased by 20%, yielding NaOH:AGU 3:1 and MCA:AGU 1.2:1. The reaction was performed on 80 g MFC pulp homogenized in 780 mL 2:1 IPA:EtOH mixture. After heating to 35 °C, 100 mL of a 6 % NaOH solution in 2:1 IPA:EtOH was added. The solution was left stirring for 30 min. The temperature was risen to 45 °C. Subsequently, 5.64 g of MCA dissolved in 30 mL 2:1 IPA:EtOH was added and the solution left stirring for 3 h at 45 °C. The solution was neutralized with 80 mL acetic acid (10 % v/v) and the fibers purified as described in chapter 02. Secondly, the reactants were increased by 40 %, yielding NaOH:AGU 3.6:1 and MCA:AGU 1.4:1. The reaction was performed as described with 120 mL of a 6 % NaOH solution, and 6.8 g MCA in 30 mL 2:1 IPA:EtOH.

*Production of alginate slurry*

The protocol to produce SHAPE gels was established by Kajtez *et al.*[151] and reproduced for comparison. Shortly, a 1 % w/v sodium alginate solution (Dynamic viscosity: 80-120 cP, 194-13325, FUJIFILM Wako) was dissolved in sterile water and stirred for 4 h at 60 °C. The solution was filtered through 0.45 µm pore size filter while it was still warm. Equal volumes of the sterile filtered alginate solution and a sterile aqueous 2 mg/mL $CaCO_3$ solution were mixed and stirred at room temperature for 1 h. Acetic acid was added in a 1:500 ratio and stirred vigorously at room temperature over night

at 650 rpm. The next day, alginate particles were generated by homogenizing the gel at 15,000 rpm for 10 min with the Ultra-Turrax homogenizer with a T25-S25N-10G dispersing element. Microparticles were centrifuged at 18,500 G for 20 min and resuspended and incubated over night at room temperature in DMEM containing 2 mM NaOH and 1 % P/S. The day after, the particles were homogenized once again at 15,000 rpm for 3 min and centrifuged at 18,500 G for 10 min. The supernatant was removed, and the alginate slurry stored at 4 °C until further use. The day before printing, the pellet was resuspended in double the volume of DMEM containing 4 % HEPES (1 M) and 4 % $NaHCO_3$ (37 g/L, pH adjusted to 9.5) and incubated over night at room temperature. The slurry suspension was centrifuged at 18,500 G for 10 min and the supernatant removed. The SHAPE gel was generated by mixing the cold alginate slurry in a 2:1 ratio with the pH adjusted collagen stock (as described in section 3.5.2).

### 3.5.2 Direct-ink-writing of inks into standard cNFC formulation and cNFC20

*Printing of spiral into cNFC hydrogel*

For direct-ink-writing experiments, a RegenHU 3D printer with pneumatic and volumetric print heads was used. A 4 % w/v alginate (Dynamic viscosity: 80-120 cP, 194-13325, FUJIFILM Wako) gel was prepared and mixed with green food dye. The ink was extruded *via* pneumatic extrusion at 250 kPa and a feed rate of 0.5 mm/s into 12 mL 2.5 % w/v original cNFC hydrogel (functionalization as described in Chapter 02 but scaled up 8x) using a steel nozzle (ID 200 µm, Cellink, Swe).

*Printing of a range of cNFC/cNFC20 inks into cNFC/cNFC20:composite hydrogels*

A stock solution of cNFC hydrogels was produced by soaking freeze-dried fibers in PBS (D8437, Sigma-Aldrich) or DMEM (D5796, Sigma-Aldrich) with 1% penicillin/streptomycin (P/S, P0718, Sigma-Aldrich) over night to reach a final concentration of 7 % w/v. The next day, the resulting hydrogel was mixed with a spatula and shortly centrifuged to get rid of air bubbles. The stock-solution was autoclaved and stored in the fridge until further use.

Different inks were prepared for embedded printing. For Fig. 26a the standard bioink formulation as used by Kajtez *et al.*[54] composed of cells mixed with 0.5 % v/v XG was used. The print was performed with a volumetric print head with a steel nozzle (ID 200 µm) at a feed rate of 0.5 mm/s and an extrusion rate of 0.1 µL/s at room temperature. The height of the needle was set to 1.25 mm to ensure printing into the gel. The meander designed to test the print parameters was designed with a line space of 0.5 mm.

For the remaining experiments, cNFC20 inks were prepared by dilution of a 7 % w/v cNFC20 stock solution described previously and addition of either blue and red polystyrene microparticles to yield a violet color (Red: 42922, Blue: 68553, Merck) or with green food dye. The printing procedure was performed using a volumetric print head, a 1 mL Hamilton Glass syringe, and a steel nozzle (ID 200 µm). The print parameters, such as extrusion rate and feed rate are noted for each experiment individually: Figure 26b were printed at an extrusion rate of 0.1 µL/s and a feed rate of 0.3 mm/s. Figure 26c, were printed at an extrusion rate of 0.2 µL/s and feed rate of 0.05 mm/s. Figure 26d is a screening of print parameters where the changed parameters are noted individually for each print.

The print was performed with a dyed 4 % v/v cNFC20 ink into a 2.8 % v/v cNFC20 support bath. Figure 27 was printed at an extrusion rate of 0.25 µL/s and a feed rate of 0.5 mm/s.

*Formulation of composite gels*

Composite gels were generated by mixing the stock solution of cNFC20 hydrogels with the respective concentrations of collagen (5mg/ml Cultrex rat collagen I, R&D Systems), xanthan gum (G1253, Sigma-Aldrich) and low Bloom gelatin (164 G bloom, 48723, Sigma-Aldrich) and the concentration adjusted by addition of PBS or cell-culture medium. The pH of the cNFC20:collagen composite gels were further adjusted to ensure polymerization of collagen. As an example, for a total volume of 5 mL cNFC20:collagen gel composed of 2.8 % v/v cNFC20 and 2 mg/mL collagen, 2 g of the 7 % w/v cNFC20 stock were mixed 3 mL of a with a pH-adjusted collagen solution consisting of 2 mL of a 5 mg/mL collagen stock mixed with 200 µL 4-(2-hydroxyethyl)-1-piperazineethanesulfonic acid buffer, 200 µL $NaHCO_3$ pH 9 and 600 µL PBS or cell-culture medium. All solutions were handled on ice and need to be kept cold. Neutralization of the collagen will initiate polymerization immediately and is clearly visible as the solution loses transparency. The hydrogel was mixed by slowly pipetting up and down with a Gilson positive-displacement pipette (F148180, Gilson). Approximately 300 µL were pipetted into each well of a 48-well plate and kept in the fridge right before printing.

### 3.5.3 Characterization of material properties

*Rheology of cNFC/cNFC20 and cNFC20:composite gels*

Rheology of cNFC/cNFC20 and cNFC20:composite gels was performed on a Discovery Hybrid Rheometer (TA instruments, DE, USA) equipped with a Peltier plate thermal controller and a plate geometry with a diameter of 20 mm and a fixed gap of 200 µm. cNFC20:collagen composite gels were freshly prepared and its rheology measured directly after deposition onto the plate geometry. In general, amplitude sweeps were performed at 1 Hz, 25 °C or 37 °C from 0.01 % to 100. Rheology on scaled-up cNFC functionalization was performed in milliQ water. cNFC20:collagen gels were prepared in PBS.

*IR of scaled up carboxymethylation reaction*

IR spectra were recorded as described in Chapter 02 on a PerkinElmer Spectrum 100 FT-IR spectrometer. The spectra were recorded with a resolution of 1 cm-1 from 4000 – 800 $cm^{-1}$. All spectra were recorded in absorbance units and normalized at 1050 $cm^{-1}$. The relative degree of substitution ($DS_{rel}$) was calculated by relating the intensity of the normalized absorbance (NA) of the stretching vibration of the carboxyl group (C=O) at 1595 $cm^{-1}$ to the stretching vibration of the glucose backbone (C-H) at 2894 cm-1 as described in Chapter 2, section 2.5.3, equation 8.

The constant C indicates the relation between these two stretching vibrations of the carboxyl group and glucose backbone in non-functionalized cellulose.

### 3.5.4 Cell experiments

*Culturing of C2C12 murine myoblasts*

Culturing of C2C12 was performed according to the protocol described in the manuscript presented in Chapter 02: C2C12 cell-culture was performed under sterile conditions and incubated at 37 °C, 100% humidity, 5% $CO_2$. C2C12 murine myoblasts were cultured in growth medium containing DMEM (D5796, Sigma-Aldrich), 10% fetal bovine serum (S1810, Sigma-Aldrich) and 1% P/S (P0718, Sigma-Aldrich). Cells were passaged and harvested at 80% confluency. All cells were kept within 10 passages from stock. Differentiation was initiated by changing growth medium to differentiation medium containing DMEM, 2% horse serum (H1270, Sigma-Aldrich).

*Embedded bioprinting with murine skeletal muscle cells*

C2C12 skeletal muscle cells were cultured as described in the main materials section. Bioinks as presented in Figure 24 were composed of C2C12 cells at a concentration of 38 mio cells/mL within 10 passages. The bioinks were prepared by mixing a 1% cNFC stock 1:1 with harvested cells. A steel nozzle (ID 250 µm) was used at a feed rate of 0.5 mm/s and 0.1 µL/s extrusion rate. Right after printing, the prints were incubated for 1 h at 37 °C to ensure cross-linking of the collagen. After, growth medium prepared as described in the main materials section was added to the gels. The next day, the medium was changed to differentiation medium. Images of the tissues were taken every day.

*Culturing of HaCaT*

HaCaT (11090081, ThermoFisher) were cultivated in DMEM/F12 (D5796, Sigma-Aldrich) supplemented with 10 % FBS (F0804, Sigma-Aldrich) and 1 % P/S as described earlier. The cells were passaged at a cell density of approximately 10,000 cells/$cm^2$ every second day and used within 10 passages from stock. Cell-culture was performed under sterile conditions and incubated at 37 °C, 100% humidity, 5% CO2.

*Culturing of HT1080*

HT1080 with a LifeAct®–TagGFP2 were acquired from Ibidi and are not longer commercially available. The cells were cultivated analogous to HaCaT in DMEM/F12 supplemented with 10 % FBS and 1 % P/S. Passaging occurred every second day at a cell density of approximately 10,000 cells/$cm^2$. The cells were used within 10 passages from stock. Cell-culture was performed under sterile conditions and incubated at 37 °C, 100% humidity, 5% $CO_2$.

*Cell adhesion on cNFC:composite gels*

Composite gels were prepared freshly before seeding of cells. A 7 % w/v cNFC stock solution in DMEM was prepared by incubating the fibers in DMEM over night at 4 °C and autoclaving them the following day. The hydrogel was centrifuged to exclude air bubbles. Composite gels were prepared always prepared freshly and on ice as described in section 3.5.2. The composite gels were prepared with a fiber content of 0.5 % to 4 % v/v and a constant concentration of 1 mg/mL pre-neutralized collagen. SHAPE gel was prepared by mixing the alginate slurry 2:1 with pre-neutralized collagen.

As an example, for 0.9 mL SHAPE gel, 40 µL HEPES (1 M), 40 µL $NaHCO_3$ (37 g/L, pH 9.5), 20 µL cell culture medium, and 200 µL collagen (5 mg/mL) were mixed carefully on ice with 0.6 mL cold alginate-slurry. The SHAPE gel was mixed carefully by pipetting up and down. The cNFC20:collagen gels and SHAPE gel were pipetted in a 96-well plate with a total volume of approx. 50 µL. The gels were cross linked for 30 min at 37 °C. After cross-linking, cell-culture medium containing 30,000 HaCaT/HT1080 cells per $cm^2$ within 10 passages of stock was added carefully to the gels. Growth medium was changed every 2 days. Images were recorded using a Discover Echo Revolve R4 microscope after 5 days.

*Cell migration within cNFC:collagen and SHAPE gel*

To avoid surface coverage of the tissue culture wells with FBS, the cells were harvested in FBS-free medium. HT1080 were seeded at a cell density of 10,000 cells per $cm^2$ in a 8-well glass bottom slide (80807, Ibidi). Freshly prepared cNFC20:collagen gels containing 4 % v/v cNFC20 and 2 mg/mL collagen and SHAPE gels were pipetted into the wells and left cross-linking for 30 min at 37 °C. FBS-free cell-culture medium was added and cellular upwards migration was imaged. Images were recorded using a Nikon Ti2 equipped with crest optics Xlight V3 and acquired with a Kinetix CMOS camera. The images were recorded in confocal mode every 5 min for 10 h in a z-range of 10-40 µm with a 3 µm distance from plane to plane. The environment during imaging was kept at 5 % $CO_2$ and 37 °C.

# Chapter 4

# Multi-material 3D Printing of Programmable and Stretchable Oral Patches for Buccal Delivery of Saquinavir

---

This chapter is based on the published manuscript on 3D printed oromucosal patches for drug delivery, in collaboration with Dr. Shaolong He from the University of Copenhagen. The sections comprising the Results and Discussion 4.3 and Experimental section 4.6 have been cited from the publication with minor changes.

## 4.1 Introduction

In the previous chapters we relied on the fibrillar structure of cNFC inks and matrices and its concomitant viscoelastic behavior to provide high shape-fidelity of printed constructs. Here, we will focus on crystalline, functionalized derivates of cellulose are well known to be shear-thinning and transparent, and have been widely used in printing applications.[105,143,158] HPMC, HPC, and MC-based inks exhibit viscous behavior and flow after deposition, and are known to have film-forming properties. Such membranes have gained importance as drug-delivery systems due to their ability of circumventing hepatic first pass metabolism of the delivered drug. Conventional fabrication methods for thin film and membranes, such as solvent casting (SC) and hot melt extrusion (HME) limit the complexity of the structure of the films and choice of solvents: SC is a common, cheap technique that relies on casting the different formulations within a solvent onto a horizontal plate/release layer and drying these to achieve membranes with several layers.[159,160] In HME the formulations are mixed, heated, extruded, and then cut into different sizes.[161,162] In these examples, drug dose and membrane design are difficult to control. Some other techniques involving printing have been explored,[163–165] such as inkjet and flexographic printing,[166–169] fused deposition modelling,[170] and DIW.[171–178]

Multi-material DIW 3D printing is a promising alternative for the fabrication of complex oromucosal patches with tunable design and control over the deposition of drugs and other agents. We achieve shape-fidelity of thin films by solvent evaporation, in contrast to cross-linking our printed structures as discussed in previous chapters. Most drugs being developed are barely soluble in aqueous medium,[179,180] while some exhibit weak ionization with pH-dependent solubility.[181,182] HPMC and MC as amphiphilic materials are easily formulated into film-forming drug-laden inks. Multi-material printing further permits to improve drug solubility and absorption locally and transiently by formulating pH-modifying inks.[182–184] In addition, high digital control over the design allows to increase comfort of application in the buccal cavity.

In the previous chapters, we discussed design features linked to the shape-fidelity of our inks. We here rely on the fabrication of thin films based on solvent-evaporation. The design of the films is comparable to *Kirigami.* It is a variation of the japanese paper folding art *origami,* in which the paper may also be cut to construct 3D structures. This approach has already been used for the fabrication of stretchable electronics, and demonstrated how mesh-like structures increased the ultimate strain to up to 370 %.[185,186]

Here, we present the use of crystalline, transparent HPMC and MC-based inks to print oral drug-delivery patches. The design of the patches will be tailored into mesh-like structures to enhance the stretchability of the printed patches. Multi-material 3D printing will be lastly used to print mesh-like, stretchable, drug-delivery patches with effervescent properties for enhanced drug-resorption in the mouth.

## 4.2 Aims

This chapter focuses on the design and multi-material printing of drug-delivery patches with inks based on crystalline cellulose derivates and is structured as follows:

I. **Automated DIW of stretchable, drug-laden membrane:** The stretchability and overall effective stiffness of commonly used drug-laden membranes will be enhanced by varying the design of the print into mesh-like structures. The design will be tailored via CAD.

II. **Controllable deposition of drug and pH modifying agent within stretchable membrane:** The drug concentration per patch will be adjusted by deposition of ink in a layer-by-layer approach. In addition, multi-material printing of drug-laden and pH modifying agents in proximity will enhance drug permeability during application.

## 4.3 Results and discussion

The design, fabrication, and mechanical characterization of the films presented in 4.3.1, as well as fabrication of the films used in section 4.3.2 for drug-release and *in vitro* permeation studies were conducted by the author of this dissertation. Experiments presented in section 4.3.2 regarding drug-release and *in vitro* permeation were conducted by Dr. Shaolong He.

### 4.3.1 Automated Direct-ink-writing of stretchable drug-laden membranes

*Rheological properties of the inks and optimization of printing procedure*

The overall design of the multi-functional patches was composed of a meandering backing membrane, onto which a drug-laden ink and effervescent ink are printed in parallel without overlapping (Fig. 32a). This requires high spatial resolution in the print procedure, with control over extrusion rate and material spreading. We evaluated the printability of the formulated inks by characterizing their rheological properties. For all inks, oscillatory studies show a dominating loss modulus G'' over storage modulus G' indicating predominantly viscous materials (Fig. 32c). Flow experiments further show shear thinning behavior, with viscosity decreasing with increasing shear rate (Fig. 32d), which is advantageous for maintaining resolution when extruding inks through narrow nozzles. Still, since all inks are in a liquid state, shape fidelity relies on solvent carrier evaporation.

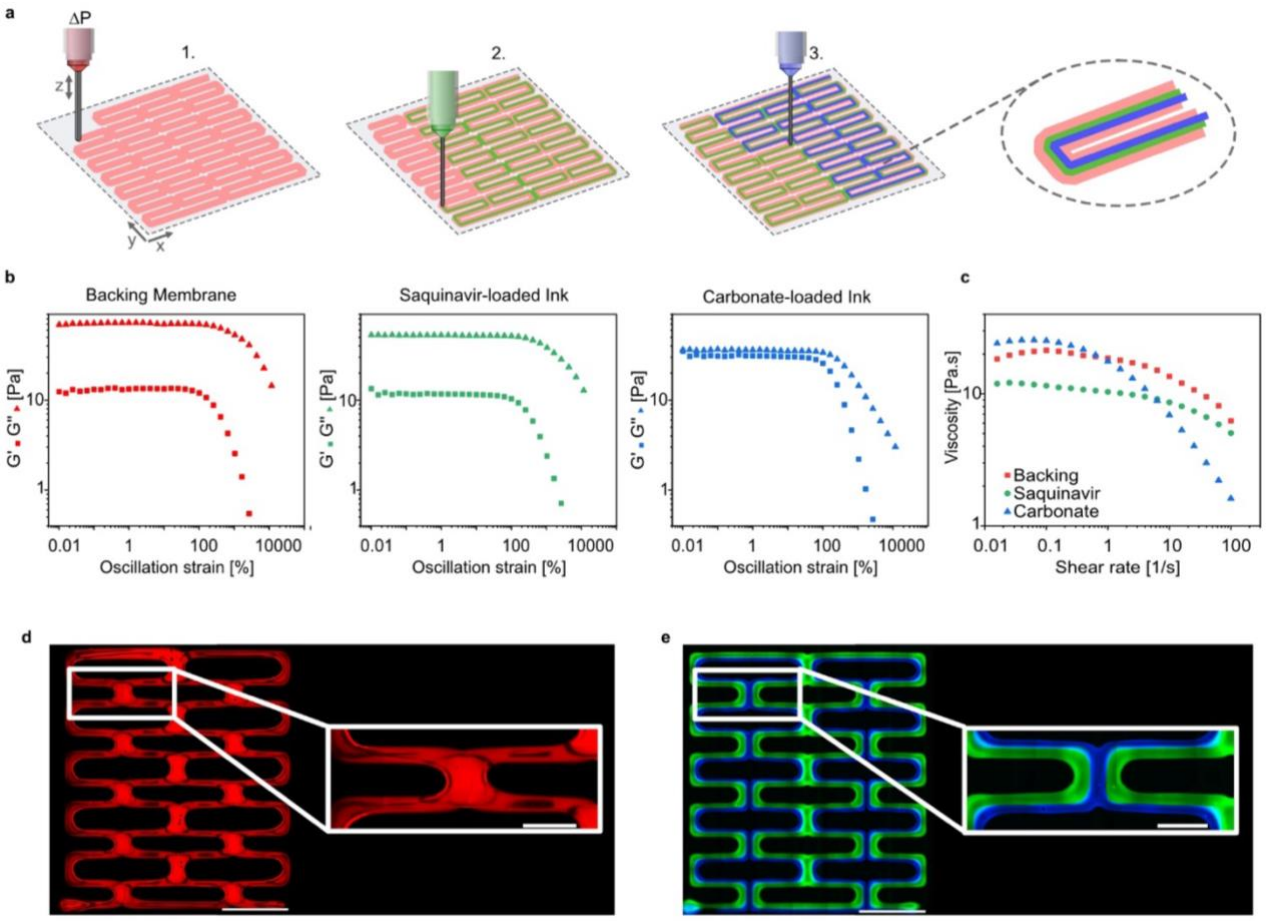


**Figure 32.** Illustration and rheology of 3D printed patches.
(a) Schematic illustration of multi-material printing of complex oral patches using a backing membrane (red), drug-laden (green) and effervescent (blue) ink. (b) Rheology of the backing membrane, drug-laden and effervescent inks. The G moduli were recorded as a function of oscillation strain at constant frequency (1 Hz). (c) The viscosity was recorded as a function of shear rate. (d), (e) Fluorescence imaging of printed patches based on effervescent (blue), drug-laden (green) ink and backing membrane (red). Scale bar: 3 mm, zoom-in Scale bar: 1 mm.

To increase solvent evaporation and facilitate multi-material and multilayer prints, we therefore applied a slightly heated stage set at 45°C, as higher temperatures may cause solvent boiling and bubble formation. The backing membrane was printed with a 0.6 mm nozzle. Due to its viscous properties, it spread after printing, providing a sufficiently large surface to print the drug-laden and effervescent ink. The deposition of drug-laden and effervescent ink occurred in a similar matter: the drug-laden and effervescent ink were be printed in parallel with a 0.4 mm nozzle and a line distance of 0.25 mm to avoid overlapping between printed traces, and prevent acid-base reaction between the malic acid and sodium carbonate. The printing procedure and design was evaluated via fluorescence microscopy to demonstrate that the drug-laden and effervescent ink were printed in parallel without overlapping (Fig. 32e,d).

*Tuning of stretchability of printed patches by varying the design*

3D printing allows for rapid design prototyping and tailoring of macroscopic properties through simple design alterations. To enable the fabrication of stretchable and compliant patches, we systematically varied a simple meandering design and evaluated the resultant mechanical properties. Specifically, the backing membrane was printed in six different designs (Fig. 33a,b). First, the line distance "A" was tuned to 2.5, 4.5 and 7.5 mm, respectively, while using the same nozzle size of 0.6 mm. Secondly, three different nozzle sizes of 0.6, 0.4 and 0.2 mm, were used, which lead to a change in line distance "B" at fixed A = 7.75 mm (Fig. 33a,b). The layer thickness was determined by printing the backing membrane with 1, 2 and 3 layers with a nozzle diameter of 0.2, 0.4 and 0.6 mm, respectively. The thickness per layer increases with increasing amount of layers and nozzle diameter (Fig. 33c). Nevertheless, mechanical tests demonstrate a drastic decrease in effective stiffness of the films with decreasing line distance A and decreasing nozzle size compared to a control uniform film without geometrical cues (Fig. 33e). In addition, by varying line distance A and B the stretchability of the films is precisely tuned. Films printed with the smallest nozzle size and biggest line distance A show an extension capacity of up to 200% (Fig. 33f). This decrease in effective stiffness and increase in extension capacity will improve the comfort and adaptation of using the stretchable films in the buccal cavity (Fig, 33d). For the drug-loaded patches, we applied 0.6 mm nozzle for the backing membrane to ensure maximum surface area to deposit drug-laden and effervescent ink, while maintaining an extension capacity of up to 50% at negligible stiffness.

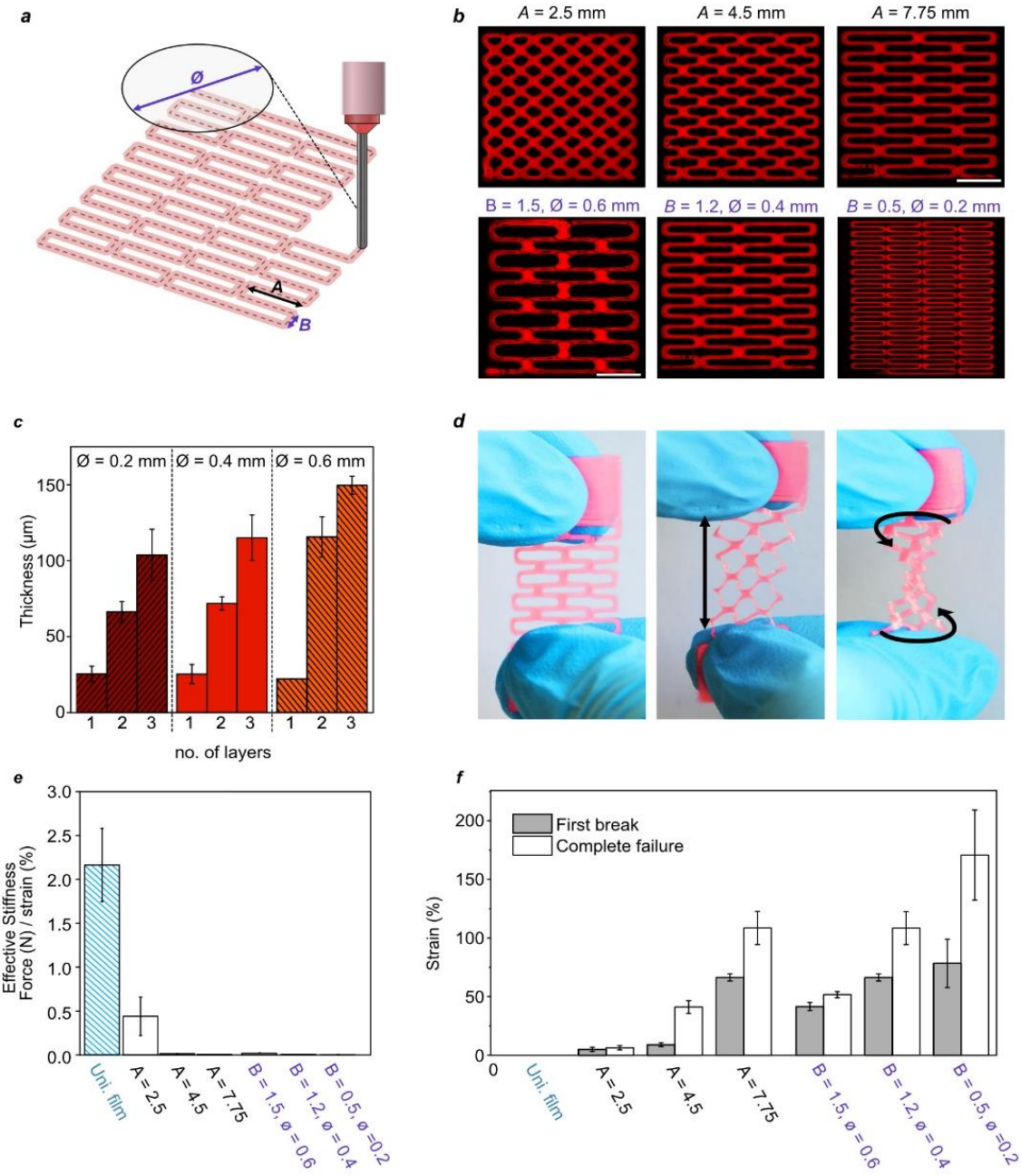


**Figure 33.** Stretchability and mechanical properties of printed patches.
(a) Illustration of print procedure of backing membrane with varying line distances A and B, as well as varying nozzle diameter Ø. (b) Fluorescent images of designs with line distance A = 2.5, 4.5, 7.75 mm at constant B = 1.2, Ø = 0.4 mm and B = 1.5, 1.2, 0.5, mm at Ø = 0.6, 0.4, 0.2 mm with fixed line distance A = 7.75 mm. Scale bar: 3 mm. (c) Layer thickness of printed backing membrane with nozzle diameter Ø = 0.2, 0.4, 0.6 mm with 1, 2, 3 layers, respectively. n = 3. (d) Stretching and twisting of printed film with line distance A = 7.75 mm and B = 1.2 mm. (e) Effective stiffness (Force (N) / Strain (%) of printed films compared to uniformly printed film. n = 3. f) Strain (%) until first break (grey) and complete failure (white) of printed films compared to uniformly printed film. n = 3. Error bars indicate standard error of the mean (SEM).

### 4.3.2 Controlled deposition of drug and pH modifying agent within stretchable patch.

*Digitally controlling drug dose in printed patches*

In order to control and adjust dose in each printed patch, we studied the drug content as a function of key printing parameters. For films used in this dosing investigation, we compared three nozzle diameters. As expected, the saquinavir content of the films increased with diameter of the nozzle (Fig. 34a). Further, for films printed using the same nozzle diameter, saquinavir content increased linearly with the number of printed layers. Thus, the drug content of the patches can easily be adjusted from ~20 to 200 µg through these parameters. The saquinavir content of each layer in the films printed using the largest nozzle (Ø = 400 µm) was ~70 µg. This nozzle size was applied in the final patches, which also included effervescent, pH-modifying inks. The mass and saquinavir content of the $pH_M$ modifying films are presented in Table 1.

**Table 1.** Characterization of the designed films

| | Saquinavir $pH_M$ modifying films | | |
|---|---|---|---|
| | F0 | F3 | F5 |
| Mass (mg) | 9.5 ± 0.0 | 10.4 ± 0.1 | 10.6 ± 0.1 |
| Saquinavir content (µg) | 79 ± 9 | - | - |

* The results are present as mean ± SD, n = 5 for the result of saquinavir content. For others, n = 3. The number of saquinavir layer in the $pH_M$ modifying films was the same and fixed (3 layers) so we measured saquinavir content of the patches without alkaline effervescent layer. F0: the films without base layer. F3: the films with three base layers. F5: the films with five base layers.

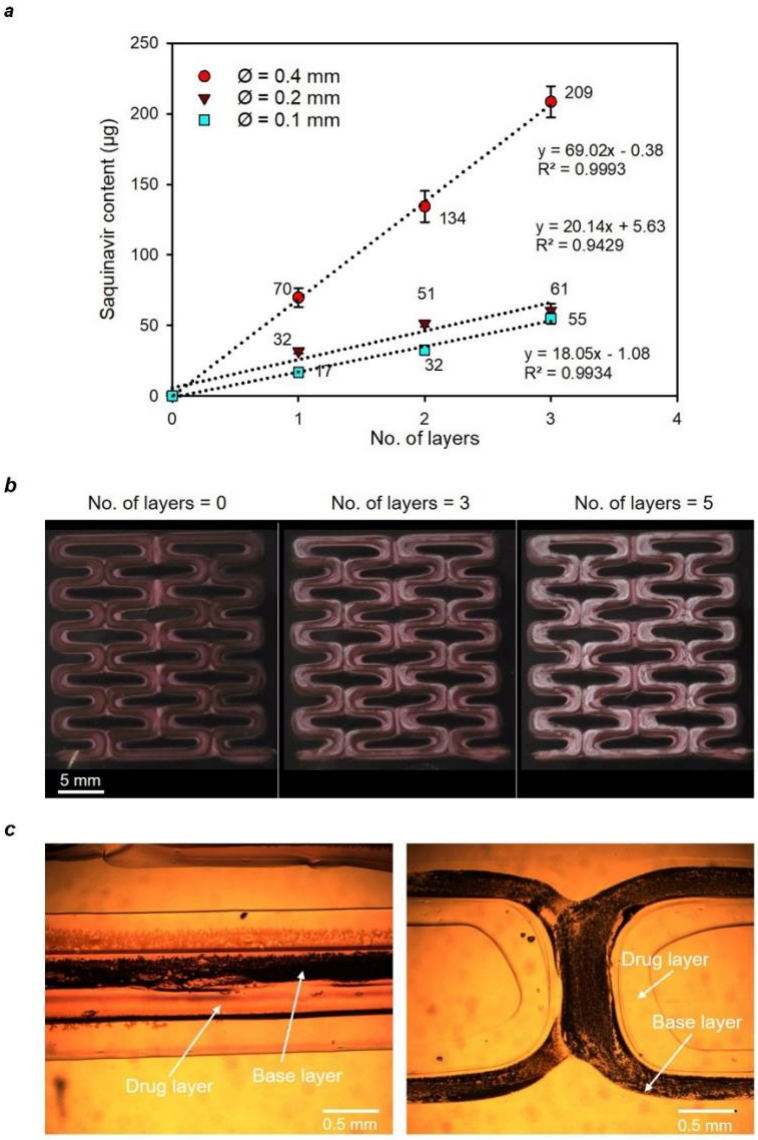


**Figure 34.** Saquinavir content and morphology of printed films.
(a) Saquinavir content-number of layers scatter profiles for the films printed using different nozzles. The average values of saquinavir content and the linear regression equation for the data were indicated in the figure. N = 3. The size of nozzle indicated in the figure was the diameter of nozzle. (b) Images of the saquinavir microenvironmental pH modifying films taken using a digital camera. (c) Select images of partial structures of the microenvironmental pH modifying films (effervescent type) taken using a light microscopy.

*Morphology of the films*

The images (Fig. 34b) showed that the mesh-like films were printed successfully using the polymer based inks and the predetermined design. White precipitation was observed in the films containing base layers due to precipitation of sodium carbonate in the film preparation. Similarly to in our initial printing studies applying fluorescent markers in the inks, the base layer with a minimal interface between the base layer and the saquinavir layer was observed (Fig. 34c).

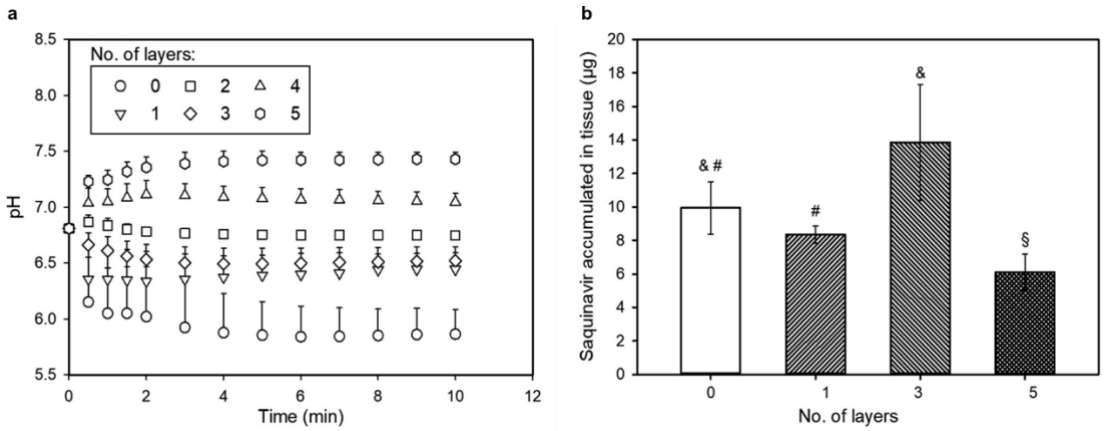


**Figure 35.** Microenvironmental pH and *ex vivo* permeation study.
(a) Microenvironmental pH-time profiles for the patches with or without sodium carbonate layer during the dissolution process. Results are presented as mean ± SD. "NO. of layers" indicates the number of the alkaline effervescent layer printed in the patches. For the patch with three layers of sodium carbonate, n = 5. For the other patches, n = 3. pH value after 10 min of dissolution are presented in the figure. (b) Amount of saquinavir in porcine buccal tissues after permeation study. Values are mean ± SD, n = 4. Symbols above the bars (&, # and §) indicate statistical significance. Bars with similar letters are not significantly different from each other. One-way analysis of variance (ANOVA) was employed, and the level of significance was $\alpha = 0.05$. Tukey's test was then preformed. A p value below 0.05 was considered statistically significant.

*Modifying the microenvironmental pH ($pH_M$)*

The $pH_M$ in the vicinity of the films during dissolution was measured using a micro-pH electrode and the results are shown in Figure 35a. After 10 min of dissolution, the $pH_M$ in patches containing no base had decreased from 6.8 to 5.9, while for samples with 5 layers of base-ink the $pH_M$ increased from 6.8 to 7.4. As expected, the $pH_M$ generally increased with the number of layers of base-ink applied in the formulations, save one outlier sample. Within the time resolution of our studies the pH was largely stable after 10 min, indicative of limited effervescent reaction between malic acid and carbonate beyond this time point. Overall, the studies show how a base-ink can be applied to conveniently control microenvironmental pH of saquinavir released from the printed patches.

*Ex vivo permeation studies*

To evaluate the performance of the printed, multi-functional patches, we conducted an *ex vivo* permeation study spanning 5 h. However, no saquinavir was detected in the receptor chamber. This might be caused by the following reasons: 1) saquinavir content in the films was very low. 2) saquinavir was too lipophilic (log P = 4.1) and accumulated in the lipid-rich tissue rather than dissolving in the aqueous solution in the receptor chamber. 3) saquinavir concentration in the receptor media was lower than the detection limit of the high-performance liquid chromatography (HPLC). As no saquinavir was detected in the receptor chambers, we evaluated the amount of saquinavir accumulated in the tested tissues, as means of quantifying the permeation of saquinavir (Fig. 35b). Among the tested films, the films with three layers of sodium carbonate led to a highest amount of saquinavir in the buccal tissues. The films with five layers of sodium carbonate exhibited a lower permeation of saquinavir than the films containing three layers of sodium carbonate, likely due to the higher $pH_M$ hindering the dissolution of saquinavir. Although $CO_2$ can also enhance drug permeation across mucosal membrane as previous described,[46] the films containing three and five layers of sodium carbonate likely induced approximately the same amount of effervescent $CO_2$, as the amount

of acidic, drug-loaded ink was kept constant. Interestingly, the films with three layers of sodium carbonate exhibited a higher permeation of saquinavir than the films with one layer of sodium carbonate although the $pH_M$ around the films with one and three layers of sodium carbonate appeared similar (Fig. 35a). Still, our results indicate that by printing a basic effervescent agents side by side an acidic drug-loaded ink the pH can be locally modulated to promote saquinavir permeation of the buccal mucosa.

### 4.4 Conclusion

Our work demonstrates the use of HPMC and MC carrier polymers multi-material Direct-ink-write printing for rapid design and manufacturing of complex oral patches where several materials are integrated on a sub-millimeter scale.

We aimed at increasing the stretchability of the drug-laden patches by printing a range of meanders and grid-like structures and observed a maximum failure strain of approx. 170 % with neglectable effective stiffness compared to uniform patches.

In addition, we demonstrated high control over the concentration of saquinavir deposited in each layer. Multi-material printing of a carbonate-laden ink in proximity of the slightly acidic saquinavir-laden ink further led to increased permeation of saquinavir when applying the patch *ex vivo*.

Our methodology is widely applicable and may thus serve as inspiration for various patches for personalized, and programmable buccal drug delivery with unique patient comfort and compliance.

## 4.5 Experimental section

*Chemicals*

Saquinavir mesylate was obtained from Hoffmann-La Roche Ltd (Basel, Switzerland). Malic acid, glycerol (> 99%), agarose (type I), Nile red, Sulforhodamine B acid chloride and bovine serum albumin were purchased from Sigma-Aldrich (MO, USA). HPMC K100 LV and MC NF 50 were obtained from Dow Chemical Ltd (MI, USA). HPMC K200 M was purchased from Colorcon Inc. (PA, USA). Monopotassium dihydrogenphosphate anhydrate, dipotassium hydrogenphosphate anhydrate, sodium chloride, phosphoric acid (85%) and citric acid anhydrate were obtained from Merck KGaA (Darmstadt, Germany). Lucifer Yellow CH was purchased from Thermo Fisher (Invitrogen, USA). Purified water from a SG ultra pure water system (SG Water, Barsbuttel, Germany) was used.

### 4.5.1 Formulation and Direct-ink-writing of stretchable oromucosal patches

*Preparation of the inks*

Separate polymer-based inks were prepared for backing membrane, saquinavir layer with malic acid, and base layer containing sodium carbonate, as detailed in Table 2. For the backing membrane ink, suitable amounts of MC, glycerol and Nile red were dissolved in 20 ml of methanol at 60-65℃. For the saquinavir drug ink, saquinavir mesylate, glycerol and malic acid were dissolved in 20 ml of purified water at 70-75℃, followed by suspending HPMC K100 LV gradually to form the white HPMC-saquinavir suspension, which was cooled down to 4-6℃ to obtain the transparent ink. For the base ink, sodium carbonate, glycerol and HPMC K200 M were dissolved in purified water at 70-75℃.

*Rheological studies of the inks.*

The rheology of each ink was analyzed using a Discovery Hybrid Rheometer (TA instruments, DE, USA) equipped with a Peltier plate thermal controller and a plate geometry with a diameter of 40 mm. The measurements were performed at 25°C. The inks were equilibrated at 25°C for 30 seconds prior to conduction of the measurements. The storage (G') and loss (G'') moduli were measured as a function of oscillatory strain (0.01 – 10,000%) at constant frequency (1 Hz). The viscosity of the inks was measured as a function of shear rate (0.01 – 100 1/s).

*3D printing of oral delivery patches*

All patches were 3D printed using a 3D-Discovery printer (RegenHU, CH) using the accompanying BioCAD software for print design. 3CC cartridges (Nordson EFD, US) were applied for containing ink, using pneumatic pressure for saquinavir and base ink extrusion. 10 CC cartridges (Nordson, EFD, US) were used for extrusion of the backing membrane.

*Preparation of the single-material patches for stretchability study*

To compare the tensile strength and elasticity of different designs based on the MC backing membrane ink, cylindrical steel nozzles with a diameter of 0.2, 0.4 and 0.6 mm (Cellink, SE) were

used, at a pneumatic pressure of 250, 100 and 50 kPa, respectively. The ink was extruded at RT onto a heated polystyrene plate (45 °C) at a feed rate of 15 mm/s in the shape of a meander with different line sizes A and B. In addition, a uniform layer was added on top and on the bottom of the design for further mounting of the sample on a biaxial stretcher. The prints were left drying for 1 h prior to testing.

*Preparation method for multi-material patches*

The stretchable films used to determine the drug-load and drug-permeability were printed with varying amount of layers and nozzle sizes to determine the effect of the effervescent ink on local pH. The backing membrane was printed in 3 layers using a 0.6 mm cylindrical steel nozzle at a pressure of 40 kPa and a feed rate of 10 mm/s on a pre-heated polystyrene plate (45 °C). The backing membrane was left drying for approx. 30 min. before further printing. The drug-load per printed layer of drug-laden-ink was determined by printing 1, 2, and 3 layers of the drug-laden ink with nozzle sizes of 0.1, 0.2 and 0.4 mm, respectively. For further experiments, a nozzle size of 0.4 mm was chosen for drug-laden and effervescent ink. The evaluation of the effect on local pH of the drug-laden ink printed in proximity to the effervescent ink was conducted by printing the drug-laden and effervescent ink in parallel with a 0.4 mm cylindrical steel nozzle at a feed rate of 15 mm/s and a pressure of 30 and 15 kPa, respectively. The drug-laden ink was printed in 3 layers, while the effervescent ink was printed in 0, 1, 2, 3, 4 and 5 layers. The final prints were left drying on the polystyrene plate until further use.

**Table 2**. Composition of individual inks

| Ink compositions in mg (%) | Saquinavir layer | Base layer | Backing membrane |
|---|---|---|---|
| Saquinavir mesylate | 100 (0.45) | - | - |
| HPMC K100 LV | 1500 (6.78) | - | - |
| Malic acid | 220 (0.99) | - | - |
| Glycerol | 300 (1.36) | 200 (0.9) | 600 |
| Sodium carbonate | - | 250 (1.13) | |
| HPMC K200 M | - | 500 (2.26) | |
| Methyl cellulose 100 FP | - | - | 6000 |
| Nile red | - | - | 4 |
| Methanol (ml) | - | - | 40 |
| Water (ml) | 20 (90.42) | 30 (96.93) | - |

* Percentage of components in the inks is wt %.

### 4.5.2 Characterization of printed oromucosal patches

*HPLC system for the quantification of saquinavir*

The Elite LaChrom HPLC system (VWR International, Tokyo, Japan) equipped with an L-2130 pump with degasser, an L-2450 diode array detector and L-2200 autosampler was applied to quantify saquinavir in different samples. Reversed phase chromatography was performed using a C18 column at 30℃ and a mobile phase of 10 mM ammonium acetate buffer: acetonitrile 60:40 (v/v). A flow rate of 0.5 ml/min and an injection volume of 20 µl were applied. Saquinavir was detected at 240 nm with a retention time of 5.5 min. The chromatograms were analyzed using EZChrom Elite software Version. A linear calibration curve with a $R^2$ value of 0.9987 was obtained in the range of 0.45-160.50 µg/mL for the drug content study. For permeation study, a linear calibration curve was used in the range of 25-850 ng/mL ($R^2$ = 0.9964). The quantification limited is 25 ng/mL.

*Analysis of saquinavir content in the printed films*

The printed films were put into a 100 ml volumetric flask followed by adding purified water to 100 ml. The flask was sonicated in an ultrasonic bath at 40 ℃ for 10 min to obtain saquinavir solution (backing membrane was insoluble in this solution). With suitable dilution, the sample was analyzed using the HPLC method described previously.

*Morphology study*

The printed $pH_M$ modifying films were observed using a Dino-Lite digital microscope (USB) (AnMo Electronics Corporation, Taiwan, China) and bright-field microscopy. For visualization studies, we further added fluorescent agents to each ink and imaged printed patches using a Zeiss Observer Z1 microscope with a mounted Zeiss AxioCam Mrm (Jena, Germany). To differentiate between the inks, the backing membrane was visualized using Nile Red (exc. 559 nm/ emis. 636 nm), for the saquinavir and effervescent ink sulforhodamine B acid chloride (exc. 543 nm/ emis. 565 nm) and Lucifer yellow (exc. 236 nm/ emis. 542 nm) were used, respectively.

*Stretchability study*

The layer thickness of the printed films was analyzed using a Stylus profiler (Dektak 150, Veeco, NY, US). The layer thickness for 1, 2 and 3 layers printed with a nozzle diameter of 0.2, 0.4 and 0.6 mm was determined. The printed, stretchable films were analyzed using a biaxial stretcher (Instron, Illinois Tool Works Inc., MA, US). The width, length, and thickness of the stretchable part of the films was measured. The additional attachment sites were used to place the samples on the uniaxial stretcher with a load cell of 500 N. The ultimate tensile strength was determined by recording the load force (N) as a function of extension (m). The effective stiffness was determined by plotting the load force (N) over tensile strain (%) and performing a linear fit of the linear regime before first break.

*Investigation of $pH_M$ during the dissolution*

Each film was placed in a 1.5 ml Eppendorf tube followed by adding 400 µl of phosphate buffer solution (PBS, 13 mM potassium phosphate and 145 mM sodium chloride, pH 6.8) simulating human saliva pH and buffer capacity as previously described.[43,44] Immediately, the pH close to the surface of the film was measured using a pH meter (744 pH meter, Mettler Toledo, OH, USA) with a micro-electrode (Biotrode, Metrohm AG, Herisau, Switzerland) and the values at predetermined time intervals were recorded.

### 4.5.3 *Ex vivo* studies of Saquinavir buccal permeation

*Preparation of the tissues*

Frozen porcine buccal tissues were used for the permeation study. The preparation procedure of the tissues was described in a previous study [45]. Briefly, fresh porcine buccal mucosae obtained from healthy experimental control pigs (approx. 30 kg Danish Landrace/Yorkshire x Durox (D-LY)) were kept cold on ice and moistened using phosphate buffered saline (pH 7.4, 0.1 M, 290 mOsm/kg). The connective tissue of the mucosae were trimmed using surgical scissors until a thickness of approximately 5 mm. The trimmed mucosae were submerged in a cryoprotectants (the phosphate buffered saline containing 40 % (w/v) glycerol and 20 % (w/v) sucrose) for 1 h followed by storing at -80 °C before use.

To thaw and equilibrate the tissues before the permeation study, the frozen mucosae were defrosted in the phosphate buffer saline (approximately 40 ml) and washed by replacing the phosphate buffered saline four times every 20 min at 4°C on a rotating plate. The connection tissue of the defrosted mucosa was trimmed again using a Thomas Stadie-Riggs tissue slicer (Thomas Scientific, Swedesboro, NJ, USA) until a thickness range of 500-700 µm as determined by a tailor-made micrometer. Glass Franz diffusion cells (orifice diameter: 5 mm, diffusion area: 0.2 $cm^2$) with a receptor volume of 3 ml were applied in this study. Each trimmed mucosa was mounted between the donor and the receptor chambers with the epithelium facing the donor chamber. Each mucosa was equilibrated while magnetic stirring at 37 °C with 250 µl of PBS simulating human saliva in the donor chamber, and 3.00 ml of 0.05 % (w/v) bovine serum albumin solution in the receptor chamber for 0.5 h.

*Saquinavir permeation study*

After the equilibrium, the PBS in the donor chamber was withdrawn. Afterwards, the diffusion cell was disassembled, and the mucosa was left on the top of the donor chamber and dried using a lab tissue. A volume of 50 µl fresh PBS simulating saliva was added onto the epithelium again and the permeation experiment was initiated by attaching the printed film on the epithelium. Immediately, the donor chamber was mounted on top again and the donor chamber was sealed with a piece of Parafilm®. Samples (250 µl) were withdrawn from the receptor chambers at predetermined time intervals (15 min, 30 min, 45 min, 1 h, 2 h, 3 h, 4h and 5h). Air bubbles induced by sampling were removed via the side arm by carefully tilting

the Franz cell after each withdrawal. The removed samples were replaced with 250 ml of pre-warmed BSA solution followed by sealing the receptor chamber using small Parafilm® pieces to prevent water evaporation. The samples were diluted two times before centrifugation (13500 rpm, 10 min, at ambient temperature), and subsequently analyzed using HPLC.

After the permeation study, each buccal mucosa was flushed with water to remove the residual film matrix on the tissue surface, and then dried under ambient condition for 24 h. The dry mucosa was kept in 1 ml of phosphoric acid solution (phosphoric acid (85%): water 10:3, v/v) at 65℃ for 10 min followed by disrupting and homogenizing using a pestle. The homogenized tissue suspension was diluted 10 folds using water followed by centrifugation (13500 rpm, 10 min, at ambient temperature). The supernatant was subsequently analyzed using the HPLC method described previously.

# Chapter 5
## Conclusion and Outlook

In **Chapter 2** we present an alternative route of functionalizing MFC with a carboxymethyl group without compromising the fibrillar structure of MFC. The resulting cNFC was shear-thinning, transparent. We further functionalized cNFC with proteins to provide cell-binding sites. Still, the low degree of substitution did not suffice to serve as adhesion site for cells. We therefore formulated composite-inks with alginate and gelatin. We found that cNFC:gelatin composite inks guided cellular alignment and maturation of murine and human skeletal muscle cells for *in vitro* tissue models. Furthermore, cNFC:gelatin composite inks showed promising results as bioinks for the extrusion of cells. In future, the possibility of increasing the degree of substitution and coupling of smaller peptide sequences, as well as cross-linkable peptides shall be explored.

In **Chapter 3** we analyzed the use of transparent cNFC formulations as support matrices for embedded printing. The low yield stress of cNFC is appealing for its use as support matrix compared to current support matrices based on cross-linked particles. We found that simple structures, such as lines, can be easily printed and maintain their shape. Murine skeletal muscle cells were printed in a line and compacted over time within the material. Furthermore, we did not find impairment of cellular migration of fluorescently labeled HT1080 epithelial cells within cNFC and granular microgel-based support matrices. Still, the use of cNFC as support matrix only allows to print simple structures, while particle-based gels allow for a higher resolution.

In **Chapter 4** crystalline cellulose derivates, namely MC and HPMC were used as carrier materials to produce stretchable oral drug-delivery patches. We tailored the design of the patch to increase its flexibility and decrease its effective stiffness. MC and HPMC as viscous inks are deposited into thin films due to solvent evaporation and allowed layer-by-layer deposition of pre-defined dosages of drug. We additionally performed multi-material printing of effervescent agents in proximity that should increase the resorption of the drug in the buccal mucosa. The ease of tuning the design and precise deposition of drug-loads demonstrates the ease in fabrication using DIW.

All in all, we demonstrated the use of cellulose-derivates for two different applications: i) *in vitro* tissue models were developed in 2D through cNFC induced cell-alignment on printed surfaces. The exploration of 3D tissue models within cNFC support matrices, while still inconclusive, shows promising results. Finally, the second application ii) multi-material printing of stretchable oral drug-delivery patches was successfully shown using CNC-based inks.

# References


1. Fermini, B., Coyne, S. T. & Coyne, K. P. Clinical Trials in a Dish: A Perspective on the Coming Revolution in Drug Development. *SLAS Discovery* **23**, 765–776 (2018).
2. Harrison, R. K. Phase II and phase III failures: 2013-2015. *Nat Rev Drug Discov* **15**, 817–818 (2016).
3. Fabre, K. *et al.* Introduction to a manuscript series on the characterization and use of microphysiological systems (MPS) in pharmaceutical safety and ADME applications. *Lab Chip* **20**, 1049–1057 (2020).
4. Monticello, T. M. *et al.* Current nonclinical testing paradigm enables safe entry to First-In-Human clinical trials: The IQ consortium nonclinical to clinical translational database. *Toxicol Appl Pharmacol* **334**, 100–109 (2017).
5. Lind, J. U. *et al.* Instrumented cardiac microphysiological devices via multimaterial three-dimensional printing. *Nat Mater* **16**, 303–308 (2017).
6. Yi, H. G. *et al.* A bioprinted human-glioblastoma-on-a-chip for the identification of patient-specific responses to chemoradiotherapy. *Nat Biomed Eng* **3**, 509–519 (2019).
7. Ahn, S. *et al.* Mussel-inspired 3D fiber scaffolds for heart-on-a-chip toxicity studies of engineered nanomaterials. *Anal Bioanal Chem* **410**, 6141–6154 (2018).
8. Zhao, Y. *et al.* A Multimaterial Microphysiological Platform Enabled by Rapid Casting of Elastic Microwires. *Adv Healthc Mater* **8**, 1–10 (2019).
9. Boudou, T. *et al.* A microfabricated platform to measure and manipulate the mechanics of engineered cardiac microtissues. *Tissue Eng Part A* **18**, 910–919 (2012).
10. Paul, S. M. *et al.* How to improve RD productivity: The pharmaceutical industry's grand challenge. *Nature Reviews Drug Discovery* **9** 203–214 (2010).
11. Qian, X. *et al.* Generation of human brain region–specific organoids using a miniaturized spinning bioreactor. *Nat Protoc* **13**, 565–580 (2018).
12. Fan, Y., Nguyen, D. T., Akay, Y., Xu, F. & Akay, M. Engineering a Brain Cancer Chip for High-throughput Drug Screening. *Sci Rep* **6**, 1–12 (2016).
13. Park, T. E. *et al.* Hypoxia-enhanced Blood-Brain Barrier Chip recapitulates human barrier function and shuttling of drugs and antibodies. *Nat Commun* **10**, 1–12 (2019).
14. Johnson, B. N. *et al.* 3D printed nervous system on a chip. *Lab Chip* **16**, 1393–1400 (2016).
15. Zhao, Y. *et al.* A Platform for Generation of Chamber-Specific Cardiac Tissues and Disease Modeling. *Cell* **176**, 913-927.e18 (2019).
16. Stucki, J. D. *et al.* Medium throughput breathing human primary cell alveolus-on-chip model. *Sci Rep* **8**, 1–13 (2018).
17. Shrestha, J. *et al.* A rapidly prototyped lung-on-a-chip model using 3D-printed molds. *Organs-on-a-Chip* **1**, 100001 (2019).

18. Kim, R. *et al.* An in vitro intestinal platform with a self-sustaining oxygen gradient to study the human gut/microbiome interface. *Biofabrication* **12**, (2020).
19. Kasendra, M. *et al.* Development of a primary human Small Intestine-on-a-Chip using biopsy-derived organoids. *Sci Rep* **8**, 1–14 (2018).
20. Wang, Y. *et al.* Formation of Human Colonic Crypt Array by Application of Chemical Gradients Across a Shaped Epithelial Monolayer. *Cmgh* **5**, 113–130 (2018).
21. Taebnia, N. *et al.* Dual-Material 3D-Printed Intestinal Model Devices with Integrated Villi-like Scaffolds. *ACS Appl Mater Interfaces* **13**, 58434–58446 (2021).
22. Agrawal, G., Aung, A. & Varghese, S. Skeletal muscle-on-a-chip: An in vitro model to evaluate tissue formation and injury. *Lab Chip* **17**, 3447–3461 (2017).
23. Maina, J. N. & West, J. B. Thin and Strong! The Bioengineering Dilemma in the Structural and Functional Design of the Blood-Gas Barrier. *Physiol Rev* **3,** 811-44 (2005)
24. Budday, S. *et al.* Mechanical properties of gray and white matter brain tissue by indentation. *J Mech Behav Biomed Mater* **46**, 318–330 (2015).
25. Lam, M. T., Sim, S., Zhu, X. & Takayama, S. The effect of continuous wavy micropatterns on silicone substrates on the alignment of skeletal muscle myoblasts and myotubes. *Biomaterials* **27**, 4340–4347 (2006).
26. Engler, A. J., Sen, S., Sweeney, H. L. & Discher, D. E. Matrix Elasticity Directs Stem Cell Lineage Specification. *Cell* **126**, 677–689 (2006).
27. Park, J. *et al.* Micropatterned conductive hydrogels as multifunctional muscle-mimicking biomaterials: Graphene-incorporated hydrogels directly patterned with femtosecond laser ablation. *Acta Biomater* **97**, 141–153 (2019).
28. Jiwlawat, N. *et al.* Micropatterned substrates with physiological stiffness promote cell maturation and Pompe disease phenotype in human induced pluripotent stem cell-derived skeletal myocytes. *Biotechnol Bioeng* **116**, 2377–2392 (2019).
29. Bettadapur, A. *et al.* Prolonged Culture of Aligned Skeletal Myotubes on Micromolded Gelatin Hydrogels. *Sci Rep* **6**, 28855 (2016).
30. Ito, T. & Okazaki, S. Pushing the limits of lithography. *Nature* **406**, 1027–1031 (2000).
31. Macqueen, L. A. *et al.* A tissue-engineered scale model of the heart ventricle. *Nat Biomed Eng* **2**, 930–941 (2018).
32. Wu, Y., Wang, L., Guo, B. & Ma, P. X. Interwoven Aligned Conductive Nanofiber Yarn/Hydrogel Composite Scaffolds for Engineered 3D Cardiac Anisotropy. *ACS Nano* **11**, 5646–5659 (2017).
33. Yongcong, F., Zhang, T., Liverani, L., Boccaccini, A. R. & Sun, W. Novel biomimetic fiber incorporated scaffolds for tissue engineering. *J Biomed Mater Res A* **107**, 2694–2705 (2019).
34. Prendergast, M. E., Davidson, M. D. & Burdick, J. A. A biofabrication method to align cells within bioprinted photocrosslinkable and cell-degradable hydrogel constructs via embedded fibers. *Biofabrication* **13**, 044108 (2021).

35. Zhang, Y., Zhang, Z., Wang, Y., Su, Y. & Chen, M. 3D myotube guidance on hierarchically organized anisotropic and conductive fibers for skeletal muscle tissue engineering. *Materials Science and Engineering C* **116**, (2020).
36. Mondschein, R. J., Kanitkar, A., Williams, C. B., Verbridge, S. S. & Long, T. E. Polymer structure-property requirements for stereolithographic 3D printing of soft tissue engineering scaffolds. *Biomaterials* vol. 140 170–188 Preprint at https://doi.org/10.1016/j.biomaterials.2017.06.005 (2017).
37. Sirringhaus, H. *et al.* High-Resolution Inkjet Printing of All-Polymer Transistor Circuits. *Science (1979)* **290**, 2123–2126 (2000).
38. McKee, C. T., Last, J. A., Russell, P. & Murphy, C. J. Indentation versus tensile measurements of young's modulus for soft biological tissues. *Tissue Eng Part B Rev* **17**, 155–164 (2011).
39. Blaeser, A. *et al.* Controlling Shear Stress in 3D Bioprinting is a Key Factor to Balance Printing Resolution and Stem Cell Integrity. *Adv Healthc Mater* **5**, 326–333 (2016).
40. Aguado, B. A., Mulyasasmita, W., Su, J., Lampe, K. J. & Heilshorn, S. C. Improving viability of stem cells during syringe needle flow through the design of hydrogel cell carriers. *Tissue Eng Part A* **18**, 806–815 (2012).
41. Ning, L. *et al.* Process-induced cell damage: pneumatic versus screw-driven bioprinting. *Biofabrication* **12**, (2020).
42. Müller, S. J. *et al.* Flow and hydrodynamic shear stress inside a printing needle during biofabrication. *PLoS One* **15**, (2020).
43. Chang, R., Nam, J. & Sun, W. Effects of dispensing pressure and nozzle diameter on cell survival from solid freeform fabrication-based direct cell writing. *Tissue Eng Part A* **14**, 41–48 (2008).
44. Fan, T. *et al.* Controllable assembly of skeletal muscle-like bundles through 3D bioprinting. *Biofabrication* **14**, (2022).
45. Kim, H. *et al.* Shear-induced alignment of collagen fibrils using 3D cell printing for corneal stroma tissue engineering. *Biofabrication* **11**, (2019).
46. Müller, M., Öztürk, E., Arlov, Ø., Gatenholm, P. & Zenobi-Wong, M. Alginate Sulfate – Nanocellulose Bioinks for Cartilage Bioprinting Applications. **45**, 210–223 (2017).
47. Markstedt, K., Mantas, A., Tournier, I., Ha, D. & Gatenholm, P. 3D Bioprinting Human Chondrocytes with Nanocellulose − Alginate Bioink for Cartilage Tissue Engineering Applications. *Biomacromolecules* **5**, 1489-96 (2015)
48. Zhao, Y. *et al.* Engineering microenvironment for human cardiac tissue assembly in heart-on-a-chip platform. *Matrix Biology* **85–86**, 189–204 (2019).
49. Shapira, A., Noor, N., Oved, H. & Dvir, T. Transparent support media for high resolution 3D printing of volumetric cell-containing ECM structures. *Biomedical Materials* **15**, (2020).
50. Noor, N. *et al.* 3D Printing of Personalized Thick and Perfusable Cardiac Patches and Hearts. *Adv Sci* **6**, (2019).

51. Hinton, T. J. *et al.* Three-dimensional printing of complex biological structures by freeform reversible embedding of suspended hydrogels. *Sci Adv* **1**, (2015).
52. Lee, A. *et al.* 3D bioprinting of collagen to rebuild components of the human heart. *Science* **365**, 482–487 (2019).
53. Banigan, E. J., Illich, M. K., Stace-Naughton, D. J. & Egolf, D. A. The chaotic dynamics of jamming. *Nat Phys* **9**, 288–292 (2013).
54. Kajtez, J. *et al.* Embedded 3D printing in self-healing annealable composites for functional patterning of human neural constructs. *Adv Sci* **9** (2021).
55. Jensen, J. H. *et al.* Large-scale spontaneous self-organization and maturation of skeletal muscle tissues on ultra-compliant gelatin hydrogel substrates. *Sci Rep* **10**, 1–10 (2020).
56. Cakal, S. D. *et al.* A simple and scalable 3D printing methodology for generating aligned and extended human and murine skeletal muscle tissues. *Biomed Mater* **17**, 045013 (2022).
57. Yang, G. H., Kim, W., Kim, J. & Kim, G. H. A skeleton muscle model using GelMA-based cell-aligned bioink processed with an electric-field assisted 3D/4D bioprinting. *Theranostics* **11**, 48–63 (2020).
58. Cuvellier, M. *et al.* 3D culture of HepaRG cells in GelMa and its application to bioprinting of a multicellular hepatic model. *Biomaterials* **269**, (2021).
59. Freeman, F. E. & Kelly, D. J. Tuning alginate bioink stiffness and composition for controlled growth factor delivery and to spatially direct MSC Fate within bioprinted tissues. *Sci Rep* **7**, 1–12 (2017).
60. Taniguchi Nagahara, M. H., Caiado Decarli, M., Inforçatti Neto, P., Lopes da Silva, J. V. & Moraes, Â. M. Crosslinked alginate-xanthan gum blends as effective hydrogels for 3D bioprinting of biological tissues. *J Appl Polym Sci* **139**, (2022).
61. Censi, R. *et al.* A printable photopolymerizable thermosensitive p(HPMAm-lactate)-PEG hydrogel for tissue engineering. *Adv Funct Mater* **21**, 1833–1842 (2011).
62. Müller, M., Becher, J., Schnabelrauch, M. & Zenobi-Wong, M. Nanostructured Pluronic hydrogels as bioinks for 3D bioprinting. *Biofabrication* **7**, (2015).
63. Markstedt, K., Escalante, A., Toriz, G. & Gatenholm, P. Biomimetic Inks Based on Cellulose Nano fi brils and Cross-Linkable Xylans for 3D Printing. *Adc Appl Materi Interfaces* **9,** 40878–40886 (2017).
64. Shin, S. & Hyun, J. Rheological properties of cellulose nanofiber hydrogel for high-fidelity 3D printing. *Carbohydr Polym* **263**, 117976 (2021).
65. Klemm, D., Heublein, B., Fink, H. P. & Bohn, A. Cellulose: Fascinating biopolymer and sustainable raw material. *Angew Chem Int Ed* **44** 3358–3393 (2005).
66. O'sullivan, A. C. Cellulose: the structure slowly unravels. *Cellulose* **4,** 173-207 (1997).
67. Parnell, E. A. *The Life and Labours of John Mercer, F.R.S., Longmans, Green, and Co.,* (1886).
68. Zhang, L., Ruan, D. & Gao, S. Dissolution and regeneration of cellulose in NaOH/Thiourea aqueous solution. *J Polym Sci B Polym Phys* **40**, 1521–1529 (2002).

69. Nishino, T., Takano, K. & Nakamae, K. Elastic modulus of the crystalline regions of cellulose polymorphs. *J Polym Sci B Polym Phys* **33**, 1647–1651 (1995).
70. Habibi, Y. & Vignon, M. R. Optimization of cellouronic acid synthesis by TEMPO-mediated oxidation of cellulose III from sugar beet pulp. *Cellulose* **15**, 177–185 (2008).
71. Singh, M., Kaushik, A. & Ahuja, D. Surface functionalization of nanofibrillated cellulose extracted from wheat straw: Effect of process parameters. *Carbohydr Polym* **150**, 48–56 (2016).
72. Okahisa, Y. *et al.* Comparison of cellulose nanofiber properties produced from different parts of the oil palm tree. *Carbohydr Polym* **198**, 313–319 (2018).
73. Siqueira, G., Oksman, K., Tadokoro, S. K. & Mathew, A. P. Re-dispersible carrot nanofibers with high mechanical properties and reinforcing capacity for use in composite materials. *Compos Sci Technol* **123**, 49–56 (2016).
74. Moon, R. J., Martini, A., Nairn, J., Simonsen, J. & Youngblood, J. Cellulose nanomaterials review: Structure, properties and nanocomposites. *Chem Soc Rev* **40**, 3941–3994 (2011).
75. Araki, J., Wada, M., Kuga, S. & Okano, T. Flow properties of microcrystalline cellulose suspension prepared by acid treatment of native cellulose. *Colloids surf A:* ***142*** (1998).
76. Revol, J.-F., Bradford, H., Giasson, J., Marchessault, R. H. & Gray, D. G. *Helicoidal self-ordering of cellulose microfibrils in aqueous suspension. Int. J. Biol. Macromol* **14 (**1992).
77. Snyder, F. W., Sandberg, K. R. & Shelton, W. *United States Patent (19) Turbak et al. (54)* Microfibrillated cellulose *OSE 75 Inventors: Albin F. Turbak, Convent Station*. (1980)
78. Iwamoto, S., Nakagaito, A. N. & Yano, H. Nano-fibrillation of pulp fibers for the processing of transparent nanocomposites. *Appl Phys A Mater Sci Process* **89**, 461–466 (2007).
79. Dufresne, A., Cavaille, J. Y. & Vignon, M. R. Mechanical behavior of sheets prepared from sugar beet cellulose microfibrils. *J Appl Polym Sci* **64**, 1185–1194 (1997).
80. Walther, A., Timonen, J. V. I., Díez, I., Laukkanen, A. & Ikkala, O. Multifunctional high-performance biofibers based on wet-extrusion of renewable native cellulose nanofibrils. *Adv Mater* **23**, 2924–2928 (2011).
81. Pääkko, M. *et al.* Enzymatic hydrolysis combined with mechanical shearing and high-pressure homogenization for nanoscale cellulose fibrils and strong gels. *Biomacromolecules* **8**, 1934–1941 (2007).
82. Engström, A. C., Ek, M. & Henriksson, G. Improved accessibility and reactivity of dissolving pulp for the viscose process: Pretreatment with monocomponent edoglucanase. *Biomacromolecules* **7**, 2027–2031 (2006).
83. da Silva Perez, D., Montanari, S. & Vignon, M. R. TEMPO-mediated oxidation of cellulose III. *Biomacromolecules* **4**, 1417–1425 (2003).
84. Isogai, A. & Kato, Y. Preparation of polyuronic acid from cellulose by TEMPO-mediated oxidation. *Cellulose* **5**, 153–164 (1998).

85. Pushpamalar, V., Langford, S. J., Ahmad, M. & Lim, Y. Y. Optimization of reaction conditions for preparing carboxymethyl cellulose from sago waste. *Carbohydr Polym* **64**, 312–318 (2006).
86. Eyholzer, C. *et al.* Preparation and characterization of water-redispersible nanofibrillated cellulose in powder form. *Cellulose* **17**, 19–30 (2010).
87. Wågberg, L. *et al.* The build-up of polyelectrolyte multilayers of microfibrillated cellulose and cationic polyelectrolytes. *Langmuir* **24**, 784–795 (2008).
88. Diaz-Gomez, L. *et al.* 3D printed carboxymethyl cellulose scaffolds for autologous growth factors delivery in wound healing. *Carbohydr Polym* **278**, 118924 (2022).
89. Im, W., Lee, S., Rajabi Abhari, A., Youn, H. J. & Lee, H. L. Optimization of carboxymethylation reaction as a pretreatment for production of cellulose nanofibrils. *Cellulose* **25**, 3873–3883 (2018).
90. Fall, A. B., Lindström, S. B., Sundman, O., Ödberg, L. & Wågberg, L. Colloidal stability of aqueous nanofibrillated cellulose dispersions. *Langmuir* **27**, 11332–11338 (2011).
91. Ahmadi, P., Jahanban-Esfahlan, A., Ahmadi, A., Tabibiazar, M. & Mohammadifar, M. Development of Ethyl Cellulose-based Formulations: A Perspective on the Novel Technical Methods. *Food Rev Int* **38,** 685–732 (2022).
92. Li, X. G., Huang, M. R. & Bai, H. Thermal decomposition of cellulose ethers. *J Appl Polym Sci* **73**, 2927–2936 (1999).
93. Dharmalingam, K. & Anandalakshmi, R. Fabrication, characterization and drug loading efficiency of citric acid crosslinked NaCMC-HPMC hydrogel films for wound healing drug delivery applications. *Int J Biol Macromol* **134**, 815–829 (2019).
94. Siepmann, J. & Peppas, N. A. Modeling of drug release from delivery systems based on hydroxypropyl methylcellulose (HPMC). *Adv Drug Deliv Rev* 163–174 (2012).
95. Kadry, H. *et al.* Multi-purposable filaments of HPMC for 3D printing of medications with tailored drug release and timed-absorption. *Int J Pharm* **544**, 285–296 (2018).
96. Zhang, J. *et al.* Hydroxypropyl methylcellulose-based controlled release dosage by melt extrusion and 3D printing: Structure and drug release correlation. *Carbohydr Polym* **177**, 49–57 (2017).
97. Girouard, N. M., Xu, S., Schueneman, G. T., Shofner, M. L. & Meredith, J. C. Site-Selective Modification of Cellulose Nanocrystals with Isophorone Diisocyanate and Formation of Polyurethane-CNC Composites. *ACS Appl Mater Interfaces* **8**, 1458–1467 (2016).
98. Wu, C., Zhang, X., Wang, X., Gao, Q. & Li, X. Surface modification of cellulose nanocrystal using succinic anhydride and its effects on poly(butylene succinate) based composites. *Cellulose* **26**, 3167–3181 (2019).
99. Zhu, W. *et al.* Synthesis and characterization of aminosilane grafted cellulose nanocrystal modified formaldehyde-free decorative paper and its CO2 adsorption capacity. *Polymers* **11**, (2019).

100. Gan, L., Wang, Y., Zhang, M., Xia, X. & Huang, J. Hierarchically spacing DNA probes on bio-based nanocrystal for spatial detection requirements. *Sci Bull* **64**, 934–940 (2019).
101. Pértile, R., Moreira, S., Andrade, F., Domingues, L. & Gama, M. Bacterial cellulose modified using recombinant proteins to improve neuronal and mesenchymal cell adhesion. *Biotechnol Prog* **28**, 526–532 (2012).
102. Hujaya, S. D. *et al.* Self-assembled nanofibrils from RGD-functionalized cellulose nanocrystals to improve the performance of PEI/DNA polyplexes. *J Colloid Interface Sci* **553**, 71–82 (2019).
103. Weishaupt, R. *et al.* Antibacterial, Cytocompatible, Sustainably Sourced: Cellulose Membranes with Bifunctional Peptides for Advanced Wound Dressings. *Adv Healthc Mater* **9**, (2020).
104. Im, S. *et al.* An osteogenic bioink composed of alginate, cellulose nanofibrils, and polydopamine nanoparticles for 3D bioprinting and bone tissue engineering. *Int J Biol Macromol* **205**, 520–529 (2022).
105. Siqueira, G. *et al.* Cellulose Nanocrystal Inks for 3D Printing of Textured Cellular Architectures. *Adv Funct Mater* **27** 1–10 (2017).
106. Sydney Gladman, A., Matsumoto, E. A., Nuzzo, R. G., Mahadevan, L. & Lewis, J. A. Biomimetic 4D printing. *Nat Mater* **15**, 413–418 (2016).
107. Skylar-Scott, M. A. *et al.* Orthogonally induced differentiation of stem cells for the programmatic patterning of vascularized organoids and bioprinted tissues. *Nat Biomed Eng* **6**, 449–462 (2022).
108. Sun, W. *et al.* The bioprinting roadmap. *Biofabrication* **12**, (2020).
109. Pless, C. J. *et al.* Emerging strategies in 3D printed tissue models for in vitro biomedical research. in *Bioprinting* (eds. Conti, M. & Marino, M.) 207–246 *Academic Press,* (2022).
110. Kuzmenko, V., Karabulut, E., Pernevik, E., Enoksson, P. & Gatenholm, P. Tailor-made conductive inks from cellulose nanofibrils for 3D printing of neural guidelines. *Carbohydr Polym* **189**, 22–30 (2018).
111. Monfared, M., Mawad, D., Rnjak-Kovacina, J. & Stenzel, M. H. 3D bioprinting of dual-crosslinked nanocellulose hydrogels for tissue engineering applications. *J Mater Chem B* **9**, 6163–6175 (2021).
112. Ojansivu, M. *et al.* Wood-based nanocellulose and bioactive glass modified gelatin-alginate bioinks for 3D bioprinting of bone cells. *Biofabrication* **11**, (2019).
113. Choi, Y. J. *et al.* A 3D cell printed muscle construct with tissue-derived bioink for the treatment of volumetric muscle loss. *Biomaterials* **206**, 160–169 (2019).
114. Brassard, J. A., Nikolaev, M., Hübscher, T., Hofer, M. & Lutolf, M. P. Recapitulating macro-scale tissue self-organization through organoid bioprinting. *Nat Mater* **20**, 22–29 (2021).
115. Kolesky, D. B., Homan, K. A., Skylar-Scott, M. A. & Lewis, J. A. Three-dimensional bioprinting of thick vascularized tissues. *Proc Natl Acad Sci U S A* **113**, 3179–84 (2016).

116. Kim, H. *et al.* Shear-induced alignment of collagen fibrils using 3D cell printing for corneal stroma tissue engineering. *Biofabrication* **11**, (2019).
117. Espinosa, E., Filgueira, D., Rodríguez, A. & Chinga-Carrasco, G. Nanocellulose-Based Inks—Effect of Alginate Content on the Water Absorption of 3D Printed Constructs. *Bioengineering* **6**, 65 (2019).
118. Shin, S. & Hyun, J. Matrix-Assisted Three-Dimensional Printing of Cellulose Nanofibers for Paper Microfluidics. *ACS Appl Mater Interfaces* **9**, 26438–26446 (2017).
119. de Nooy, A. E. J., Besemer, A. C. & van Bekkum, H. Highly selective nitroxyl radical-mediated oxidation of primary alcohol groups in water-soluble glucans. *Carbohydr Res* **269**, 89–98 (1995).
120. Saito, T. & Isogai, A. TEMPO-mediated oxidation of native cellulose. The effect of oxidation conditions on chemical and crystal structures of the water-insoluble fractions. *Biomacromolecules* **5**, 1983–1989 (2004).
121. Orelma, H. *et al.* Surface functionalized nanofibrillar cellulose (NFC) film as a platform for immunoassays and diagnostics. *Biointerphases* **7**, 1–12 (2012).
122. Orelma, H., Teerinen, T., Johansson, L. S., Holappa, S. & Laine, J. CMC-modified cellulose biointerface for antibody conjugation. *Biomacromolecules* **13**, 1051–1058 (2012).
123. Tanaka, R., Saito, T., Ishii, D. & Isogai, A. Determination of nanocellulose fibril length by shear viscosity measurement. *Cellulose* **21**, 1581–1589 (2014).
124. Fukuzumi, H., Saito, T. & Isogai, A. Influence of TEMPO-oxidized cellulose nanofibril length on film properties. *Carbohydr Polym* **93**, 172–177 (2013).
125. Yang, Z. *et al.* Fabrication and repair of cartilage defects with a novel acellular cartilage matrix scaffold. *Tissue Eng Part C Methods* **16**, 865–876 (2010).
126. Wågberg, L. *et al.* The build-up of polyelectrolyte multilayers of microfibrillated cellulose and cationic polyelectrolytes. *Langmuir* **24**, 784–795 (2008).
127. Eyholzer, C. *et al.* Preparation and characterization of water-redispersible nanofibrillated cellulose in powder form. *Cellulose* **17**, 19–30 (2010).
128. Shin, S. & Hyun, J. Rheological properties of cellulose nanofiber hydrogel for high-fidelity 3D printing. *Carbohydr Polym* **263**, 117976 (2021).
129. Shin, S. & Hyun, J. Matrix-Assisted Three-Dimensional Printing of Cellulose Nanofibers for Paper Microfluidics. *ACS Appl Mater Interfaces* **9**, 26438–26446 (2017).
130. Pushpamalar, V., Langford, S. J., Ahmad, M. & Lim, Y. Y. Optimization of reaction conditions for preparing carboxymethyl cellulose from sago waste. *Carbohydr Polym* **64**, 312–318 (2006).
131. Miyamoto, K., Tsuji, K., Nakamura, T., Tokita, M. & Komai, T. Preparation of carboxymethyl-gellan. *Carbohydr Polym* **30**, 161–164 (1996).
132. Bhattacharyya, D., Singhal, R. S. & Kulkarni, P. R. A comparative account of conditions for synthesis of sodium carboxymethyl starch from corn and amaranth starch. *Carbohydr Polym* **27**, 247–253 (1995).

133. Kroon-Batenburg, L. M. J. & Kroon, J. The crystal and molecular structures of cellulose I and II. *Glycoconj J* **14**, 677–690 (1997).
134. Maeno, H. *et al.* A 3d microfluidic elisa for the detection of severe dengue: Sensitivity improvement and vroman effect amelioration by edc–nhs surface modification. *Micromachines* **12**, (2021).
135. Haske-Cornelius, O. *et al.* Environmentally friendly covalent coupling of proteins onto oxidized cellulosic materials. *New Journal of Chemistry* **43**, 14536–14545 (2019).
136. Tang, Z. *et al.* A General Protein Unfolding-Chemical Coupling Strategy for Pure Protein Hydrogels with Mechanically Strong and Multifunctional Properties. *Adv Sci* **9**, (2022).
137. Lagunas, A. *et al.* Cell adhesion and focal contact formation on linear RGD molecular gradients: Study of non-linear concentration dependence effects. *Nanomedicine* **8**, 432–439 (2012).
138. Maheshwari, G., Brown, G., Lauffenburger, D. A., Wells, A. & Griffith, L. G. Cell adhesion and motility depend on nanoscale RGD clustering. *J Cell Sci* **113**, 1677–1686 (2000).
139. Markstedt, K. *et al.* 3D Bioprinting Human Chondrocytes with Nanocellulose–Alginate Bioink for Cartilage Tissue Engineering Applications. *Biomacromolecules* **16**, 1489–1496 (2015).
140. Engler, A. J. *et al.* Myotubes differentiate optimally on substrates with tissue-like stiffness: Pathological implications for soft or stiff microenvironments. *J Cell Bio* **166**, 877–887 (2004).
141. Sydney Gladman, A., Matsumoto, E. A., Nuzzo, R. G., Mahadevan, L. & Lewis, J. A. Biomimetic 4D printing. *Nat Mater* **15**, 413–418 (2016).
142. Siqueira, G. *et al.* Cellulose Nanocrystal Inks for 3D Printing of Textured Cellular Architectures. *Adv Funct Mater* **27**, 1604619 (2017).
143. Melilli, G. *et al.* DLP 3D printing meets lignocellulosic biopolymers: Carboxymethyl cellulose inks for 3D biocompatible hydrogels. *Polymers* **12**, 1–11 (2020).
144. McCain, M. L., Agarwal, A., Nesmith, H. W., Nesmith, A. P. & Parker, K. K. Micromolded gelatin hydrogels for extended culture of engineered cardiac tissues. *Biomaterials* **35**, 5462–5471 (2014).
145. Fonck, E. *et al.* Effect of aging on elastin functionality in human cerebral arteries. *Stroke* **40**, 2552–2556 (2009).
146. Hansen, A. *et al.* Development of a drug screening platform based on engineered heart tissue. *Circ Res* **107**, 35–44 (2010).
147. Takebe, T. *et al.* Vascularized and functional human liver from an iPSC-derived organ bud transplant. *Nature* **499**, 481–484 (2013).
148. Friedrich, L. M. & Seppala, J. E. Simulated filament shapes in embedded 3D printing. *Soft Matter* **17**, 8027–8046 (2021).
149. Friedrich, L. M., Gunther, R. T. & Seppala, J. E. Suppression of Filament Defects in Embedded 3D Printing. *ACS Appl Mater Interfaces* **14**, 32561–32578 (2022).

150. Bhattacharjee, T. *et al.* Writing in the granular gel medium. *Sci Adv* **1**, (2015).
151. Kajtez, J. *et al.* Embedded 3D Printing in Self-Healing Annealable Composites for Precise Patterning of Functionally Mature Human Neural Constructs. *Advanced Science* **9**, (2022).
152. Jeon, O. *et al.* Individual cell-only bioink and photocurable supporting medium for 3D printing and generation of engineered tissues with complex geometries. *Mater Horiz* **6**, 1625–1631 (2019).
153. O'Bryan, C. S., Bhattacharjee, T., Marshall, S. L., Gregory Sawyer, W. & Angelini, T. E. Commercially available microgels for 3D bioprinting. *Bioprinting* **11**, (2018).
154. Shin, S., Kwak, H. & Hyun, J. Transparent cellulose nanofiber based open cell culture platform using matrix-assisted 3D printing. *Carbohydr Polym* **225**, 115235 (2019).
155. Moxon, S. R. *et al.* Suspended Manufacture of Biological Structures. *Advanced Materials* **29**, (2017).
156. Sousa, C. F. V. *et al.* Bioinstructive layer-by-layer-coated customizable 3d printed perfusable microchannels embedded in photocrosslinkable hydrogels for vascular tissue engineering. *Biomolecules* **11**, (2021).
157. Yamada, K. M. & Sixt, M. Mechanisms of 3D cell migration. *Nat Rev Mol Cell Biol* **20,** 738-752 (2019).
158. Cheng, Y., Qin, H., Acevedo, N. C., Jiang, X. & Shi, X. 3D printing of extended-release tablets of theophylline using hydroxypropyl methylcellulose (HPMC) hydrogels. *Int J Pharm* **591**, (2020).
159. Morales, J. O. & McConville, J. T. Manufacture and characterization of mucoadhesive buccal films. *Eur J Pharm Biopharm* **77**, 187–199 (2011).
160. Pechová, V., Gajdziok, J., Muselík, J. & Vetchý, D. Development of Orodispersible Films Containing Benzydamine Hydrochloride Using a Modified Solvent Casting Method. *AAPS PharmSciTech* **19**, 2509–2518 (2018).
161. Dixit, R. P. & Puthli, S. P. Oral strip technology: Overview and future potential. *Journal of Controlled Release* **139**, 94–107 (2009).
162. Repka, M. A. & Mcginity, J. W. Physical-mechanical, moisture absorption and bioadhesive properties of hydroxypropylcellulose hot-melt extruded films. *Biomaterials* **21**, (2000).
163. Krampe, R. *et al.* Oromucosal film preparations: points to consider for patient centricity and manufacturing processes. *Expert Opin Drug Deliv* **13**, 493–506 (2016).
164. Preis, M., Breitkreutz, J. & Sandler, N. Perspective: Concepts of printing technologies for oral film formulations. *Int J Pharm* **494**, 578–584 (2015).
165. Tian, Y. *et al.* Oromucosal films: from patient centricity to production by printing techniques. *Expert Opin Drug Deliv* **16**, 981–993 (2019).
166. Genina, N., Janßen, E. M., Breitenbach, A., Breitkreutz, J. & Sandler, N. Evaluation of different substrates for inkjet printing of rasagiline mesylate. *Eur J Pharm Biopharm* **85**, 1075–1083 (2013).

167. Raijada, D. *et al.* A Step Toward Development of Printable Dosage Forms for Poorly Soluble Drugs. *J Pharm Sci* **102**, 3694–3704 (2013).
168. Janßen, E. M., Schliephacke, R., Breitenbach, A. & Breitkreutz, J. Drug-printing by flexographic printing technology—A new manufacturing process for orodispersible films. *Int J Pharm* **441**, 818–825 (2013).
169. Wickström, H. *et al.* Improvement of dissolution rate of indomethacin by inkjet printing. *Drug Deliv Syst* **75**, 91–100 (2015).
170. Eleftheriadis, G. K. *et al.* Fabrication of Mucoadhesive Buccal Films for Local Administration of Ketoprofen and Lidocaine Hydrochloride by Combining Fused Deposition Modeling and Inkjet Printing. *J Pharm Sci* **109**, 2757–2766 (2020).
171. Cho, H. W., Baek, S. H., Lee, B. J. & Jin, H. E. Orodispersible polymer films with the poorly water-soluble drug, olanzapine: Hot-melt pneumatic extrusion for single-process 3D printing. *Pharmaceutics* **12**, 1–16 (2020).
172. Ehtezazi, T. *et al.* The Application of 3D Printing in the Formulation of Multilayered Fast Dissolving Oral Films. *J Pharm Sci* **107**, 1076–1085 (2018).
173. Elbadawi, M., Nikjoo, D., Gustafsson, T., Gaisford, S. & Basit, A. W. Pressure-assisted microsyringe 3D printing of oral films based on pullulan and hydroxypropyl methylcellulose. *Int J Pharm* **595**, 120197 (2021).
174. Eleftheriadis, G. K. *et al.* Unidirectional drug release from 3D printed mucoadhesive buccal films using FDM technology: In vitro and ex vivo evaluation. *Eur J Pharm Biopharm* **144**, 180–192 (2019).
175. Musazzi, U. M. *et al.* Personalized orodispersible films by hot melt ram extrusion 3D printing. *Int J Pharm* **551**, 52–59 (2018).
176. Rahman, J. & Quodbach, J. Versatility on demand – The case for semi-solid micro-extrusion in pharmaceutics. *Adv Drug Deliv Rev* **172**, 104–126 (2021).
177. Seoane-Viaño, I., Januskaite, P., Alvarez-Lorenzo, C., Basit, A. W. & Goyanes, A. Semi-solid extrusion 3D printing in drug delivery and biomedicine: Personalised solutions for healthcare challenges. *J Control Release* **332**, 367–389 (2021).
178. Speer, I., Preis, M. & Breitkreutz, J. Novel Dissolution Method for Oral Film Preparations with Modified Release Properties. *AAPS PharmSciTech* **20**, (2019).
179. Kalepu, S. & Nekkanti, V. Insoluble drug delivery strategies: review of recent advances and business prospects. *Acta Pharm Sin B* **5**, 442–453 (2015).
180. Loftsson, T. & Brewster, M. E. Pharmaceutical applications of cyclodextrins: basic science and product development. *J Pharm* **62**, 1607–1621 (2010).
181. Bassi, P. & Kaur, G. pH modulation: a mechanism to obtain pH-independent drug release. *Expert Opin Drug Deliv* **7**, 845–857 (2010).
182. Taniguchi, C., Kawabata, Y., Wada, K., Yamada, S. & Onoue, S. Microenvironmental pH-modification to improve dissolution behavior and oral absorption for drugs with pH-dependent solubility. *Expert Opin Drug Deliv* **11**, 505–516 (2014).

183. Bergström, C. A. S., Luthman, K. & Artursson, P. Accuracy of calculated pH-dependent aqueous drug solubility. *European Journal of Pharmaceutical Sciences* **22**, 387–398 (2004).
184. Sieger, P., Cui, Y. & Scheuerer, S. pH-dependent solubility and permeability profiles: A useful tool for prediction of oral bioavailability. *Eur J Pharm Biopharm* **105**, 82–90 (2017).
185. Shyu, T. C. *et al.* A kirigami approach to engineering elasticity in nanocomposites through patterned defects. *Nat Mater* **14**, 785–789 (2015).
186. Guo, C. F., Sun, T., Liu, Q., Suo, Z. & Ren, Z. Highly stretchable and transparent nanomesh electrodes made by grain boundary lithography. *Nat Commun* **5**, (2014).

# Publications

ACS APPLIED MATERIALS & INTERFACES

www.acsami.org Research Article

## Transparent and Cell-Guiding Cellulose Nanofiber 3D Printing Bioinks

Carmen Radeke, Raphaël Pons, Marko Mihajlovic, Jonas R. Knudsen, Sarkhan Butdayev, Paul J. Kempen, Charis-Patricia Segeritz, Thomas L. Andresen, Christian K. Pehmøller, Thomas E. Jensen, and Johan U. Lind*

Cite This: ACS Appl. Mater. Interfaces 2023, 15, 2564−2577 Read Online

ACCESS | Metrics & More | Article Recommendations | Supporting Information



**ABSTRACT:** For three-dimensional (3D) bioprinting to fulfill its promise and enable the automated fabrication of complex tissue-mimicking constructs, there is a need for developing bioinks that are not only printable and biocompatible but also have integrated cell-instructive properties. Toward this goal, we here present a scalable technique for generating nanofiber 3D printing inks with unique tissue-guiding capabilities. Our core methodology relies on tailoring the size and dispersibility of cellulose fibrils through a solvent-controlled partial carboxymethylation. This way, we generate partially negatively charged cellulose nanofibers with diameters of ∼250 nm and lengths spanning tens to hundreds of microns. In this range, the fibers structurally match the size and dimensions of natural collagen fibers making them sufficiently large to orient cells. Yet, they are simultaneously sufficiently thin to be optically transparent. By adjusting fiber concentration, 3D printing inks with excellent shear-thinning properties can be established. In addition, as the fibers are readily dispersible, composite inks with both carbohydrates and extracellular matrix (ECM)-derived proteins can easily be generated. We apply such composite inks for 3D printing cell-laden and cross-linkable structures, as well as tissue-guiding gel substrates. Interestingly, we find that the spatial organization of engineered tissues can be defined by the shear-induced alignment of fibers during the printing procedure. Specifically, we show how myotubes derived from human and murine skeletal myoblasts can be programmed into linear and complex nonlinear architectures on soft printed substrates with intermediate fiber contents. Our nanofibrillated cellulose inks can thus serve as a simple and scalable tool for engineering anisotropic human muscle tissues that mimic native structure and function.

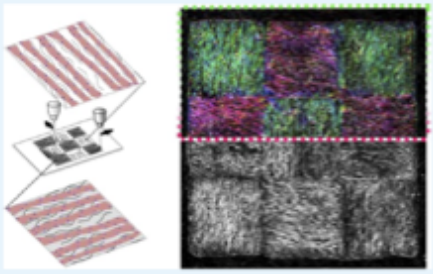

**KEYWORDS:** *extrusion-based bioprinting, nanofibrillated cellulose, carboxymethylation, skeletal muscle, tissue models*

### INTRODUCTION

Extrusion-based three-dimensional (3D) printing is redefining in vitro and in vivo biomedical research by enabling the automated fabrication of complex biomaterial scaffolds,[1] engineered tissues,[2] and microphysiological systems.[3] Across these areas, a core challenge in 3D bioprinting is the formulation of biomaterial inks that facilitate the formation of functional tissues from embedded cells or spheroids, while simultaneously assuring printability and shape fidelity.[4,5] Bioinks incorporating nano- and microfibrils are intriguing in both of these regards. In the first regard, fibrillar inks may structurally mimic extracellular matrix (ECM) nanofibers derived from, e.g., collagen and fibronectin that guide cellular adhesion, migration, proliferation, differentiation, and organization in the native tissue.[6] In the second regard, fibrillary components can be potent thixotropic agents at low concentrations, capable of forming viscous shear-thinning solutions or viscoelastic gels with low yield stress for extrusion-based printing.[7−11]

Two diverse approaches currently coexist within fibrillary bioinks: the most widespread approach relies on simply applying ECM-derived biomaterials as the core component of the inks. Here, nanofiber polymerization generally occurs after deposition and often leads to the formation of viscoelastic gels. Common examples are collagen where a post-printing temperature increase to physiological levels induces the polymerization of soluble collagen into fibers, or fibrin, where thrombin is applied to induce the polymerization of fibrinogen to fibrin.[12] Similarly, for inks based on decellularized ECM (dECM) derived from primary tissues, or from

Received: September 7, 2022
Accepted: December 23, 2022
Published: January 4, 2023





https://doi.org/10.1021/acsami.2c16126
ACS Appl. Mater. Interfaces 2023, 15, 2564−2577

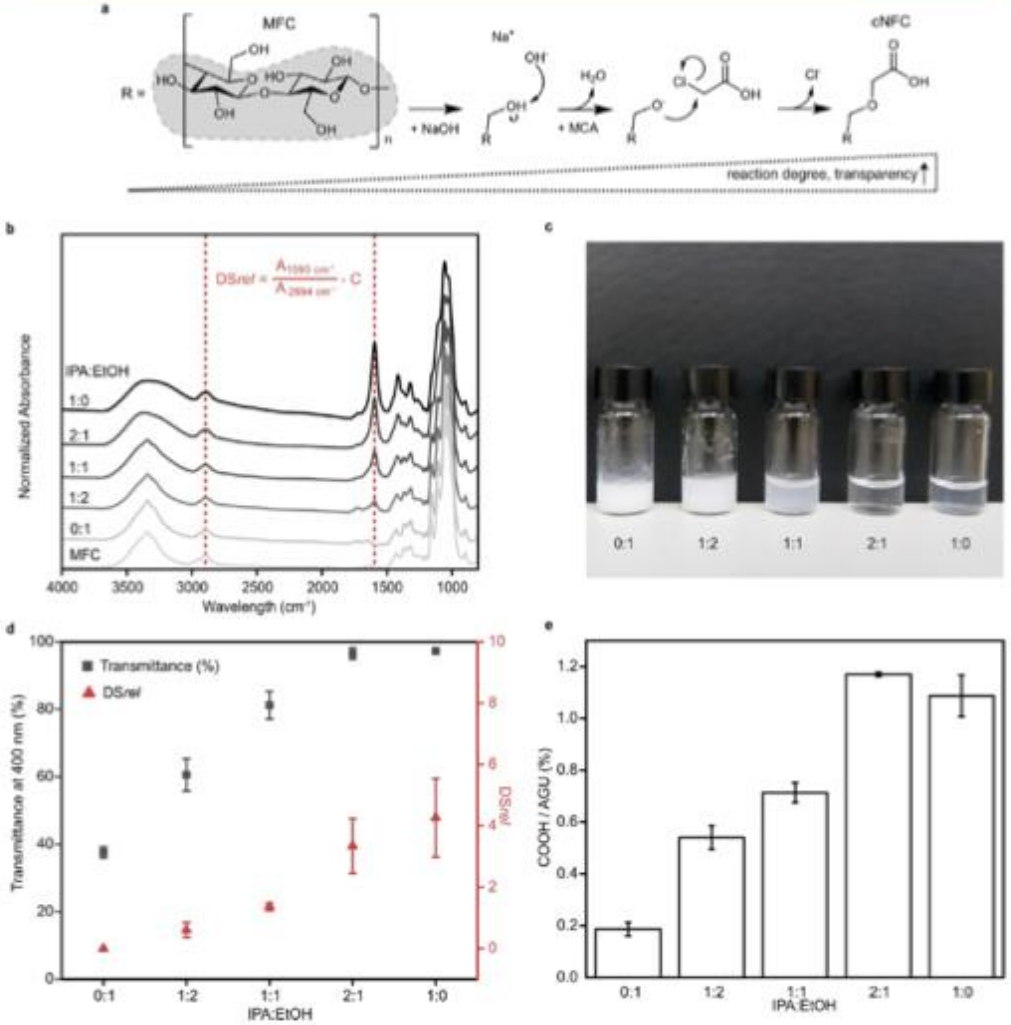


**Figure 1.** Carboxymethylation of MFC in different solvent compositions: comparison of $DS_{rel}$ and transmittance. (a) Reaction mechanism of carboxymethylation of MFC. Increasing the degree of reaction increases the transparency of substituted fibers. (b) FT-IR of MFC reacted in 0:1, 1:2, 1:1, 2:1, and 1:0 IPA:EtOH. Normalized absorbance used to calculate the degree of substitution (rel). (c) Photograph of 1% w/v aqueous dispersions of fibers reacted in the respective IPA:EtOH mixes at 2.5:1 NaOH:AGU/1:1 MCA:AGU. (d) Transmittance of 1% w/v dispersions at 400 nm in % and $DS_{rel}$ calculated based on IR data of 2.5:1 NaOH:AGU/1:1 MCA:AGU. Full transmission spectra across the UV−vis region can be found in the Supporting Information. (e) Degree of substitution calculated by the titration of fibers. Error bars indicate the standard error of the mean (SEM) for $n = 3$.

commercial Matrigel, gel formation is induced by ECM fiber polymerization in response to physiological temperature.[13,14] The other key direction within nanofibrillar inks relies on producing micro- or nanofibrils prior to ink formulation and subsequent printing. In these cases, the fibrils simultaneously serve as rheological modifiers, ensuring reliable extrusion or multilayer stacking.[7] Various types of nano- and microfibrils have been introduced, including fibrils derived from collagen,[15] modified hyaluronic acid,[16] mechanically fractured electrospun polymers such as polycaprolactone (PCL),[17] and cellulose.[5−11]

Cellulose nanomaterials and nanofibers are highly diverse, and nomenclature is often inconsistent. They span from tiny cellulose nanocrystals (CNCs) with diameters of ~2 to 20 nm and lengths of 100−600 nm to microfibrillated cellulose (MFC) where diameters span from the nano- to microrange, but where lengths are generally much longer than 1 μm.


https://doi.org/10.1021/acsami.2c16126
ACS Appl. Mater. Interfaces 2023, 15, 2564−2577

Nanofibrillated cellulose (NFC) usually refers to fibrils with lengths similar to MFC (≫1 μm), but where diameters are consistently below 1 μm. Regardless of inconsistencies in nomenclature, CNC, NFC, and MFC have all been applied in a range of 3D printing applications as they all can display shear-thinning behavior, biocompatibility, and low cost.[7,18−22] Early on, biomimetic 3D structures such as a human ear had, for instance, been printed by combining MFC with alginate, followed by ionic cross-linking.[7] However, a key challenge for MFC-derived inks is the limited transparency caused by light diffraction by the larger fibers and aggregates. This is particularly problematic for cell and tissue engineering applications wherein optical microscopy is an essential tool. One potential solution is to degrade the cellulose using, e.g., chemical oxidation. For instance, the oxidization of fibrillary cellulose using 2,2,6,6-tetramethylpyperidine-1-oxyl (TEMPO) yields a transparent gel with shear-thinning rheological properties.[9−11,23,24] This approach has been applied to yield bioprinting inks that, e.g., incorporate gelatin to provide cell-adhesive motifs.[10,13] However, TEMPO oxidation of MFC generally yields fibers in the single micron range or less,[25,26] far shorter than single collagen fibers that range between 20 and 200 μm.[27] This compromises the ability of such highly degraded cellulose fibers for guiding tissue organization.

As an alternative to such procedures, we here present a robust protocol for generating optically transparent MFC inks that retain lengths of tens to several hundred microns. Specifically, we tailored the well-known carboxymethylation reaction[28−31] to partially functionalize and oxidize MFC. Thereby, we generated transparent fibers with widths in the range of a few hundreds of nanometers, just below the wavelength of visible light. In tuning the reaction, we found that adjusting the polarity of mixed alcohol reaction solvent is effective in controlling the degree of reaction. The partially carboxymethylated nanofibrillated cellulose (cNFC) readily disperses in aqueous buffers but displays less pronounced shear-thinning properties than the nontreated MFC counterparts. However, we found that excellent printability can be reestablished by increasing the cNFC concentration slightly. The cNFC is further readily miscible with protein biomaterials, such as gelatin and collagen, which we leveraged to create cell-adhesive composite bioprinting inks. Interestingly, these composite inks can serve as programmable biomaterial scaffolds for aligning skeletal muscle myotubes derived from human or murine myoblasts. Notably, replicating the native alignment of skeletal myotubes, has been found beneficial for generating in vitro tissue models with physiomimetic myotube lengths and functions.[32−37] In our approach, myotube extension follows the print direction of soft, planar cNFC:gelatin substrates in accordance with the shear-induced orientation of the embedded fibers during extrusion. We demonstrate the robustness of our procedure by organizing muscle tissues into a range of anisotropic, linear, and complex architectures. The cNFC-based inks are thus promising as a scalable material for generating physiologically relevant models of striated muscle.

## RESULTS

As our base material, we applied a commercially available aqueous MFC paste, which was generated from wood pulp cellulose by mechanical shearing. Without further modifications, the MFC was readily printable from concentrations ≥1% w/v with a characteristic white appearance, indicative of fibers and aggregates scattering visible light. To improve material transparency, we chose carboxymethylation, which has previously been applied to generate transparent MFC.[30,31] However, similarly to cellulose nanofibrils generated using TEMPO oxidation, the reported transparent carboxymethylated fibers have diameters <20 nm and lengths ∼1 μm, limiting their structural similarity to ECM protein nanofibers.[21,22,30] To gain transparency while retaining structural properties, we here aimed to generate fibrils with diameters just below the wavelength of visible light.

To control the degree of carboxymethylation, we investigated the effect of adjusting solvent composition in detail. In addition to the amount of reactants, solvents have previously been shown to influence the overall degree of reaction[29] in bulk cellulose treatments. In general, the reaction comprised two steps: (i) dispersing a stock MFC aqueous paste (10% w/v) in polar organic solvent for mercerization with sodium hydroxide (NaOH) and (ii) etherification with monochloroacetic acid (MCA) (see Figure 1a). For the majority of our studies, the amounts of reactants relative to cellulose anhydroglucose units (AGUs) were 2.5:1 NaOH:AGU and 1:1 MCA:AGU. To evaluate the degree of reaction, we applied Fourier transformed-infrared spectroscopy (FT-IR) and quantified the relative degree of substitution ($DS_{rel}$) by relating the stretching vibration of the carboxylate peak at 1595 $cm^{-1}$ to the stretching vibration of the C−H group at 2894 $cm^{-1}$, similarly to Miyamoto et al.[38]

We initially screened common polar alcohols including methanol (MeOH), ethanol (EtOH), and isopropanol (IPA). Only in the least polar alcohol—IPA—did we observe a notable carboxylate peak, indicative of a successful reaction (Figure S1). We therefore hypothesized that the degree of reaction may be tuned by adjusting the polarity of IPA:EtOH mixtures. FT-IR indicated that this was indeed the case (Figure 1b). We further observed that the optical transparency qualitatively increased with decreasing solvent polarity (Figure 1c). Notably, the absorption was decreased across the visible spectrum and into the UV range, with minimal absorption for all wavelengths ≥250 nm (Figure S2).

This was confirmed quantitatively, as we found that both $DS_{rel}$ and transparency increased gradually with decreasing polarity of the solvent mix from 1:2 IPA:EtOH to pure IPA (Figure 1d). This trend was further confirmed when determining the degree of substitution via titration (Figure 1e). Interestingly, when we repeated the solvent composition study with lower amounts of reactants 1.25:1 NaOH:AGU and 0.5:1 MCA:AGU, the degree of control was somewhat diminished. For this set of reactants, the $DS_{rel}$ as well as the transmittance was negligible for all solvent mixtures except pure IPA (Figure S3). Also, for this condition, we observed a large variance in the degree of reaction. We speculate that this could be due to a larger sensitivity to external factors that were not controlled, such as the humidity. We thus conclude that the degree of substitution can be fine-tuned by changing the polarity of IPA:EtOH mixed solvents for a reactant concentration of at least 2.5:1 NaOH:AGU and 1:1 MCA:AGU. The degree of substitution further correlated with transparency, yielding highly transparent fibers for IPA:EtOH solvent mixtures containing at least 66% v/v IPA.

The increasing transparency of the fibers indicates a decrease in fiber size as well as a better dispersion of the fibers. To evaluate fiber size as a function of the IPA:EtOH solvent composition, we applied electron microscopy (see Figure 2).


https://doi.org/10.1021/acsami.2c16126
ACS Appl. Mater. Interfaces 2023, 15, 2564−2577

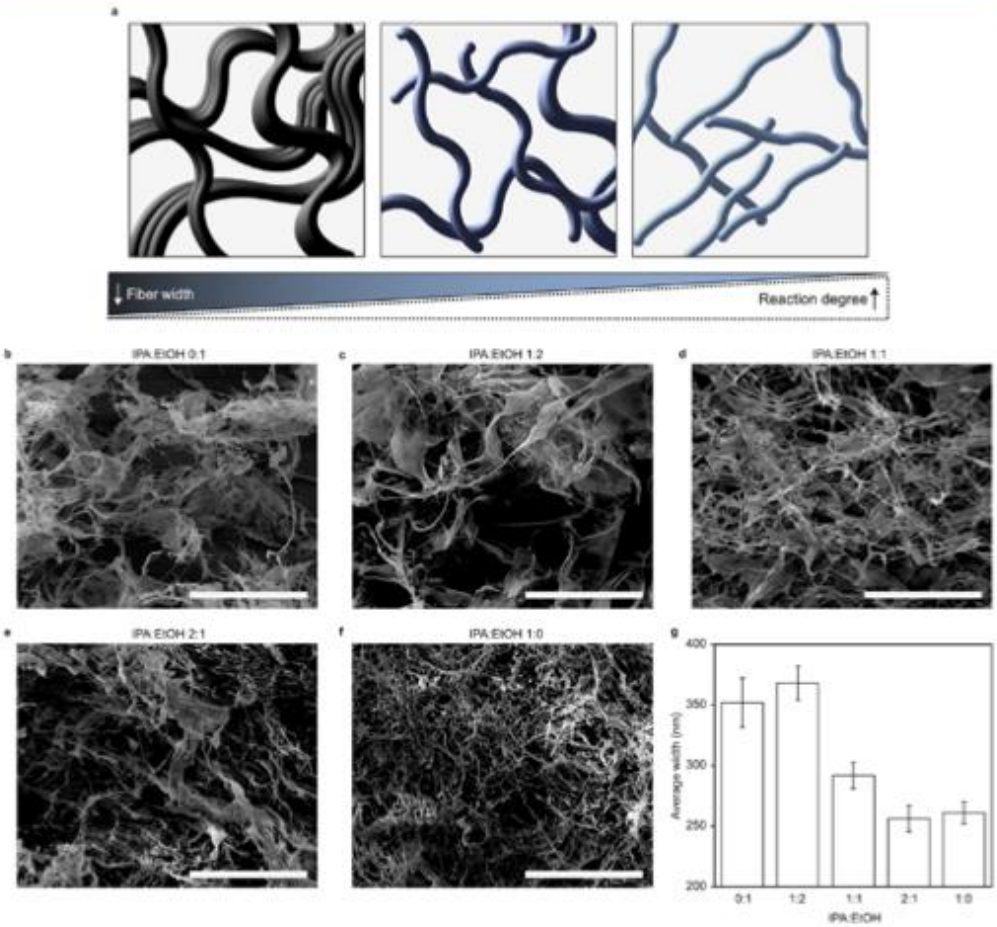


**Figure 2.** Size and appearance of carboxymethylated fibers analyzed via SEM. (a) Illustration of the breakdown of fibers with increasing degree of reaction. (b) SEM images of fibers reacted in 0:1, (c) 1:2, (d) 1:1, (e) 2:1, and (f) 1:0 IPA:EtOH. Scale bar: 50 $\mu$m. (g) Average fiber width in nanometer and SEM for $n = 100$; calculation based on different fields of view of the same sample.

Interestingly, SEM analysis showed that the average fiber diameter gradually decreased from roughly 350 to 250 nm when increasing the IPA content. This decrease in diameter is in excellent correlation with the observed increase in transparency. Moreover, the SEM data showed that we successfully achieved transparent fiber samples that maintained physiologically relevant sizes, as the fibers maintained lengths of tens of microns or more, across all conditions. Still, while micrometer-long fibers dominated, smaller structures could also be identified in TEM, especially for the reactions in pure IPA (Figure S4). Thus, for the majority of our subsequent studies, we focused on the transparent nanofiber samples obtained when performing the carboxymethylation in 2:1 IPA:EtOH. Given their dimensions, we will refer to the modified cellulose fibers as carboxymethylated nanofibrillar cellulose (cNFC) in the remainder of the manuscript.

While all of the carboxymethylated cellulose fibers preserved lengths of at least tens of micrometers, the rheological properties were affected notably with an increasing degree of substitution (see Figure 3a–f). For samples with a low degree of substitution, shear-thinning gels with a defined yield stress were maintained for 1% w/v samples. However, for transparent samples with a higher degree of reaction, these beneficial properties for 3D printing were largely lost (Figure 3g). However, the rheological properties required for 3D printing can be recovered by adjusting fiber concentration. (Figure 4a–c). Specifically, by increasing the concentration up to 3% w/v, the transparent fibers obtained by carboxymethylation in 2:1 IPA:EtOH, shear-thinning gels were reestablished. As expected, these rheological improvements are immediately reflected in excellent 3D printing properties (Figure 4d–f). Moreover, the storage modulus of the shear-thinning gels


https://doi.org/10.1021/acsami.2c16126
ACS Appl. Mater. Interfaces 2023, 15, 2564−2577

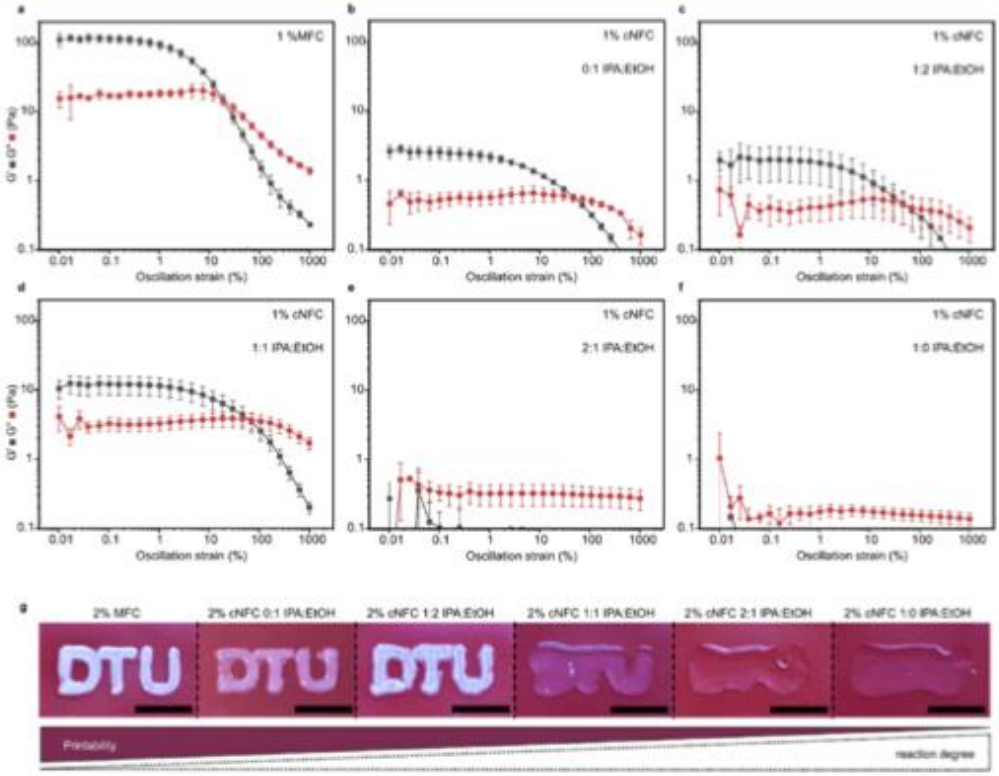


**Figure 3.** Rheology and printability of carboxymethylated fibers at 1% in milliQ water. Storage modulus $G'$ and loss modulus $G''$ of (a) MFC; fibers functionalized in (b) 0:1, (c) 1:2, (d) 1:1, (e) 2:1, and (f) 1:0 IPA:EtOH. Determined in oscillation sweep recorded at 25 °C in milliQ water at 1 Hz. SEM for $n = 3$. (g) Optical appearance and print of DTU logo with steel needle (ID 400 $\mu$m) with 2% MFC, 2% cNFC 0:1, 2% cNFC 1:2, 2% cNFC 1:1, 2% cNFC 2:1, and 2% cNFC 1:0. Scale bars = 1 cm.

could be tuned in the printable window from ~50 Pa to ~2.5 kPa by increasing the cNFC concentration, thus spanning a large part of the physiologically relevant range for soft tissues (Figure 4g). Importantly, increasing the fiber concentration only leads to minor decreases in sample transparency and the transmittance did not fall below 95% in a 3% w/v fiber solution (Figure 4h). Therefore, it is possible to recover printability and shape fidelity of the fiber dispersion by increasing its concentration, without losing transparency.

The excellent shape fidelity at higher cNFC concentrations allowed us to develop cross-linkable inks for complex structures. As an example, we formulated composite inks composed of cNFC and alginate. Notably, MFC:alginate inks have been studied extensively for bioprinting, yet for unreacted fibers, these composites have very limited transparency.[7] To generate an optically transparent alternative, we formulated a cNFC:alginate ink with similar rheology to MFC:alginate. This required using a slightly higher concentration of cNFC than that of MFC (Figure 5a–c). The shape fidelity and transparency of an example octopus figurine were intact throughout printing and cross-linking for cNFC:alginate (Figure 5d).

Although alginate is a widely applied biomaterial, cNFC:alginate is largely irrelevant as ECM-mimicking bioink since it lacks the native protein landscape and cell-adhesive motifs. As a simple solution, we found that the cNFC was readily miscible with both gelatin and collagen-based gels at a wide range of ratios and concentrations. Notably, this is not the case for unmodified MFC, where phase separation occurs. For formulating cNFC:gelatin inks, we aimed to decouple ink gelation and rheology during printing from the stiffness of the final printed construct (Figures 6 and S6). This would be advantageous as compared to pure gelatin or gelatin-methacrylate inks, where these properties are highly correlated and thermal control during printing is essential. For our composite inks, we thus focused on low Bloom gelatin at low concentrations that do not gel at RT (Figure 6a). On the other hand, since cNFC behaves like physical gels with concentration-defined yield stress for concentrations ≥3% w/v, the rheology of cNFC:gelatin inks at RT can be completely dominated by the fiber content at RT (Figures 6b,c and S6). Yet, while the cNFC content dominates printability, the gelatin content largely defines the stiffness of the final material after cross-linking enzymatic microbial transglutaminase (mTG)


https://doi.org/10.1021/acsami.2c16126
ACS Appl. Mater. Interfaces 2023, 15, 2564−2577

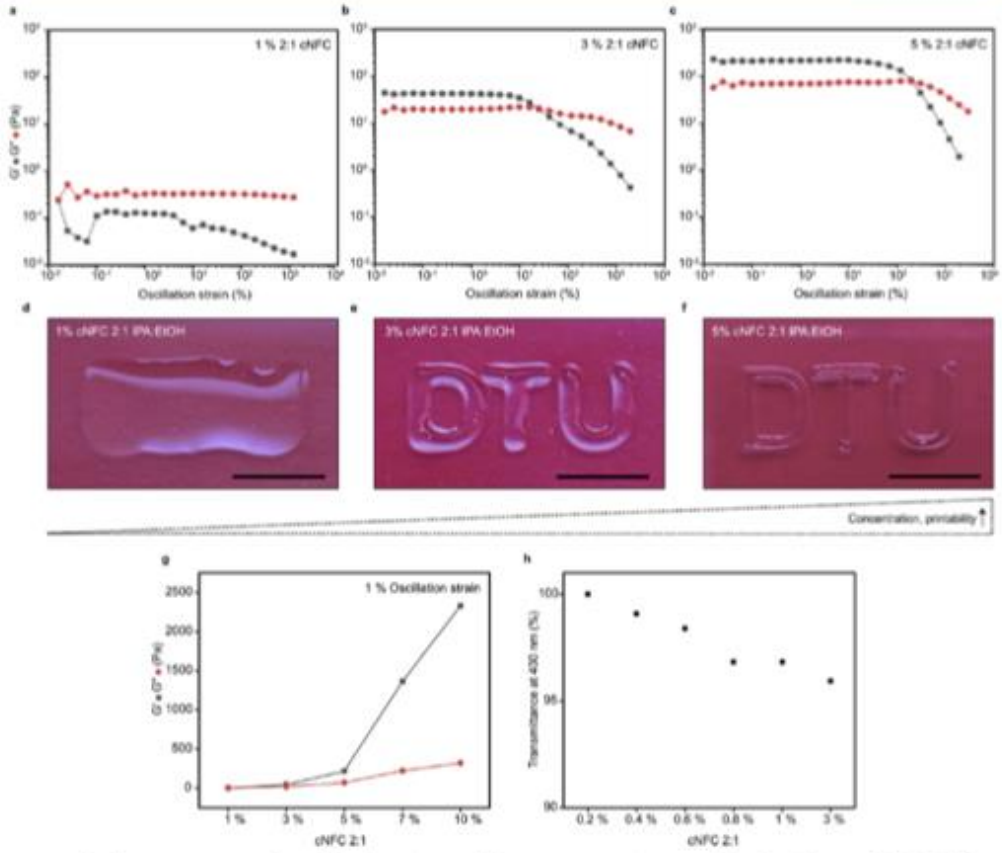


**Figure 4.** Rheology, transmittance, and printability of cNFC 2:1 at higher concentrations. Storage modulus $G'$ and loss modulus $G''$ of (a) 1% cNFC 2:1, (b) 3% cNFC 2:1, and (c) 5% cNFC 2:1. The oscillation sweeps were recorded at 25 °C in milliQ water at 1 Hz. (d) Printability of DTU logo at 1%, (e) 3%, and (f) 5% cNFC 2:1 in milliQ water. Scale bar = 1 cm. (g) Storage $G'$ and loss $G''$ modulus at a 1% oscillation strain as a function of the increasing concentration of cNFC 2:1 in %. (h) Transmittance at 400 nm in (%) as a function of the increasing concentration of cNFC 2:1 in milliQ water.

(Figures 6d,e and S6). It is thus straightforward to formulate printable cNFC:gelatin composite inks with independent control of the flow and final material mechanics (Figure S6). We found that Young's modulus of cNFC:gelatin matched well with that of the native muscle tissue[39] when combining ~5% w/v cNFC and ~5% w/v gelatin (Figure 6e).

Given their structural similarity to native collagen, we hypothesized that the cNFC fibers may serve as cell-guiding structures within cNFC:gelatin composites. Further, inspired by previous studies that have used the extrusion-driven orientation of cellulose fibrils during 3D printing as a basis for composites with programmable swelling or diffraction,[18,19] we aimed to explore if cNFCs would suffice to define the orientation of cells and tissues. To test this hypothesis, we printed a range of planar cNFC:gelatin tissue culture substrates and studied whether murine C2C12 myoblasts developed into myotubes that followed the print direction. At a constant gelatin concentration of 4% w/v, we observed a gradual improvement in the orientation of myotubes with increasing fiber concentration and highly parallel alignment for cNFC concentrations ≥4% w/v (Figure S7) and at 5% w/v gelatin with 5% w/v cNFC (Figures 7a–d and S8). Notably, the macroscopic surface roughness from filaments was negligible (Figure S9), and cellular orientation was thus in all likelihood caused by the shear-induced orientation of fibers (Figure S10). This print-guided orientation was highly controllable, as we could easily generate complex circular and checkerboard geometries (Figure 7e,f).

Beyond C2C12 cells, the substrates were also well-suited for orienting human skeletal myotubes derived from primary myoblasts (Figure 8). These substrates enabled the extended myotube culture and maturation, as we observed no indication of cytotoxicity or myotube delamination during 17 days of maturation of the human samples (Figure S11). Moreover, we observed an improvement in myotube thickness during extended culture and physiological responses to insulin


https://doi.org/10.1021/acsami.2c16126
ACS Appl. Mater. Interfaces 2023, 15, 2564−2577

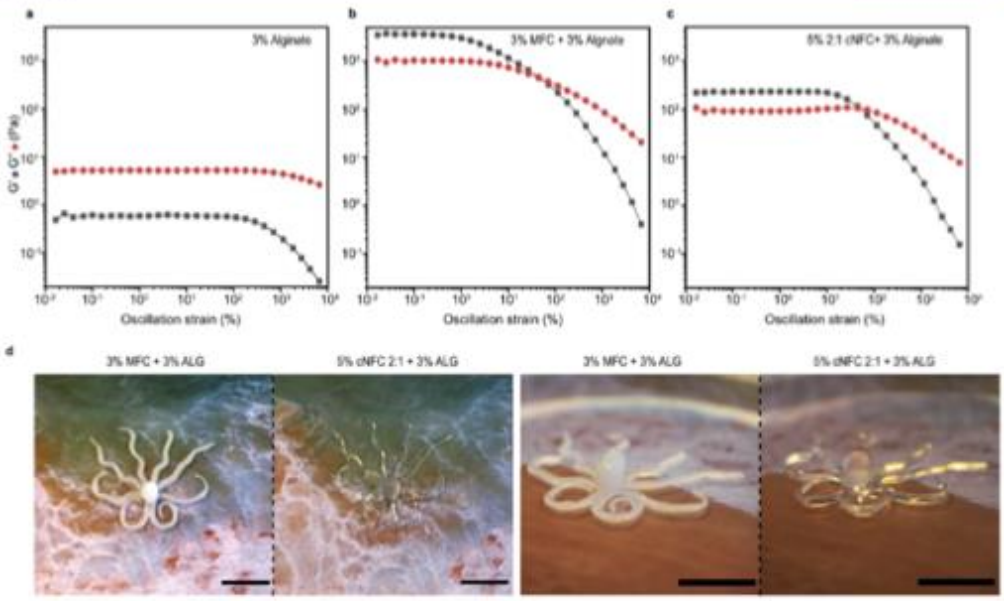


**Figure 5.** Rheology and 3D print of cross-linkable cNFC:alginate composite inks. Storage modulus $G'$ and loss modulus $G''$ for (a) 3% alginate. (b) 3% MFC + 3% alginate composite ink. (c) 5% cNFC 2:1 + 3% alginate composite ink. The oscillation sweeps were recorded at 25 °C in milliQ water at 1 Hz. (d) Side-by-side comparison of Octopus figurine printed with 3% MFC + 3% alginate and 5% cNFC 2:1 + 3% alginate composite inks (scale bars = 1 cm).

stimulation, indicative of native-like metabolic functionality (Figure S11). Beyond programmable soft tissue culture substrates, cNFC:gelatin could also be formulated into bioinks with embedded myoblasts for room-temperature bioprinting. Here, our preliminary studies indicated that a high fiber content could limit cell spreading and division. We therefore applied a lower cNFC content of 2% w/v and 4% w/v gelatin in the inks. During culture, these bioprinted myoblasts developed into polynucleated myotubes (Figure S12).

## DISCUSSION

Cellulose nanofibers are appealing for extrusion-based 3D printing and biomedical applications due to their accessibility, biocompatibility, and shear-thinning properties. However, such fibers may have radically different properties and size, dependent on their preparation. Thus far, micron-scale opaque MFC or tiny nanocrystalline fibers have received considerable attention,[7−11,21,22] as these can be generated with relative ease.[24,30] We hypothesized that intermediate sizes that mimic the size of native collagen fibers may have unique properties for tissue engineering applications. To generate such fibers, we established a procedure for tuning the carboxymethylation of MFC to yield transparent, tens to hundreds of micrometer-long cNFCs. In the process, we observed that the carboxymethylation reaction can be closely controlled by adjusting the composition of IPA:EtOH solvent mixes. This is likely caused by the low solubility of NaOH in IPA: when NaOH is added to the dispersed fibers, the driving force to accumulate on the surface of the hydrated fibers is higher with increasing IPA content.[29] The activation of the alcohol groups by NaOH is therefore the highest in pure IPA, followed by 2:1 IPA:EtOH, which is reflected in the final DS. Following the reaction, we observed a decrease in viscoelasticity with increasing DS. However, SEM images indicated that long fibrils remained for all reaction conditions, which seems to exclude fiber breakdown as the reason for the decrease in mechanical properties. Instead, we propose that the accumulation of surface charge and recrystallization of the cellulose are likely explanations. Indeed, organic solvents can induce decrystallization and changes in the polymorphism of cellulose, which can notably decrease cellulose stiffness.[40,41] Still, we were able to restore the shear-thinning properties and shape fidelity by increasing the concentration of fibers in solution without a significant loss in transparency.

As cNFC fibers were readily dispersible and miscible with common hydrogel biomaterials, such as alginate, collagen, and gelatin, we were able to formulate a range of composite bioinks. Importantly, while cNFC provided excellent printability to such inks, the mechanical properties of, e.g., cNFC:gelatin was dominated by gelatin after cross-linking. It is thus possible to decouple and independently control the mechanics during and after printing in these composite inks. Most importantly, we further found that cNFC provided unique anisotropic and cell-instructive properties to these common biomaterials. When differentiating human or mouse myoblast into myotubes on planar, 3D-printed cNFC:gelatin substrates, we observed a unidirectional alignment of myotubes along the toolpath applied in the printing. Notably, the degree of control was so high that we could easily organize myotubes into complex nonlinear patterns. Previously, similar shear-


https://doi.org/10.1021/acsami.2c16126
ACS Appl. Mater. Interfaces 2023, 15, 2564−2577

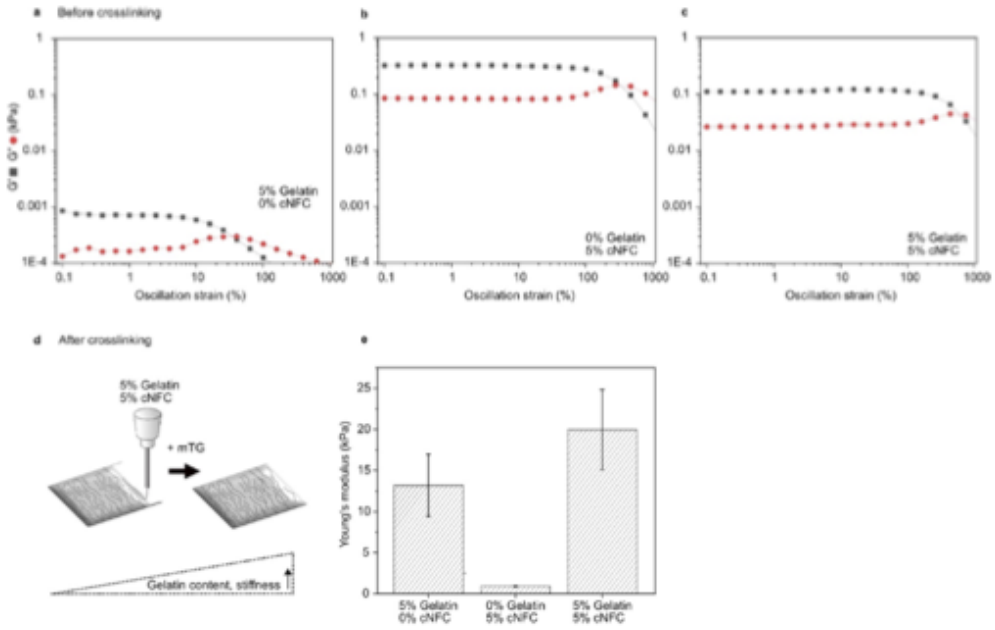


**Figure 6.** Rheology and stiffness of cNFC:gelatin composite inks before and after cross-linking. The oscillation sweeps were recorded at 25 °C in Dulbecco's modified Eagle's medium (DMEM) at 1 Hz. Rheology of (a) 5% gelatin + 5% cNFC, (b) 0% gelatin + 5% cNFC, and (c) 5% gelatin + 0% cNFC composite inks. (d) Illustration of the printing of cell-instructive coatings: substrates are subsequently cross-linked with mTG at 4 °C overnight. (e) Young's modulus $E$ in kPa of cross-linked substrates printed with 5% gelatin + 5% cNFC, 5% gelatin + 0% cNFC, and 0% gelatin + 5% cNFC composite inks. $E$ calculated from $G'$ at a 1% oscillation strain and SEM for $n = 3$.

induced alignment of cellulose fibrils has been applied as the basis of 3D-printed composites with programmable swelling or optical properties;[18,19] however, to the best of our knowledge, this effect has not been demonstrated as a method for organizing engineered tissues. We speculate that the significant length of our transparent cNFC may be critically important in this regard. Notably, the fiber length significantly exceeds that of a single myoblast, meaning that each fiber may serve as a physical cue for several myoblasts prior to their fusion into myotubes.

Soft and structured hydrogel substrates have previously been shown beneficial for self-organization, long-term culturing, and maturation of engineered striated muscle tissues.[32−34,42] Similarly, synthetic nanofiber scaffolds produced, e.g., by force-spinning or electrospinning are efficient for generating anisotropic engineered muscle tissues.[35,36,43] More recently, printed composites composed of cellulose fibrils and hyaluronic acid methacrylate have also been explored from organizing fibroblasts.[44] Similarly, previous anisotropic soft substrates for muscle-printed cNFC:gelatin enable the maturation of human myotubes for at least several weeks. The myotubes displayed a steady increase in size and basic metabolic function, indicating that cNFC:gelatin composites were not cytotoxic. This is in good agreement with earlier reports studying where CNF and CNCs were found not to be cytotoxic.[45] Further, we speculate that the extensive length of the present cNFCs will lower the risks of cellular uptake or lysosomal damage. Indeed, such risks have been reported to occur mainly for tiny CNCs with lengths in the order of hundreds of nanometers.[45] It is worth stressing that we have not considered or studied the use of cNFC for in vivo uses where, e.g., foreign body reaction could be a concern.

However, we believe that the 3D printing of cNFC:gelatin carries unique practical advantages for in vitro tissue modeling, as the procedure can readily be customized and adapted to a range of culturing formats, not least multiwell plates. Moreover, since it does not rely on high-resolution nozzles and is inherently a single-step procedure conducted at RT, it is highly scalable. Given the thixotropic and tissue-guiding properties of the cNFC, an additional and potentially larger impact may lie within their application in the 3D bioprinting of cell-laden inks. Within this paper, we showcased this application in the proof of principle printing of 3D muscle strips, where we again combined cNFC with gelatin to achieve cross-linkable bioinks. In these studies, we observed that cell spreading and division appeared to be diminished when applying high cNFC concentrations. We propose that this was mainly caused by the lack of cell-adhesive motifs on the cNFCs. It is, however, worth noting that for high fiber concentrations the risk of damaging embedded cells is also increased, as the high viscosity will produce a higher shear stress on the cells upon extrusion.[46] We therefore applied only 2% w/v in these inks. Given the low fiber concentration, the myotube elongation and alignment were in this case largely a product of filament geometry. Therefore, for broadening our approach and tailoring cNFC-based bioinks more closely to a



https://doi.org/10.1021/acsami.2c16126
ACS Appl. Mater. Interfaces 2023, 15, 2564−2577

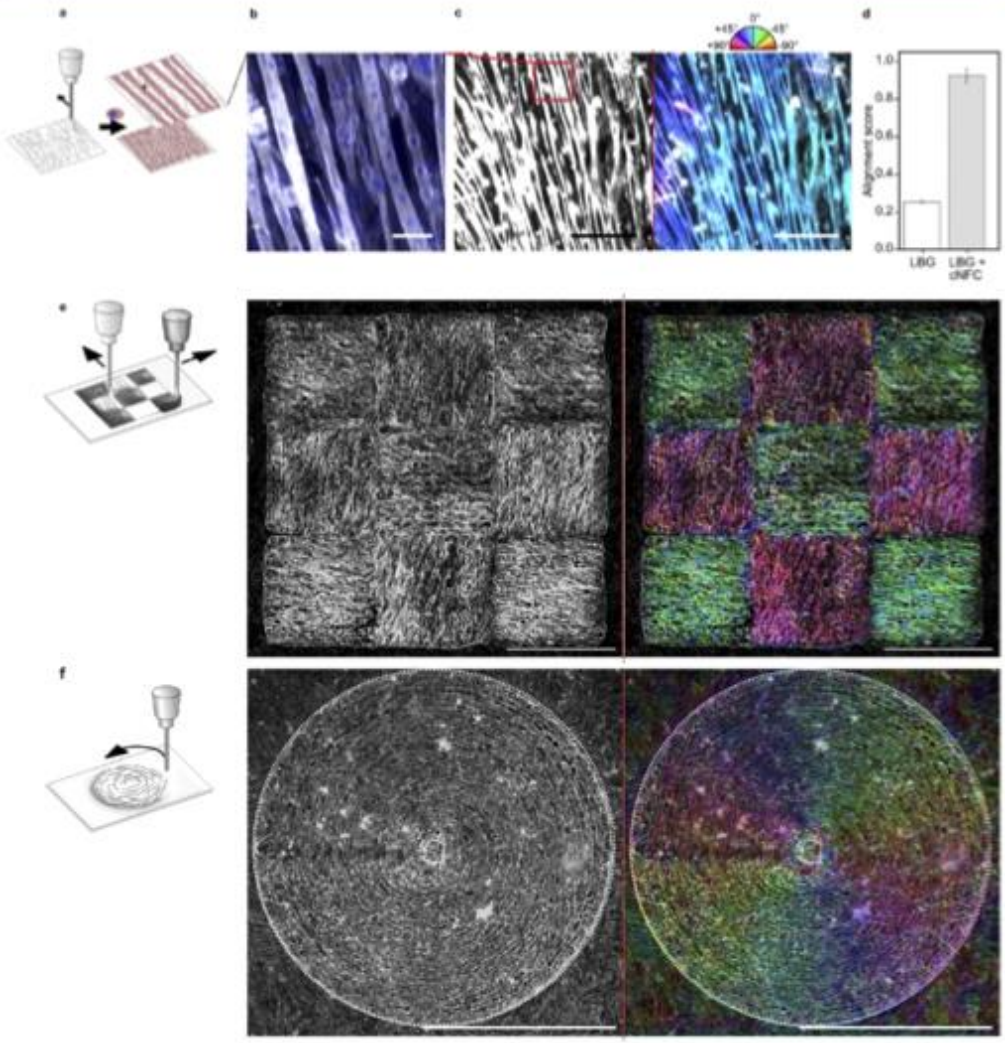


**Figure 7.** Self-alignment of C2C12 on cNFC:gelatin substrates. (a) Illustration of the seeding of C2C12 muscle cells onto cross-linked, printed substrates. (b) Polynucleated myotubes of seeded cells differentiated on a printed substrate. White: actin; blue: nucleus. Scale bar: 50 μm. (c) False-color mapping of myotube (actin) orientation with OrientationJ. Scale bar: 500 μm. (d) Alignment score (0−1) of the C2C12 myotube alignment on 5% LBG compared to that on 5% LBG + 5% cNFC. SEM for $n = 3$. (e) Illustration of the printing of alternating blocks of horizontal and vertical lines in a checkerboard-like fashion and false-colored 15 mm × 15 mm checkerboard with the alternating orientation of seeded cells. Scale bar: 5 mm. (f) Illustration of the printing of concentric circles with $r = 3.5$ mm and false-colored print with circular oriented cells. Scale bar: 5 mm.

given tissue, an important future direction will be the functionalization of carboxylic groups of cNFC with tissue-specific and cell-adhesive proteins and peptides. This may ultimately enable more specific inks and cross-linkable inks based solely on cNFCs.

## CONCLUSIONS

In this study, we detailed a robust procedure for generating transparent, dispersible, and cell-instructive cellulose nanofibrils and 3D printing bioinks. A key foundation for the procedure is the observation that the degree of carboxymethylation can be accurately controlled by adjusting the polarity of ethanol−isopropanol reaction solvents. In doing so, we



https://doi.org/10.1021/acsami.2c16126
ACS Appl. Mater. Interfaces 2023, 15, 2564−2577

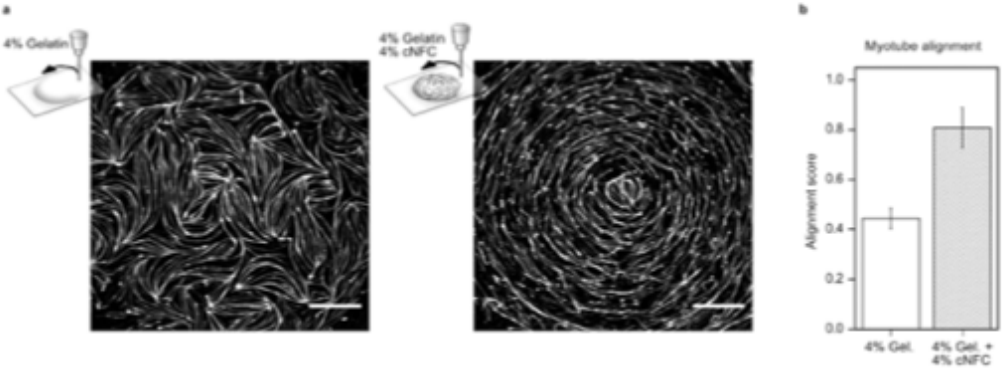


**Figure 8.** Self-alignment of human skeletal myocytes (HSkMs) on printed cNFC:gelatin substrates. (a) Alignment of HSkM according to the print direction. Substrates were printed with a steel nozzle (ID 250 μm) in a circular motion with 4% gelatin (left) and 4% LB gelatin + 4% cNFC (right). White: actin stain. Scale bar: 1.5 mm. (b) Alignment score (0−1) of human myotubes aligned on 4% LB gelatin and 4% LB gelatin + 4% cNFC. SEM for $n = 3$.

generated transparent cellulose fibers with excellent 3D printing properties that mimic the size and shape of native ECM protein fibers. When applying these cellulose nanofibers in composite bioinks, we were able to predict and control the tissue-level organization of human and murine skeletal myotubes by extrusion direction and pattern. The aligned and extended myotubes could be matured for several weeks, making our approach appealing as a scalable method for generating physiologically relevant models of human muscles. The functional groups introduced through the carboxymethylation further provide means of tailoring nanofiber biochemistry, which significantly broadens their future relevance for tissue engineering applications.

## MATERIALS AND METHODS

**Carboxymethylation.** MFC was obtained from Norwegian spruce by Borregaard in Sarpsborg (NO) and delivered as a 10% aqueous paste. Isopropanol (IPA), methanol, and absolute ethanol ≥99.9% were purchased from VWR and always freshly opened before each experiment as the usage of old IPA and EtOH will reduce the reactivity of the reactants. NaOH (S5881) and monochloroacetic acid (MCA, 402923) were purchased at Sigma-Aldrich as solids. First, MFC was disintegrated using an Ultra-Turrax homogenizer with an S25N-18G-ST dispersing element. The dispersion was conducted in pure solvent and the following solvent combinations IPA:EtOH: 0:1, 1:2, 1:1, 2:1, and 1:0. The day before the experiment, a 5% w/v NaOH (2% w/v in pure IPA) solution was prepared in the respective solvent. The day after, 10 g of MFC pulp (1 g dry content) was homogenized for 10 min at 10,000 rpm. The homogenized MFC was heated up to 35 °C while stirring. Twelve milliliters of a 5% w/v NaOH solution (600 mg) was added to the dispersed fibers and left stirring at 35 °C for 30 min. Afterward, the temperature was increased to 45 °C. Once the temperature was reached, 4 mL of a 142.2 mg/mL (570 mg total) MCA solution in the respective solvent was added and left stirring at 45 °C for 3 h. The substitution reaction was repeated in the same solvents with half the amount of reactants (300 mg NaOH and 285 mg MCA).

Around 10 mL of a 10% v/v acetic acid solution was added to the fibers for neutralization, and the fibers were filtered. The filtered fibers were washed 3× with methanol, followed by dialysis against deionized water for 3 days in a 12−14 kDa cutoff dialysis tube with two daily water changes. The dialyzed fibers were freeze-dried and stored at room temperature until further use.

**IR.** IR spectra were recorded on a PerkinElmer Spectrum 100 FT-IR spectrometer. The spectra were recorded with a resolution of 1 from 4000 to 800 $cm^{-1}$. All spectra were recorded in absorbance units and normalized at 1050 $cm^{-1}$. The relative degree of substitution ($DS_{rel}$) was calculated by relating the intensity of the normalized absorbance (NA) of the stretching vibration of the carboxyl group (C═O) at 1595 $cm^{-1}$ to the stretching vibration of the glucose backbone (C−H) at 2894 $cm^{-1}$

$$DS_{rel} = \frac{NA_{1595\ cm^{-1}}}{NA_{2894\ cm^{-1}}} - C \quad (1)$$

The constant $C$ indicates the relation between these two stretching vibrations of the carboxyl group and glucose backbone in nonoxidized cellulose.

**Titration.** Between 20 and 50 mg of cNFCs were weighed in and transferred to a clean 100 mL Erlenmeyer flask. Calcium acetate (10229177, Thermo Fisher) solution (2% w/v) was added to the fibers (10 mL), and the solid material was allowed to imbibe for 30 min. Two drops of phenolphthalein indicator (A0424229, Thermo Fisher) were added to the flask (prepared as 1.0% w/v in ethanol). A buret was filled with the standardized NaOH solution (0.0121 or 0.00121 M). The cNFC solution was titrated until the faint, pink endpoint was reached (persisting for at least 30 s). Three separate weighed samples of each cNFC sample were analyzed. The percentage of the carboxyl content was calculated using the following equation

$$\text{carboxyl groups [\%]} = \frac{N \cdot V \cdot MW_{COOH}}{m[\text{mg}] \cdot 100} \quad (2)$$

where $N$ is the normality of the NaOH solution, $V$ is the volume of NaOH consumed to reach the endpoint (corrected for the blank), and $MW_{COOH}$ is 59, corresponding to the introduced group $-CH_2COOH$.

**Transmittance.** The absorbance of MFC and cNFC was measured using a Thermo Scientific NanoDrop 2000 at a path length of 1 mm. In general, the samples were homogenized at 1% w/v for 10 min using an Ultra-Turrax homogenizer at 10,000 rpm for 10 min. The absorbance was measured immediately after homogenization.

**Rheology.** The rheology of each ink was analyzed using a Discovery Hybrid Rheometer (TA instruments, DE) equipped with a Peltier plate thermal controller and a plate geometry with a diameter of 40 mm and a fixed gap of 1 mm. All samples were freshly prepared right before the measurement. The fiber dispersion was prepared right before the measurement and homogenized as described before. As a standard, amplitude sweeps were recorded at 25 °C in milliQ water at


https://doi.org/10.1021/acsami.2c16126
ACS Appl. Mater. Interfaces 2023, 15, 2564−2577

1 Hz at an oscillation strain of 0.01−10,000%. For the calculation of Young's modulus, hydrogel precursor solutions with desired conditions (gelatin and cNFC content) were casted in between two poly(methyl methacrylate) (PMMA) slides with a 1 mm spacer. Prior to gelation, the slides were coated with poly(vinyl alcohol) to avoid the hydrogel from sticking to the PMMA surfaces. The hydrogels are incubated at 4 °C for 30 min to achieve prepolymerization of gelatin. Then, the PMMA slides were removed and the gels were replaced in the microplate with 10 U/mL mTG solution for 1 day at 4 °C to achieve the enzymatic cross-linking. The storage modulus of the gels was determined by performing oscillatory shear experiments with parallel plate geometry, as described above. Young's modulus $E$ is calculated as follows $E = 2G'(1 + \nu)$, assuming $\nu = 0.5$.

**SEM.** Freeze-dried fibers were deposited on a carbon sticker. The samples were sputtered with a 2.4 nm gold layer. Images were recorded using a Quanta 200 FEG Cryo ESEM at an acceleration voltage of 5 kV, an aperture of 40 $\mu$m, a spot size of 3.5 $\mu$m, and a working distance of 6 mm. Different fields of view of the same sample were analyzed at different magnifications and used for fiber counting.

**TEM.** Five microliters of fiber solution was drop-cast onto freshly glow-discharged carbon-stabilized formvar-coated 200 mesh nickel TEM grids (EMS Diasum). The fibers were allowed to adsorb for 5 min before the excess solution was wicked away using filter paper. The fibers were imaged using a Tecnai T20 G2 TEM at 200 kV, and images were acquired using a TVIPS XF416 CCD camera.

**Printing of 3D Figurine.** A 3D computer-aided design (CAD) of an octopus was created using Fusion360 and printed on a RegenHU 3D Discovery bioprinter. A cross-linkable composite ink based on nonreacted MFC was prepared using 3% w/w MFC and 3% w/v alginate (dynamic viscosity: 80−120 cP, 194−13325, FUJIFILM Wako) in milliQ water. The MFC:alginate composite ink was printed with a pneumatic syringe and a steel nozzle (ID 250 $\mu$m, Cellink Swe) at a pressure of ∼230 kPa. A transparent, cross-linkable composite ink was prepared using 5% w/v cNFC and 3% w/v alginate in milliQ water and printed with a pneumatic syringe and steel nozzle (ID 250 $\mu$m, Cellink Swe) at ∼560 kPa.

**Culturing of C2C12 Murine Myoblasts.** C2C12 cell culture was performed under sterile conditions and incubated at 37 °C, 100% humidity, 5% $CO_2$. C2C12 murine myoblasts were cultured in growth medium containing DMEM (D5796, Sigma-Aldrich), 10% fetal bovine serum (S1810, Sigma-Aldrich), and 1% P/S (P0718, Sigma-Aldrich). Cells were passaged and harvested at an 80% confluency. All cells were kept within 10 passages from stock. Differentiation was initiated by changing the growth medium to differentiation medium containing DMEM and 2% horse serum (H1270, Sigma-Aldrich).

**Culturing of Human Primary Skeletal Muscle Cells.** Human single-donor skeletal muscle cells (SK111, Cook Myocite) were maintained and passaged in myotonic basal media (MB-2222, Cook Myocite) supplemented with 10% myotonic growth supplement (MS-3333, Cook Myocite) and 1% P/S antibiotic in a humidified atmosphere containing 5% $CO_2$ and 95% air at 37 °C.

**Printing of Cell-Instructive Surface and Cell Seeding.** The following procedure was performed under sterile conditions: sterile solvents with 1% penicillin/streptomycin (P/S, P0718, Sigma-Aldrich) were used, and cross-linking solutions were sterile-filtered with a 0.45 $\mu$m pore-sized filter. All syringes and needles were additionally sterilized with UV light. A composite ink consisting of 5% w/v low bloom gelatin (164 G bloom, 48723, Sigma-Aldrich) and 5% w/v cNFC was prepared as follows: dried fibers were suspended in DMEM at 10,000 rpm for 10 min. Low bloom gelatin was added to the fiber suspension and heated to 45 °C for approx 45 min. The solution was stirred from time to time with a spatula and shortly centrifuged to exclude air bubbles. The composite ink was printed with a steel nozzle (ID 200 $\mu$m, Cellink Swe) at a pressure of 580 kPa and a feed rate of 12 mm/s. Subsequently, the print was cross-linked with a 5 U/mL microbial transglutaminase (mTG, ACTIVA TI transglutaminase, 100 U/g, 1002, Modernist Pantry) solution overnight at 4 °C. Before cell seeding, the prints were washed 3× for 10 min with PBS (D8537, Sigma-Aldrich). The alignment experiment in Figure 7 was performed with murine C2C12 myocytes at a density of 20,000 cells per well of a 12-well plate. Differentiation was initiated after day 3 by changing the medium from growth medium to differentiation medium. The experiment ended on differentiation day 7 by fixing the cells. The alignment experiment in Figure 8 was performed with human skeletal muscle cells at a density of 200,000 cells per well in 12-well plates directly on the printed substrates and kept in MEM (41090-028, Gibco) with 10% myotonic growth supplement for 2 days before differentiation was initiated by switching to 2% horse serum as growth supplement (26050088, Gibco). The samples in Figure 8 were fixed after 8 days of differentiation. The samples in Figure S11 were fixed after 10 and 17 days of differentiation.

**Immunoblotting.** Immunoblotting of S6 Ser235/236 and Akt Ser473 phosphorylation was performed by starving the myotubes from serum and glucose for 3 h and then keeping them basal or stimulated with 1 or 100 nm insulin for 15 min prior to harvest. Samples were lysed in lysis buffer 50 mM tris base, 150 mM NaCl, 1 mM EDTA, 1 mM EGTA, 50 mM sodium fluoride, 5 mM pyrophosphate, 2 mM sodium orthovanadate, 1 mM dithiothreitol, 1 mM benzamidine, 0.5% protease inhibitor cocktail (P8340, Sigma-Aldrich), 20% NP-40, pH 7.4. Western blot procedure was conducted as previously described.[34] The following antibodies from Cell Signaling Technology were used: phospho (p)-Akt Ser473 (#9271), p-S6 Ser235/236 (#2211).

**Bioprinting.** A sacrificial ink was prepared consisting of 8% alginate (Dynamic viscosity: 300−400 cp, 192-09995, FUJIFILM Wako), and 10 U/mL of mTG was prepared under sterile conditions. The sacrificial ink was printed at a feed rate of 15 mm/s with a pneumatic printhead at ∼130 kPa with a plastic nozzle (ID 250 $\mu$m). A bioink consisting of 3% w/v cNFC and 6% w/v low bloom gelatin was prepared under sterile conditions. C2C12 skeletal muscle cells were harvested and mixed 1:4 with the bioink. The final concentrations were 2% of cNFC, 4% of low bloom gelatin, and 10 mio/mL of C2C12. The print was performed at a feed rate of 15 mm/s with a pneumatic printhead at approx. 25 kPa with a steel nozzle (ID 250 $\mu$m). Sacrificial and bioink were printed in parallel into a 12-well plate. The print was incubated at 4 °C for 5−10 min to allow the gelation of gelatin. Afterward, a cold 10 U/mL mTG solution was added to each well and the print was incubated at 37 °C for 1 h. The mTG solution was discarded, and growth medium was added to the wells. Differentiation was initiated on day 2. The samples were fixed on differentiation day 7.

**Cell Staining, Fiber Staining, and Imaging.** Printed constructs were washed 3× with PBS. Afterward, cells were permeabilized and fixed with 0.1% v/v Triton X and 4% v/v paraformaldehyde and incubated for 20 min at RT. The prints were washed 3× with PBS while shaking. A 1:1000 dilution of 4′,6-diamidino-2-phenylindole and dihydrochloride (DAPI, 62247, Thermo Scientific) and a 1:200 dilution of Alexa Fluor Plus 555 Phalloidin (A30106, Thermo Fisher) for F-actin staining in PBS were added and incubated overnight at 4 °C. The prints were washed 3× with PBS and kept in PBS at 4 °C until further use. MFC was stained with calcofluor white (18909, VWR) by immersing the printed, dried substrate in 5 mL of a 0.01% solution calcofluor white with 5 drops of 10% KOH for 2 h. The substrate was rinsed and imaged with ProLong Gold Antifade (P10144, Molecular Probes). A 5% w/v cNFC ink was prepared by directly mixing 100 $\mu$L of 0.01% calcofluor solution per 1 mL ink. The sample was printed and directly mounted with ProLong Gold Antifade. Images of fluorescent stains were recorded with a Nikon Eclipse Ti2 microscope and NIS-Elements software and a Zeiss Observer Z1 microscope with a mounted Zeiss AxioCam.

**Myotube Orientation Quantification.** The ImageJ plugin OrientationJ[47] was used to determine the orientation of the myotubes on printed substrates. For this, F-actin stain was recorded after 7 days of differentiation. The hue and saturation of the false-colored images correspond to the orientation angle and coherency, respectively. The distribution of orientation was plotted against the principal orientation angle. The alignment score corresponds to the total fraction of distribution within ±15° of the principal orientation angle to the total count of oriented pixels. The alignment score was



https://doi.org/10.1021/acsami.2c16126
ACS Appl. Mater. Interfaces 2023, 15, 2564−2577

calculated for $n = 3$ fields of view of 1.75 mm × 1.65 mm of three different samples.

## ■ ASSOCIATED CONTENT

### Supporting Information

The Supporting Information is available free of charge at https://pubs.acs.org/doi/10.1021/acsami.2c16126.

It contains additional experimental data including IR screening of carboxymethylation in different solvents; transmittance and absorbance spectra of cNFC reacted in IPA:EtOH mixtures; transmittance and $DS_{rel}$ of carboxymethylation reaction with lower reactant content; TEM images; rheological studies; fiber-dependent alignment score analysis; brightfield image of the fiber gel; stained fiber gels and cross section of aligned cells on gel; human skeletal muscle cell myotube width analysis and immunoblotting; and bioprints as examples (PDF)

## ■ AUTHOR INFORMATION


### Corresponding Author

**Johan U. Lind** − *Department of Health Technology, Technical University of Denmark, 2800 Kgs. Lyngby, Denmark;* orcid.org/0000-0002-0358-3999; Phone: +45 42 803 802; Email: joli@dtu.dk

### Authors

**Carmen Radeke** − *Department of Health Technology, Technical University of Denmark, 2800 Kgs. Lyngby, Denmark*

**Raphaël Pons** − *Department of Health Technology, Technical University of Denmark, 2800 Kgs. Lyngby, Denmark*

**Marko Mihajlovic** − *Department of Health Technology, Technical University of Denmark, 2800 Kgs. Lyngby, Denmark;* orcid.org/0000-0002-4315-0338

**Jonas R. Knudsen** − *August Krogh Section for Molecular Physiology, Department of Nutrition, Exercise and Sports, Faculty of Science, University of Copenhagen, 2100 Copenhagen, Denmark; Heart and Skeletal Muscle Biology, Global Drug Discovery, Novo Nordisk A/S, 2760 Maaloev, Denmark*

**Sarkhan Butdayev** − *Department of Health Technology, Technical University of Denmark, 2800 Kgs. Lyngby, Denmark*

**Paul J. Kempen** − *Department of Health Technology, Technical University of Denmark, 2800 Kgs. Lyngby, Denmark; The National Centre for Nano Fabrication and Characterization, DTU Nanolab, Technical University of Denmark, 2800 Kgs. Lyngby, Denmark*

**Charis-Patricia Segeritz** − *Heart and Skeletal Muscle Biology, Global Drug Discovery, Novo Nordisk A/S, 2760 Maaloev, Denmark*

**Thomas L. Andresen** − *Department of Health Technology, Technical University of Denmark, 2800 Kgs. Lyngby, Denmark*

**Christian K. Pehmøller** − *Heart and Skeletal Muscle Biology, Global Drug Discovery, Novo Nordisk A/S, 2760 Maaloev, Denmark*

**Thomas E. Jensen** − *August Krogh Section for Molecular Physiology, Department of Nutrition, Exercise and Sports, Faculty of Science, University of Copenhagen, 2100 Copenhagen, Denmark*

Complete contact information is available at: https://pubs.acs.org/10.1021/acsami.2c16126


### Author Contributions

C.R.: designed and performed the experiments and composed the draft for the manuscript, R.P.: assisted with the experimental work and screening of reaction conditions, M.M. and S.B.: performed rheology studies and chemical characterizations, J.R.K. and C.-P.S.: performed experiments with human cells, P.J.K.: performed TEM analysis, T.L.A., C.K.P., T.E.J., and J.U.L.: secured funding and designed the study, and J.U.L.: supervised the project and prepared the manuscript. All authors revised and approved the final manuscript.

### Notes

The authors declare no competing financial interest.

## ■ ACKNOWLEDGMENTS

C.R., R.P., S.B., M.M., and J.U.L. would like to gratefully acknowledge the Lundbeck Foundation (R250-2017-1425) and the Independent Research Fund Denmark (8048-00050 and 1032-00435) for their support. J.R.K. acknowledges the generous support from the Danish Diabetes Academy (Novo Nordisk Foundation, NNF17SA0031406).

## ■ ABBREVIATIONS

3D, three-dimensional
AGUs, anhydroglucose units
CNCs, cellulose nanocrystals
cNFC, carboxymethylated nanofibrillated cellulose
ECM, extracellular matrix
EtOH, ethanol
dECM, decellularized ECM
IPA, isopropanol
MCA, monochloroacetic acid
MeOH, methanol
MFC, microfibrillated cellulose
mTG, microbial transglutaminase
NFC, nanofibrillated cellulose
PCL, polycaprolactone
PMMA, poly(methyl methacrylate)
TEMPO, 2,2,6,6-tetramethylpyperidine-1-oxyl

## ■ REFERENCES


(1) Lee, A.; Hudson, A. R.; Shiwarski, D. J.; Tashman, J. W.; Hinton, T. J.; Yerneni, S.; Bliley, J. M.; Campbell, P. G.; Feinberg, A. W. 3D Bioprinting of Collagen to Rebuild Components of the Human Heart. *Science* **2019**, *365*, 482−487.

(2) Skylar-Scott, M. A.; Huang, J. Y.; Lu, A.; Ng, A. H. M.; Duenki, T.; Liu, S.; Nam, L. L.; Damaraju, S.; Church, G. M.; Lewis, J. A. Orthogonally Induced Differentiation of Stem Cells for the Programmatic Patterning of Vascularized Organoids and Bioprinted Tissues. *Nat. Biomed. Eng.* **2022**, *6*, 449−462.

(3) Lind, J. U.; Busbee, T. A.; Valentine, A. D.; Pasqualini, F. S.; Yuan, H.; Yadid, M.; Park, S. J.; Kotikian, A.; Nesmith, A. P.; Campbell, P. H.; Vlassak, J. J.; Lewis, J. A.; Parker, K. K. Instrumented Cardiac Microphysiological Devices via Multimaterial Three-Dimensional Printing. *Nat. Mater.* **2017**, *16*, 303−308.

(4) Sun, W.; Starly, B.; Daly, A. C.; Burdick, J. A.; Groll, J.; Skeldon, G.; Shu, W.; Sakai, Y.; Shinohara, M.; Nishikawa, M.; Jang, J.; Cho, D. W.; Nie, M.; Takeuchi, S.; Ostrovidov, S.; Khademhosseini, A.; Kamm, R. D.; Mironov, V.; Moroni, L.; Ozbolat, I. T. The Bioprinting Roadmap. *Biofabrication* **2020**, *12*, No. 022002.

(5) Pless, C. J.; Radeke, C.; Cakal, S. D.; Kajtez, J.; Pasqualini, F. S.; Lind, J. U.Emerging Strategies in 3D Printed Tissue Models for in Vitro Biomedical Research. In *Bioprinting*; Conti, M.; Marino, M., Eds.; Academic Press: Cambridge, US, 2022; pp 207−246. DOI: 10.1016/B978-0-323-85430-6.00007-8.
(6) Bowers, S. L. K.; Banerjee, I.; Baudino, T. A. The Extracellular Matrix: At the Center of It All. *J. Mol. Cell. Cardiol.* **2010**, *48*, 474−482.
(7) Markstedt, K.; Mantas, A.; Tournier, I.; Martínez Ávila, H.; Hägg, D.; Gatenholm, P. 3D Bioprinting Human Chondrocytes with Nanocellulose−Alginate Bioink for Cartilage Tissue Engineering Applications. *Biomacromolecules* **2015**, *16*, 1489−1496.
(8) Kuzmenko, V.; Karabulut, E.; Pernevik, E.; Enoksson, P.; Gatenholm, P. Tailor-Made Conductive Inks from Cellulose Nanofibrils for 3D Printing of Neural Guidelines. *Carbohydr. Polym.* **2018**, *189*, 22−30.
(9) Im, S.; Choe, G.; Seok, J. M.; Yeo, S. J.; Lee, J. H.; Kim, W. D.; Lee, J. Y.; Park, S. A. An Osteogenic Bioink Composed of Alginate, Cellulose Nanofibrils, and Polydopamine Nanoparticles for 3D Bioprinting and Bone Tissue Engineering. *Int. J. Biol. Macromol.* **2022**, *205*, 520−529.
(10) Monfared, M.; Mawad, D.; Rnjak-Kovacina, J.; Stenzel, M. H. 3D Bioprinting of Dual-Crosslinked Nanocellulose Hydrogels for Tissue Engineering Applications. *J. Mater. Chem. B* **2021**, *9*, 6163−6175.
(11) Ojansivu, M.; Rashad, A.; Ahlinder, A.; Massera, J.; Mishra, A.; Syverud, K.; Finne-Wistrand, A.; Miettinen, S.; Mustafa, K. Wood-Based Nanocellulose and Bioactive Glass Modified Gelatin-Alginate Bioinks for 3D Bioprinting of Bone Cells. *Biofabrication* **2019**, *11*, No. 035010.
(12) Kolesky, D. B.; Homan, K. A.; Skylar-Scott, M. A.; Lewis, J. A. Three-Dimensional Bioprinting of Thick Vascularized Tissues. *Proc. Natl. Acad. Sci. U.S.A.* **2016**, *113*, 3179−3184.
(13) Choi, Y. J.; Jun, Y. J.; Kim, D. Y.; Yi, H. G.; Chae, S. H.; Kang, J.; Lee, J.; Gao, G.; Kong, J. S.; Jang, J.; Chung, W. K.; Rhie, J. W.; Cho, D. W. A 3D Cell Printed Muscle Construct with Tissue-Derived Bioink for the Treatment of Volumetric Muscle Loss. *Biomaterials* **2019**, *206*, 160−169.
(14) Kim, B. S.; Das, S.; Jang, J.; Cho, D. W. Decellularized Extracellular Matrix-Based Bioinks for Engineering Tissue- And Organ-Specific Microenvironments. *Chem. Rev.* **2020**, *120*, 10608−10661.
(15) Kim, H. H. K.; Jang, J.; Park, J.; Lee, K. P.; Lee, S.; Lee, D. M.; Kim, K. H.; Kim, H. H. K.; Cho, D. W. Shear-Induced Alignment of Collagen Fibrils Using 3D Cell Printing for Corneal Stroma Tissue Engineering. *Biofabrication* **2019**, *11*, No. 035017.
(16) Prendergast, M. E.; Davidson, M. D.; Burdick, J. A. A Biofabrication Method to Align Cells within Bioprinted Photo-crosslinkable and Cell-Degradable Hydrogel Constructs via Embedded Fibers. *Biofabrication* **2021**, *13*, No. 044108.
(17) Yongcong, F.; Zhang, T.; Liverani, L.; Boccaccini, A. R.; Sun, W. Novel Biomimetic Fiber Incorporated Scaffolds for Tissue Engineering. *J. Biomed. Mater. Res., Part A* **2019**, *107*, 2694−2705.
(18) Sydney Gladman, A.; Matsumoto, E. A.; Nuzzo, R. G.; Mahadevan, L.; Lewis, J. A. Biomimetic 4D Printing. *Nat. Mater.* **2016**, *15*, 413−418.
(19) Siqueira, G.; Kokkinis, D.; Libanori, R.; Hausmann, M. K.; Gladman, A. S.; Neels, A.; Tingaut, P.; Zimmermann, T.; Lewis, J. A.; Studart, A. R. Cellulose Nanocrystal Inks for 3D Printing of Textured Cellular Architectures. *Adv. Funct. Mater.* **2017**, *27*, No. 1604619.
(20) Espinosa, E.; Filgueira, D.; Rodríguez, A.; Chinga-Carrasco, G. Nanocellulose-Based Inks—Effect of Alginate Content on the Water Absorption of 3D Printed Constructs. *Bioengineering* **2019**, *6*, No. 65.
(21) Shin, S.; Hyun, J. Matrix-Assisted Three-Dimensional Printing of Cellulose Nanofibers for Paper Microfluidics. *ACS Appl. Mater. Interfaces* **2017**, *9*, 26438−26446.
(22) Shin, S.; Hyun, J. Rheological Properties of Cellulose Nanofiber Hydrogel for High-Fidelity 3D Printing. *Carbohydr. Polym.* **2021**, *263*, No. 117976.
(23) de Nooy, A. E. J.; Besemer, A. C.; van Bekkum, H. Highly Selective Nitroxyl Radical-Mediated Oxidation of Primary Alcohol Groups in Water-Soluble Glucans. *Carbohydr. Res.* **1995**, *269*, 89−98.
(24) Saito, T.; Isogai, A. TEMPO-Mediated Oxidation of Native Cellulose. The Effect of Oxidation Conditions on Chemical and Crystal Structures of the Water-Insoluble Fractions. *Biomacromolecules* **2004**, *5*, 1983−1989.
(25) Fukuzumi, H.; Saito, T.; Isogai, A. Influence of TEMPO-Oxidized Cellulose Nanofibril Length on Film Properties. *Carbohydr. Polym.* **2013**, *93*, 172−177.
(26) Tanaka, R.; Saito, T.; Ishii, D.; Isogai, A. Determination of Nanocellulose Fibril Length by Shear Viscosity Measurement. *Cellulose* **2014**, *21*, 1581−1589.
(27) Yang, L.; Van Der Werf, K. O.; Koopman, B. F. J. M.; Subramaniam, V.; Bennink, M. L.; Dijkstra, P. J.; Feijen, J. Micromechanical Bending of Single Collagen Fibrils Using Atomic Force Microscopy. *J. Biomed. Mater. Res., Part A* **2007**, *82A*, 160−168.
(28) Im, W.; Lee, S.; Rajabi Abhari, A.; Youn, H. J.; Lee, H. L. Optimization of Carboxymethylation Reaction as a Pretreatment for Production of Cellulose Nanofibrils. *Cellulose* **2018**, *25*, 3873−3883.
(29) Pushpamalar, V.; Langford, S. J.; Ahmad, M.; Lim, Y. Y. Optimization of Reaction Conditions for Preparing Carboxymethyl Cellulose from Sago Waste. *Carbohydr. Polym.* **2006**, *64*, 312−318.
(30) Wågberg, L.; Decher, G.; Norgren, M.; Lindström, T.; Ankerfors, M.; Axnäs, K. The Build-up of Polyelectrolyte Multilayers of Microfibrillated Cellulose and Cationic Polyelectrolytes. *Langmuir* **2008**, *24*, 784−795.
(31) Eyholzer, C.; Bordeanu, N.; Lopez-Suevos, F.; Rentsch, D.; Zimmermann, T.; Oksman, K. Preparation and Characterization of Water-Redispersible Nanofibrillated Cellulose in Powder Form. *Cellulose* **2010**, *17*, 19−30.
(32) Bettadapur, A.; Suh, G. C.; Geisse, N. A.; Wang, E. R.; Hua, C.; Huber, H. A.; Viscio, A. A.; Kim, J. Y.; Strickland, J. B.; McCain, M. L. Prolonged Culture of Aligned Skeletal Myotubes on Micromolded Gelatin Hydrogels. *Sci. Rep.* **2016**, *6*, No. 28855.
(33) Cakal, S. D.; Radeke, C.; Alcala, J. F.; Ellman, D. G.; Butdayev, S.; Andersen, D. C.; Calloe, K.; Lind, J. U. A Simple and Scalable 3D Printing Methodology for Generating Aligned and Extended Human and Murine Skeletal Muscle Tissues. *Biomed. Mater.* **2022**, *17*, No. 045013.
(34) Jensen, J. H.; Cakal, S. D.; Li, J.; Pless, C. J.; Radeke, C.; Jepsen, M. L.; Jensen, T. E.; Dufva, M.; Lind, J. U. Large-Scale Spontaneous Self-Organization and Maturation of Skeletal Muscle Tissues on Ultra-Compliant Gelatin Hydrogel Substrates. *Sci. Rep.* **2020**, *10*, No. 13305.
(35) Choi, J. S.; Lee, S. J.; Christ, G. J.; Atala, A.; Yoo, J. J. The Influence of Electrospun Aligned Poly(Epsilon-Caprolactone)/Collagen Nanofiber Meshes on the Formation of Self-Aligned Skeletal Muscle Myotubes. *Biomaterials* **2008**, *29*, 2899−2906.
(36) Wade, R. J.; Bassin, E. J.; Gramlich, W. M.; Burdick, J. A.; Wade, R. J.; Burdick, J. A.; Bassin, E. J.; Gramlich, W. M. Nanofibrous Hydrogels with Spatially Patterned Biochemical Signals to Control Cell Behavior. *Adv. Mater.* **2015**, *27*, 1356−1362.
(37) Khodabukus, A.; Madden, L.; Prabhu, N. K.; Koves, T. R.; Jackman, C. P.; Muoio, D. M.; Bursac, N. Electrical Stimulation Increases Hypertrophy and Metabolic Flux in Tissue-Engineered Human Skeletal Muscle. *Biomaterials* **2019**, *198*, 259−269.
(38) Miyamoto, K.; Tsuji, K.; Nakamura, T.; Tokita, M.; Komai, T. Preparation of Carboxymethyl-Gellan. *Carbohydr. Polym.* **1996**, *30*, 161−164.
(39) Engler, A. J.; Griffin, M. A.; Sen, S.; Bönnemann, C. G.; Sweeney, H. L.; Discher, D. E. Myotubes Differentiate Optimally on Substrates with Tissue-like Stiffness: Pathological Implications for Soft or Stiff Microenvironments. *J. Cell Biol.* **2004**, *166*, 877−887.
(40) Bhattacharyya, D.; Singhal, R. S.; Kulkarni, P. R. A Comparative Account of Conditions for Synthesis of Sodium Carboxymethyl Starch from Corn and Amaranth Starch. *Carbohydr. Polym.* **1995**, *27*, 247−253.

(41) Nishino, T.; Takano, K.; Nakamae, K. Elastic Modulus of the Crystalline Regions of Cellulose Polymorphs. *J. Polym. Sci., Part B: Polym. Phys.* **1995**, *33*, 1647−1651.
(42) McCain, M. L.; Agarwal, A.; Nesmith, H. W.; Nesmith, A. P.; Parker, K. K. Micromolded Gelatin Hydrogels for Extended Culture of Engineered Cardiac Tissues. *Biomaterials* **2014**, *35*, 5462−5471.
(43) Gonzalez, G. M.; MacQueen, L. A.; Lind, J. U.; Fitzgibbons, S. A.; Chantre, C. O.; Huggler, I.; Golecki, H. M.; Goss, J. A.; Parker, K. K. Production of Synthetic, Para-Aramid and Biopolymer Nanofibers by Immersion Rotary Jet-Spinning. *Macromol. Mater. Eng.* **2017**, *302*, No. 1600365.
(44) Dong, L.; Liang, M.; Guo, Z.; Wang, A.; Cai, G.; Yuan, T.; Mi, S.; Sun, W. A Study on Dual-Response Composite Hydrogels Based on Oriented Nanocellulose. *Int. J. Bioprinting* **2022**, *8*, 126−139.
(45) Wang, X.; Chang, C. H.; Jiang, J.; Liu, Q.; Liao, Y. P.; Lu, J.; Li, L.; Liu, X.; Kim, J.; Ahmed, A.; Nel, A. E.; Xia, T. The Crystallinity and Aspect Ratio of Cellulose Nanomaterials Determine Their Pro-Inflammatory and Immune Adjuvant Effects In Vitro and In Vivo. *Small* **2019**, *15*, No. 1901642.
(46) Blaeser, A.; Campos, D. F. D.; Puster, U.; Richtering, W.; Stevens, M. M.; Fischer, H. Controlling Shear Stress in 3D Bioprinting Is a Key Factor to Balance Printing Resolution and Stem Cell Integrity. *Adv. Healthcare Mater.* **2016**, *5*, 326−333.
(47) Fonck, E.; Feigl, G. G.; Fasel, J.; Sage, D.; Unser, M.; Rüfenacht, D. A.; Stergiopulos, N. Effect of Aging on Elastin Functionality in Human Cerebral Arteries. *Stroke* **2009**, *40*, 2552−2556.





https://doi.org/10.1021/acsami.2c16126
*ACS Appl. Mater. Interfaces* 2023, 15, 2564−2577

International Journal of Pharmaceutics 610 (2021) 121236

Contents lists available at ScienceDirect

International Journal of Pharmaceutics

journal homepage: www.elsevier.com/locate/ijpharm

# Multi-material 3D printing of programmable and stretchable oromucosal patches for delivery of saquinavir

Shaolong He [a,1], Carmen Radeke [b,1], Jette Jacobsen [a], Johan Ulrik Lind [b,*], Huiling Mu [a,*]

[a] Department of Pharmacy, Faculty of Health and Medical Sciences, University of Copenhagen, Universitetsparken 2, DK-2100 Copenhagen, Denmark
[b] Department of Health Technology, Technical University of Denmark, Building 423, 2800 Kgs. Lyngby, Denmark

ARTICLE INFO

*Keywords:*
Buccal delivery
Oromucosal patch
Direct ink writing
3D printing
Saquinavir
Microenvironmental pH

ABSTRACT

Oromucosal patches for drug delivery allow fast onset of action and ability to circumvent hepatic first pass metabolism of drugs. While conventional fabrication methods such as solvent casting or hot melt extrusion are ideal for scalable production of low-cost delivery patches, these methods chiefly allow for simple, homogenous patch designs. As alternative, a multi-material direct-ink-write 3D printing for rapid fabrication of complex oromucosal patches with unique design features was demonstrated in the present study. Specifically, three print-materials: an acidic saquinavir-loaded hydroxypropyl methylcellulose ink, an alkaline effervescent sodium carbonate-loaded ink, and a methyl cellulose backing material were combined in various designs. The $CO_2$ content and pH of the microenvironment were controlled by adjusting the number of alkaline layers in the patch. Additionally, the rigid and brittle patches were converted to compliant and stretchable patches by implementing mesh-like designs. Our results illustrate how 3D printing can be used for rapid design and fabrication of multifunctional or customized oromucosal patches with tailored dosages and changed drug permeation.

## 1. Introduction

Drug delivery using oromucosal patches has several advantages. It bypasses the hepatic first pass metabolism, provides fast onset of action, and has good patient compliance (Chinna Reddy et al., 2011; Lam et al., 2014; Madhav et al., 2009; Sudhakar et al., 2006). It is especially relevant for potent drugs where the metabolism associated with conventional oral administration can be a major challenge. Drug release kinetics from an oromucosal patch and subsequent transport across the buccal mucosa is dependent on the physico-chemical properties of the drug(s) in question, as well as the carrier materials applied in the patch. For instance, 40% of approved drugs and nearly 90% of drugs in development are poorly water soluble (Kalepu and Nekkanti, 2015; Loftsson and Brewster, 2010), some of them are weakly ionizable with pH-dependent solubility (Bassi and Kaur, 2010; Taniguchi et al., 2014). In such cases, the carrier materials applied in an oromucosal patch present an opportunity to locally and transiently control drug solubility and improve drug absorption (Bergström et al., 2004; Sieger et al., 2017; Taniguchi et al., 2014). In addition, the patch should be of minimal discomfort to the recipient and contain an appropriate or even tailored dosage.

A smart and delicate fabrication method needs the ability to tune the fundamental properties of oromucosal patches. At present, solvent casting (SC) and hot melt extrusion (HME) are the standard methods for fabrication of oromucosal patches (Krampe et al., 2016; Vetchý et al., 2014). Of these, SC is the widely used one in industry due to its relative simplicity and low cost. In SC, the components of the formulation are dissolved in a suitable solvent, that is cast onto a horizontal plate/release liner and dried to obtain layered patches (Morales and McConville, 2011; Pechová et al., 2018). In HME, patch formulations are mixed and heated, extruded, and cut into the desired size (Dixit and Puthli, 2009). While these methods provide means of large-scale fabrication of uniform patches, they offer limited opportunities to integrate multiple functional materials in complex designs for optimized or patient-tailored dosing and release. On the other hand, emerging additive manufacturing technologies –widely referred to as 3D printing– are highly appealing for generating pharmaceutical delivery systems with personalized dosages, drug combinations, mechanics, and release characteristics (Alomari et al., 2015; Buanz et al., 2015; Daly et al., 2015; Seoane-Viaño et al., 2021b).

Several printing techniques have been explored for design and fabrication of oral patches (Krampe et al., 2016; Preis et al., 2015; Tian

* Corresponding authors.
*E-mail addresses:* joli@dtu.dk (J.U. Lind), huiling.mu@sund.ku.dk (H. Mu).
[1] Contributed equally.

https://doi.org/10.1016/j.ijpharm.2021.121236
Received 21 September 2021; Received in revised form 19 October 2021; Accepted 23 October 2021
Available online 5 November 2021

et al., 2019), including inkjet and flexographic printing (Genina et al., 2013, 2012; Janßen et al., 2013; Raijada et al., 2013; Wickström et al., 2015), fused deposition modelling (FDM) (Eleftheriadis et al., 2020) and direct ink writing (DIW) (Cho et al., 2020; Ehtezazi et al., 2018; Elbadawi et al., 2021; Eleftheriadis et al., 2019; Musazzi et al., 2018; Rahman and Quodbach, 2021; Seoane-Viaño et al., 2021a; Speer et al., 2018) – also known as robocasting or pressure-assisted micro-syringe 3D printing. DIW relies on volumetric or pneumatic extrusion of viscous or viscoelastic inks composed e.g. of particles or polymers in a carrier solvent, that solidifies or dries following extrusion. DIW is particularly interesting for printing of complex oromucosal patches, as it allows for combining several materials and solvents in a single procedure (Lind et al., 2017). Moreover, materials and casting solutions used in traditional SC can generally be applied in DIW either directly or following minor modifications. DIW thus opens for new concept and designs based on well-studied and regulatory approved materials. For instance, Tagami *et al.* printed mono-material mucoadhesive patches based on hydroxypropyl methylcellulose (HPMC) inks loaded with catechin in various macroscopic geometries (Tagami et al., 2019). More recently, Elbadawi *et al.* combined HPMC and pullulan loaded with caffeine, in macroscopic-side by side or layered designs and studied the influence on patch mechanics (Elbadawi et al., 2021).

The present study demonstrates the use of DIW 3D printing for creating truly complex and multi-functional patches through sub-millimeter integration of three inks based on well-established carrier materials such as HPMC and methyl cellulose (MC). More specifically, the patches were designed for buccal delivery of antiretroviral drug saquinavir, a poorly water-soluble compound with low oral bioavailability, due to extensive hepatic first pass metabolism (Branham et al., 2012; Caon et al., 2015; Kim et al., 1998; Kupferschmidt et al., 1998). Drug dose of the oromucosal patches was rapidly altered by changing the digital design of the patches during fabrication. Further, a slightly acidic saquinavir ink optimized for high drug solubility(Buchanan et al., 2008; Obonga et al., 2013; Takano et al., 2016) and an ink containing alkaline effervescent carbonate were printed side-by-side, to alter the microenvironment pH ($pH_M$) and saquinavir transport across a buccal barrier in an *ex vivo* assay. Moreover, highly stretchable patches were created by implementing simple mesh-like designs that provides a better patient comfort, especially for long-term dosing applications, when it is applied in mechanically active spots in the oral cavity.

## 2. Materials and methods

### 2.1. Chemicals

Saquinavir mesylate (SQM) was obtained from Hoffmann-La Roche Ltd (Basel, Switzerland). Malic acid, glycerol (>99%), agarose (type I), Nile red, Sulforhodamine B acid chloride and bovine serum albumin were purchased from Sigma-Aldrich (MO, USA). Hydroxypropyl methylcellulose (HPMC) K100 LV (viscosity: 80–120 mPa•s, 2% (v/v %) at 20 °C) (DOW chemical company, 2013.) and methyl cellulose (EC) NF 50 were obtained from Dow Chemical Ltd (MI, USA). HPMC K200 M (viscosity: 75,000–140,000 cP) (DOW chemical company and Colorcon, 2021.) was purchased from Colorcon Inc. (PA, USA). Monopotassium dihydrogenphosphate anhydrate, dipotassium hydrogenphosphate anhydrate, sodium chloride, phosphoric acid (85%) and citric acid anhydrate were obtained from Merck KGaA (Darmstadt, Germany). Lucifer Yellow CH was purchased from Thermo Fisher (Invitrogen, USA). Purified water from a SG ultra pure water system (SG Water, Barsbuttel, Germany) was used.

### 2.2. Preparation of the inks

Separate polymer-based inks were prepared for backing membrane, saquinavir layer with malic acid, and alkaline layer containing sodium carbonate, as detailed in Table 1. For the backing membrane ink, suitable amounts of MC, glycerol and Nile red were dissolved in 20 mL of methanol at 60–65 °C. For the saquinavir drug ink, saquinavir mesylate, glycerol and malic acid were dissolved in 20 mL of water at 70–75 °C, followed by suspending HPMC K100 LV gradually to form a white HPMC-saquinavir suspension, which was cooled down to 4–6 °C to obtain a transparent ink. For the alkaline ink, sodium carbonate, glycerol and HPMC K200 M were dissolved in water at 70–75 °C.

**Table 1**
Composition of the inks.

| | Ink for saquinavir layer, g (%)* | Ink for alkaline layer, g (%)* | Ink for backing membrane, g |
|---|---|---|---|
| Saquinavir mesylate | 0.10 (0.45) | – | – |
| HPMC K100 LV | 1.50 (6.78) | – | – |
| Malic acid | 0.22 (0.99) | – | – |
| Glycerol | 0.30 (1.36) | 0.20 (0.9) | 0.60 |
| Sodium carbonate | – | 0.25 (1.13) | – |
| HPMC K200 M | – | 0.50 (2.26) | – |
| Methyl cellulose 100 FP | – | – | 6.00 |
| Nile red | – | – | 0.004 |
| Methanol (ml) | – | – | 0.04 |
| Water | 20.0 (90.42) | 30.0 (96.93) | – |

* Percentage of components in the inks is wt%.

### 2.3. Rheological studies of the inks

The rheology of each ink was analyzed using a Discovery Hybrid Rheometer (TA instruments, DE, USA) equipped with a Peltier plate thermal controller and a plate geometry with a diameter of 40 mm. The measurements were performed at 25 °C. The inks were equilibrated at 25 °C for 30 s prior to conduction of the measurements. The storage (G') and loss (G") moduli were measured as a function of oscillatory strain (0.01–10,000%) at constant frequency (1 Hz). The viscosity of the inks was measured as a function of shear rate (0.01–100 1/s).

### 2.4. 3D printing of oral delivery patches

All patches were 3D printed using a 3D-Discovery printer (RegenHU, CH) and the accompanying BioCAD software for print design. 3 CC cartridges (Nordson EFD, US) were applied for containing ink, using pneumatic pressure for saquinavir and alkaline ink extrusion. 10 CC cartridges (Nordson, EFD, US) were used for extrusion of the backing membrane.

#### 2.4.1. Preparation of the single-material patches for stretchability study

To compare the tensile strength and elasticity of different designs based on the MC backing membrane ink, cylindrical steel nozzles with a diameter of 0.2, 0.4 and 0.6 mm (Cellink, SE) were used, at a pneumatic pressure of 250, 100 and 50 kPa, respectively. The ink was extruded at RT onto a heated polystyrene plate (45 °C) at a feed rate of 15 mm/s in the shape of a meander with different line sizes A and B. In addition, a uniform layer was added on top and on the bottom of the design for further mounting of the sample on a biaxial stretcher. The prints were left drying for 1 h prior to testing.

#### 2.4.2. Preparation of multi-material patches

The stretchable patches used to determine the drug-content and drug-permeability were printed with varying number of layers and nozzle sizes to determine the effect of the alkaline ink on the local pH. The backing membrane was printed in 3 layers using a 0.6 mm cylindrical steel nozzle at a pressure of 40 kPa and a feed rate of 10 mm/s on a pre-heated polystyrene plate (45 °C). The printed backing membrane was left on the polystyrene plate and dried for approx. 30 min before

further printing. The drug-laden-ink was printed on the dry backing membrane, and the patches with different number (1, 2 and 3) of drug-laden layers used for the drug content measurement were printed using different nozzles with diameters of 0.1, 0.2 and 0.4 mm, respectively. For further experiments, a nozzle size of 0.4 mm was chosen for drug-laden and alkaline inks, which were printed with a 0.4 mm cylindrical steel nozzle at a feed rate of 15 mm/s and a pressure of 30 and 15 kPa, respectively. The drug-laden ink was printed in 3 layers. Afterwards, the alkaline ink was printed in parallel to the printed drug-laden ink in 0, 1, 2, 3, 4 and 5 layers. The final prints were left drying on the polystyrene plate until further use.

### 2.5. HPLC system for the quantification of saquinavir

The Elite LaChrom HPLC system (VWR International, Tokyo, Japan) equipped with an L-2130 pump with degasser, an L-2450 diode array detector and L-2200 autosampler was applied to quantify saquinavir in different samples. Reversed phase chromatography was performed using a C18 column at 30 °C and a mobile phase of 10 mM ammonium acetate buffer: acetonitrile 60:40 (v/v). A flow rate of 0.5 mL/min and an injection volume of 20 µL were applied. Saquinavir was detected at 240 nm with a retention time of 5.5 min. The chromatograms were analyzed using EZChrom Elite software Version. A linear calibration curve with a $R^2$ value of 0.9987 was obtained in the range of 0.45–160.50 µg/mL for the drug content study. For permeation study, a linear calibration curve was used in the range of 25–850 ng/mL ($R^2$ = 0.9964). The quantification limit was 25 ng/mL.

### 2.6. Analysis of saquinavir content in the printed patches

Each printed patch as described in Sections 2.4.1 and 2.4.2 was put into a volumetric flask followed by adding water to 100 mL. The flask was sonicated in an ultrasonic bath at 40 °C for 10 min to obtain saquinavir solution (backing membrane was insoluble in this solution). With suitable dilution, the sample was analyzed using the HPLC method described in Section 2.5.

### 2.7. Morphology study

The printed $pH_M$ modifying patches described in Section 2.4.2 were observed using a Dino-Lite digital microscope (USB) (AnMo Electronics Corporation, Taiwan, China) and a bright-field microscope (Zeiss Axioskop 40, Jena, Germany). For visualization studies, different fluorescent agents were added to each ink and the dry patches with fluorescent agents were imaged using a Zeiss Observer Z1 microscope with a mounted Zeiss AxioCam Mrm (Jena, Germany). To differentiate between the inks, the backing membrane was visualized using Nile Red (exc. 559 nm/ emis. 636 nm), for the saquinavir and alkaline ink sulforhodamine B acid chloride (exc. 543 nm/ emis. 565 nm) and Lucifer yellow (exc. 236 nm/ emis. 542 nm) were used, respectively.

### 2.8. Mechanical study

The thickness of backing membranes with 1, 2 and 3 layers printed with a nozzle diameter of 0.2, 0.4 and 0.6 mm was determined using a Stylus profiler (Dektak 150, Veeco, NY, US). The mechanical properties of the printed backing membranes was analyzed using a biaxial stretcher (Instron, Illinois Tool Works Inc., MA, US). The width and length of the stretchable part of the backing membranes were also measured. The additional attachment sites were used to place the samples on the uniaxial stretcher with a load cell of 500 N. The ultimate tensile strength was determined by recording the load force (N) as a function of extension (m). The effective stiffness was determined by plotting the load force (N) over tensile strain (%) and performing a linear fit of the linear regime before first break.

### 2.9. Investigation of $pH_M$ during the dissolution

Each patch was placed in an Eppendorf tube followed by adding 400 µL of phosphate buffer solution (PBS, 13 mM potassium phosphate and 145 mM sodium chloride, pH 6.8) simulating human saliva pH and buffer capacity as previously described (Gittings, 2017; He et al., 2020). Immediately, the pH close to the surface of the patch was measured using a pH meter (744 pH meter, Mettler Toledo, OH, USA) with a micro-electrode (Biotrode, Metrohm AG, Herisau, Switzerland) and the values at predetermined time intervals were recorded.

### 2.10. Ex vivo studies of saquinavir permeation

#### 2.10.1. Preparation of the tissues

Cryo-protected porcine buccal tissues were used for the permeation study. The preparation procedure of the tissues was described in a previous study (Marxen et al., 2016). Briefly, fresh porcine buccal mucosae obtained from healthy experimental control pigs (approx. 30 kg Danish Landrace/Yorkshire × Durox (D-LY)) were kept cold on ice and moistened using phosphate buffered saline (pH 7.4, 0.1 M, 290 mOsm/kg). The connective tissue of the mucosae were trimmed using surgical scissors until a thickness of approximately 5 mm. The trimmed mucosae were submerged in a cryoprotectants (the phosphate buffered saline containing 40% (w/v) glycerol and 20% (w/v) sucrose) for 1 h followed by storing at −80 °C before use.

To thaw and equilibrate the tissues before the permeation study, the frozen mucosae were defrosted in the phosphate buffer saline (approximately 40 mL) and washed by replacing the phosphate buffered saline four times every 20 min at 4 °C on a shaking plate. The connection tissue of the defrosted mucosa was trimmed again using a Thomas Stadie-Riggs tissue slicer (Thomas Scientific, Swedesboro, NJ, USA) until a thickness range of 500–700 µm as determined by a tailor-made micrometer. Glass Franz diffusion cells (orifice diameter: 5 mm, diffusion area: 0.2 $cm^2$) with a receptor volume of 3 mL were applied in this study. Each trimmed mucosa was mounted between the donor and the receptor chambers with the epithelium facing the donor chamber. Each mucosa was equilibrated for 0.5 h at 37 °C with 250 µL of PBS simulating human saliva (as described in Section 2.9) in the donor chamber, and 3.00 mL of 0.05% (w/v) bovine serum albumin solution in the receptor chamber.

#### 2.10.2. Saquinavir permeation study

The PBS in the donor chamber was withdrawn after the equilibrium, and there was no change for the medium in the receptor chambers. Afterwards, the diffusion cell was disassembled, and the mucosa was left on the top of the donor chamber and dried using a lab tissue. A volume of 50 µL fresh PBS was added onto the epithelium again and the permeation experiment was initiated by attaching the printed patch on the epithelium. Immediately, the donor chamber was mounted and was sealed with a piece of Parafilm®. Samples (250 µL) were withdrawn from the receptor chambers at predetermined time intervals (15 min, 30 min, 45 min, 1 h, 2 h, 3 h, 4 h and 5 h). Air bubbles induced by sampling were removed via the side arm by carefully tilting the Franz cell after each withdrawal. The removed samples were replaced with 250 µL of pre-heated BSA solution followed by sealing the receptor chamber using small Parafilm® pieces to prevent water evaporation. The samples were diluted two times before centrifugation (13,500 rpm, 10 min, at ambient temperature), and subsequently analyzed using the HPLC method described in Section 2.5.

After the permeation study, each buccal mucosa was flushed with water to remove the residual patch matrix on the tissue surface, and then dried under ambient condition for 24 h. The dried mucosa was kept in 1 mL of phosphoric acid solution (phosphoric acid (85%): water 10:3, v/v) at 65 °C for 10 min followed by disrupting and homogenizing using a pestle. The homogenized tissue suspension was diluted 10 folds using water followed by centrifugation (13,500 rpm, 10 min, at ambient temperature). The supernatant was subsequently analyzed using the

HPLC method described previously.

## 3. Results and discussion

### 3.1. Rheological properties of the inks and optimization of printing procedure

The overall design of the multi-functional patches was composed of a meandering backing membrane, onto which a drug-laden ink and an alkaline ink are printed in parallel without overlapping (Fig. 1a). This requires high spatial resolution in the print procedure, with control over extrusion rate and material spreading. The printability of the formulated inks was evaluated by characterizing their rheological properties. For all the inks, oscillatory studies show a dominating loss modulus $G''$ over storage modulus $G'$ indicating predominantly viscous materials (Fig. 1b). Flow experiments further show shear thinning behavior, i.e. the viscosity decreases with increasing shear rate (Fig. 1c), which is beneficial for maintaining resolution when extruding inks through narrow nozzles. Still, since all inks are in a liquid state, shape fidelity relies on solvent carrier evaporation. To increase solvent evaporation and facilitate multi-material and multilayer prints, a slightly heated stage was set at 45 °C, as higher temperatures may cause solvent boiling and bubble formation. The backing membrane was printed with a 0.6 mm nozzle. It spread after printing due to the low viscosity and provided a sufficiently large surface to print the drug-laden and alkaline inks. The drug-laden and alkaline inks were printed in parallel with a 0.4 mm nozzle and a line distance of 0.25 mm to avoid overlapping between printed traces and the acid-base reaction between the malic acid and sodium carbonate. The printing procedure and design was evaluated via fluorescence microscopy to demonstrate that the drug-laden and alkaline inks were indeed printed in parallel without overlapping (Fig. 1d and 1e). The viscosity of inks are increased by using polymers with a high viscosity grade or/and increasing the concentration of polymers in the inks. The viscosity of the inks affects the manufacture process of the patches and saquinavir release from the patches. Optimal ink formulations should be printable and their viscosity should not hinder the release of saquinavir.

### 3.2. Tuning of stretchability of printed patches by varying the design

3D printing allows for rapid design prototyping and tailoring of macroscopic properties through simple design alterations. To enable the fabrication of stretchable and compliant patches, a simple mesh-like design was systematically varied and the resultant mechanical properties were evaluated. Specifically, the backing membrane was printed in six different designs (Fig. 2a & 2b). First, the line distance "A" was tuned to 2.5, 4.5 and 7.5 mm, respectively, using the same nozzle size of 0.6 mm. Secondly, three different nozzle sizes (0.6, 0.4 and 0.2 mm) were

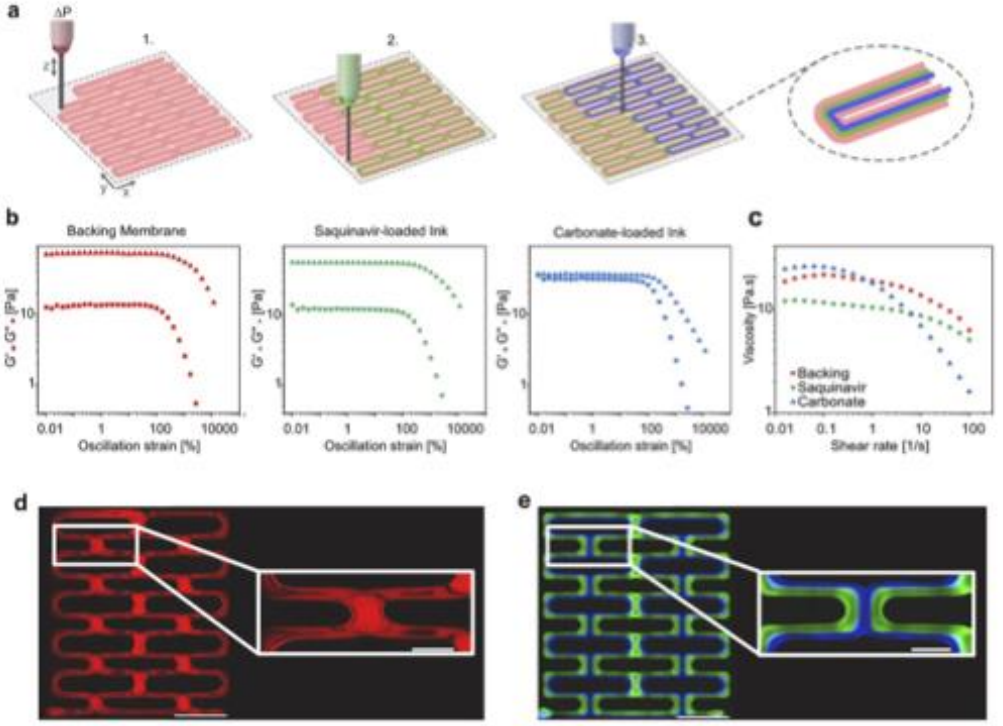


**Fig. 1.** a) Schematic illustration of multi-material printing of complex oral patches using a backing membrane (red), drug-laden (green) and alkaline (blue) ink. b) Rheology of the backing membrane, drug-laden and alkaline inks. The G moduli were recorded as a function of oscillation strain at constant frequency (1 Hz). c) The viscosity was recorded as a function of shear rate. d), e) Fluorescence imaging of printed patches based on alkaline (blue), drug-laden (green) ink and backing membrane (red). SB: 3 mm, zoom-in SB: 1 mm. (For interpretation of the references to colour in this figure legend, the reader is referred to the web version of this article.)

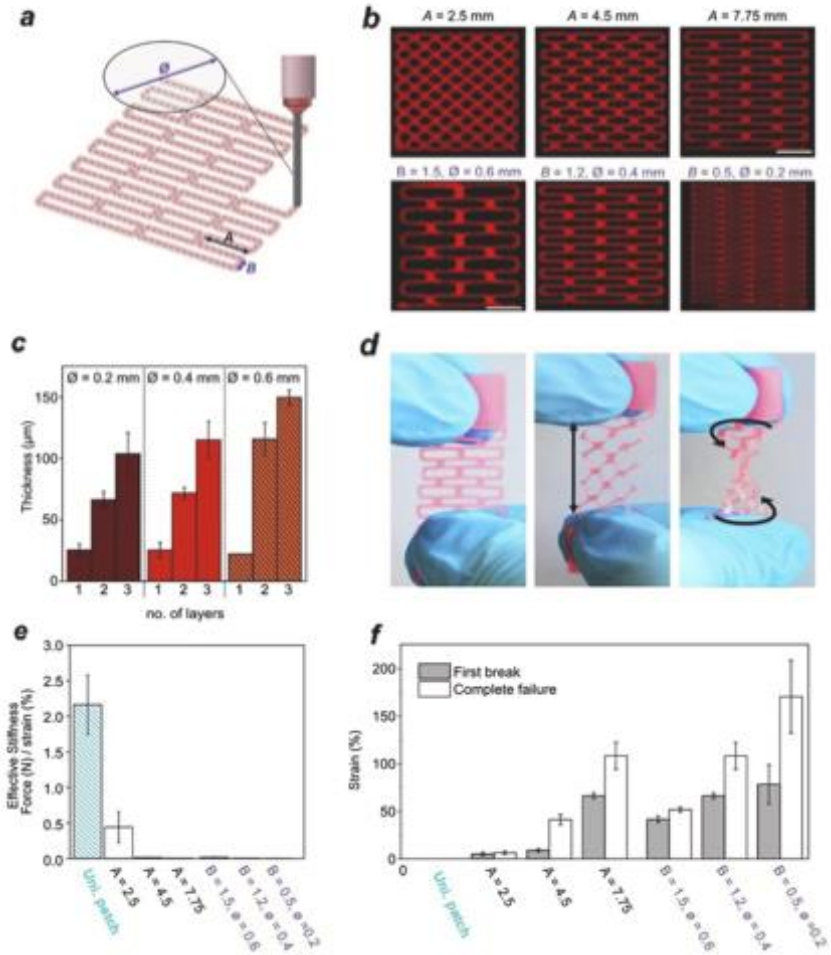


**Fig. 2.** a) Illustration of print procedure of backing membrane with varying line distances A and B, as well as varying nozzle diameter Ø. b) Fluorescent images of designs with line distance A = 2.5, 4.5, 7.75 mm at constant B = 1.2, Ø = 0.4 mm and B = 1.5, 1.2, 0.5, mm at Ø = 0.6, 0.4, 0.2 mm with fixed line distance A = 7.75 mm. SB: 3 mm. c) Layer thickness of printed backing membrane with nozzle diameter Ø = 0.2, 0.4, 0.6 mm with 1, 2, 3 layers, respectively. N = 3. d) Stretching and twisting of printed patches with line distance A = 7.75 mm and B = 1.2 mm. e) Effective stiffness (Force (N) / Strain (%) of printed patches compared to the uniformly printed patch (Uni. patch). N = 3. f) Strain (%) until first break (grey) and complete failure (white) of printed patches compared to the uniformly printed patch. N = 3. Error bars indicate SEM.

used to change the line distance "B" when A was fixed to 7.75 mm (Fig. 2a & 2b). The thickness of the backing membranes was affected by the number of the printed layers and nozzle diameters (Fig. 2 c). Compared to a control uniform patch without geometrical cues, a drastic decrease in effective stiffness of the patches was observed with decreasing line distance A and decreasing nozzle size (Fig. 2e). In addition, the stretchability of the patches could be tuned by varying line distance A and B. Patches printed with the smallest nozzle size and longest line distance A showed an extension capacity of up to 200% compared to the uniform patch (Fig. 2f). The stretchable patches (Fig. 2d) will improve the comfort and adaptation of using in the buccal cavity. For the drug-loaded patches, 0.6 mm nozzle was used for the backing membrane to ensure maximum surface area to deposit drug-laden and alkaline ink, while maintaining an extension capacity of up to 50% at negligible stiffness.

### 3.3. Digitally controlling drug dose in printed patches

In order to control and adjust dose in each printed patch, nozzles with three different diameters were used in the evaluation of the drug content as a function of key printing parameters. As expected, the saquinavir content of the patches increased with increasing the diameter of the nozzles (Fig. 3a). Additionally, for patches printed using the same nozzle diameter, the saquinavir content increased linearly with the increased number of printed layers. The drug content of the patches can easily be adjusted from −20 to 200 µg through these parameters. The

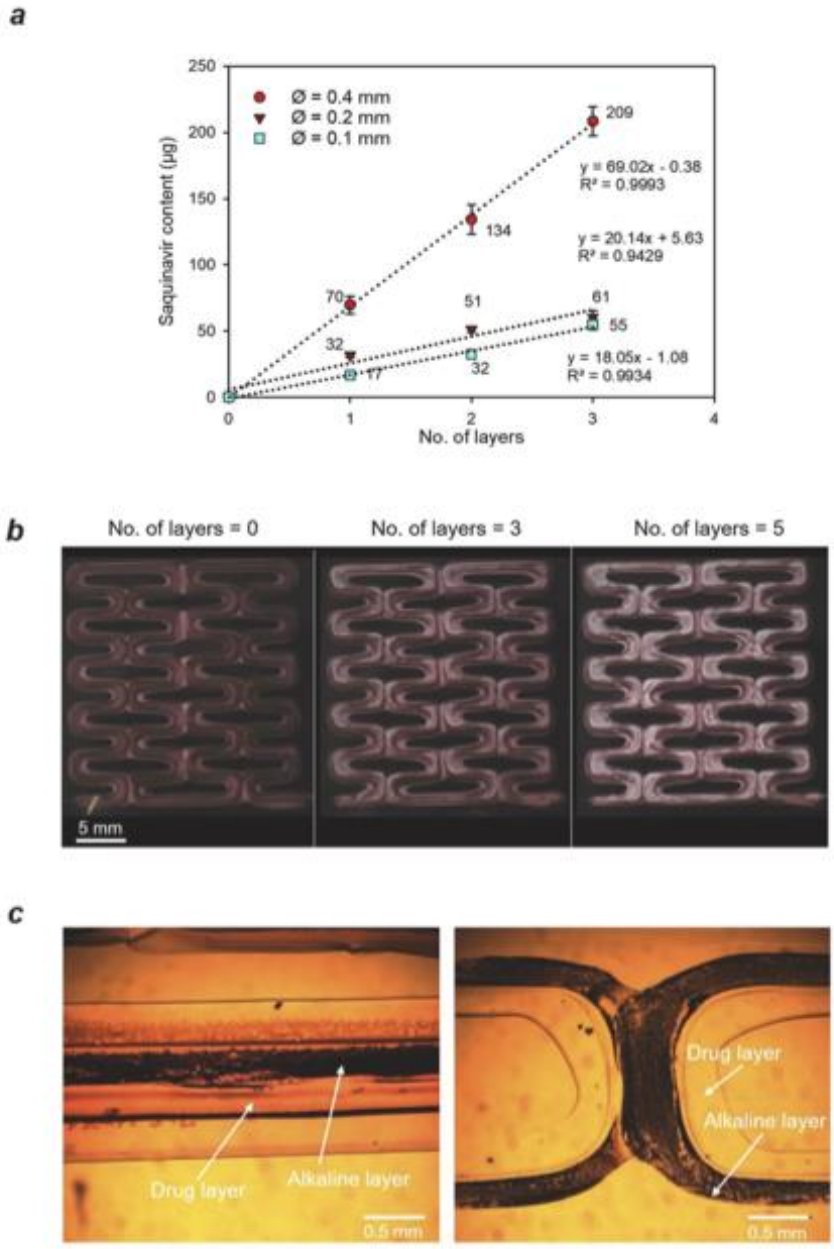


**Fig. 3.** a) Saquinavir content-number of layers scatter profiles for the patches printed using different nozzles. The average values of saquinavir content and the linear regression equation for the data are indicated in the figure. N = 3. The size of nozzle indicated in the figure was the diameter of nozzle. b) Images of the saquinavir microenvironmental pH modifying patches obtained using a digital camera. c). Select images of partial structures of the microenvironmental pH modifying patches (effervescent type) obtained using a bright-field microscope.

saquinavir content of each layer in the patches printed using the largest nozzle (Ø = 400 μm) was ~70 μg. This nozzle size was applied in the final patches for both the alkaline and drug-laden inks. The mass and saquinavir content of the $pH_M$ modifying patches are presented in Table 2.

### 3.4. Morphology of the patches

The images (Fig. 3b) show that the mesh-like patches were printed successfully using the polymer-based inks and the predetermined design. White precipitation was observed in the patches containing alkaline layers due to precipitation of sodium carbonate in the preparation of the patches. Similar to the results obtained from the patches containing fluorescent agents (Fig. 1e), a minimal interface between the alkaline layer and the saquinavir layer was observed (Fig. 3c).

### 3.5. Modifying the microenvironmental pH ($pH_M$)

The $pH_M$ in the vicinity of the patches during dissolution was measured using a micro-pH electrode and the results are shown in Fig. 4a. After 10 min of dissolution, the $pH_M$ in patches containing no sodium carbonate decreased from 6.8 to 5.9, while the $pH_M$ for the patches with 5 layers of alkaline-ink increased from 6.8 to 7.4. As expected, the $pH_M$ generally increased with the increasing number of alkaline layers in the patches. The pH was stable in the time period of 6–10 min during the study period, suggesting that the effervescent reaction between malic acid and carbonate stopped. Overall, the studies show that DIW is a rapid and effective method (without reformulating the inks) to modulate the $pH_M$ by adjusting the layers of acidic and alkaline materials printed in the patches.

### 3.6. Ex vivo permeation studies

According to Hederson-Hasselbalch equation, shifts in pH might affect the dissociation degree of a weakly dissociable drug. The unionized form of the drug is more lipophilic than its ionized form, hence it can better cross the lipid-rich biological membrane. Previous studies showed that saquinavir ($pK_a$ values 7.0 and 5.5) (Branham et al., 2012) has a pH-dependent solubility, increasing pH decreased the solubility of saquinavir and saquinavir mesylate in the pH range of 4.5 to 7.0 (Pathak et al., 2010). Therefore, pH might influence the solubility and tissue partitioning of saquinavir, consequently affect its permeation across oral mucosa. Additionally, $CO_2$ can enhance drug permeation across mucosal membrane as previous described (Eichman and Robinson, 1998). In the present study, microenvironmental pH modifying oromucosal patches with and without $CO_2$ effervescence were fabricated. An *ex vivo* permeation study spanning 5 h was conducted to evaluate the performance of the printed patches. No saquinavir was detected in the receptor chamber. This might be caused by the following reasons: 1) saquinavir content in the patches was too low, 2) saquinavir was too lipophilic (log P = 4.1) and accumulated in the lipid-rich tissue, 3) saquinavir concentration in the receptor media was lower than the detection limit of the HPLC method. As no saquinavir was detected in the receptor chambers, the amount of saquinavir accumulated in the tested tissues was evaluated, as means of quantifying the permeation of saquinavir (Fig. 4b).

**Table 2**
Mass and saquinavir content of the designed patches.

| | Saquinavir microenvironmental pH ($pH_M$) modifying patch | | |
|---|---|---|---|
| | Patch without alkaline layer | Patch with three alkaline layers | Patch with five alkaline layers |
| Saquinavir content (μg) | 79 ± 9 | – | – |
| Mass (mg) | 9.5 ± 0.0 | 10.4 ± 0.1 | 10.6 ± 0.1 |

* The results are present as mean ± SD, n = 5 for the result of saquinavir content. For others, n = 3. The number of saquinavir layer in the all $pH_M$ modifying patches was the same and fixed (3 layers), so we only measured saquinavir content of the patches without alkaline effervescent layer.

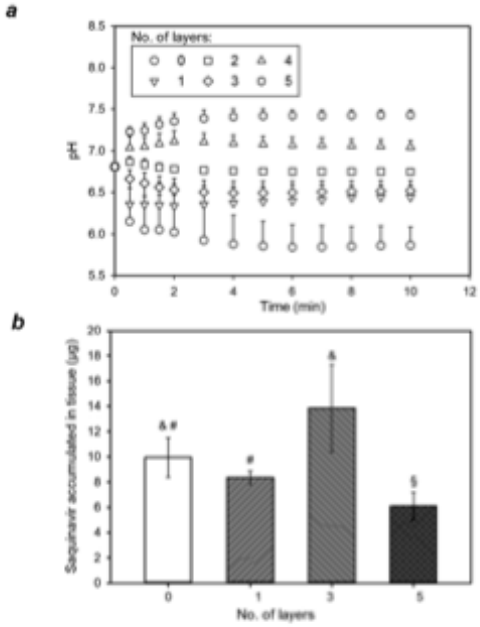


**Fig. 4.** a) Microenvironmental pH-time profiles for the patches with or without sodium carbonate layer during the dissolution process. Results are presented as mean ± SD. "NO. of layers" indicates the number of the alkaline effervescent layer printed in the patches. For the patch with three layers of sodium carbonate, n = 5. For the other patches, n = 3. pH value after 10 min of dissolution are presented in the figure. b) Amount of saquinavir in porcine buccal tissues after permeation study. Values are mean ± SD, n = 4. Symbols above the bars (&, # and §) indicate statistical significance. Bars with similar letters are not significantly different from each other. One-way analysis of variance (ANOVA) was employed and the level of significance was α = 0.05. Tukey's test was then preformed. A p value below 0.05 was considered statistically significant.

Among the tested effervescent patches, the patches containing three and five alkaline layers likely induced approximately the same amount of $CO_2$, because the amount of acidic drug-loaded ink was kept constant. The patches with five alkaline layers exhibited a lower penetration of saquinavir than the patches containing three alkaline layers, which could be due to the higher $pH_M$ hindering the dissolution of saquinavir. Thus, the $pH_M$ had a crucial impact on the permeation of saquinavir for the patches containing three and five alkaline layers. Interestingly, the $pH_M$ around the patches with three alkaline layers and with one alkaline layer appeared similar (Fig. 4a), although more sodium carbonate was added in the patch with three alkaline layers. This might be attributed to that the patch with three alkaline layers produced more $CO_2$ which decreased the $pH_M$. The patches with three alkaline layers exhibited a higher penetration of saquinavir than the patches with one alkaline layer, which also suggests the amount of $CO_2$ played a significant role on saquinavir permeation across mucosal membrane when $pH_M$ around the patches was similar. Although the effervescent patches with three alkaline layers had a higher accumulation of saquinavir in tissues than the patches without effervescence, the difference in saquinavir accumulation upon application of the two types of patches was not

significant. This phenomenon might attribute to that the $pH_M$ around the patches with three alkaline layers was not low enough or/and the amount of $CO_2$ induced by the patches was low. The results indicate that by printing an alkaline effervescent ink and an acidic drug-loaded ink side by side, the pH and the amount of $CO_2$ can be locally modulated. However, the optimal effervescent oromucosal patches should have an appropriate $pH_M$ and induce a suitable amount of $CO_2$ to promote saquinavir penetration in buccal mucosa. However, further studies are required to clarify the mechanism of the increased penetration of saquinavir in the buccal mucosa caused by $CO_2$.

## 4. Conclusion

The present work demonstrates the use of multi-material direct-ink-write printing for rapid design and manufacturing of complex oromucosal patches where several materials are integrated on a sub-millimeter scale. By applying inks based on well-established hydroxypropyl methylcellulose (HPMC) and methyl cellulose (MC) carrier polymers, it was possible to create saquinavir-loaded, $pH_M$-modifying buccal patches with mesh-like geometries that displayed programmable doses as well as unique stretchable mechanical properties. Based on alterations in the digital design, effervescent $pH_M$-modifying buccal patches with intermediate amounts of carbonate and weakly acidic microenvironments could be prepared. However, an optimal effervescent oromucosal patches should have an appropriate $pH_M$ and induce a suitable amount of $CO_2$ in order to promote saquinavir penetration in buccal mucosa. The presented methodology is widely applicable and may thus serve as an inspiration for programmable producing patches for personalized buccal drug delivery with unique patient comfort and compliance.

### *CRediT authorship contribution statement*

**Shaolong He:** Conceptualization, Data curation, Investigation, Formal analysis, Writing – original draft. **Carmen Radeke:** Conceptualization, Data curation, Investigation, Formal analysis, Writing – original draft. **Jette Jacobsen:** Methodology, Data curation, Writing-review & editing. **Johan Ulrik Lind:** Conceptualization, Methodology, Funding acquisition, Writing-review & editing. **Huiling Mu:** Conceptualization, Methodology, Funding acquisition, Writing-review & editing.

### Declaration of Competing Interest

The authors declare that they have no known competing financial interests or personal relationships that could have appeared to influence the work reported in this paper.

### Acknowledgements

The China Scholarship Council (201708510087) is acknowledged for the financial support to Shaolong He. Johan Ulrik Lind and Carmen Radeke would like to acknowledge The Lundbeck Foundation (R250-2017-1425 & R250-2017-1426) and The Independent Research Fund Denmark (8048-00050) for their support. We would also like to acknowledge Susan Weng Larsen for the help of HPLC analysis, Rita Wulff Rasmussen and Mette Frandsen for the technical support.

### References

Alomari, M., Mohamed, F.H., Basit, A.W., Gaisford, S., 2015. Personalised dosing: Printing a dose of one's own medicine. Potential 2D 3D Print. Pharm. Dev. 494 (2), 568–577. https://doi.org/10.1016/j.ijpharm.2014.12.006.

Bassi, P., Kaur, G., 2010. pH modulation: a mechanism to obtain pH-independent drug release. Expert Opin. Drug Deliv. 7 (7), 845–857. https://doi.org/10.1517/17425247.2010.491508.

Bergström, C.A.S., Luthman, K., Artursson, P., 2004. Accuracy of calculated pH-dependent aqueous drug solubility. Eur. J. Pharm. Sci. 22 (5), 387–398. https://doi.org/10.1016/j.ejps.2004.04.006.

Branham, M.L., Moyo, T., Govender, T., 2012. Preparation and solid-state characterization of ball milled saquinavir mesylate for solubility enhancement. Eur. J. Pharm. Biopharm. 80 (1), 194–202. https://doi.org/10.1016/j.ejpb.2011.08.005.

Buanz, A., Gaisford, S., Hilton, S., 2015. Foreword: 3i printing pharmaceuticals. Potential 2D 3D Print. Pharm. Dev. 494 (2), 553. https://doi.org/10.1016/j.ijpharm.2015.05.044.

Buchanan, C.M., Buchanan, N.L., Edgar, K.J., Little, J.L., Ramsey, M.G., Ruble, K.M., Wacher, V.J., Wempe, M.F., 2008. Pharmacokinetics of Saquinavir After Intravenous and Oral Dosing of Saquinavir: Hydroxybutenyl-β-Cyclodextrin Formulations. Biomacromolecules 9 (1), 305–313. https://doi.org/10.1021/bm700827h.

Caon, T., Kratz, J.M., Kuminek, G., Heller, M., Konig, R.A., Micke, G.A., Koester, L.S., Simões, C.M.O., 2015. Oral saquinavir mesylate solid dispersions: In vitro dissolution, Caco-2 cell model permeability and in vivo absorption studies. Powder Technol. 269, 200–206. https://doi.org/10.1016/j.powtec.2014.09.012.

Chinna Reddy, P., Chaitanya, K.S.C., Madhusudan Rao, Y., 2011. A review on bioadhesive buccal drug delivery systems: current status of formulation and evaluation methods. Daru. J. Fac. Pharm. Tehran Univ. Med. Sci. 19, 385–403. http://www.ncbi.nlm.nih.gov/pmc/articles/PMC3436075/.

Cho, H.-W., Baek, S.-H., Lee, B.-J., Jin, H.-E., 2020. Orodispersible Polymer Films with the Poorly Water-Soluble Drug, Olanzapine: Hot-Melt Pneumatic Extrusion for Single-Process 3D Printing. Pharmaceutics 12 (8), 692. https://doi.org/10.3390/pharmaceutics12080692.

Daly, R., Harrington, T.S., Martin, G.D., Hutchings, I.M., 2015. Inkjet printing for pharmaceutics – A review of research and manufacturing. Potential 2D 3D Print. Pharm. Dev. 494 (2), 554–567. https://doi.org/10.1016/j.ijpharm.2015.03.017.

Dixit, R.P., Puthli, S.P., 2009. Oral strip technology: Overview and future potential. J. Controlled Release 139 (2), 94–107. https://doi.org/10.1016/j.jconrel.2009.06.014.

DOW chemical company, 2013. Chemistry of METHOCEL, Cellulose Ethers - A Technical Review. Chem. METHOCEL Cellul. Ethers - Tech. Rev. URL https://www.stobec.com/DATA/PRODUIT/1688~v~data_8733.pdf (accessed 10.14.21).

DOW chemical company and Colorcon, 2021. Technical Bulletin - METHOCEL. Tech. Bull. - METHOCEL. URL https://www.colorcon.com/cn/products-formulation/all-products/download/777/2558/34?method=view (accessed 10.14.21).

Ehtezazi, T., Algellay, M., Islam, Y., Roberts, M., Dempster, N.M., Sarker, S.D., 2018. The Application of 3D Printing in the Formulation of Multilayered Fast Dissolving Oral Films. J. Pharm. Sci. 107 (4), 1076–1085. https://doi.org/10.1016/j.xphs.2017.11.019.

Eichman, J.D., Robinson, J.R, 1998. Mechanistic Studies on Effervescent-Induced Permeability Enhancement. Pharm. Res. 15 (6), 925–930. https://doi.org/10.1023/A:1011936901638.

Elbadawi, M., Nikjoo, D., Gustafson, T., Gaisford, S., Basit, A.W., 2021. Pressure-assisted microsyringe 3D printing of oral films based on pullulan and hydroxypropyl methylcellulose. Int. J. Pharm. 595, 120197. https://doi.org/10.1016/j.ijpharm.2021.120197.

Eleftheriadis, G.K., Monou, P.K., Bouropoulos, N., Boetker, J., Rantanen, J., Jacobsen, J., Vizirianakis, I.S., Fatouros, D.G., 2020. Fabrication of Mucoadhesive Buccal Films for Local Administration of Ketoprofen and Lidocaine Hydrochloride by Combining Fused Deposition Modeling and Inkjet Printing. J. Pharm. Sci. 109 (9), 2757–2766. https://doi.org/10.1016/j.xphs.2020.05.022.

Eleftheriadis, G.K., Ritzoulis, C., Bouropoulos, N., Tzetzis, D., Andreadis, D.A., Boetker, J., Rantanen, J., Fatouros, D.G., 2019. Unidirectional drug release from 3D printed mucoadhesive buccal films using FDM technology: In vitro and ex vivo evaluation. Eur. J. Pharm. Biopharm. 144, 180–192. https://doi.org/10.1016/j.ejpb.2019.09.018.

Genina, N., Fors, D., Vakili, H., Ihalainen, P., Pohjala, L., Ehlers, H., Kassamakov, I., Haeggström, E., Vuorela, P., Peltonen, J., Sandler, N., 2012. Tailoring controlled-release oral dosage forms by combining inkjet and flexographic printing techniques. Eur. J. Pharm. Sci. 47 (3), 615–623. https://doi.org/10.1016/j.ejps.2012.07.020.

Genina, N., Janßen, E.M., Breitenbach, A., Breitkreutz, J., Sandler, N., 2013. Evaluation of different substrates for inkjet printing of rasagiline mesylate. Eur. J. Pharm. Biopharm. 85 (3), 1075–1083. https://doi.org/10.1016/j.ejpb.2013.03.017.

Gittings, S, 2017. Development of bioelevant simulated salivary fluids for application in dissolution testing (PhD Thesis). University of Nottingham, University Park, Nottingham, UK. http://eprints.nottingham.ac.uk/39862/1/Thesis%20FINAL%20version%20for%20submission_Sally%20Gittings.pdf.

He, S., Østergaard, J., Ashna, M., Nielsen, C.U., Jacobsen, J., Mu, H., 2020. Microenvironmental pH modifying films for buccal delivery of saquinavir: Effects of organic acids on pH and drug release in vitro. Int. J. Pharm. 585, 119567. https://doi.org/10.1016/j.ijpharm.2020.119567.

Janßen, E.M., Schliephacke, R., Breitenbach, A., Breitkreutz, J., 2013. Drug-printing by flexographic printing technology—A new manufacturing process for orodispersible films. Int. J. Pharm. 441 (1-2), 818–825. https://doi.org/10.1016/j.ijpharm.2012.12.023.

Kalepu, S., Nekkanti, V., 2015. Insoluble drug delivery strategies: review of recent advances and business prospects. Acta Pharm. Sin. B 5 (5), 442–453. https://doi.org/10.1016/j.apsb.2015.07.003.

Kim, A.E., Dintaman, J.M., Waddell, D.S., Silverman, J.A., 1998. Saquinavir, an HIV Protease Inhibitor, Is Transported by P-Glycoprotein. J. Pharmacol. Exp. Ther. 286, 1439.

Krampe, R., Visser, J.C., Frijlink, H.W., Breitkreutz, J., Woerdenbag, H.J., Preis, M., 2016. Oromucosal film preparations: points to consider for patient centricity and manufacturing processes. Expert Opin. Drug Deliv. 13 (4), 493–506. https://doi.org/10.1517/17425247.2016.1118048.

Kupferschmidt, H.H.T., Fattinger, K.E., Ha, H.R., Follath, F., Krähenbühl, S., 1998. Grapefruit juice enhances the bioavailability of the HIV protease inhibitor saquinavir

in man. Br. J. Clin. Pharmacol. 45 (4), 355–359. https://doi.org/10.1046/j.1365-2125.1998.t01-1-00687.x.
Lam, J.K.W., Xu, Y., Worsley, A., Wong, I.C.K., 2014. Oral transmucosal drug delivery for pediatric use. Drug Deliv. Paediatr. Popul. Are We At 73, 50–62. https://doi.org/10.1016/j.addr.2013.08.011.
Lind, J.U., Busbee, T.A., Valentine, A.D., Pasqualini, F.S., Yuan, H., Yadid, M., Park, S.-J., Kotikian, A., Nesmith, A.P., Campbell, P.H., Vlassak, J.J., Lewis, J.A., Parker, K.K., 2017. Instrumented cardiac microphysiological devices via multimaterial three-dimensional printing. Nat. Mater. 16 (3), 303–308. https://doi.org/10.1038/nmat4782.
Loftsson, T., Brewster, M.E., 2010. Pharmaceutical applications of cyclodextrins: basic science and product development. J. Pharm. Pharmacol. 62, 1607–1621. https://doi.org/10.1111/j.2042-7158.2010.01030.x.
Madhav, N.V.S., Shakya, A.K., Shakya, P., Singh, K., 2009. Orotransmucosal drug delivery systems: A review. J. Controlled Release 140 (1), 2–11. https://doi.org/10.1016/j.jconrel.2009.07.016.
Marxen, E., Axelsen, M.C., Pedersen, A.M.L., Jacobsen, J., 2016. Effect of cryoprotectants for maintaining drug permeability barriers in porcine buccal mucosa. Int. J. Pharm. 511 (1), 599–605. https://doi.org/10.1016/j.ijpharm.2016.07.014.
Morales, J.O., McConville, J.T., 2011. Manufacture and characterization of mucoadhesive buccal films. Eur. J. Pharm. Biopharm. 77 (2), 187–199. https://doi.org/10.1016/j.ejpb.2010.11.023.
Musazzi, U.M., Selmin, F., Ortenzi, M.A., Mohammed, G.K., Franzé, S., Minghetti, P., Cilurzo, F., 2018. Personalized orodispersible films by hot melt ram extrusion 3D printing. Int. J. Pharm. 551 (1-2), 52–59. https://doi.org/10.1016/j.ijpharm.2018.09.013.
Obonga, W., Nnadi, C., Onyechi, A., 2013. Preformulation Study of Saquinavir: pH-Dependent Solubility, Ionization and Partition Coefficients. ARPN J. Sci. Technol. 3, 551–556. https://www.semanticscholar.org/paper/ARPN-Journal-of-Science-and-Study-of-Saquinavir%3A-Obonga-Nnadi/7abfc9e15c48aac2a4758dd68fb426f21816e3e8.
Pathak, S.M., Musmade, P., Dengle, S., Karthik, A., Bhat, K., Udupa, N., 2010. Enhanced oral absorption of saquinavir with Methyl-Beta-Cyclodextrin—Preparation and in vitro and in vivo evaluation. Eur. J. Pharm. Sci. 41 (3-4), 440–451. https://doi.org/10.1016/j.ejps.2010.07.013.
Pechová, V., Gajdziok, J., Musilík, J., Vetchý, D., 2018. Development of Orodispersible Films Containing Benzydamine Hydrochloride Using a Modified Solvent Casting Method. AAPS PharmSciTech 19 (6), 2509–2518. https://doi.org/10.1208/s12249-018-1088-y.
Preis, M., Breitkreutz, J., Sandler, N., 2015. Perspective: Concepts of printing technologies for oral film formulations. Potential 2D 3D Print. Pharm. Dev. 494 (2), 578–584. https://doi.org/10.1016/j.ijpharm.2015.02.032.
Rahman, J., Quodbach, J., 2021. Versatility on demand – The case for semi-solid micro-extrusion in pharmaceutics. Adv. Drug Deliv. Rev. 172, 104–126. https://doi.org/10.1016/j.addr.2021.02.013.
Raijada, D., Genina, N., Fors, D., Wisaeus, E., Peltonen, J., Rantanen, J., Sandler, N., 2013. A Step Toward Development of Printable Dosage Forms for Poorly Soluble Drugs. J. Pharm. Sci. 102 (10), 3694–3704. https://doi.org/10.1002/jps.23678.
Sexane-Viaño, L., Januskaite, P., Alvarez-Lorenzo, C., Basit, A.W., Goyanes, A., 2021a. Semi-solid extrusion 3D printing in drug delivery and biomedicine: Personalised solutions for healthcare challenges. J. Controlled Release 332, 367–389. https://doi.org/10.1016/j.jconrel.2021.02.027.
Sexane-Viaño, L., Trenfield, S.J., Basit, A.W., Goyanes, A., 2021b. Translating 3D printed pharmaceuticals: From hype to real-world clinical applications. Adv. Drug Deliv. Rev. 174, 553–575. https://doi.org/10.1016/j.addr.2021.05.003.
Sieger, P., Cui, Y., Scheuerer, S., 2017. pH-dependent solubility and permeability profiles: A useful tool for prediction of oral bioavailability. Eur. J. Pharm. Sci. 105, 82–90. https://doi.org/10.1016/j.ejps.2017.04.016.
Speer, I., Preis, M., Breitkreutz, J., 2018. Novel Dissolution Method for Oral Film Preparations with Modified Release Properties. AAPS PharmSciTech 20, 7. https://doi.org/10.1208/s12249-018-1255-1.
Sudhakar, Y., Kuotsu, K., Bandyopadhyay, A.K., 2006. Buccal bioadhesive drug delivery — A promising option for orally less efficient drugs. J. Controlled Release 114 (1), 15–40. https://doi.org/10.1016/j.jconrel.2006.04.012.
Tagami, T., Yoshimura, N., Goto, E., Noda, T., Ozeki, T., 2019. Fabrication of Muco-Adhesive Oral Films by the 3D Printing of Hydroxypropyl Methylcellulose-Based Catechin-Loaded Formulations. Biol. Pharm. Bull. 42 (11), 1898–1905. https://doi.org/10.1248/bpb.b19-00481.
Takano, J., Maeda, K., Bolger, M.B., Sugiyama, Y., 2016. The Prediction of the Relative Importance of CYP3A/P-glycoprotein to the Nonlinear Intestinal Absorption of Drugs by Advanced Compartmental Absorption and Transit Model. Drug Metab. Dispos. 44 (11), 1808–1818. https://doi.org/10.1124/dmd.116.070011.
Taniguchi, C., Kawabata, Y., Wada, K., Yamada, S., Onoue, S., 2014. Microenvironmental pH-modification to improve dissolution behavior and oral absorption for drugs with pH-dependent solubility. Expert Opin. Drug Deliv. 11 (4), 505–516. https://doi.org/10.1517/17425247.2014.881798.
Tian, Y.u., Orlu, M., Woerdenbag, H.J., Scarpa, M., Kiefer, O., Kottke, D., Sjöholm, E., Öblom, H., Sandler, N., Hinrichs, W.L.J., Frijlink, H.W., Breitkreutz, J., Visser, J.C., 2019. Oromucosal films: from patient centricity to production by printing techniques. Expert Opin. Drug Deliv. 16 (9), 981–993. https://doi.org/10.1080/17425247.2019.1652595.
Vetchý, D., Landová, H., Gajdziok, J., Doležel, P., Daněk, Z., Štembírek, J., 2014. Determination of dependencies among in vitro and in vivo properties of prepared mucoadhesive buccal films using multivariate data analysis. Eur. J. Pharm. Biopharm. 86 (3), 498–506. https://doi.org/10.1016/j.ejpb.2013.12.002.
Wickström, H., Palo, M., Rijckaert, K., Kolakovic, R., Nyman, J.O., Määttänen, A., Ihalainen, P., Peltonen, J., Genina, N., de Beer, T., Löbmann, K., Rades, T., Sandler, N., 2015. Improvement of dissolution rate of indomethacin by inkjet printing. Drug Deliv. Specif. Popul. 75, 91–100. https://doi.org/10.1016/j.ejps.2015.03.009.